UNIVERSITY OF ICELAND

Ph.D. Thesis

in Geology

Surtsey: Basalt alteration by seawater in a low-temperature geothermal system

Simon Prause

March 2023

FACULTY OF EARTH SCIENCES

Surtsey: Basalt alteration by seawater in a low-temperature geothermal system

Simon Prause

Dissertation submitted in partial fulfillment of a
Philosophiae Doctor degree in Geology

Ph.D. Committee

Dr. Tobias B. Weisenberger
Dr. Andri Stefánsson
Dr. Barbara I. Kleine
Institute of Earth Sciences, University of Iceland

Opponents

Dr. Alessio Langella
Università degli Studi di Napoli Federico II, Dipartimento di Scienze della Terra, dell'Ambiente e delle Risorse (DiSTAR), Naples, Italy

Dr. Benjamin Tutolo
Department of Geoscience, University of Calgary, Calgary, Canada

Faculty of Earth Sciences
School of Engineering and Natural Sciences
University of Iceland
Reykjavik, March 2023

Surtsey: Basalt alteration by seawater in a low-temperature geothermal system
Surtsey: Low-T basalt alteration by seawater
Dissertation submitted in partial fulfillment of a *Ph.D.* degree in Geology

Faculty of Earth Sciences
School of Engineering and Natural Sciences
University of Iceland
Sturlugata 7
102, Reykjavik
Iceland

Telephone: 525 4000

Bibliographic information:
Simon Prause, 2023, *Surtsey: Basalt alteration by seawater in a low-temperature geothermal system*, PhD dissertation, Faculty of Earth Sciences,
University of Iceland, 132 pp.

Author ORCID: 0000-0003-4613-6512
ISBN: 978-9935-9555-9-3

Printing: Háskólaprent
Reykjavik, Iceland, March 2023

Abstract

The chemical interaction between seawater and basalt at low temperatures (≤150°C) ranks among the more significant factors controlling the composition of seawater and the oceanic crust. However, the time-integrated geochemical and petrographic outcomes of this process remain understudied. This work investigates the effects of time, temperature, crystallinity, and water-rock ratio on seawater-basalt interaction through a combination of petrographic and geochemical analyses of drill-cores obtained in 1979 and 2017 from the volcanic ocean island of Surtsey as well as through geochemical modeling.

The rates of basaltic glass palagonitization and formation of secondary minerals are positively correlated with temperature. Palagonitized glass undergoes maturation from mostly amorphous to increasingly crystalline clay mineral-rich textures. Direction and magnitude of the element flux associated with the different stages of glass alteration are distinct for most elements. Rare earth elements, Hf, Ta, Zr, Nb and Y remain immobile, whereas FeO and TiO_2 are slightly mobile during palagonite maturation. The entire process of basaltic tuff alteration at Surtsey indicates a net source of dissolved Ca, Al and SiO_2 and a net sink of dissolved Mg and Na for seawater.

Geochemical modeling of the alteration process suggests that crystalline and glassy basalts progress through a similar series of reactions, characterized by initial dissolution of glasses and primary minerals, followed by formation of phyllosilicates, oxides, hydroxides, carbonates, sulfates, sulfides and eventually zeolites. Water-rock ratio and pH are identified as the main factors determining the dominant mineral assemblage, whereas temperature and rock crystallinity are less important for the outcome of alteration.

Útdráttur

Einn af ríkjandi þáttum sem stýra samsetningu sjós og úthafsskorpu er efnafræðilegt samspil sjós og basalts við lágan hita (≤150°C). Jarðefnafræði og þau efnahvörf sem hafa áhrif á þetta ferli hins vegar ekki vel skilgreind. Í þessu verki voru áhrif tíma, hita, kristöllunar bergs og á sampil sjós og basalts rannsökuð með samþættingu jarðefnafræðilegra líkana og jarðefnafræðilegra greininga á borholukjörnum sem safnað var í Surtsey á árunum 1979 og 2017.

Ummyndunarhraði basaltglers í mógler (palagónít) og myndun síðsteinda eru jákvætt fylgin hitastigi. Móglerið undirgengst umbreytingu úr því að vera að mestu ókristallað og yfir í vaxandi kristallaða og leirsteindaríka textúra. Hreyfnaleiki frumefna í tengslum við mismunandi stig glerummyndunar er skýr fyrir flest frumefni. Frumefnin Hf, Ta, Zr, Nb og Y haldast óhreyfanleg á meðan FeO og TiO_2 eru örlítið hreyfanleg. Heildarferli ummyndunar á basalttúffi í Surtsey bendir til útskolunar á Ca, Al og SiO_2 úr berginu og upptöku á uppleystu Mg og Na úr sjó.

Jarðefnafræðileg líkön af ummyndunarferlinu gefa til kynna að bæði kristallað og glerjað basalt fari í gegnum samskonar röð efnahvarfa. Þau einkennast í fyrstu af uppleysingu glers og frumsteinda, þvínæst myndun lagsílíkata, oxíða, hýdroxíða, karbónata, súlfata, súlfíða og að lokum zeólíta. Hlutfall vatns og bergs ásamt sýrustigi eru meginþættir sem ákvarða ríkjandi steindafylki og samsetningu, en hitastig og kristöllun bergs eru þýðingarminni fyrir útkomu ummyndunarinnar.

Dedicated to Yingying, who stubbornly refused to stop believing in me.

Preface

This doctoral thesis presents the results of research carried out at the University of Iceland (Háskóli Íslands, HÍ) and the Iceland GeoSurvey (Íslenskar Orkurannsóknir, ÍSOR) between 2017 and 2022. The PhD project was funded through a grant by the Icelandic Science Fund, ICF-RANNÍS (project number 163083-051) and the Landsvirkjun Energy Research Fund (contract number NÝR-29-2021). The product of this research is presented in the form of three manuscripts, two of which have been published at the time of writing and one of which is ready to be submitted for publication. The manuscripts are listed below:

1. **Prause, S.**, Weisenberger, T.B., Cappelletti, P., Grimaldi, C., Rispoli, C., Jónasson, K., Jackson, M.D., Gudmundsson, M.T. (2020). Alteration progress within the Surtsey hydrothermal system, SW Iceland – A time-lapse petrographic study of cores drilled in 1979 and 2017. *Journal of Volcanology and Geothermal Research*, 392, 106754
2. **Prause, S.**, Weisenberger, T.B., Kleine, B.I., Monien, P., Rispoli, C., Stefánsson, A., (2022). Alteration of basaltic glass within the Surtsey hydrothermal system, Iceland – Implication to oceanic crust seawater interaction. *Journal of Volcanology and Geothermal Research*, 429, 107581
3. **Prause, S.**, Kleine, B.I., Weisenberger, T.B., Stefánsson, A. (in prep.). Low-temperature seafloor alteration and its impact on the mineralogy and chemical composition of the oceanic crust – A kinetic reaction path model. In preparation for *Chemical Geology*

Further contributions were made to the following articles that are not subject to this thesis:

Jackson, M.D., Gudmundsson, M.T., Weisenberger, T.B., Michael Rhodes, J., Stefánsson, A., Kleine, B.I., Lippert, P.C., Marquardt, J.M., Reynolds, H.I., Kück, J., Marteinsson, V. þ., Vannier, P., Bach, W., Barich, A., Bergsten, P., Bryce, J.G., Cappelletti, P., Couper, S., Fahnestock, M.F., Gorny, C.F., Grimaldi, C., Groh, M., Gudmundsson, Á., Gunnlaugsson, Á.T., Hamlin, C., Högnadóttir, T., Jónasson, K., Jónsson, S.S., Jørgensen, S.L., Klonowski, A.M., Marshall, B., Massey, E., McPhie, J., Moore, J.G., Ólafsson, E.S., Onstad, S.L., Perez, V., **Prause, S.**, Snorrason, S.P., Türke, A., White, J.D., Zimanowski, B. (2019). SUSTAIN drilling at Surtsey volcano, Iceland, tracks hydrothermal and microbiological interactions in basalt 50 years after eruption. *Scientific Drilling*, 25, 35–46.

Kleine, B.I., Stefánsson, A., Kjartansdóttir, R., **Prause, S.**, Weisenberger, T.B., Reynolds, H.I., Sveinbjörnsdóttir, Á.E., Jackson, M.D., Gudmundsson, M.T. (2020). The Surtsey volcano geothermal system: An analogue for seawater-oceanic crust interaction with implications for the elemental budget of the oceanic crust. *Chemical Geology*, 550, 119702.

Weisenberger, T.B., Guðmundsson, M.T., Jackson, M.D., Gorny, C.F., Türke, A., Kleine, B.I., Marshall, B., Jørgensen, S.L., Marteinsson, V. þ., Stefánsson, A., White, J.D.L., Barich, A., Bergsten, P., Bryce, J., Couper, S., Fahnestock, M.F., Franzson, H., Grimaldi, C., Groh, M., Guðmundsson, Á., Gunnlaugsson, Á. þ., Hamelin, C., Högnadóttir, Þ., Jónasson, K., Jónsson, S.S., Klonowski, A.M., Kück, J., Magnússon, R.L., Massey, E., McPhie, J., Ólafsson, E.S., Onstad, S.L., **Prause, S.**, Perez, V., Rhodes, J.M., Snorrason, S.P. (2019). Operational Report for the 2017 Surtsey Underwater volcanic System for Thermophiles, Alteration processes and INnovative Concretes (SUSTAIN) drilling project at Surtsey Volcano, *ICDP Operational Report*.

Table of Contents

List of Figures

List of Tables

Acknowledgements

The history of science is the story of many great people making revolutionary breakthroughs on their own – or so I thought when I began working on this project. Today, I understand that the game of science more closely resembles a team sport rather than a heavyweight boxing championship. Many individuals are working together day by day to keep the wheels of scientific progress turning. Over the past five years, I had the privilege of meeting a great number of extraordinary and hard-working people whose abilities and achievements have taught me no small amount of humility while inspiring me to strive to become a better researcher myself. All of them have lent their support to the success of this thesis. Without them, this work would not have been possible. They are named below.

First and foremost, I thank my main supervisor, Tobias Weisenberger, for mentoring my early stumbling steps as a scientist. Over the years, I have come to appreciate Tobias' goal-oriented mindset and experience, which helped put me back on track when I got lost in the jungle of research. His ability to remain focused on what's important no matter what helped to guide my work, especially in the early stages. Thank you, Tobias, for your advice and mentorship over the past five years!

I am grateful to my second supervisor, Andri Stefánsson, for the many thought-provoking exchanges that often delivered new insights into the problems I sought to tackle in my research. More than once did his unique perspective and acumen help to reshape and improve my understanding of the subject and to truly see the bigger picture.

I would like to thank Barbara Kleine, who shared with me her considerable expertise in the area of kinetic reaction path modeling by teaching me the ropes of PHREEQC and patiently answering my *many* questions on the subject. Thank you for all the helpful conversations and for being an excellent teacher.

Many people contributed to the writing of the three papers summarized in this thesis. I thank Piergiulio Cappelletti, Carla Grimaldi and Concetta Rispoli of the University of Naples, Kristján Jónasson of the Icelandic Institute of Natural History, Magnús Tumi Gudmundsson of Nordvulk, Marie Jackson of the University of Utah and Patrick Monien of the University of Bremen for all of their input that helped to shape this work. P. Bergsten, C. Gorny and G.H. Guðfinnsson contributed valuable feedback on matters related to microbiology, volcanology and electron microprobe analysis, respectively. The Iceland GeoSurvey (ÍSOR) and University of Iceland are thanked for providing me with a space to perform my research. This project would not have been possible without funding by the Icelandic Research Fund (ICF-RANNÍS), the International Continental Scientific Drilling Program (ICDP) and the Landsvirkjun Energy Research Fund.

Last, but certainly not least, I wish to express my gratitude to my family, including my parents Birgit and Achim, my sister Esther and my quasi-brother-in-law Frank who all were highly supportive during my work on this project. My wife accompanied me through the many ups and downs, supporting and encouraging me throughout my journey. I would do it all over again, just to meet you here in Iceland, Yingying. Thank you for being you!

1 Introduction

The ocean floor represents nearly three quarters of Earth's surface. As continental plates are pulled apart along the Mid-Ocean Ridges (MOR), the underlying mantle is subjected to partial decompression melting. The resulting melts ascend and cool, forming the basaltic rock that makes up most of the oceanic crust. Permeability provides pathways for seawater to enter crustal aquifers, where chemical exchange between the infiltrating fluids and basaltic minerals and glasses takes place. This natural "chemical reactor" has a profound influence on both the composition of seawater and the oceanic crust, which is eventually subducted back into the mantle at convergent plate margins.

The importance of seafloor hydrothermal processes to global elemental budgets was first recognized in the 1960s and 70s when it became apparent that conduction-based models consistently overestimated the magnitude of crustal heat-flow (e.g., Davis and Lister, 1974; Langseth et al., 1966; McKenzie, 1967; Parsons and Sclater, 1977; Von Herzen and Uyeda, 1963), due to the interference of convective cooling by geothermal activity (Lister, 1972; Williams et al., 1974). Since then, further studies have revealed that hydrothermal processes significantly enhance plate cooling of oceanic crust younger than 65 ± 10 Ma (Alt, 2003; Stein and Stein, 1994; Wheat and Fisher, 2008), indicating high rates of annual fluid flux. Today, a distinction is generally made between high-temperature hydrothermal circulation (250-400°C) taking place along or near MOR and off-axis low-temperature (≤150°C) processes that dominate the remaining seafloor (e.g., Alt, 2003, 1995; Coogan and Gillis, 2018; Fisher and Wheat, 2010; Staudigel, 2014; Wheat and Fisher, 2008; Wheat and Mottl, 2000). While the former is known to cause more drastic fluid and bulk rock geochemical changes, the latter is of global significance due to the larger associated volumes of seawater interacting with the oceanic crust (Coogan and Gillis, 2018; Staudigel, 2014).

Current models propose marine sediments to act as an isolating thermal blanket that partially or fully inhibits fluid flow in and out of the crustal aquifer (Coogan and Gillis, 2018; Spinelli et al., 2004). Therefore, low-temperature geothermal activity and fluid flow are likely focused between areas of rough basement topography, e.g., seamounts, where the crustal aquifer penetrates through the superimposed sediment cover (Fig. 1.1). However, studies of the geochemistry and geohydrology of such settings are challenging and potentially biased towards zones of high flow rates that may not be representative of the entire oceanic floor (e.g., Staudigel, 2014; Alt et al., 1996a; Bach et al., 2003; Coogan and Gillis, 2018). The chemical composition, elemental mobility, and alteration mineralogy of altered oceanic crust (AOC) thus remain uncertain.

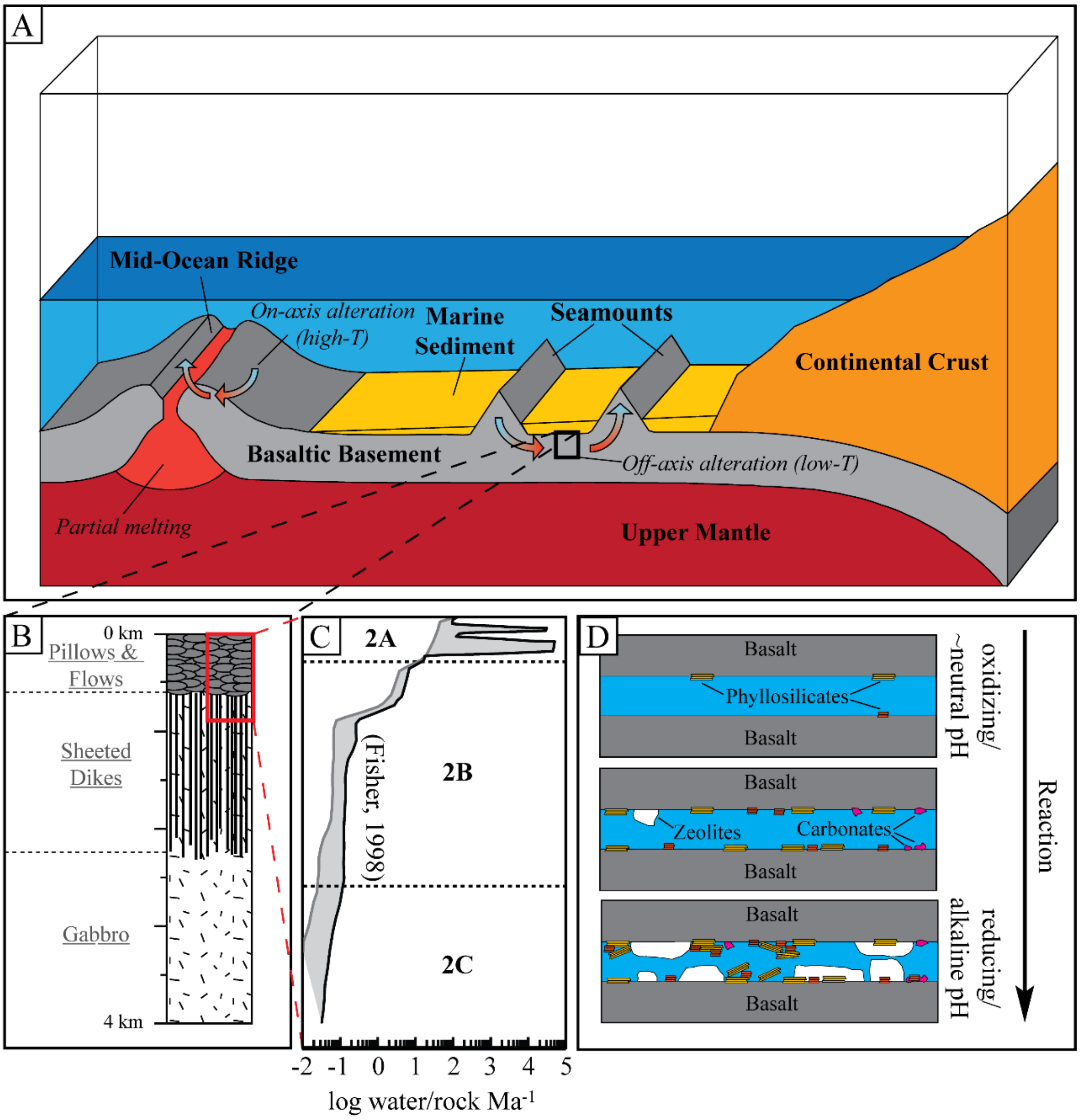

Figure 1.1 *A) Sketch of the oceanic crust environment. Basaltic crust is generated at Mid-Ocean Ridges and initially subjected to high-temperature (≥250°C) on-axis alteration. Over time the crust cools, thickens and moves away from the ridge axis due to seafloor spreading. Sediment thickness increases with crustal age. At this stage, off-axis geothermal circulation takes place at generally lower temperatures (≤150°C), for example at high-topography basement outcrops such as seamounts. B) Schematic cross section of the oceanic crust showing upper volcanic sections (pillows and flows), sheeted dike complex and massive gabbro. C) Physical water-rock ratios per million years with depth after Fisher (1998). D) Schematic progression of low-temperature basalt alteration by seawater, including secondary mineral formation and changes in water composition.*

The ocean island of Surtsey, SW Iceland, is the youngest member of the Vestmannaeyjar archipelago. Shortly after the island formed in a series of phreatomagmatic and effusive eruptions on the ocean floor between 1963 and 1967 (details below) a low-temperature geothermal system developed in the seawater-flushed alkali-basaltic tephra deposits of the island (Jakobsson, 1979; Jakobsson and Moore, 1982; Schipper et al., 2015; Thórarinsson, 1967a). Surtsey is considered to represent an accessible analogue to seafloor-hosted off-axis geothermal systems (e.g., Jackson et al., 2015, 2019; Kleine et al., 2020). Drill cores retrieved from the island during 1979 and 2017 present a unique opportunity to study the effects of time and temperature on the alteration process of young basaltic crust by unravelling the changes that have occurred over five decades of hydrothermal water-rock interaction. This work summarizes the results of three research papers on the mineralogical, petrographic, and geochemical outcomes of low-temperature basalt alteration. Results include the documentation of alteration behavior and changing abundances of secondary phases as well as the quantification of chemical fluxes during fluid-rock interaction over 50 years of basaltic tuff alteration at Surtsey. Furthermore, geochemical modeling is used to assess the effects of crystallinity, temperature, pH, reaction progress, and water-rock ratio in low-temperature basalt-hosted hydrothermal processes on the ocean floor in general.

1.1 Aims

The aims of the research presented in this doctoral thesis are:

- To explore time- and temperature-integrated changes associated with low-temperature (≤150°C) hydrothermal seawater-basalt interaction
- To document the effects of 50 years of hydrothermal alteration on secondary mineral parageneses and the palagonitization of basaltic glass at Surtsey volcano (**Paper I**)
- To quantify element flux between glassy basaltic rock and seawater as a function of reaction progress at Surtsey volcano (**Paper II**)
- To assess the major factors controlling seawater-basalt interaction, including rock crystallinity, temperature, and time (**Paper III**)

1.2 Alteration of mafic igneous rock

1.2.1 General aspects

Mafic igneous rock is among the most common constituents in the Earth's crust, making its chemical interaction with water an important subject in the study of global geochemical cycles. The exact petrographic and mineralogical outcome of alteration is unique to each environment, depending essentially on the initial compositions of the fluid and the host rock as well as on pH, redox conditions, temperature, water-rock ratio, and reaction progress (e.g., Alt et al., 1996b; Alt and Teagle, 2003; Bach et al., 2003; Gysi and Stefánsson, 2011; Kleine et al., 2020; Stefánsson, 2010; Stefánsson and Gíslason, 2001). However, the reported alteration mineral parageneses from natural systems and laboratory experiments at low temperatures most commonly include Fe-(Al-)oxyhydroxides, various phyllosilicates (e.g., nontronite, saponite, celadonite, talc, kaolinite, imogolite, allophane), carbonates (e.g., calcite), and zeolites as well as lesser amounts of sulfates (e.g., anhydrite), sulfides (e.g., pyrite), and silica (e.g., quartz, chalcedony) (Alt et al., 1996a; Alt and Teagle, 2003; Bach et al., 2001; Coogan and Gillis, 2018; Gíslason et al., 1993; Gysi and Stefánsson, 2011; Seyfried Jr. and Bischoff, 1979; Staudigel, 2014; Stefánsson, 2010; Stefánsson and Gíslason, 2001). This low-temperature alteration profile is particularly common for the upper 600 m of the oceanic crust in off-axis settings (Bach et al., 2001; Staudigel, 2014). Alteration minerals in high-temperature (≥250°C) environments commonly include chlorite or chlorite-smectite and smectite-chlorite mixed layers, as well as sulfides, sulfates, epidote, secondary pyroxenes, feldspars, pumpellyite, prehnite, actinolite, titanite, quartz, and Fe-oxides (Alt, 2003; Alt et al., 1996a; Humphris and Thompson, 1978; Seyfried Jr. and Mottl, 1982; Staudigel, 2014; Von Damm, 1990).

Seawater-basalt interactions in geothermal systems may significantly influence the composition of both seawater and the ocean crust and either offset or enhance the riverine fluxes of elements into the oceans (Fig. 1.2). However, assessing the effects of seawater-basalt interaction on global chemical exchange is challenging due to the limited data and uncertainties in estimating the relative contributions of high- and low-temperature systems. The former is considered to act as a source of Li, K, Ca, Si, Mn, Fe, and possibly Al for seawater but a sink of S and Mg (Alt, 2003; Bach et al., 2003; Huang et al., 2018; Kleine et al., 2022; Mottl and Wheat, 1994; Staudigel, 2014). Off-axis geothermal activity is considered to enhance the axial sources of Ca and Si, while also acting as a sink for K, Rb, and CO_2 (Alt, 2003; Bach et al., 2003; Huang et al., 2018; Staudigel, 2014; Wheat and Mottl, 2000). Several workers (e.g., Bach et al., 2003; Huang et al., 2018; Wheat and Fisher, 2008; Wheat and Mottl, 2000) concluded that off-axis-hydrothermal processes result in a Mg sink, whereas others (e.g., Staudigel et al., 1996) identified the process as a source of Mg instead. Furthermore, considerable uncertainties also persist for the budgets of Ca, Si, and Al (Fig. 1.2).

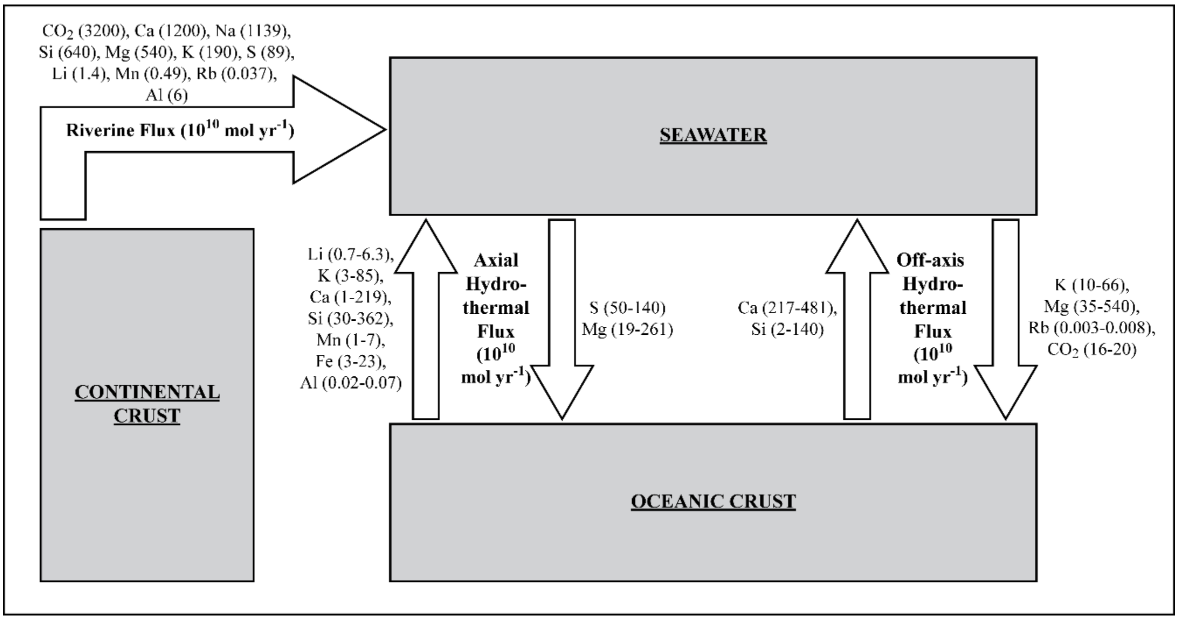

Figure 1.2 *Estimates for riverine and hydrothermal geochemical solute fluxes between the continental crust, seawater, and the oceanic crust for several elements in* 10^{10} *mol* yr^{-1}*. Fluxes were compiled from Huang et al. (2018), Staudigel (2014), Alt (2003), Bach et al. (2003), and Wheat and Mottl (2000). Note that the fluxes of several elements, including Ca, Si, Al, and Mg are associated with significant uncertainties.*

1.2.2 Palagonitization

Mafic igneous rock may be subdivided into holocrystalline (e.g., basalt, diabase, gabbro), hypocrystalline (e.g., hyaloclastites, pillow lavas) and glassy (e.g., vitric tuff) lithologies based on their crystallinity. Rocks containing high amounts of basaltic glass, also referred to as “sideromelane”, are of particular interest to the study of seawater-ocean-crust chemical interactions, because the reactivity of silicate glasses generally exceeds that of their crystalline counterparts by several orders of magnitude (e.g., Gíslason and Eugster, 1987). Sideromelane occurs frequently on the ocean floor, being a common phase in hyaloclastite rocks, pillow lavas, and pyroclastics. The chemical alteration of sideromelane by water is referred to as “palagonitization” and the resulting metastable alteration product is known as “palagonite” or “palagonitized glass”. Palagonite, named after the commune of *Palagonia* where it was first described by Von Waltershausen (1845), initially replaces sideromelane at the water-solid interface, followed by the gradual movement of the alteration front into the glass over time (Fig. 1.3).

Palagonite consists of a mixture of alteration phases, both crystalline and amorphous, (Staudigel and Hart, 1983). The most immediate alteration product, often termed “gel-palagonite” due to its smooth uniform texture, is a largely amorphous mixture of residual glass and traces of typically smectitic clay minerals as well as minor Fe-Ti-oxides that nucleate within the palagonitized glass matrix (Berkgaut et al., 1994; Crovisier et al., 2003; Drief and Schiffman, 2004; Matthews, 1971; Pauly et al., 2011; Peacock, 1926; Singer, 1974; Stroncik and Schmincke, 2001; Zhou and Fyfe, 1989). The fraction of crystalline components gradually increases as the material ages into a form often referred to as “fibropalagonite”, signified by the development of a fibrous texture and high birefringence (Peacock, 1926; Stroncik and Schmincke, 2001, 2002). Thus, palagonitized glass represents a continuum of alteration products from mostly vitreous to mostly crystalline depending on the stage of devitrification. Both the rates of palagonitization and palagonitized glass maturation are largely dependent on temperature, fluid-rock ratios, pH, serial affinity of the precursor glass (alkaline vs tholeiitic), and salinity of the fluid phase (Crovisier et al., 2003; Jakobsson and Moore, 1986; Moore, 1966; Pauly et al., 2011; Singer and Banin, 1990; Stroncik and Schmincke, 2002). The formation of palagonitized glass may occur both abiotically/geochemically or involve the metabolic processes of certain microorganisms (Kruber et al., 2008; Pedersen et al., 2015; Staudigel et al., 2008; Thorseth et al., 1992; Türke et al., 2015).

It is unresolved if palagonitization causes any significant volume changes upon alteration (Crovisier et al., 1992; Pauly et al., 2011; Zhou and Fyfe, 1989; Hay and Iijima, 1968; Jercinovic et al., 1990; Stroncik and Schmincke, 2001; Walton et al., 2005). Element mobilities during palagonitization have also been debated (Jakobsson, 1972; Staudigel and Hart, 1983; Stroncik and Schmincke, 2001; Pauly et al., 2011; Walton et al., 2005). As a result, mass balance estimates for basalt glass alteration, which are typically linked to assumptions regarding the immobility of certain elements or conservation of volume, are associated with significant uncertainties.

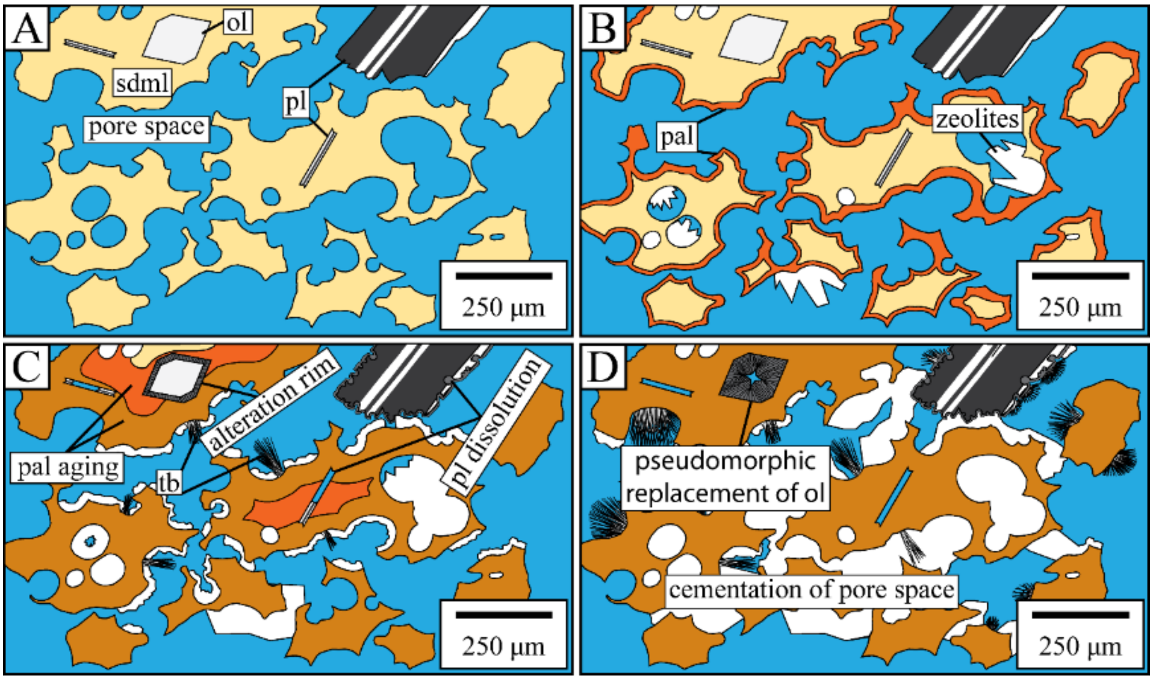

Figure 1.3 *Sketch of progressive palagonitic alteration of basaltic glass (sideromelane, sdml). Initially, palagonitization (pal) begins at the outer margin of glass particles, moving inward over time. Elements leached from palagonitized glass are enriched in the hydrothermal fluid and cause the precipitation of authigenic minerals, such as zeolites or, in case of Surtsey, tobermorite (tb). Palagonitized glass over time undergoes an aging and devitrification process leading to its progressive transformation into a poorly crystalline authigenic clay mineral assemblage. Primary minerals such as olivine (ol) or plagioclase (pl) may undergo varying degrees of dissolution and replacement by authigenic phases (mostly clay minerals). Modified after Prause et al. (2020).*

The volcanic island of Surtsey provides a unique opportunity to study the effects of time, temperature, and reaction progress on the process of palagonitization. The island's basaltic hyalotuff deposits host a low-temperature seawater-dominated geothermal system. The basaltic glass component has been subjected to palagonitization after the emplacement of the tuff in 1963 and 1964. The availability of drill core sample material from 1979 and 2017, combined with extensive geophysical logging and fluid geochemical data, makes Surtsey an ideal natural laboratory for the time-integrated study of low-temperature palagonitic alteration on the ocean floor.

1.3 Surtsey

Surtsey is a volcanic ocean island situated 33 km south of the coast of Iceland. It is the youngest and southernmost member of the Vestmannaeyjar archipelago (Fig. 1.4). The island's origins are closely connected to the evolution of the regional tectonics defining southern Iceland: In recent geologic history, Iceland's Eastern Rift Zone (ERZ) has been extending southwards to accommodate an active rift jump from the receding western Reykjanes Langjökull Rift Zone (RLZR) (Einarsson, 2008; Khodayar and Franzson, 2007; Martin et al., 2011; Óskarsson et al., 1985). Consequently, the Surtsey eruptions may be linked to the volcano-tectonic processes commonly associated with propagating rift tips

(Schipper et al., 2015, 2016). Such processes generally include the development of small ephemeral magma chambers that grow progressively more interconnected with increasing distance from the propagating rift tip as magmatic supply increases and cooling rates decrease (Christie and Sinton, 1981; Sinton et al., 1983). In the case of the Surtseyan eruptions, this likely led to the injection of a primitive ridge-like melt into poorly connected volumes of alkali basaltic magma, causing the development of overpressure and initiating the volcanic activity on the seafloor which subsequently built up the island (Schipper et al., 2015, 2016).

The Surtsey eruptions are estimated to have begun on November 12, 1963 (Sayyadi et al., 2021), and were first observed on November 14 by the Icelandic fishing trawler *Ísleifur II* (Thórarinsson, 1967a). Vigorous phreatomagmatic activity, initially focused on a 300-400 m long volcanic fissure at the *Surtur* vent site (originally named *Surtur I*), proceeded to raise the island above sea level on November 15 (Jakobsson and Moore, 1982). A 100 m high submarine edifice, *Surtla*, which never reached the surface, was built up between December 28, 1963, and January 6, 1964, 2.5 km ENE off Surtsey (Jakobsson and Moore, 1982; Kokelaar and Durant, 1983; Moore, 1985). On January 3, 1964, eruptions ceased at the *Surtur* vent, but were reinitiated one day later at the western vent *Surtungur* (originally named *Surtur II*), where eruption behavior transitioned from explosive to effusive on April 4 (Jakobsson and Moore, 1982; Thórarinsson, 1967b). This transition marked the end of explosive volcanism on Surtsey, and no further phreatomagmatic activity was initiated on the main island for the remainder of the eruptions. Two smaller volcanic edifices named *Syrtlingur* and *Jólnir* emerged during May to mid-October 1965 and December 1965 to early August 1966, respectively, both of which were rapidly eroded by ocean wave currents due to a lack of effusive activity (Jakobsson and Moore, 1982).

After the end of eruptive activity on Surtsey in June 1967, a low-temperature hydrothermal system emerged in the tuff deposits above and below sea level, which was visually recognizable on the surface due to steam rising from the tephra pile (Friedman and Williams, 1970; Jakobsson, 1978; Jakobsson et al., 2000). Originally, it was hypothesized that shallow intrusive bodies delivered the requisite energy to drive hydrothermal activity (e.g., Jackson et al., 2015), but recent data from the 2017 drilling campaign do not support this hypothesis (Weisenberger et al., 2019; Jackson et al., 2019).

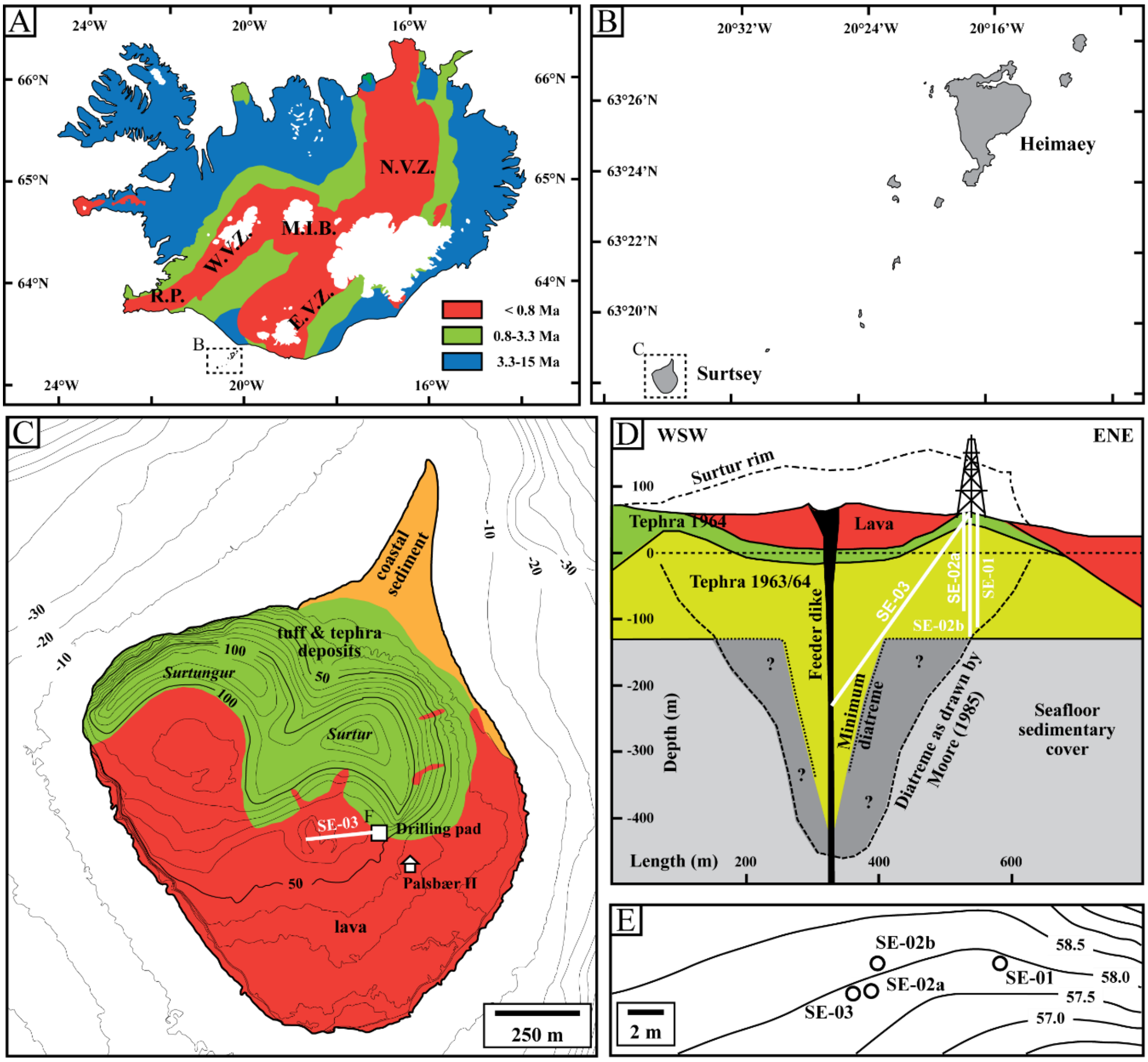

Figure 1.4 *Overview of the island of Surtsey, representing a potential analogue for low-temperature alteration of basaltic rocks on the seafloor. A) Basic geologic map of Iceland showing the age of rocks and the positions of major Icelandic volcanic provinces: N.V.Z. – North Volcanic Zone, M.I.B. – Mid-Iceland Belt, W.V.Z. – West Volcanic Zone, E.V.Z. – East Volcanic Zone, R.P. – Reykjanes Peninsula. The Vestmannaeyjar archipelago is located in the southern seaward extension of the East Volcanic Zone (dashed rectangle). B) The position of Surtsey (dashed rectangle) as part of the Vestmannaeyjar archipelago. C) Geologic map of Surtsey, also showing the position of the drilling pad of the 2017 SUSTAIN expedition. D) Cross section of the Surtur tephra cone showing the orientation and vertical depth of the four Surtsey wells. E) Magnified top-down view of the positions of the wells.*

The hydrothermal fluid within the submerged section of the system is of modified seawater composition (Kleine et al., 2020). Boiling may locally occur close to sea level (Axelsson et al., 1982; Stefánsson et al., 1985; Jackson et al., 2019; Kleine et al., 2020). Above sea level, the system is steam-dominated, and fluids are at least partially meteoric in origin (Jackson et al., 2019; Weisenberger et al., 2019). Hydrothermal alteration occurs primarily by palagonitization of sideromelane in the glassy tuff deposits and pseudomorphic replacement of olivine phenocrysts below sea level (Jakobsson and Moore, 1986).

1.4 The 2017 SUSTAIN Drilling Expedition

During the summer of 2017, the Surtsey Underwater volcanic System for Thermophiles, Alteration processes and Innovative concretes (SUSTAIN) project launched a drilling campaign on Surtsey (Jackson et al., 2015, 2019; Weisenberger et al., 2019). The project was supported by the International Continental Scientific Drilling Program, ICDP (https://www.icdp-online.org/projects/world/europe/surtsey-iceland/details/) and the Icelandic Centre for Research, Rannís (project number 163083-051). In addition, the campaign was made possible by the combined effort of an international team of researchers, the Icelandic coast guard and DOSECC Exploration Services, LLC.

A three-man advance party arrived on the island on July 23, 2017 and was joined two days later by three members of the drilling crew. During the next days, equipment, supplies, and personnel were transported to the island and the base camp was set up (Fig. 1.5). Rigging-up operations and waterline assembly were completed on August 9. The utilized drill rig was an Atlas Copco1000. Coring of well SE-02a began on the next day and proceeded until August 16 when the drill became stuck in poorly consolidated tuff at a vertical depth of 151 m. SE-02a subsequently collapsed on the next day, making the retrieval of the rods impossible. Cores from the SE-02a well were airlifted to Heimaey for core processing. On August 19, spudding of a new vertical well, dubbed SE-02b, commenced at a ~1.6 m horizontal distance from the abandoned SE-02a well, reaching a final vertical depth of 192 m on August 26, close to the estimated depth of the pre-eruption seafloor. Geophysical logging of SE-02b was carried out to a vertical depth of 180 m immediately after drilling had stopped. The aluminum casing for the Surtsey subsurface observatory was installed on August 27. The following day, spudding of the third well, SE-03, which was inclined towards west (azimuth 264°) at an angle of 35° from vertical, was started. Drilling of this well proceeded until September 4 to a total measured depth of 354 m. The next day, temperature measurements were conducted in the new drill holes and water samples were collected for fluid geochemical analyses. Incubation experiments were installed in the Surtsey subsurface observatory on September 6. Over the following days, equipment was prepared for transport off the island and camp disassembly commenced. All personnel and equipment were removed from the island by September 12. The drilling equipment was cleaned and packed for transport to the USA and Reykjavík between September 13 and 18. For further information on the SUSTAIN expedition, the reader is referred to the operational report by Weisenberger et al. (2019).

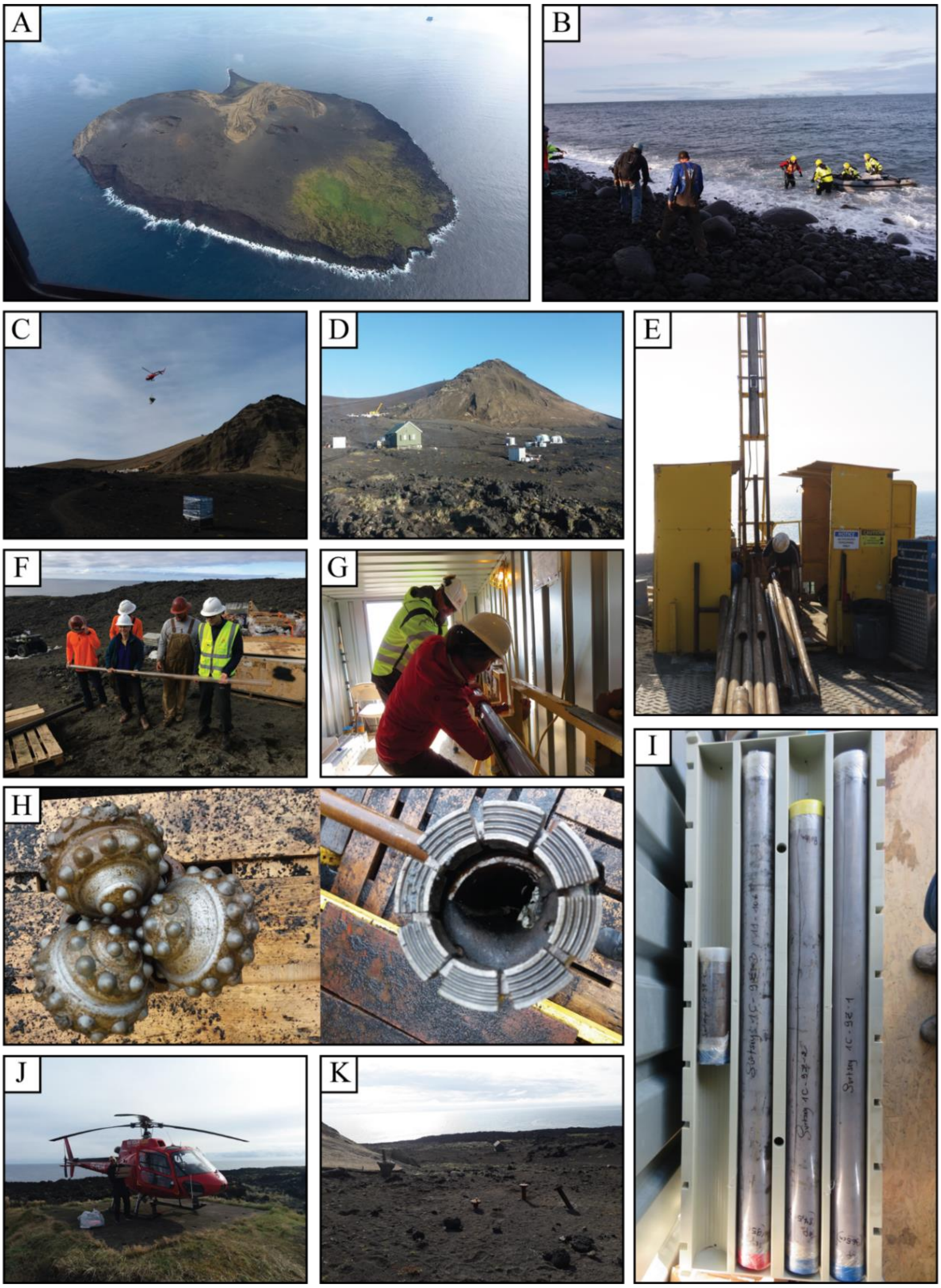

Figure 1.5 *Pictures from the 2017 SUSTAIN Surtsey drilling expedition. A) Helicopter view of the island. B) Transport of 300 kg cement to the island by boat. C) Airlifting of equipment to the island. D) View of the base camp (Pálsbær hut and sleeping tents) and drilling site (background). E) The drill rig (Atlas Copco 1000). F) Members of the drilling crew and the science team holding the first recovered drill core. G) Members of the science team processing a newly recovered drill core. H) Drill bits. I) Drill core pieces of a core run stored in liners. J) Delivery of essential food supplies to the island via helicopter. K) Well-heads of the three newly drilled wells (SE-02a, -02b, and -03) next to the 1979 borehole (left).*

1.5 Samples and methods

1.5.1 Samples

Samples used for the research presented in this thesis originated from the 1979 and 2017 Surtsey drilling campaigns. The sample set includes core material from the 1979 drill core (SE-01), archived at the Icelandic Institute of Natural History (IINH) and from one of the 2017 vertical drill cores (SE-02b), retrieved as part of the SUSTAIN project (Jackson et al., 2019; Weisenberger et al., 2019). Materials included 29 and 46 thin sections (thickness ≈ 30 μm) from SE-01 and SE-02b, respectively. A total of 12 thick sections (thickness ≈ 100 μm) were included for trace element analyses. Furthermore, 13 pore fluid samples were included in the geochemical dataset of **Paper II**. Thin- and thick sections were soaked in epoxy resin before polishing. Heating of the resin above 50°C was avoided to prevent dehydration of the tuff.

1.5.2 Methods

A wide range of investigative approaches has been applied as part of the research presented in this thesis. Individual techniques are described in detail in the methods sections of the included papers. In brief, these techniques included:

- **Polarization Microscopy (POLMI)** was used for the characterization of alteration style with depth in the two studied Surtsey drill cores as well as for the measurement of alteration rim thicknesses of palagonitized glass and pseudomorphic olivine replacement by clay minerals; the point count method was applied for the quantification of primary and secondary phases in thin section samples.
- **Electron Probe Microanalysis (EPMA)** and **Scanning Electron Microscopy (SEM)** were carried out on sideromelane, palagonitized glass, and secondary minerals to characterize chemical effects of alteration.
- **Laser Ablation Inductively Coupled Plasma Mass Spectrometry (LA-ICP-MS)** was performed on sideromelane and palagonitized glass and included the analysis of 26 trace elements; immobile REE (La, Ce and Lu) were used for the calculation of mass flux budgets during palagonitization.
- **Inductively Coupled Plasma Optical Emission Spectrometry (ICP-OES)** was used for major cation (SiO_2, Na, K, Al, Fe, Mg, Ca, B) analysis of pore fluid samples.
- **Ion Chromatography (IC)** was used for major anion (Cl, SO_4) analysis of pore fluid samples.
- **Kinetic Reaction Path Modeling** using the geochemical software *PHREEQC* (Parkhurst and Appelo, 1999), the *carbfix.dat* thermodynamic database (Voigt et al., 2018) and the *carbfix_kin.dat* kinetic database (Heřmanská et al., 2022) was utilized to simulate the dissolution of glassy and crystalline basalt in seawater and evaluate the relative importance and effects of variable crystallinity, temperature, reaction progress, and time during seafloor alteration.

1.6 Summary of papers

The results of the thesis are the subject of three scientific papers. Two of them have been published in international peer-reviewed journals and one is to be submitted for publication.

1.6.1 Paper I

Prause, S., Weisenberger, T.B., Cappelletti, P., Grimaldi, C., Rispoli, C., Jónasson, K., Jackson, M.D., Gudmundsson, M.T. (2020). Alteration progress within the Surtsey hydrothermal system, SW Iceland – A time-lapse petrographic study of cores drilled in 1979 and 2017. *Journal of Volcanology and Geothermal Research*, 392, 106754

The ocean island of Surtsey represents a unique opportunity to study basaltic tuff alteration as a function of time and temperature due to the very well constrained age of the island's hydrothermal system and a set of temperature logging data that represents several decades of continued monitoring. The SUSTAIN drilling expedition of 2017 successfully recovered three new drill cores from the island. Petrographic thin sections from one of the vertical cores (SE-02b) were contrasted with depth-equivalent samples from the archived 1979 Surtsey core (SE-01) to track the alteration progress in terms of the extent of palagonitization and pseudomorphic replacement of olivine phenocrysts by secondary clay minerals and to document the evolution of authigenic mineral parageneses at variable depths. The most important findings are summarized below:

Alteration of basaltic tuff is found to have progressed at variable rates depending on depth and temperature between 1979 and 2017. The main alteration minerals are zeolites (phillipsite and analcime), tobermorite and clay minerals. Anhydrite, gypsum and calcite occur in lesser quantities. Phillipsite, clay minerals, and anhydrite are identified as the earliest secondary minerals, whereas analcime and tobermorite become increasingly abundant at more advanced alteration stages and higher temperatures. Five zones of distinct alteration style are defined based on petrographic criteria that correlate well between the two drill cores. Alteration progresses more slowly above sea level as well as in the submerged parts of the system at ~138 to 150 m vertical depth where tuffs remain poorly altered. The alteration front has moved downwards between 1979 and 2017 from a maximum vertical depth of 157 m in SE-01 to 178 m in SE-02b. Palagonitized glass in the tuff samples can be categorized into three different petrographic types that range from mostly amorphous (type I) to increasingly crystalline (type II and III), representing progressive stages of glass devitrification. The rates of palagonitization and olivine replacement, as well as the process of palagonitized glass devitrification, are found to be positively correlated with temperature.

1.6.2 Paper II

Prause, S., Weisenberger, T.B., Kleine, B.I., Monien, P., Rispoli, C., Stefánsson, A., (2022). Alteration of basaltic glass within the Surtsey hydrothermal system, Iceland – Implication to oceanic crust seawater interaction. *Journal of Volcanology and Geothermal Research*, 429, 107581

Major and trace element analyses of sideromelane and palagonitized glass were combined with fluid and bulk rock data to evaluate chemical fluxes at different stages of basaltic tuff alteration. Results revealed that the mobility of several chemical species differs drastically depending on reaction progress. Elements that remain immobile during palagonitization of sideromelane include FeO, TiO_2, REE, Hf, Ta, Zr, Nb and Y. Silica, Al_2O_3, MgO, Na_2O, K_2O, CaO, Sr, Rb, V and Ba were leached from the glass and at least partially exchanged for H_2O. During maturation of mostly amorphous gel palagonite (type I) into a poorly crystalline clay mineral assemblage (type III) FeO and TiO_2 are both mobilized on a limited scale. Further, palagonitized glass maturation led to the reuptake of SiO_2, Al_2O_3, MgO, and K_2O from solution. Trace elements REE, Hf, Ta, Zr, Nb, and Y showed no signs of mobilization throughout the entire alteration process. On the bulk rock scale, including both glass and authigenic minerals, alteration of basaltic tuff in the Surtsey hydrothermal system is identified as a net sink of dissolved Mg and Na and a net source of dissolved Ca, Al and SiO_2 for seawater.

1.6.3 Paper III

Prause, S., Kleine, B.I., Weisenberger, T.B., Stefánsson, A., (in prep.). Low-temperature seafloor alteration and its impact on the mineralogy and chemical composition of the oceanic crust – A kinetic reaction path model. In preparation for *Chemical Geology*

This paper presents a novel kinetic reaction path model on low-temperature seafloor alteration of basaltic rocks between 50 and 150°C. The model examines the influence of the parameters of crystallinity, temperature, water-rock ratio and dissolved CO_2 on the qualitative and quantitative nature of the secondary mineral assemblage, as well as resulting fluid compositions.

The model reproduces typical observed secondary mineral assemblages and fluid compositions as well as several previous estimates of the global element fluxes of Si, Ca, Na, SO_4, and Mg at water-rock ratios thought to be common in the oceanic crust. Simulations indicate that crystalline and glassy mafic rocks undergo a similar series of reactions, that can be summarized in four steps: 1) the initial dissolution of primary minerals and glass, 2) the formation of simple oxides, hydroxides, Mg-Fe(III)-clays, montmorillonite, and celadonite at high water-rock ratios and mildly acidic to circumneutral pH, 3) the partial replacement of Mg-Fe(III)-clays by Mg-Fe(II)-clays and the formation of calcite at increasingly alkaline conditions, and 4) alkalinization of the fluid at low water-rock ratios and reducing conditions, accompanied by the depletion of Mg and SO_4 from solution and enrichment of dissolved Al, leading to the formation of zeolite minerals. These reaction stages were observed regardless of temperature or crystallinity, which mainly affected reaction rates rather than qualitative reaction outcome. This indicates that temperature and crystallinity should not strongly affect the process of seafloor alteration, given sufficient time for a water-rock system to reach an equilibrium state. However, fluid temperatures and relative quantities of crystalline and glassy phases may be of increasing importance for short-lived systems, e.g., in the case of ocean islands. The supply of dissolved CO_2 affected the secondary mineral assemblage by controlling the relative amounts of calcite, anhydrite, clays and zeolites. Increased acid supply from CO_2 dissolution also led to lower pH, buffering the system against alkalinization.

1.7 Conclusions and outlook

Interaction of basalts with seawater has been studied through petrographic and geochemical analysis of samples from Surtsey volcano (SW Iceland) and using geochemical modeling to gain quantitative and qualitative knowledge of the process of alteration, associated elemental mobilities and the effects of temperature and time.

- Alteration of basaltic tuff at Surtsey is found to have progressed over time, with the extent depending primarily on depth and temperature. The alteration products observed include: palagonitized glass, clay minerals, various zeolites (analcime, phillipsite), tobermorite, calcite, anhydrite, and gypsum.

- Palagonitized glass over time undergoes a maturation process that causes progressive devitrification from a mostly amorphous gel-like texture into a poorly crystalline assemblage of clay minerals.

- Element mobilities depend upon the progress of seawater-basalt interaction. Iron and TiO_2 are immobile during palagonitization but show minor mobility (exchange) during palagonitized glass maturation. Other elements likewise showed changing mobilities depending on reaction progress with initial palagonitization leaching SiO_2, Al_2O_3, MgO, Na_2O, K_2O, CaO, Sr, Rb, V and Ba from the glass and palagonitized glass maturation causing a re-enrichment of SiO_2, Al_2O_3, MgO, and K_2O. The only elements found to be immobile throughout the entire process were REE, Hf, Ta, Zr, Nb, and Y. Assessment of the combined processes of palagonitization, palagonitized glass maturation, and secondary mineral formation indicates a net long-term sink of dissolved Mg and Na and a net long-term source of Ca, Al, and SiO_2 for seawater.

- Geochemical modeling reveals that reaction time, water-rock ratio (or reaction progress) and associated seawater pH changes are the primary variables controlling the alteration process of basalts by seawater. Temperature and rock crystallinity had lesser effects on the outcome of the alteration process. However, reaction rates increased rapidly with increasing temperature and higher abundance of basalt glass versus primary igneous minerals. The findings of the geochemical modeling closely reflect the observed geochemical and petrographic observations at Surtsey. Modeling results were also evaluated by comparison with other natural systems and used to estimate global annual molar fluxes of Si, Ca, Na, K, SO_4 and Mg between the oceans and the upper oceanic crust in off-axis settings.

The results of this thesis highlight the importance of future investigations that should focus on establishing a higher resolution for the available data on the representative composition of AOC and the effects of off-axis hydrothermal alteration. Additional understanding may also be gained by a focused effort to locate and sample warm springs on the ocean floor and by contrasting fluid data with associated bulk rock observations. Such ventures will ultimately be necessary if a comprehensive understanding of global geochemical fluxes is to be achieved.

References

Alt, J.C., 2003. Hydrothermal fluxes at mid-ocean ridges and on ridge flanks. Comptes Rendus. Geosci. 335, 853–864.

Alt, J.C., 1995. Subseafloor processes in mid-ocean ridge hydrothermal systems. Geophys. Monogr. Ser. 91, 85–114.

Alt, J.C., Laverne, C., Vanko, D.A., Tartarotti, P., Teagle, D.A.H., Bach, W., Zuleger, E., Erzinger, J., Honnorez, J., Pezard, P.A., Becker, K., Salisbury, M.H., Wilkens, R.H., 1996a. Hydrothermal alteration of a section of upper oceanic crust in the Eastern Equatorial Pacific: A synthesis of results from Site 504 (DSDP Legs 69, 70, and 83, and ODP Legs 111, 137, 140, and 148). Proc. Ocean Drill. Program, Sci. Results 148, 417–434.

Alt, J.C., Teagle, D.A.H., 2003. Hydrothermal alteration of upper oceanic crust formed at a fast-spreading ridge: mineral, chemical, and isotopic evidence from ODP Site 801. Chem. Geol. 201, 191–211.

Alt, J.C., Teagle, D.A.H., Laverne, C., Vanko, D.A., Bach, W., Honnorez, J., Becker, K., Ayadi, M., Pezard, P.A., 1996b. Ridge-Flank Alteration of Upper Ocean Crust in the Eastern Pacific: Synthesis of Results for Volcanic Rocks of Holes 504B and 896A. Proc. Ocean Drill. Program, Sci. Results 148, 438-450.

Axelsson, G., Stefánsson, V., Gudmundsson, G., Steingrímsson, B., 1982. Thermal condition of Surtsey. Surtsey Research Progress Report 9, 102-110.

Bach, W., Alt, J.C., Niu, Y., Humphris, S.E., Erzinger, J., Dick, H.J.B., 2001. The geochemical consequences of late-stage low-grade alteration of lower ocean crust at the SW Indian Ridge: Results from ODP Hole 735B (Leg 176). Geochim. Cosmochim. Acta 65, 3267–3287.

Bach, W., Peucker-Ehrenbrink, B., Hart, S.R., Blusztajn, J.S., 2003. Geochemistry of hydrothermally altered oceanic crust: DSDP/ODP Hole 504B-Implications for seawater-crust exchange budgets and Sr-and Pb-isotopic evolution of the mantle. Geochem. Geophys. Geosyst. 4, 8904.

Berkgaut, V., Singer, A., Stahr, K., 1994. Palagonite reconsidered: Paracrystalline illite-smectites from regoliths on basic pyroclastics. Clays Clay Miner. 42, 582–592.

Christie, D.M., Sinton, J.M., 1981. Evolution of abyssal lavas along propagating segments of the Galapagos spreading center. Earth Planet. Sci. Lett. 56, 321–335.

Coogan, L.A., Gillis, K.M., 2018. Low-Temperature Alteration of the Seafloor: Impacts on Ocean Chemistry. Annu. Rev. Earth Planet. Sci. 46, 21–45.

Crovisier, J.-L., Honnorez, J., Fritz, B., Petit, J.-C., 1992. Dissolution of subglacial volcanic glasses from Iceland: laboratory study and modelling. Appl. Geochemistry, Suppl. Iss. 1, 55–81.

Crovisier, J.L., Advocat, T., Dussossoy, J.L., 2003. Nature and role of natural alteration gels formed on the surface of ancient volcanic glasses (Natural analogs of waste containment glasses). J. Nucl. Mater. 321, 91–109.

Davis, E.E., Lister, C.R.B., 1974. Fundamentals of ridge crest topography. Earth Planet. Sci. Lett. 21, 405–413.

Drief, A., Schiffman, P., 2004. Very low-temperature alteration of sideromelane in hyaloclastites and hyalotuffs from Kilauea and Mauna Kea volcanoes: Implications for the mechanism of palagonite formation. Clays Clay Miner. 52, 623–635.

Einarsson, P., 2008. Plate boundaries, rifts and transforms in Iceland. Jökull 58, 35–58.

Fisher, A.T., 1998. Permeability within basaltic oceanic crust. Rev. Geophys. 36, 143–182.

Fisher, A.T., Wheat, C.G., 2010. Seamounts as Conduits for Massive Fluid, Heat, and Solute Fluxes on Ridge Flanks. Oceanography 23, 74–87.

Friedman, J.D., Williams, R.S., 1970. Changing patterns of thermal emission from Surtsey, Iceland, between 1966 and 1969. US Geol. Surv. Prof. Pap. 700-D, 116–124.

Gíslason, S.R., Eugster, H.P., 1987. Meteoric water-basalt interactions. I: A laboratory study. Geochim. Cosmochim. Acta 51, 2827–2840.

Gíslason, S.R., Veblen, D.R., Livi, K.J.T., 1993. Experimental meteoric water-basalt interactions: Characterization and interpretation of alteration products. Geochim. Cosmochim. Acta 57, 1459–1471.

Gysi, A.P., Stefánsson, A., 2011. CO_2-water-basalt interaction. Numerical simulation of low temperature CO_2 sequestration into basalts. Geochim. Cosmochim. Acta 75, 4728–4751.

Hay, R.L., Iijima, A., 1968. Nature and origin of palagonite tuffs of the Honolulu Group on Oahu, Hawaii. Geol. Soc. Am. 116, 331–376.

Heřmanská, M., Voigt, M.J., Marieni, C., Declercq, J., Oelkers, E., 2022. A comprehensive and consistent mineral dissolution rate database: Part I: Primary silicate minerals and glasses. Chem. Geol. 597, 120807.

Huang, K.J., Teng, F.Z., Plank, T., Staudigel, H., Hu, Y., Bao, Z.Y., 2018. Magnesium isotopic composition of altered oceanic crust and the global Mg cycle. Geochim. Cosmochim. Acta 238, 357–373.

Humphris, S.E., Thompson, G., 1978. Hydrothermal alteration of oceanic basalts by seawater. Geochim. Cosmochim. Acta 42, 107–125.

Jackson, M.D., Gudmundsson, M.T., Bach, W., Cappelletti, P., Coleman, N.J., Ivarsson, M., Jónasson, K., Jørgensen, S.L., Marteinsson, V., McPhie, J., Moore, J.G., Nielson, D., Rhodes, J.M., Rispoli, C., Schiffman, P., Stefánsson, A., Türke, A., Vanorio, T., Weisenberger, T.B., White, J.D.L., Zierenberg, R., Zimanowski, B., 2015. Time-lapse characterization of hydrothermal seawater and microbial interactions with basaltic tephra at Surtsey Volcano. Sci. Drill. 20, 51–58.

Jackson, M.D., Gudmundsson, M.T., Weisenberger, T.B., Michael Rhodes, J., Stefánsson, A., Kleine, B.I., Lippert, P.C., Marquardt, J.M., Reynolds, H.I., Kück, J., Marteinsson, V. þ., Vannier, P., Bach, W., Barich, A., Bergsten, P., Bryce, J.G., Cappelletti, P., Couper, S., Fahnestock, M.F., Gorny, C.F., Grimaldi, C., Groh, M., Gudmundsson, Á., Gunnlaugsson, Á.T., Hamlin, C., Högnadóttir, T., Jónasson, K., Jónsson, S.S., Jørgensen, S.L., Klonowski, A.M., Marshall, B., Massey, E., McPhie, J., Moore, J.G., Ólafsson, E.S., Onstad, S.L., Perez, V., Prause, S., Snorrason, S.P., Türke, A., White, J.D., Zimanowski, B., 2019. SUSTAIN drilling at Surtsey volcano, Iceland, tracks hydrothermal and microbiological interactions in basalt 50 years after eruption. Sci. Drill. 25, 35–46.

Jakobsson, S.P., 1979. Petrology of Recent basalts of the Eastern Volcanic Zone, Iceland. Acta Nat. Islandica 26, 103 pp.

Jakobsson, S.P., 1978. Environmental factors controlling the palagonitization of the Surtsey tephra, Iceland. Bull. Geol. Soc. Denmark 27, 91–105.

Jakobsson, S.P., 1972. On the Consolidation and Palagonitization on the Tephra of the Surtsey Volcanic Island, Iceland. Surtsey Res. Prog. Rep. 121–128.

Jakobsson, S.P., Gudmundsson, G., Moore, J.G., 2000. Geological monitoring of Surtsey, Iceland, 1967-1998. Surtsey Res. 11, 99–108.

Jakobsson, S.P., Moore, J.G., 1986. Hydrothermal minerals and alteration rates at Surtsey volcano, Iceland. Geol. Soc. Am. Bull. 97, 648–659.

Jakobsson, S.P., Moore, J.G., 1982. The Surtsey Research Drilling Project of 1979. Surtsey Res. 9, 76–93.

Jercinovic, M.J., Keil, K., Smith, M.R., Schmitt, R.A., 1990. Alteration of basaltic glasses from north-central British Columbia, Canada. Geochim. Cosmochim. Acta 54, 2679–2696.

Khodayar, M., Franzson, H., 2007. Fracture pattern of Thjórsárdalur central volcano with respect to rift-jump and a migrating transform zone in South Iceland. J. Struct. Geol. 29, 898–912.

Kleine, B.I., Stefánsson, A., Kjartansdóttir, R., Prause, S., Weisenberger, T.B., Reynolds, H.I., Sveinbjörnsdóttir, Á.E., Jackson, M.D., Gudmundsson, M.T., 2020. The Surtsey volcano geothermal system: An analogue for seawater-oceanic crust interaction with implications for the elemental budget of the oceanic crust. Chem. Geol. 550, 119702.

Kleine, B.I., Stefánsson, A., Zierenberg, R.A., Jeon, H., Whitehouse, M.J., Jónasson, K., Fridleifsson, G.O., Weisenberger, T.B., 2022. Sulfate (re-)cycling in the oceanic crust: Effects of seawater-rock interaction, sulfur reduction and temperature on the abundance and isotope composition of anhydrite. Geochim. Cosmochim. Acta 317, 65–90.

Kokelaar, B.P., Durant, G.P., 1983. The submarine eruption and erosion of Surtla (Surtsey). J. Volcanol. Geotherm. Res. 19, 239–246.

Kruber, C., Thorseth, I.H., Pedersen, R.B., 2008. Seafloor alteration of basaltic glass: Textures, geochemistry, and endolithic microorganisms. Geochem. Geophys. Geosyst. 9, 1–18.

Langseth, M.G., Le Pichon, X., Ewing, M., 1966. Crustal structure of the mid-ocean ridges. J. Geophys. Res. 71, 5321–5355.

Lister, C.R.B., 1972. On the thermal balance of a mid-ocean ridge. Geophys. J. R. Astron. Soc. 26, 515–535.

Martin, E., Paquette, J.L., Bosse, V., Ruffet, G., Tiepolo, M., Sigmarsson, O., 2011. Geodynamics of rift-plume interaction in Iceland as constrained by new 40Ar/39Ar and in situ U-Pb zircon ages. Earth Planet. Sci. Lett. 311, 28–38.

Matthews, D.H., 1971. III. Weathered And Metamorphosed Basalts. Altered basalts from Swallow Bank, an abyssal hill in the NE Atlantic, and from a nearby seamount. Philos. Trans. R. Soc. London 268, 551–571.

McKenzie, D.P., 1967. Some remarks on heat flow and gravity anomalies. J. Geophys. Res. 72, 6261–6273.

Moore, J.G., 1985. Structure and eruptive mechanisms at Surtsey Volcano, Iceland. Geol. Mag. 122, 649–661.

Moore, J.G., 1966. Rate of palagonitization of submarine basalt adjacent to Hawaii. US Geol. Surv. Prof. Pap. 550-D, 163–171.

Mottl, M.J., Wheat, C.G., 1994. Hydrothermal circulation through mid-ocean ridge flanks: Fluxes of heat and magnesium. Geochim. Cosmochim. Acta 58, 2225–2237.

Óskarsson, N., Steinthorsson, S., Sigvaldason, G.E., 1985. Iceland geochemical anomaly: origin, volcanotectonics, chemical fractionation and isotope evolution of the crust. J. Geophys. Res. Solid Earth 90, 10011–10025.

Parkhurst, D.L., Appelo, C.A.J., 1999. User's guide to PHREEQC (Version 2): a computer program for speciation, batch-reaction, one-dimensional transport, and inverse geochemical calculations. Water-resources Investig. Rep. 99, 312.

Parsons, B., Sclater, J.G., 1977. An analysis of the variation of ocean floor bathymetry and heat flow with age. J. Geophys. Res. 82, 803–827.

Pauly, B.D., Schiffman, P., Zierenberg, R.A., Clague, D.A., 2011. Environmental and chemical controls on palagonitization. Geochem. Geophys. Geosyst. 12, Q12017.

Peacock, M.A., 1926. The petrology of Iceland, part 1. The basic tuffs. Trans. R. Soc. Edinburgh 55, 53–76.

Pedersen, L.R., McLoughlin, N., Vullum, P.E., Thorseth, I.H., 2015. Abiotic and candidate biotic micro-alteration textures in subseafloor basaltic glass: A high-resolution in-situ textural and geochemical investigation. Chem. Geol. 410, 124–137.

Prause, S., Weisenberger, T.B., Cappelletti, P., Grimaldi, C., Rispoli, C., Jónasson, K., Jackson, M.D., Gudmundsson, M.T., 2020. Alteration progress within the Surtsey hydrothermal system, SW Iceland – A time-lapse petrographic study of cores drilled in 1979 and 2017. J. Volcanol. Geotherm. Res. 392, 106754.

Sayyadi, S., Einarsson, P., Gudmundsson, M.T., 2021. Seismic activity associated with the 1963–1967 Surtsey eruption off the coast of South Iceland. Bull. Volcanol. 83, 1–14.

Schipper, C.I., Jakobsson, S.P., White, J.D.L., Palin, J.M., Bush-Marcinowski, T., 2015. The Surtsey Magma Series. Sci. Rep. 5, 11498.

Schipper, C.I., Le Voyer, M., Moussallam, Y., White, J.D.L., Thordarson, T., Kimura, J., Chang, Q., 2016. Degassing and magma mixing during the eruption of Surtsey Volcano (Iceland, 1963–1967): the signatures of a dynamic and discrete rift propagation event. Bull. Volcanol. 78, 33.

Seyfried Jr., W.E., Bischoff, J.L., 1979. Low temperature basalt alteration by seawater: an experimental study at 70 °C and 150 °C. Geochim. Cosmochim. Acta 43, 1937–1947.

Seyfried Jr., W.E., Mottl, M.J., 1982. Hydrothermal alteration of basalt by seawater under seawater-dominated conditions. Geochim. Cosmochim. Acta 46, 985–1002.

Singer, A., 1974. Mineralogy of palagonitic material from the Golan Heights, Israel. Clays Clay Miner. 22, 231–240.

Singer, A., Banin, A., 1990. Characteristics and mode of palagonite - A review. Sci. Géologiques, Bull. mémoires 88, 173–181.

Sinton, J.M., Wilson, D.S., Christie, D.M., Hey, R.N., Delaney, J.R., 1983. Petrologic consequences of rift propagation on oceanic spreading ridges. Earth Planet. Sci. Lett. 62, 193–207.

Spinelli, G.A., Giambalvo, E.R., Fisher, A.T., 2004. Sediment permeability, distribution, and influence on fluxes in oceanic basement, in: Davis, E.E., Elderfield, H. (Eds.), Hydrogeology of the Oceanic Lithosphere. Cambridge University Press, Cambridge, pp. 151–188.

Staudigel, H., 2014. Chemical Fluxes from Hydrothermal Alteration of the Oceanic Crust, in: Holland, H.D., Turekian, K.K. (Eds.), Treatise on Geochemistry. Elsevier Ltd., Oxford, pp. 583–606.

Staudigel, H., Furnes, H., McLoughlin, N., Banerjee, N.R., Connell, L.B., Templeton, A., 2008. 3.5 billion years of glass bioalteration: Volcanic rocks as a basis for microbial life? Earth-Science Rev. 89, 156–176.

Staudigel, H., Hart, S.R., 1983. Alteration of basaltic glass: Mechanisms and significance for the oceanic crust-seawater budget. Geochim. Cosmochim. Acta 47, 337–350.

Staudigel, H., Plank, T., White, B., Schmincke, H.U., 1996. Geochemical fluxes during seafloor alteration of the basaltic upper oceanic crust: DSDP sites 417 and 418, in: Bebout, G.E., Scholl, S.W., Kirby, S.H., Platt, J.P. (Eds.), Subduction, Top to Bottom, Geophys. Monogr. Ser. AGU, Washington D.C., pp. 19–38.

Stefánsson, A., 2010. Low-temperature alteration of basalts - the effects of temperature, acids, and extent of reaction on mineralization and water chemistry. Jökull 60, 165–184.

Stefánsson, A., Gíslason, S.R., 2001. Chemical weathering of basalts, Southwest Iceland: effect of rock crystallinity and secondary minerals on chemical fluxes to the ocean. Amer. J. Sci. 301, 513-556.

Stefánsson, V., Axelsson, G., Sigurdsson, O., Gudmundsson, G., Steingrímsson, B., 1985. Thermal condition of Surtsey. J. Geodyn. 4, 91-106.

Stein, C.A., Stein, S., 1994. Constraints on hydrothermal heat flux through the oceanic lithosphere from global heat flux. J. Geophys. Res. 99, 3081–3095.

Stroncik, N.A., Schmincke, H., 2002. Palagonite - a review. Int. J. Earth Sci. 91, 680–697.

Stroncik, N.A., Schmincke, H., 2001. Evolution of palagonite: Crystallization, chemical changes, and element budget. Geochem. Geophys. Geosyst. 2, 1017.

Thórarinsson, S., 1967a. Surtsey: the new island in the North Atlantic. Viking Press.

Thórarinsson, S., 1967b. The Surtsey eruption and related scientific work. Polar Rec. (Gr. Brit). 13, 571.

Thorseth, I.H., Furnes, H., Heldal, M., 1992. The importance of microbiological activity in the alteration of natural basaltic glass. Geochim. Cosmochim. Acta 56, 845–850.

Türke, A., Nakamura, K., Bach, W., 2015. Palagonitization of basalt glass in the flanks of mid-ocean ridges: implications for the bioenergetics of oceanic intracrustal ecosystems. Astrobiology 15, 793–803.

Voigt, M., Marieni, C., Clark, D.E., Gíslason, S.R., Oelkers, E.H., 2018. Evaluation and refinement of thermodynamic databases for mineral carbonation. Energy Procedia 146, 81–91.

Von Damm, K.L., 1990. Seafloor hydrothermal activity: black smoker chemistry and chimneys. Annu. Rev. Earth Planet. Sci. 18, 173–204.

Von Herzen, R.P., Uyeda, S., 1963. Heat flow through the eastern Pacific ocean floor. J. Geophys. Res. 68, 4219–4250.

Von Waltershausen, S., 1845. Ueber die submarinen vulkanischen Ausbrüche in der Tertiär-Formation des Val di Noto im Vergleich mit verwandten Erscheinungen am Aetna. Göttinger Studien.

Walton, A.W., Schiffman, P., Macpherson, G.L., 2005. Alteration of hyaloclastites in the HSDP 2 Phase 1 Drill Core: 2. Mass balance of the conversion of sideromelane to palagonite and chabazite. Geochem. Geophys. Geosyst. 6, Q09G19.

Weisenberger, T.B., Guðmundsson, M.T., Jackson, M.D., Gorny, C.F., Türke, A., Kleine, B.I., Marshall, B., Jørgensen, S.L., Marteinsson, V. þ., Stefánsson, A., White, J.D.L., Barich, A., Bergsten, P., Bryce, J., Couper, S., Fahnestock, M.F., Franzson, H., Grimaldi, C., Groh, M., Guðmundsson, Á., Gunnlaugsson, Á. þ., Hamelin, C., Högnadóttir, Þ., Jónasson, K., Jónsson, S.S., Klonowski, A.M., Kück, J., Magnússon, R.L., Massey, E., McPhie, J., Ólafsson, E.S., Onstad, S.L., Prause, S., Perez, V., Rhodes, J.M., Snorrason, S.P., 2019. Operational Report for the 2017 Surtsey Underwater volcanic System for Thermophiles, Alteration processes and INnovative Concretes (SUSTAIN) drilling project at Surtsey Volcano, ICDP Operational Report.

Wheat, C.G., Fisher, A.T., 2008. Massive, low-temperature hydrothermal flow from a basaltic outcrop on 23 Ma seafloor of the Cocos Plate: Chemical constraints and implications. Geochem. Geophys. Geosyst. 9, Q12O14.

Wheat, C.G., Mottl, M.J., 2000. Composition of pore and spring waters from Baby Bare: Global implications of geochemical fluxes from a ridge flank hydrothermal system. Geochim. Cosmochim. Acta 64, 629–642.

Williams, D.L., Von Herzen, R.P., Sclater, J.G., Anderson, R.N., 1974. The Galapagos spreading centre: Lithospheric cooling and hydrothermal circulation. Geophys. J. R. Astron. Soc. 38, 587–608.

Zhou, Z., Fyfe, W.S., 1989. Palagonitization of basaltic glass from DSDP Site 335, Leg 37: textures, chemical composition, and mechanism of formation. Am. Mineral. 74, 1045–1053.

2 Paper I

Alteration progress within the Surtsey hydrothermal system, SW Iceland – A time-lapse petrographic study of cores drilled in 1979 and 2017

Simon Prause[1], Tobias Björn Weisenberger[1], Piergiulio Cappelletti[2], Carla Grimaldi[2], Concetta Rispoli[2], Kristján Jónasson[3], Marie Dolores Jackson[4], Magnús Tumi Gudmundsson[5]

[1]*Iceland GeoSurvey (ÍSOR), Reykjavík, Iceland*
[2]*Dipartimento di Scienze della Terra, dell'Ambiente e delle Risorse (DiSTAR), Università degli Studi di Napoli Federico II, Naples, Italy*
[3]*Icelandic Institute of Natural History (IINH), Garðabær, Iceland*
[4]*Department of Geology and Geophysics, University of Utah, Salt Lake City, USA*
[5]*Nordvulk, Institute of Earth Sciences, University of Iceland, Reykjavík, Iceland*

Published in 2020 in *Journal of Volcanology and Geothermal Research* (vol. 392, 106754)

Journal of Volcanology and Geothermal Research 392 (2020) 106754

Contents lists available at ScienceDirect

Journal of Volcanology and Geothermal Research

journal homepage: www.elsevier.com/locate/jvolgeores

Alteration progress within the Surtsey hydrothermal system, SW Iceland – A time-lapse petrographic study of cores drilled in 1979 and 2017

Simon Prause [a,*], Tobias Björn Weisenberger [a], Piergiulio Cappelletti [b], Carla Grimaldi [b], Concetta Rispoli [b], Kristján Jónasson [c], Marie D. Jackson [d], Magnús Tumi Gudmundsson [e]

[a] Iceland GeoSurvey (ÍSOR), Reykjavík, Iceland
[b] Dipartimento di Scienze della Terra, dell'Ambiente e delle Risorse (DiSTAR), Università degli Studi di Napoli Federico II, Naples, Italy
[c] Icelandic Institute of Natural History (IINH), Garðabær, Iceland
[d] Department of Geology and Geophysics, University of Utah, Salt Lake City, USA
[e] Nordvulk, Institute of Earth Sciences, University of Iceland, Reykjavík, Iceland

ARTICLE INFO

Article history:
Received 29 August 2019
Received in revised form 6 November 2019
Accepted 12 December 2019
Available online 13 December 2019

Keywords:
Surtsey volcano
ICDP
SUSTAIN
Palagonitization
Basaltic glass
Hydrothermal alteration

ABSTRACT

The evolution of hydrothermal alteration in glassy and variably palagonitized tuff, erupted as tephra in 1963–1964 on Surtsey, an island built in the offshore extension of Iceland's southeast rift zone, is documented through a comparative petrographic study of samples from drill cores recovered in 1979 and 2017. Time-lapse alteration within the low-temperature meteoric to seawater dominated hydrothermal system of the volcano is characterized in terms of secondary mineral contents, alteration rates and alteration style with depth. Between 1979 and 2017 palagonitization and cementation by secondary minerals has progressed into previously poorly altered parts of the system, leading to increased consolidation of the basaltic tephra. Alteration rates range between 1.05 and 42.5 $\mu m \cdot yr^{-1}$ for palagonitization of glass and 0.4–8.33 $\mu m \cdot yr^{-1}$ for pseudomorphic olivine replacement by clay minerals over a temperature interval of 47–140 °C. Five distinct zones of alteration style, distinguished through alteration mineralogy, development of authigenic phases over time, as well as degree of alteration are described. Alteration of basaltic tephra at Surtsey volcano is defined by an early stage of phillipsite and clay mineral formation, followed by a later stage of analcime and tobermorite formation as well as replacement of phillipsite below the water table in zone 2 between 65.4 and 138.4 m. Only minor advancement of alteration is detected in zone 3 between 138.4 and 150.3 m depth, where the primary tephra remains largely unpalagonitized and unconsolidated. In contrast, from 1979 to 2017 alteration has increased between 150.3 and 177.8 m depth, in zone 4, leading to rapid and extensive glass and olivine alteration. The quantification of these time-lapse hydrothermal alteration processes at Surtsey provides an important reference for studies of the evolution of young oceanic islands hosting hydrothermal systems.

1. Introduction

In active geothermal systems, hydrothermal fluid flow is known to cause changes in host rock mineral content via fluid-rock interaction, through processes such as geochemical leaching, as well as precipitation of secondary mineral phases from the equilibrating geothermal fluid. The formation of secondary minerals is essentially dependent on time, temperature, pressure, initial rock composition, dissolved aqueous species, pH, fluid-rock-ratio and porosity/permeability (Browne, 1978; Giggenbach, 1984; Henley et al., 1985; Pauly et al., 2011). Thus, the nature and quantitative composition of a hydrothermal system's secondary mineral assemblage at depth may be considered to be indicative of the physicochemical properties and history of both host rock and hydrothermal fluid (e.g. Weisenberger and Selbekk, 2009; Kousehlar et al., 2012; Spürgin et al., 2019). As the geothermal system undergoes change with time, these properties too will be subject to variation, thereby resulting in an altered chemistry of the hydrothermal fluid, as well as a shift in the stability of secondary minerals. The effects of time as well as chemical and thermal changes are therefore an important aspect to consider in the petrographic study of hydrothermal alteration.

Within systems containing fresh basaltic glass (sideromelane), heat and chemical interaction with circulating fluids may cause devitrification of the glass (Marshall, 1961; Crovisier et al., 2003), leading to the formation of a metastable alteration product called palagonite.

---

* Corresponding author.
E-mail addresses: simon.prause@isor.is (S. Prause), tbw@isor.is (T.B. Weisenberger).

https://doi.org/10.1016/j.jvolgeores.2019.106754

Palagonite, first described by Von Waltershausen (1845), occurs as a yellow to dark reddish brown amorphous to cryptocrystalline gel-like phase, commonly found as a surface alteration product of sideromelane, which can fully replace the original basaltic glass at advanced stages of the reaction. Palagonitization is recognized as a key factor in the lithification of loose vitric basalt tephra, fortifying volcanic edifices against erosion and increasing slope stability (Schiffman et al., 2006; Frolova, 2010; Romagnoli and Jakobsson, 2015), as well as being of global importance for oceanic crust-seawater chemical budgets (Staudigel and Hart, 1983; Walton et al., 2005; Pauly et al., 2011; Gernon et al., 2016). Additionally, the formation of palagonite and associated authigenic mineral assemblages from sideromelane is widely considered as a natural counterpart to alteration processes that may take place in radioactive waste storage borosilicate glasses, making the study of basaltic glass alteration relevant for the assessment of challenges involved in the long-term storage of these hazardous materials (Techer et al., 2001; Crovisier et al., 2003; Parruzot et al., 2015). Despite this potential relevance, the mineralogical nature of palagonite and its formation mechanism remain subject of research. Generally, it is accepted today, that palagonite forms as a result of dissolution of sideromelane in conjunction with glass hydration, which is usually accompanied by the precipitation of diverse mineral assemblages (Stroncik and Schmincke, 2002; Crovisier et al., 2003; Drief and Schiffman, 2004; Pauly et al., 2011). In this process, mobile elements are released from the glass (Singer and Banin, 1990; Stroncik and Schmincke, 2001; Pauly et al., 2011) and eventually form secondary minerals, such as clay minerals, zeolites and carbonates (Nayudu, 1964; Fisher and Schmincke, 1984; Walton and Schiffman, 2003; Pauly et al., 2011). Immobile elements become passively enriched (Stroncik and Schmincke, 2001). Palagonite may thus be considered as a residual material, containing both amorphous and microcrystalline phases, that remains after selective dissolution of the initial basaltic parent glass (Thorseth et al., 1991; Drief and Schiffman, 2004). The process of glass alteration and palagonitization can occur both abiotically, through purely geochemical processes, and also through microbial activity (Thorseth et al., 1992; Staudigel et al., 2008; Pedersen et al., 2015; Türke et al., 2015).

Previous studies have shown that palagonitization rates are strongly dependent on temperature, with the process proceeding more rapidly at higher temperatures (Furnes, 1975; Jakobsson, 1978; Jakobsson and Moore, 1986; Singer and Banin, 1990). Other important factors that affect the process of palagonitization are porosity and water-rock ratio, fluid chemistry (including dissolved species, salinity and pH), fluid flow and original glass composition (Moore, 1966; Jakobsson and Moore, 1986; Stroncik and Schmincke, 2002; Crovisier et al., 2003; Pauly et al., 2011). As a result, palagonite does not have a single fixed composition, but rather its specific chemical composition and the type of secondary mineral phases, that may form from it, are strongly dependent on the abovementioned parameters. For this reason, the name "palagonite" is to be taken as a descriptive expression, which designates the product of a specific alteration process, rather than being a strictly defined term for a chemically well constrained phase, as it may describe both crystalline and amorphous material of varying composition (e.g. Staudigel and Hart, 1983). In addition, palagonite is known to change its composition and structure as it ages due to progressive devitrification and diffusive processes (Thorseth et al., 1991; Stroncik and Schmincke, 2001; Pauly et al., 2011). Due to the ambiguity of the term some authors, such as Honnorez (1978) have opted to forego the word palagonite entirely, in favor of the broader designation of "palagonitized glass".

Many previous investigations have focused on palagonitization in a relatively low-temperature environment, with studies on hydrothermal palagonitization rates being less common. Since palagonitization under non-hydrothermal diagenetic conditions tends to be a relatively slow process, with estimated palagonitization rates typically ranging between a few 10^{-3}–10^{-2} $\mu m \cdot yr^{-1}$ (Hekinian and Hoffert, 1975; Walton and Schiffman, 2003; Pauly et al., 2011), many aspects of palagonitization and the evolution of the resulting secondary mineral assemblages over time remain poorly understood. In this regard, the volcanic island of Surtsey, with its low-temperature meteoric to seawater dominated hydrothermal system, offers a unique opportunity to study palagonitization and its resulting authigenic smectite/zeolite/tobermorite mineral assemblage over time. The hydrothermal system at Surtsey is hypothesized to have initiated in response to heating by the basaltic intrusions that fed lava flows from 1964 to 1967 (Friedman and Williams, 1970; Jakobsson and Moore, 1982, 1986; Stefánsson et al., 1985). Since this time, the vitric basaltic tephra deposits have been undergoing progressive hydrothermal alteration, through the diverse processes that produce palagonitization of basaltic glass and cementation of the deposits by authigenic minerals (Fig. 1).

The first Surtsey drill core, SE-01, was retrieved in 1979 from the vicinity of the island's southeastern vent, *Surtur* (Fig. 2). Investigations of the 181 m long core by Jakobsson and Moore (1986) indicated that palagonitization of Surtsey tephra deposits is influenced by hydrothermal processes and varies with temperature. Below sea level alteration rims of smectitic clay mineral, mainly nontronite, were found to form around olivine crystal fragments. The thicknesses of these rims, much like the thicknesses of palagonitization rims on basaltic glass particles, were positively correlated with temperature.

A 192 m long drill core, SE-02b, was recovered at about 7 m lateral distance from SE-01 (Fig. 2) by the International Continental Scientific Drilling Program (ICDP) SUSTAIN project in 2017 (Jackson et al., 2019a; Weisenberger et al., 2019). The new core will allow us to build upon the prior research by Jakobsson and Moore (1986) to investigate how alteration of basaltic tephra in a low-temperature, hydrothermal system varies as a function of time, depth and temperature. For this purpose, the archived 1979 Surtsey drill core is revisited for petrographic analysis and a comparison is made with observations from corresponding depths of the 2017 drill core. The goal of this study is to evaluate and quantify changes in secondary mineralization, palagonitization and lithification of the Surtsey tephra, to characterize time-lapse alteration and constrain alteration rates. The petrographic results obtained from this study form the groundwork for future geochemical investigations of the Surtsey drill cores.

2. Geological setting

Surtsey is the youngest and southernmost member of the Vestmannaeyjar archipelago, which marks the seaward extension of Iceland's East Volcanic Zone (Moore, 1985; Jackson et al., 2015; Schipper et al., 2016) (Fig. 2). First emerging from the ocean surface on November 15, 1963, Surtsey was subsequently built up until June 5, 1967 by an interplay of early stage phreatomagmatic and mid to late stage effusive volcanism (Jakobsson and Moore, 1982). The eruption that formed the island took place in several episodes along a 4.5 km long ENE-trending array of five NNE-trending short submarine volcanic fissures approximately 33 km off Iceland's southern coast (Thorarinsson et al., 1964; Moore, 1985). Two smaller edifices, *Syrtlingur* and *Jólnir* developed, but were subsequently eroded (Jakobsson and Moore, 1982; Moore, 1985). Another volcanic ridge, *Surtla*, formed on the seafloor, between late December 1963 and early January 1964, but did not grow large enough to rise above sea level. On Surtsey an estimated amount of 0.7–0.8 km^3 of very poorly sorted, alkali-basaltic, glassy tephra was emplaced as bedded air fall and base surge deposits primarily via explosive discharge (cock's tails) and continuous uprush (tephra fingers) (Thorarinsson, 1965; Jakobsson and Moore, 1982). These deposits make up 60–70 vol% of all erupted material on Surtsey with the remaining fraction composed of crystalline alkali basalt, reworked sediments and sand/tephra layers at depths ≥118.5 m below sea level (Lorenz, 1974; Jakobsson and Moore, 1982).

One year after the cessation of volcanic activity, the first signs of an incipient hydrothermal system were observed in the form of visible

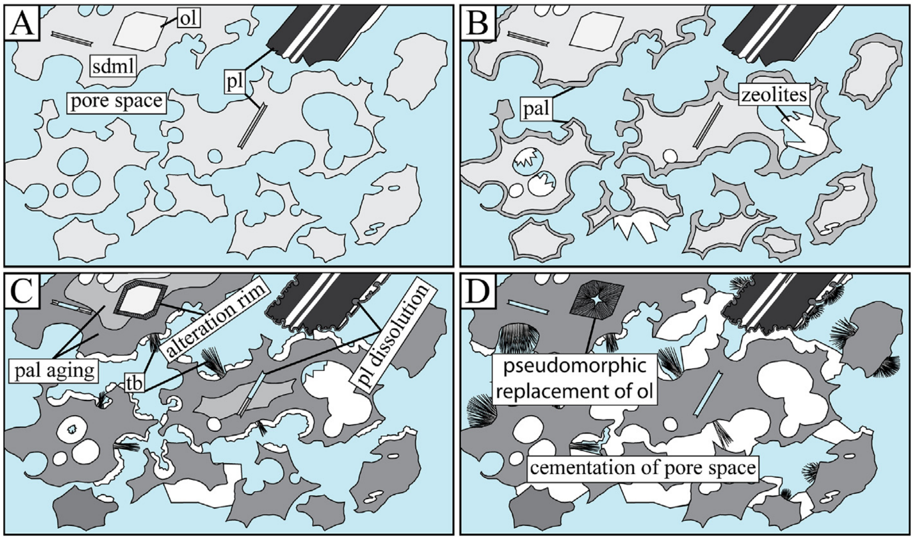

Fig. 1. Schematic outline of progressive alteration of vitric tephra deposits at Surtsey: A) Fresh, unaltered tephra, composed of sideromelane (sdml) and containing (micro-)phenocrysts of primary minerals, principally olivine (ol) and plagioclase (pl). B) Incipient stage of palagonitization, marked by the presence of thin amorphous gel-palagonite rims and scattered zeolite surface coatings. C) Progression of palagonitization with ongoing glass alteration and maturation of gel-palagonite rims. Zeolite cements become increasingly widespread and tobermorite (tb) begins to crystallize. Plagioclase dissolves, forming a thin coating of phyllosilicate minerals on the surface of larger crystals, while smaller crystals dissolve and leave voids within palagonitized glass. Below water level clay minerals form rims around olivine crystals and progressively encroach over time. D) More advanced alteration, most sideromelane has undergone palagonitization and most olivine grains have been altered to clay minerals. Cementation of the pore space is extensive, leading to a high degree of consolidation of the tuff and fortifying the material against erosion. The width of each image corresponds to about 5 mm. Mineral Abbreviations, where applicable, after Whitney and Evans (2010).

steam rising from the tephra pile and a zone of anomalous heat exchange (Friedman and Williams, 1970). The nature of hydrothermal processes on the island and associated alteration of the tephra deposits have been subject to earlier detailed studies (e.g. Jakobsson, 1972, 1978; Jakobsson and Moore, 1986; Jakobsson et al., 2000). In 1969, the first signs of palagonitization of the basaltic glass fraction of the tephra became evident and by 1976 most tephra within the thermal zone had undergone palagonitization (Jakobsson, 1971, 1972, 1978). Hydrothermal alteration of vitric basaltic tephra by palagonitization together with the formation of natural secondary mineral cements, have been recognized as key factors to the island's resistance to erosion, by causing the lithification of the tephra deposits (Jakobsson et al., 2000; Jackson et al., 2015; Romagnoli and Jakobsson, 2015). In addition, Surtsey has been recognized as having a secondary mineral assemblage that is unique in both the Vestmannaeyjar archipelago as well as in greater Iceland (Jakobsson and Moore, 1986; Jackson et al., 2019b).

3. The Surtsey hydrothermal system

The hydrothermal system at Surtsey is characterized by several distinct hydrological zones. The uppermost zone above the water table is dominated by meteoric fluids that are derived from rainwater. Surface vapors indicate that this depth interval contains steam zones.

The water table, which is influenced by tidal fluctuations, is located at ca. 58 m measured depth for the two studied drill cores (Weisenberger et al., 2019). Geophysical borehole logging conducted after drilling of SE-02b indicates a freshwater lens at this depth (Jackson et al., 2019a; Weisenberger et al., 2019). The exact thickness of the lens remains unclear since fluids in the borehole were still disturbed due to drilling when the measurements were conducted. The freshwater lens overlies more saline fluids of modified seawater composition (Jackson et al., 2019a).

Temperature profiles obtained over the course of 37 years show, that the system has gradually undergone cooling (Fig. 3). The system's temperature maximum occurs at a vertical depth of about 105–110 m below the surface for the two vertical boreholes considered in this study. Temperature at this depth has decreased from 141 °C in 1980 to 124 °C in 2019. The temperature logs indicate a cooling point at a depth of about 145 m below the surface, which likely represents a cold inflow zone (Weisenberger et al., 2019; Jackson et al., 2019a).

4. Methods and materials

4.1. Thin section petrography

Petrographic thin sections were prepared for samples from the archive of the SE-01 drill core, stored in core boxes at ambient temperatures since 1979, and the SE-02b drill core. All SE-01 thin sections as well as reference samples from the SE-02b core (see Weisenberger et al., 2019) were prepared using yellow epoxy resin. An additional series of thin sections from the SE-02b core was prepared from selected research samples using blue epoxy resin. All samples were soaked in epoxy resin prior to polishing, due to the fragility and friable nature of the sample material. Heating the epoxy resin above 50 °C was avoided in all thin sections in order to preserve temperature-sensitive hydration. Table 1 provides an overview of selected samples for this study.

Primary mineral phases and authigenic features, such as altered glass and secondary minerals, were quantified by point counts, using a step interval of 0.18 mm. The number of counted points was dependent on the individual sample and ranged from 603 to 4557 points, with an average number of counts per sample of 2322. The degree of palagonitization was determined as the fraction of basaltic glass (sideromelane) in a sample, which has become palagonitized, given as

$$\frac{V_{\text{palagonitized glass}}}{(V_{\text{palagonitized glass}}+V_{\text{glass}})}\cdot 100\text{vol}\%$$

where $V_{\text{palagonitized glass}}$ and V_{glass} refer to the total volume of palagonitized glass and sideromelane within a given thin section as indicated by point counts. Thicknesses of alteration rims (i.e. palagonitized glass and clay mineral rims around olivine) were obtained by conducting as many measurements as possible by use of a petrographic microscope followed by determination of median values for each sample. Sideromelane was identified purely based on its distinct coloration as well as its optical isotropy (complete extinction under cross-polarized light). However, as a recent study by Jackson et al. (2019b) has demonstrated, such seemingly unaltered glasses may also

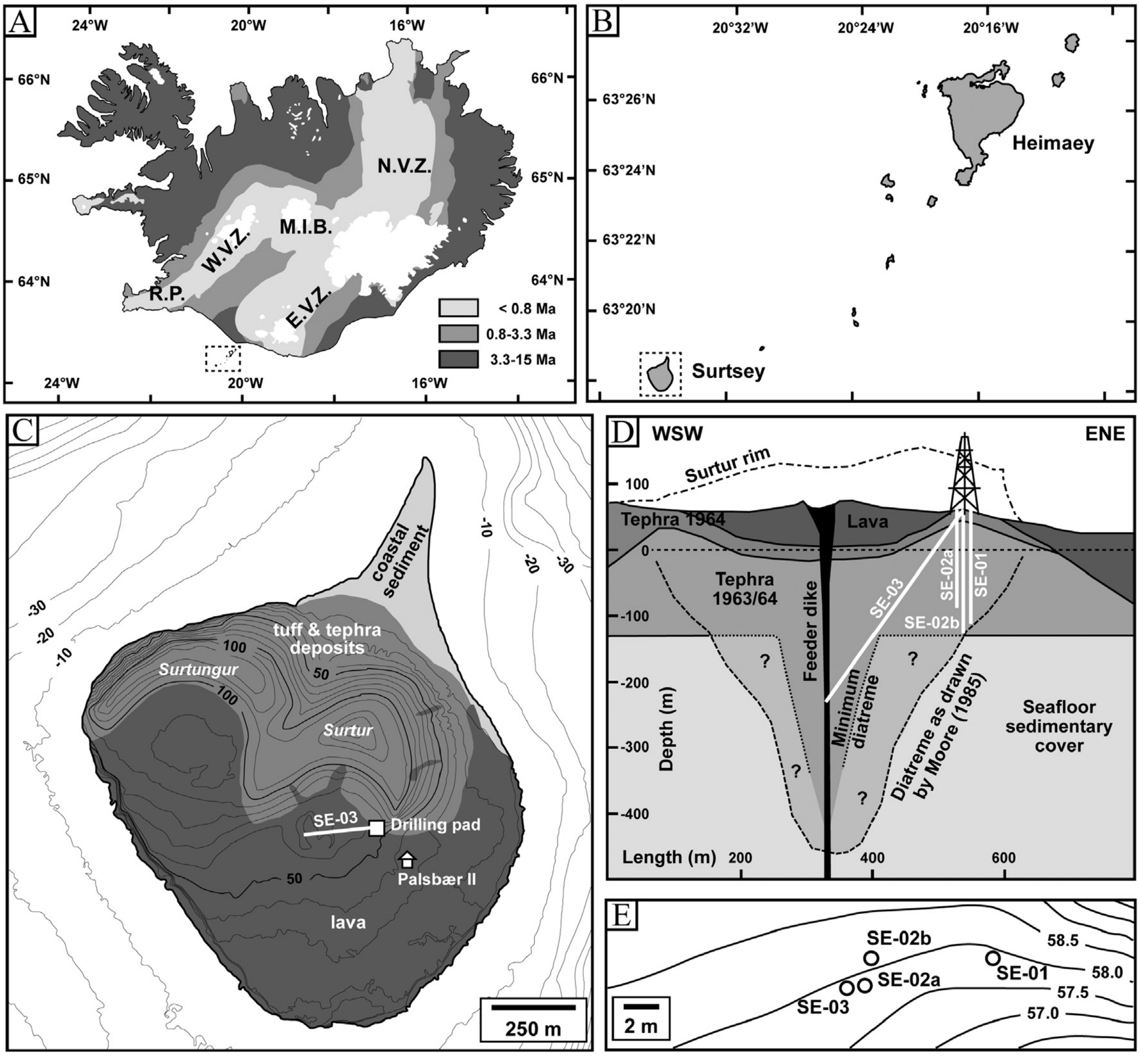

Fig. 2. Overview of Surtsey and the 1979 and 2017 drilling projects. A) Simplified geologic map showing the age distribution of rocks in greater Iceland in Ma and the main volcanic provinces (N.V.Z: North Volcanic Zone, M.I.B.: Mid-Iceland Belt, W.V.Z.: West Volcanic Zone, E.V.Z.: East Volcanic Zone, R.P.: Reykjanes Peninsula). The Vestmannaeyjar archipelago (dashed rectangle) marks the southern seaward extension of the E.V.Z. B) The Surtsey eruptions form the southernmost extension of the archipelago. C) Geologic map of Surtsey highlighting the position of the drill pad and the Pálsbær II hut. D) Schematic cross-section through the Surtur tuff cone showing depth and orientation of the boreholes as well as the island's subsurface structure, based on Moore (1985). The drill holes from 1979 (SE-01) and 2017 (SE-02a, SE-02b and SE-03) are situated in close proximity at the eastern edge of the Surtur tephra pile. E) The relative position of the boreholes. After Jackson et al. (2019a) and Weisenberger et al. (2019).

contain nanocrystalline clay minerals, which are unobservable under the microscope. Here we use the term "sideromelane" to refer to the fraction of glassy lapilli, which appears unaltered based purely on optical microscopy.

4.2. X-ray powder diffraction

X-ray powder diffraction (XRPD) analysis was performed on samples of the 1979 core (SE-01) in order to confirm the results of the point count data. XRD analyses were carried out using a Panalytical X'Pert Pro diffractometer (RTMS X'Celerator detector) and Bruker D2 Phaser (LINKEYE detector) diffractometer at the Department of Earth Sciences, Environment and Resources (DiSTAR) of the University of Naples Federico II.

The following operative conditions were used: CuKα radiation, 40 kV, 40 mA, 2ϑ range from 4 to 70°, equivalent step size 0.017° 2ϑ, 30 s per step counting time for X'Pert Pro; CuKα radiation, 30 kV, 15 mA, 2ϑ range from 4 to 70°, 0.02 2ϑ step size, 66 s per step counting time for Bruker D2 Phaser. The analyses were used to obtain a calibration between the two different diffractometers. Each sample was disaggregated by hand in an agate mortar to obtain a homogeneous powder (particle size <200 μm). An amount of 20 wt% corundum (α-Al_2O_3, Buehler micropolish, 1 μm grain size) was added as an internal standard. This mixture was subsequently micronized (grain size <10 μm) by using a McCrone Micronising Mill, with agate cylinders and 10 mL of deionized water for 15 min of grinding time. This technique was used to reduce preferred orientation, primary extinction or crystallite size issues which commonly affect clay minerals (Bish and Chipera, 1987). For the qualitative interpretations of XRPD patterns the Panalytical HighScore Plus 3.0d software was used, while BRUKER TOPAS 5.0 software was employed for quantitative evaluations with the combined RIR/Rietveld approach.

4.3. Surtsey drill cores

Two drill cores have been selected for this study: SE-01 and SE-02b (Fig. 2). The studied drill core samples, except for the samples obtained from crystalline basalt, can universally be described as hypocrystalline (lapilli-) tuff of inequigranular grain size distribution at different stages of palagonitization, which contains varying amounts of secondary minerals associated with palagonitic glass alteration. The principal constituents of the samples are angular to slightly rounded ash to lapilli-sized fragments of sideromelane. The outline given below is only intended as a very brief overview of macroscopic lithological characteristics. For a more comprehensive description of the 1979 and 2017 Surtsey drill cores the reader is referred to Jakobsson and Moore (1982) and Weisenberger et al. (2019).

4.3.1. SE-01

Above water level the tuff is beige to brown in color and remains poorly altered. The degree of consolidation is typically low. Some primary layering may be observed locally. At 55.3 m, which is close to the uppermost tidal dominated water level, the first macroscopically visible signs of alteration in the form of white mineral cements in pore space become apparent. These increase in abundance downcore, leading to a progressive reduction of estimated pore space with depth as the rock begins to take on a greenish hue and increases in hardness and density, as inferred by weight. Between 72.3 and 83.4 m a basaltic intrusion is present. The tuff is more poorly consolidated and friable in the zone between ca. 139.3–150.3 m, locally leading to poor core recovery between 140.0–143.8 and 148.5–150.3 m. Below this depth, the material becomes slightly more consolidated up until 157.3 m. Below 157.3 m core recovery was again poor with the recovered tuff being dark gray in coloration as well as very friable. Alteration mineralogy at this depth consists mainly of anhydrite, which occurs as a macroscopically visible white to translucent phase in the pore space and along fractures. Between 170.5 and 180.1 m only cuttings were recovered.

4.3.2. SE-02b

Armored lapilli were locally described above water level as well as down to ca. 62.6 m depths (Weisenberger et al., 2019). The basaltic intrusion found in SE-01 at 72.3–83.4 m depths is not present in SE-02b, despite the horizontal distance between the cores being <7 m, possibly indicating a complex geometry of the intrusive body. Unlike in SE-01, fully consolidated core material was recovered from the area between 139.3–150.3 m and below 157.3 m. Despite this, the tuff remains poorly altered in the depth interval between 138.4 and 150.3 m. Here the main secondary minerals are anhydrite, gypsum and calcite, rather than zeolites or tobermorite, which dominate in the more strongly altered zones. Estimated porosities (Table 1) for this poorly altered zone are high, reaching up to 38.6 vol%. The tuff in the depth interval below 150 m down to 178 m is more consolidated and shows extensive signs of alteration in the form of macroscopically visible cementation and darkened coloration as well as palagonitization. Below 178 m the rock remains poorly altered and very friable.

5. Results

5.1. Primary phases

The primary crystalline phases present in the Surtsey tuff samples are plagioclase, clinopyroxene and olivine. These occur as (micro-) phenocrysts in the glassy particles and as crystal fragments. Minor amounts of opaque phases are present as well. A brief description of the primary phases is given below.

5.1.1. Sideromelane

Sideromelane appears in thin section as a vesicular bright yellow to pink gel-like phase containing sporadic phenocrysts of plagioclase, olivine and clinopyroxene. It is distinguished from palagonitized glass mainly by its characteristic color, as opposed to the darker reddish brown of type I palagonitization rims (see Section 5.2.1 Palagonitized glass). Furthermore, the complete optical isotropy of sideromelane makes it distinct from type II and III palagonitized glass. Despite this seemingly obvious distinction, it should be noted that "fresh" sideromelane is identified here under purely optical criteria and thus some alteration of the glass may have occurred on a microscale. Since submicroscopic nanocrystalline phases, such as clay minerals, as identified by Jackson et al. (2019b), cannot be identified by optical microscopy, our definition of "sideromelane" cannot possibly account for their presence.

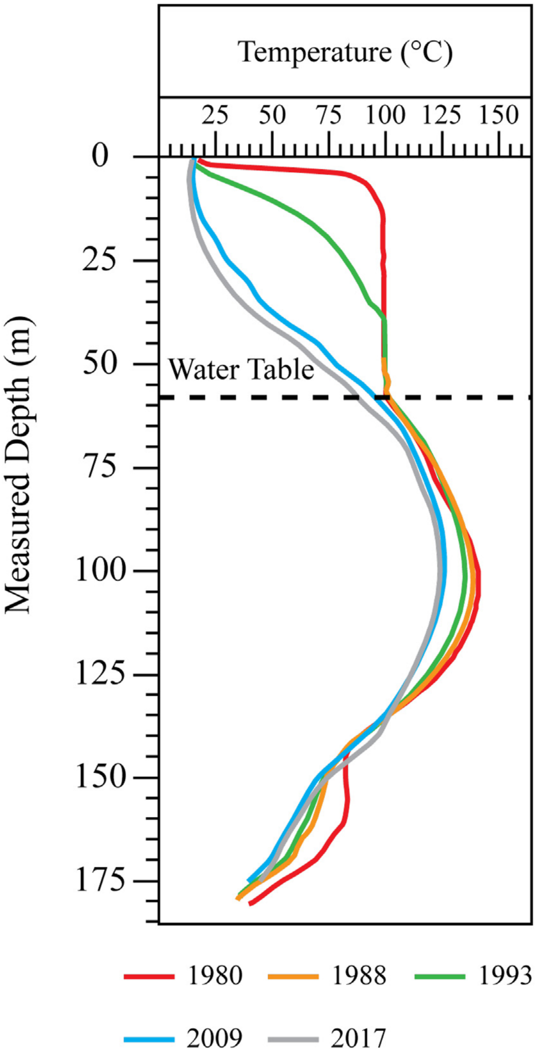

Fig. 3. Borehole temperature profiles for SE-01 obtained between 1980 and 2017 by downholelogging.

5.1.2. Plagioclase

Plagioclase typically occurs in the form of anhedral, single crystals or granular aggregates with an average grainsize between 150 and 200 μm, typically forming a microlitic texture within sideromelane. Some rare larger phenocrysts of up to 1 cm can be found in the Surtsey lapilli-tuff. Both above and below water level some of these larger massive phenocrysts show minor signs of dissolution in the form of serrated or frayed grain boundaries and occasional low amounts of secondary clay mineral formation. Smaller plagioclase microphenocrysts generally decrease in abundance within the temperature maximum of the system at 105–110 m, leaving behind voids in glass upon their dissolution. According to XRPD, the amount of plagioclase in the tuff lies between 2 and 19 wt% with an average of 9 wt% (Grimaldi, 2018).

5.1.3. Clinopyroxene

Clinopyroxene is very common in the Surtsey tephra, making up a fraction between 2 and 9 wt% (average: 6 wt%) of the phases identified in the tuff samples by XRPD (Grimaldi, 2018). It occurs in the form of anhedral granular to columnar microphenocrysts in sideromelane. These typically have an average size of about 230 μm.

Table 1
Samples and petrographic results from optical thin section microscopy.

Drill hole	Depth (m)	IGSN #	Rock type	Sample type	Primary minerals (vol%)	Glass Alteration (vol%)		Secondary minerals (vol%)					Porosity (vol%)	Degree of palagonitization (vol%)	Palagonitization extent[b] (vol%)	Rim thickness (μm)	
					(Pl + Cpx + Ol)[a]	Sdml[a]	Pal[a]	Php[a]	Anl[a]	Tb[a]	Anh[a]	Gp[a]				Pal[a]	Ol[a]
SE-01	4.9	–	Lapilli-Tuff	Core	4.5	9.7	42.9	3.1	8.6	0.0	0.2	n.a.	31.1	81.5	84.9	75.0	0.0
SE-01	22.0	–	Lapilli-Tuff	Core	3.2	12.8	35.1	5.5	4.1	0.3	1.4	n.a.	37.6	73.3	77.9	120.0	0.0
SE-01	43.6	–	Lapilli-Tuff	Core	2.4	48.5	13.4	1.2	0.0	0.3	0.3	n.a.	33.9	21.6	23.5	8.8	0.0
SE-01	55.8	–	Lapilli-Tuff	Core	4.6	10.0	46.8	3.5	1.4	5.0	0.3	n.a.	28.4	82.4	85.0	75.0	0.0
SE-01	65.4	–	Lapilli-Tuff	Core	4.7	2.2	47.7	4.5	7.8	2.4	0.4	n.a.	30.2	95.5	96.5	240.0	0.0
SE-01	72.4	–	Lapilli-Tuff	Core	5.6	0.0	57.6	10.2	0.0	0.0	0.5	n.a.	26.2	100.0	100.0	n.a.	30.0
SE-01	72.4	–	Crystalline basalt	Core	95.1	0.0	0.0	0.0	0.0	1.9	1.0	n.a.	2.0	n.a.	n.a	n.a.	n.a.
SE-01	76.1	–	Crystalline basalt	Core	96.4	0.0	0.0	0.0	0.0	0.1	0.0	n.a.	3.6	n.a.	n.a.	n.a.	n.a.
SE-01	83.5	–	Crystalline basalt	Core	96.1	0.0	0.0	0.0	0.0	0.4	1.3	n.a.	2.1	n.a.	n.a.	n.a.	n.a.
SE-01	83.5	–	Lapilli-Tuff	Core	3.7	0.0	57.9	1.2	10.4	0.0	5.3	n.a.	21.5	100.0	100.0	n.a.	70.0
SE-01	86.6	–	Lapilli-Tuff	Core	3.8	0.3	53.4	1.7	6.7	5.3	2.2	n.a.	26.6	99.5	99.6	510.0	70.0
SE-01	90.1	–	Lapilli-Tuff	Core	1.4	0.0	56.7	5.7	2.6	6.7	0.9	n.a.	26.0	100.0	100.0	n.a.	60.0
SE-01	92.6	–	Lapilli-Tuff	Core	3.1	0.0	55.7	0.8	7.8	5.2	1.4	n.a.	26.0	100.0	100.0	n.a.	75.0
SE-01	95.4	–	Lapilli-Tuff	Core	15.3	26.4	35.4	1.7	1.8	3.7	0.0	n.a.	15.8	57.3	61.7	n.a.	50.0
SE-01	95.5	–	Lapilli-Tuff	Core	3.7	2.9	64.4	1.6	2.1	7.8	0.0	n.a.	17.5	95.7	96.4	257.5	n.a.
SE-01	95.6	–	Lapilli-Tuff	Core	3.3	0.2	52.3	0.8	9.7	0.1	12.8	n.a.	20.9	99.6	99.7	420.0	n.a.
SE-01	105.0	–	Lapilli-Tuff	Core	3.8	0.0	52.3	1.2	3.7	7.1	4.3	n.a.	27.6	100.0	100.0	n.a.	60.0
SE-01	111.0	–	Lapilli-Tuff	Core	0.9	0.6	61.5	2.7	6.1	1.6	0.1	n.a.	26.6	99.0	99.2	440.0	95.0
SE-01	120.6	–	Lapilli-Tuff	Core	3.6	1.5	56.1	0.6	6.4	4.5	0.1	n.a.	27.2	97.3	97.8	360.0	50.0
SE-01	137.8	–	Lapilli-Tuff	Core	11.2	14.0	41.0	9.6	2.4	3.9	0.2	n.a.	17.7	74.6	80.3	120.0	25.0
SE-01	140.0–141.0	–	Lapilli-Tuff	Cuttings	n.a.	n.a.	n.a.	n.a.	n.a.	n.a.	n.a.	n.a.	n.a.	n.a.	n.a.	0.0	0.0
SE-01	143.0–144.0	–	Lapilli-Tuff	Cuttings	n.a.	n.a.	n.a.	n.a.	n.a.	n.a.	n.a.	n.a.	n.a.	n.a.	n.a.	0.0	0.0
SE-01	148.0–149.0	–	Lapilli-Tuff	Cuttings	n.a.	n.a.	n.a.	n.a.	n.a.	n.a.	n.a.	n.a.	n.a.	n.a.	n.a.	0.0	0.0
SE-01	148.3	–	Lapilli-Tuff	Core	5.4	43.3	24.6	8.1	0.0	0.0	0.7	n.a.	17.9	36.2	43.0	40.0	0.0
SE-01	149.0–150.0	–	Lapilli-Tuff	Cuttings	n.a.	n.a.	n.a.	n.a.	n.a.	n.a.	n.a.	n.a.	n.a.	n.a.	n.a.	0.0	0.0
SE-01	150.3	–	Lapilli-Tuff	Core	5.4	47.8	15.2	5.9	0.2	0.0	2.5	n.a.	23.1	24.1	30.8	40.0	0.0
SE-01	156.9	–	Lapilli-Tuff	Core	7.4	23.2	43.8	3.0	2.0	2.7	0.0	n.a.	18.0	65.4	69.0	50.0	20.0
SE-01	157.3–158.0	–	Lapilli-Tuff	Cuttings	n.a.	n.a.	n.a.	n.a.	n.a.	n.a.	n.a.	n.a.	n.a.	n.a.	n.a.	0.0	0.0
SE-01	165.0–166.0	–	Lapilli-Tuff	Cuttings	n.a.	n.a.	n.a.	n.a.	n.a.	n.a.	n.a.	n.a.	n.a.	n.a.	n.a.	0.0	0.0
SE-01	169.5	–	Lapilli-Tuff	Core	4.0	55.7	0.0	0.0	0.0	0.0	19.6	n.a.	20.6	0.0	0.0	0.0	0.0
SE-01	176.5–177.7	–	Lapilli-Tuff	Cuttings	n.a.	n.a.	n.a.	n.a.	n.a.	n.a.	n.a.	n.a.	n.a.	n.a.	n.a.	0.0	0.0
SE-01	178.7–180.1	–	Lapilli-Tuf	Cuttings	n.a.	n.a.	n.a.	n.a.	n.a.	n.a.	n.a.	n.a.	n.a.	n.a.	n.a.	0.0	0.0
SE-02b	13.2	ICDP5059EX3J001	Lapilli-Tuff	Core	5.6	18.3	31.4	6.8	5.6	0.0	0.9	0.0	31.4	63.1	70.5	52.5	0.0
SE-02b	22.6	ICDP5059EX1A701	Lapilli-Tuff	Core	6.9	7.5	43.6	6.8	10.9	3.4	0.9	0.0	20.0	85.3	89.6	135.0	0.0
SE-02b	31.2	ICDP5059EX7J001	Lapilli-Tuff	Core	5.8	9.5	44.1	5.2	9.8	3.6	0.1	1.1	20.7	82.2	86.8	132.5	0.0
SE-02b	34.8	ICDP5059EXBA701	Lapilli-Tuff	Core	5.2	11.5	39.3	5.0	5.6	9.3	1.4	0.0	22.6	77.4	83.8	n.a.	0.0
SE-02b	40.4	ICDP5059EX8J001	Lapilli-Tuff	Core	6.6	9.7	52.7	4.8	4.3	3.8	0.2	0.2	17.7	84.4	87.1	90.0	0.0
SE-02b	43.7	ICDP5059EXLA701	Lapilli-Tuff	Core	6.8	9.4	38.6	9.4	2.7	5.1	0.3	0.0	27.7	80.4	85.6	150.0	0.0
SE-02b	56.0	ICDP5059EXVA701	Lapilli-Tuff	Core	3.9	8.5	46.2	4.1	3.3	6.0	0.4	0.0	27.7	84.5	87.6	145.0	0.0
SE-02b	56.1	ICDP5059EXGJ001	Lapilli-Tuff	Core	5.2	4.7	44.7	6.5	12.6	5.4	0.0	0.0	20.8	90.4	93.6	260.0	0.0
SE-02b	58.9	ICDP5059EXHJ001	Lapilli-Tuff	Core	n.a.	n.a.	n.a.	n.a.	n.a.	n.a.	n.a.	n.a.	n.a.	n.a.	n.a.	480.0	0.0

SE-02b	62.1	ICDP5059EXIJ001	Lapilli-Tuff	Core	5.1	1.2	49.1	6.9	9.6	7.2	0.0	0.0	20.9	97.6	98.3	n.a.	20.0
SE-02b	65.4	ICDP5059EX5B701	Lapilli-Tuff	Core	4.3	0.3	52.7	4.4	14.1	6.3	0.0	0.0	17.9	99.4	99.6	n.a.	30.0
SE-02b	67.5	ICDP5059EXJJ001	Lapilli-Tuff	Core	n.a.	n.a.	n.a.	n.a.	n.a.	n.a.	n.a.	n.a.	n.a.	n.a.	n.a.	430.0	60.0
SE-02b	70.1	ICDP5059EXLJ001	Lapilli-Tuff	Core	n.a.	n.a.	n.a.	n.a.	n.a.	n.a.	n.a.	n.a.	n.a.	n.a.	n.a.	420.0	80.0
SE-02b	75.0	ICDP5059EXMJ001	Lapilli-Tuff	Core	n.a.	n.a.	n.a.	n.a.	n.a.	n.a.	n.a.	n.a.	n.a.	n.a.	n.a.	400.0	70.0
SE-02b	78.4	ICDP5059EXFB701	Lapilli-Tuff	Core	9.2	0.5	51.3	2.9	9.6	5.7	0.1	0.0	20.6	99.1	99.3	n.a.	n.a.
SE-02b	80.5	ICDP5059EXNJ001	Lapilli-Tuff	Core	n.a.	n.a.	n.a.	n.a.	n.a.	n.a.	n.a.	n.a.	n.a.	n.a.	n.a.	n.a.	72.5
SE-02b	86.5	ICDP5059EXPB701	Lapilli-Tuff	Core	2.3	0.0	61.4	1.2	12.6	3.9	0.0	0.0	18.5	99.9	99.9	n.a.	125.0
SE-02b	87.8	ICDP5059EXOJ001	Lapilli-Tuff	Core	n.a.	n.a.	n.a.	n.a.	n.a.	n.a.	n.a.	n.a.	n.a.	100.0	n.a.	n.a.	150.0
SE-02b	89.2	ICDP5059EXPJ001	Lapilli-Tuff	Core	n.a.	n.a.	n.a.	n.a.	n.a.	n.a.	n.a.	n.a.	n.a.	100.0	n.a.	n.a.	107.5
SE-02b	89.5	ICDP5059EXQJ001	Lapilli-Tuff	Core	n.a.	n.a.	n.a.	n.a.	n.a.	n.a.	n.a.	n.a.	n.a.	100.0	n.a.	n.a.	n.a.
SE-02b	92.6	ICDP5059EXZB701	Lapilli-Tuff	Core	2.0	0.0	56.2	0.1	18.1	1.8	0.3	0.0	21.5	100.0	100.0	n.a.	165.0
SE-02b	97.5	ICDP5059EXRJ001	Lapilli-Tuff	Core	n.a.	n.a.	n.a.	n.a.	n.a.	n.a.	n.a.	n.a.	n.a.	100.0	n.a.	n.a.	150.0
SE-02b	101.5	ICDP5059EX9C701	Lapilli-Tuff	Core	1.5	0.0	58.0	0.4	15.7	2.4	0.9	0.0	21.1	100.0	100.0	n.a.	175.0
SE-02b	106.1	ICDP5059EXSJ001	Lapilli-Tuff	Core	n.a.	n.a.	n.a.	n.a.	n.a.	n.a.	n.a.	n.a.	n.a.	100.0	n.a.	n.a.	n.a.
SE-02b	111.0	ICDP5059EXJC701	Lapilli-Tuff	Core	1.8	0.0	67.5	2.0	10.0	6.5	0.3	0.0	12.0	100.0	100.0	n.a.	160.0
SE-02b	120.8	ICDP5059EXTC701	Lapilli-Tuff	Core	3.4	0.0	68.4	0.4	5.4	6.6	0.0	0.0	15.8	100.0	100.0	n.a.	n.a.
SE-02b	121.4	ICDP5059EXUJ001	Lapilli-Tuff	Core	n.a.	n.a.	n.a.	n.a.	n.a.	n.a.	n.a.	n.a.	n.a.	100.0	n.a.	n.a.	n.a.
SE-02b	128.0	ICDP5059EX3D701	Lapilli-Tuff	Core	1.1	0.0	59.7	0.8	17.8	3.7	0.1	0.0	16.8	100.0	100.0	n.a.	n.a.
SE-02b	134.3	ICDP5059EXVJ001	Lapilli-Tuff	Core	5.4	0.0	60.5	0.8	15.0	3.1	0.0	0.0	15.2	100.0	100.0	n.a.	50.0
SE-02b	138.4	ICDP5059EXDD701	Lapilli-Tuff	Core	3.7	1.2	61.0	2.9	8.6	7.3	0.2	0.0	15.2	98.0	98.5	410.0	32.5
SE-02b	141.5	ICDP5059EXWJ001	Lapilli-Tuff	Core	3.9	16.4	39.2	9.3	1.9	0.0	10.4	0.0	18.9	70.6	75.5	n.a.	0.0
SE-02b	142.6	ICDP5059EXXJ001	Lapilli-Tuff	Core	4.4	48.6	0.0	0.0	0.0	0.0	7.2	1.2	38.6	0.0	0.0	0.0	0.0
SE-02b	144.1	ICDP5059EXYJ001	Lapilli-Tuff	Core	5.3	57.9	0.0	0.0	0.0	0.0	1.0	4.3	31.5	0.0	0.0	0.0	0.0
SE-02b	147.1	ICDP5059EXZJ001	Lapilli-Tuff	Core	10.2	53.3	9.5	0.1	0.1	0.0	1.0	1.0	24.8	15.2	15.5	22.5	0.0
SE-02b	148.7	ICDP5059EXND701	Lapilli-Tuff	Core	7.7	11.3	50.1	9.6	4.1	6.1	0.1	0.0	10.9	81.5	86.0	130.0	0.0
SE-02b	150.3	ICDP5059EX0K001	Lapilli-Tuff	Core	7.5	15.7	46.0	9.9	6.6	3.4	0.3	0.2	10.4	74.6	80.8	170.0	0.0
SE-02b	153.3	ICDP5059EX1K001	Lapilli-Tuff	Core	n.a.	n.a.	n.a.	n.a.	n.a.	n.a.	n.a.	n.a.	n.a.	n.a.	n.a.	n.a.	n.a.
SE-02b	157.5	ICDP5059EXXD701	Lapilli-Tuff	Core	5.3	0.0	62.6	3.0	10.2	5.6	1.1	0.0	12.3	99.9	99.9	n.a.	45.0
SE-02b	159.0	ICDP5059EX2K001	Lapilli-Tuff	Core	n.a.	n.a.	n.a.	n.a.	n.a.	n.a.	n.a.	n.a.	n.a.	n.a.	n.a.	480.0	25.0
SE-02b	165.6	ICDP5059EX7E701	Lapilli-Tuff	Core	9.5	0.4	64.0	1.5	6.8	5.0	0.1	0.0	12.7	99.4	99.5	480.0	50.0
SE-02b	168.1	ICDP5059EX3K001	Lapilli-Tuff	Core	n.a.	n.a.	n.a.	n.a.	n.a.	n.a.	n.a.	n.a.	n.a.	n.a.	n.a.	330.0	40.0
SE-02b	176.1	ICDP5059EXHE701	Lapilli-Tuff	Core	7.2	2.0	66.0	1.3	5.4	4.8	0.6	0.0	12.7	97.1	97.5	n.a.	n.a.
SE-02b	176.4	ICDP5059EX4K001	Lapilli-Tuff	Core	n.a.	n.a.	n.a.	n.a.	n.a.	n.a.	n.a.	n.a.	n.a.	n.a.	n.a.	340.0	35.0
SE-02b	177.8	ICDP5059EX5K001	Lapilli-Tuff	Core	8.6	5.1	55.3	1.3	7.0	14.3	0.0	0.0	8.3	91.6	93.9	215.0	20.0
SE-02b	180.9	ICDP5059EXRE701	Lapilli-Tuff	Core	10.5	51.3	0.5	0.0	0.0	0.0	0.2	0.0	37.4	1.0	1.0	n.a.	0.0
SE-02b	181.5	ICDP5059EX6K001	Lapilli-Tuff	Core	n.a.	n.a.	n.a.	n.a.	n.a.	n.a.	n.a.	n.a.	n.a.	0.0	n.a.	0.0	0.0

---

[a] Abbreviations: Pl: Plagioclase, Cpx: Clinopyroxene, Ol: Olivine, Sdml: Sideromelane, Pal: Palagonite, Php: Phillipsite, Anl: Analcime, Tb: Tobermorite, Anh: Anhydrite, Gp: Gypsum, n.a.: not analyzed.

[b] Palagonitization extent based on the method used by Pauly et al. (2011), calculated using relative quantities of authigenic phases and primary glass: (%Pal + %Php + %Anl + %Tb)/(%Sdml + %Pal + %Php + %Anl + %Tb) · 100%.

5.1.4. Olivine

Olivine commonly occurs as granular, massive and rarely prismatic anhedral to subhedral crystals. Very few euhedral crystals are present. Below water level olivine crystals are commonly rimmed by authigenic clay minerals. Within the zone of maximum temperature at 105–110 m (Weisenberger et al., 2019) unaltered olivine is uncommon and most crystals are altered to nanocrystalline clay mineral. At this depth, fresh unaltered olivine, as determined by XRPD, forms 0–3 wt% (average: 1 wt%) of the lapilli tuff (Grimaldi, 2018). Crystal size typically ranges between 200 and 600 μm, with some larger phenocrysts reaching up to 3 mm in diameter. The thickness of the alteration rims on olivine, much like that of the palagonitized glass rims, is positively correlated with temperature and has noticeably increased between 1979 and 2017 in samples from corresponding depths (Fig. 4).

5.2. Authigenic alteration phases

Alteration in both Surtsey drill cores is dominated by palagonitization of sideromelane and the formation of phillipsite, analcime as well as acicular tobermorite. Other secondary phases include clay minerals, which occur either as highly birefringent microcrystalline mineral aggregates in altered glass or as replacement rims on olivine, calcium sulphates (anhydrite, gypsum and bassanite), and calcite.

5.2.1. Palagonitized glass

Based on petrographic investigations of lapilli-sized fragments in thin sections of the archived 1979 Surtsey SE-01 drill core and the 2017 SE-02b drill core, we distinguish three principal types of palagonitic textures.

5.2.1.1. Type I (gel-palagonite). The altered glass falling into this category is clear, translucent and reddish brown in coloration (Fig. 5A). Its appearance is gel-like and amorphous to slightly crystalline (e.g. Stroncik and Schmincke, 2001, 2002). This type of palagonite commonly marks zones, where the degree of palagonitization is ≤80.0 vol%. Type I palagonitization rims are comparatively thin as well as optically isotropic.

5.2.1.2. Type II (fibro-palagonite). Type II altered glass (Fig. 5B) rims possess a grainy to fibrous texture. In plane polarized light they are reminiscent of type I rims, yet they may be slightly brighter in appearance. Rims belonging to this category are cryptocrystalline and show strong birefringence with colorful yellow, green and red interference colors, which strongly resemble those of clay minerals – a property, which sets them apart from type I palagonitized glass rims. Type II occurs in depth intervals of intermediate temperature. Between 1979 and 2017 type II has replaced type I at the lower end of the temperature spectrum and in turn has become replaced by type III palagonitized glass rims in depth intervals of comparatively higher temperatures.

5.2.1.3. Type III. Type III altered glass (Fig. 5C) occurs below water level in both drill cores. It is darkened, opaque and spotty rather than translucent in appearance. Interference colors are far less intense than in type II and in some instances the material might appear completely opaque under cross polarized light. In SE-01 this kind of palagonitization is only found close to the hydrothermal system's zone of maximum temperature. In SE-02b it has spread both upwards and downwards to become the dominant type of palagonitized glass between 67.5 and 134.3 m as well as being present together with type II below 153.3 m.

In instances, where different types appear together, most prominently in SE-02b between 150.3 and 177.8 m, they are generally concentrically arranged around sideromelane in the order of type III → type II → type I → sideromelane (Fig. 6).

5.2.2. Analcime

Analcime (general formula: $NaAlSi_2O_6 \cdot (H_2O)$) is the most abundant secondary mineral phase in terms of both volume and weight percentages according to XRPD and point counts in most of the samples. The

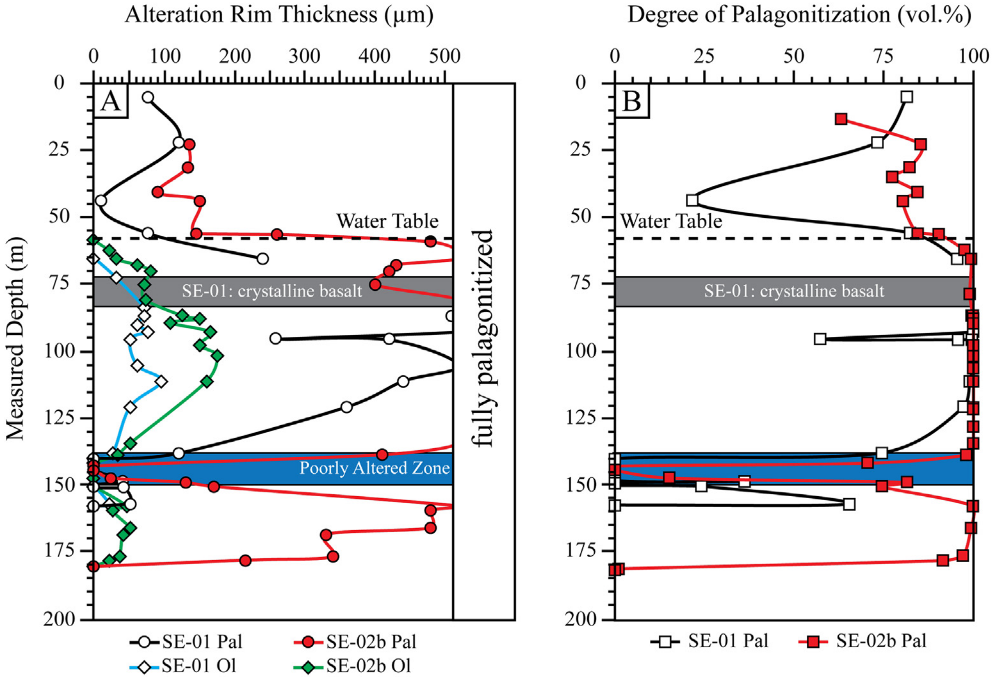

Fig. 4. A) Thicknesses of palagonitization rims on altered glass lapilli and clay mineral rims on olivine crystals in the archived 1979 SE-01 drill core and the 2017 drill core, SE-02b, plotted versus depth and measured through petrographic studies of thin sections. In both drill cores, several samples from the poorly altered zone contain neither palagonitic nor olivine rims. B) Comparison of the measured degree of palagonitization with depth between SE-01 and SE-02b.

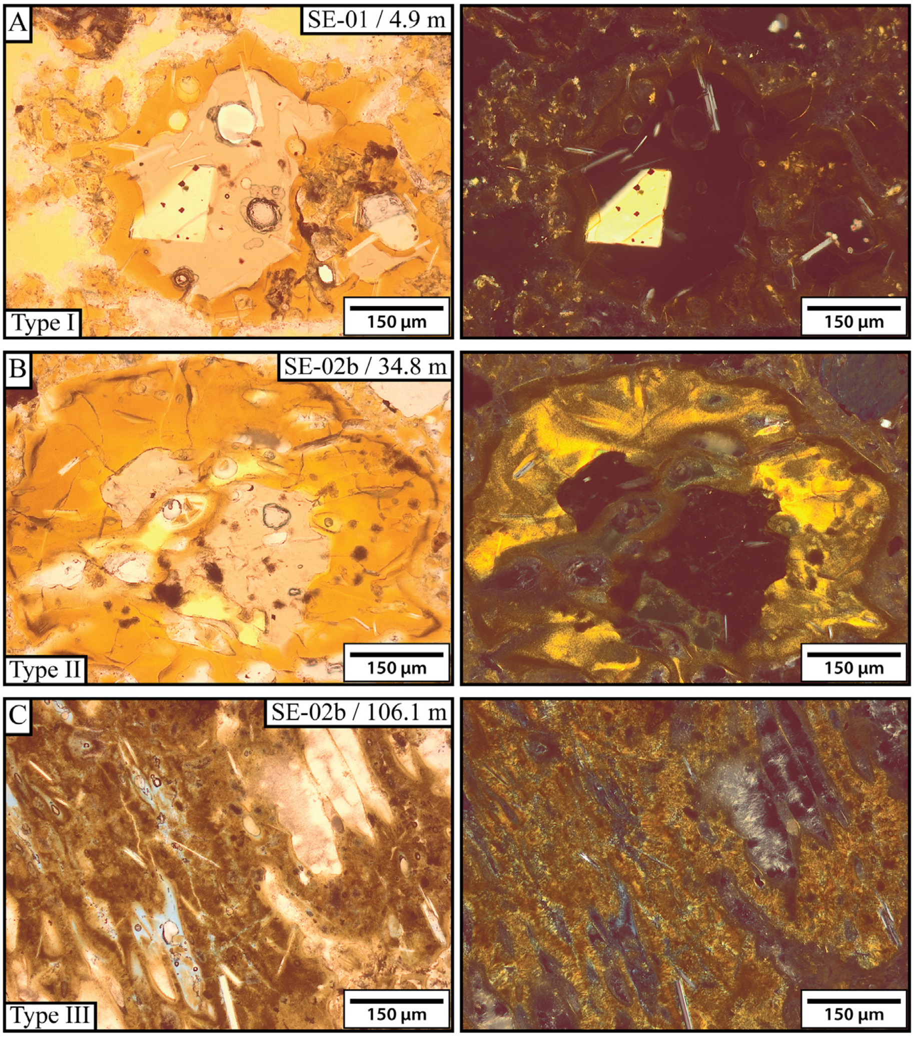

Fig. 5. Three different types of palagonitized glass recognized in the Surtsey samples. A) Type I, or gel-palagonite, is mainly isotropic and shows little to no birefringence. B) Type II, showing bright and high intensity interference colors reminiscent of clay minerals as well as a weakly granular to fibrous texture. C) Type III, displaying less intense interference colors, pronounced fibrous texture and a slightly opaque, mottled appearance.

mineral is typically present as colorless surface textures of massive habit inside the inner walls of cavities, identifiable under crossed polarizers due to its optical isotropy (Fig. 7a). The relative abundance of analcime is positively correlated with both temperature and the degree of palagonitization. The amount of analcime is found to generally have increased in samples from nearly all depths from 1979 to 2017.

5.2.3. Clay minerals

A variety of clay minerals, identified through XRPD (Grimaldi, 2018) as consisting of nontronite, montmorillonite and vermiculite, are present within all tuff samples investigated in this study. Granular to platy mineral aggregates displaying high interference colors are commonly found in available pore space. Clay minerals also occur in the form of alteration rims around olivine phenocrysts. Lastly, submicroscopic to microscopic clay minerals appear as replacement product of sideromelane in palagonitized glass. XRPD does not allow for discrimination between different clay mineral species at their distinct structural positions. The abovementioned highly birefringent dark brown cryptocrystalline clay mineral rims on olivine grains (Fig. 7b, c) are observed exclusively below water level. Above water level olivine typically appears unaltered under the microscope in both SE-01 and SE-02b. The thickness of the olivine alteration rims is positively correlated with temperature. The rims are not observed in samples from the poorly altered zones in the cores between ca. 138–150 m, as well as from the very bottom of both drill holes below 159 m in SE-01 and 178 m in SE-02b respectively.

5.2.4. Tobermorite

Tobermorite (general formula: $Ca_5Si_6O_{16}(OH)_2 \cdot 7H_2O$) is present as colorless acicular crystals, arranged as either discrete needles or sheaf like bundles (Jakobsson and Moore, 1986) (Fig. 7d). It commonly forms within cavities and is frequently associated with analcime as well as phillipsite in some samples, particularly below water level (Fig. 8b).

5.2.5. Phillipsite

In thin section phillipsite (general formula: $(K,Na,Ca)_{1-2}(Si,Al)_8O_{16} \cdot 6H_2O$) occurs as colorless intergrowing prismatic crystals often radiating from a common point of origin. Under crossed polarizers it is distinguishable by its low interference colors (gray I) (Fig. 7e). It commonly fills smaller (50–200 µm) pores and, unlike analcime, only rarely occurs as surface textures in larger cavities. Phillipsite concentrations in the tuff samples appear to have decreased in the higher temperature zones, most likely due to dissolution and/or replacement by other phases (Figs. 7f, 8). Samples that are particularly high in phillipsite are generally marked by a low degree of palagonitization and occasionally by the presence of type I palagonitized glass.

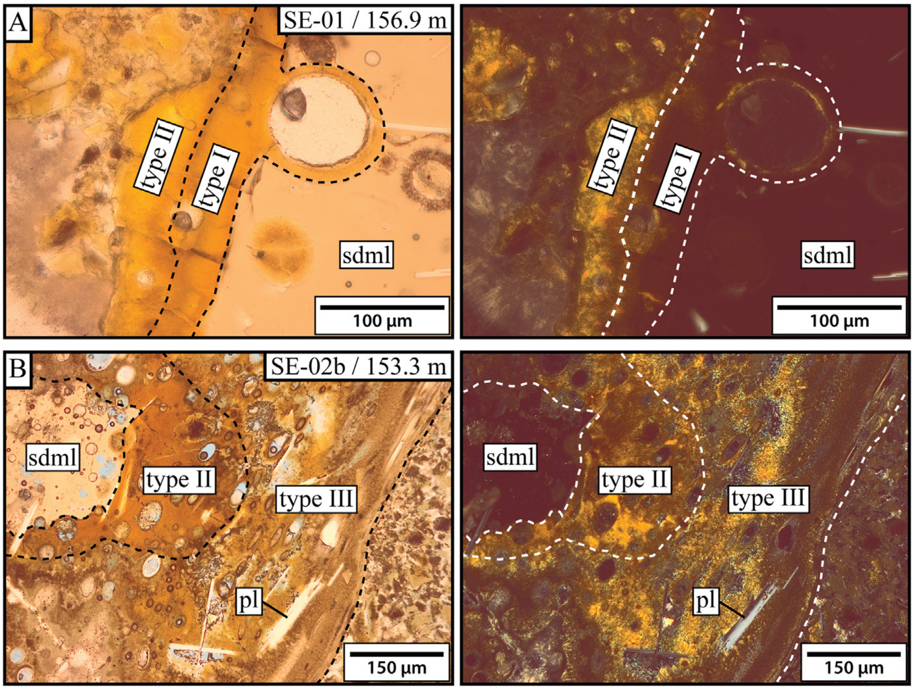

Fig. 6. Spatial relationships between the three different types of palagonitized glass textures. Where these occur together in the same lapillus, types I-III are typically concentrically arranged around sideromelane (i.e. seemingly "fresh" glass) in the sequence "type III → type II → type I → sideromelane" starting at the outer edge of the grain and moving towards the glass-palagonite interface. This observation is consistent with a model of progressive palagonite maturation, in which gel-palagonite, i.e. type I, is first formed along the glass-fluid interface, before undergoing a continuum of alteration processes over time and forming types II-III as the palagonitization front progresses inwards towards the core of fresh glass in the basaltic lapillus.

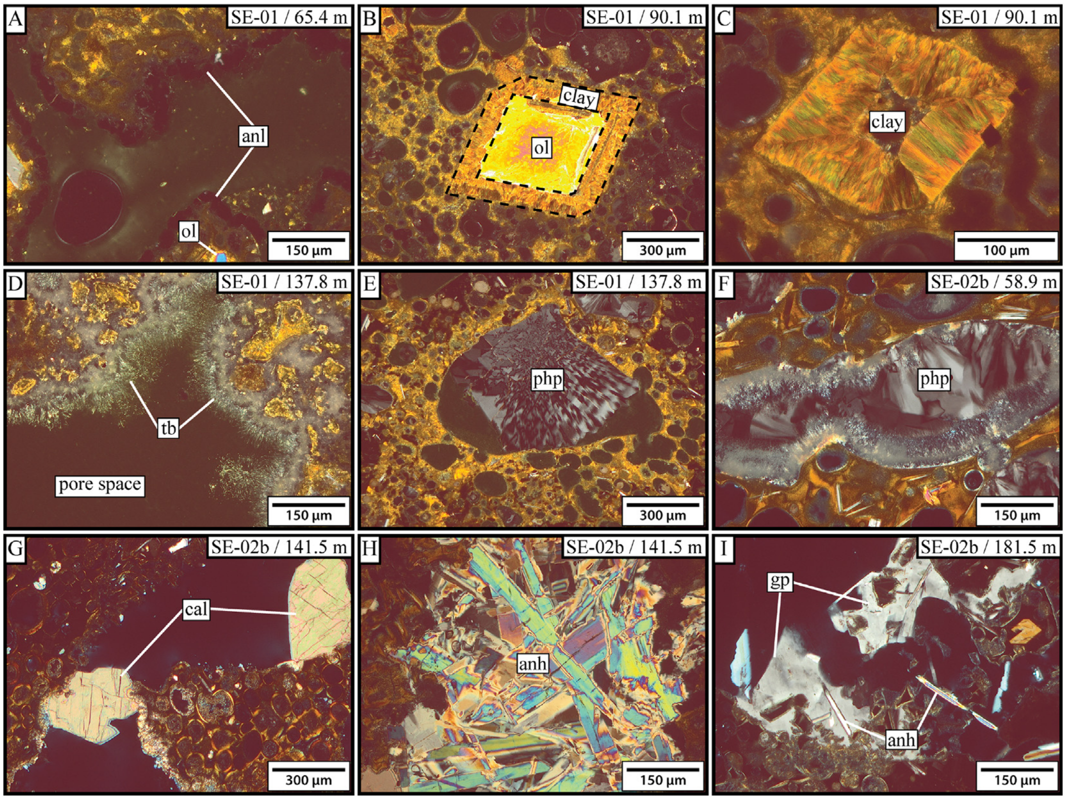

Fig. 7. Overview of the most common authigenic minerals in Surtsey tuff from the archived 1979 SE-01 drill core and the 2017 SE-02b drill core. A) Optically isotropic analcime surface textures in pores. B) Clay mineral alteration rim on an olivine single crystal. C) Nearly complete pseudomorphic alteration of olivine to clay minerals. D) Acicular tobermorite surface texture in a pore. E) Prismatic phillipsite in a vesicle. F) Precipitation of phillipsite in a pore with tobermorite surface texture and subsequent dissolution below water level. G) Massive calcite in the poorly altered zone. F) Prismatic intergrowths of anhydrite from the poorly altered zone. G) Gypsum and anhydrite near the base of the SE-02b drill hole. Mineral Abbreviations, where applicable, after Whitney and Evans (2010).

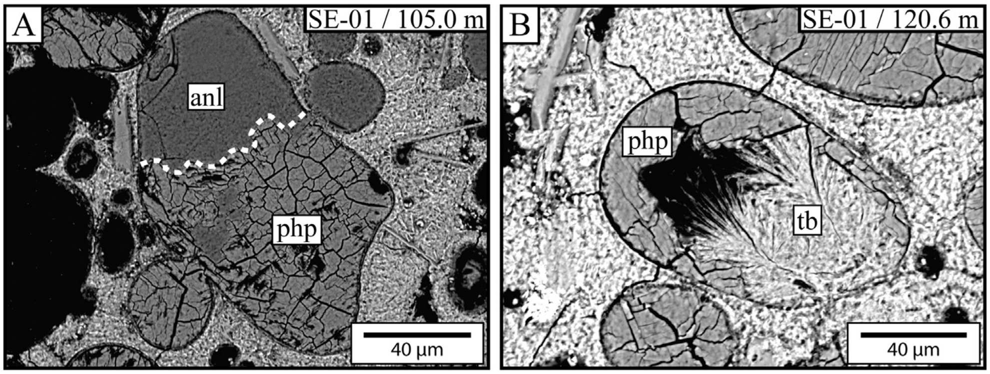

Fig. 8. Backscatter electron micrographs showing A) the partial alteration of phillipsite to analcime in a lapillus vesicle and B) the growth of tobermorite in a vesicle with phillipsite surface texture.

5.2.6. Calcite

Calcite occurs infrequently above and below water level. In more shallow depths, calcite is present as small (≤10 μm) massive to prismatic grains displaying characteristically high interference colors. Calcite crystals below water level are frequently larger than their counterparts above water level. In SE-02b between 140 and 150 m, several samples show particularly high calcite contents (Fig. 7g).

5.2.7. Calcium sulphate minerals

Anhydrite ($CaSO_4$) and gypsum ($CaSO_4 \cdot 2H_2O$) are generally present in trace amounts in most samples. Anhydrite occurs as granular to prismatic crystals ≤10 μm in size, which appear to have precipitated after tobermorite as a result of late stage hydrothermal alteration. Samples from the poorly altered portion of the cores between ~138 and 150 m and from the bottom of the drill holes contain larger prismatic or, more rarely, massive anhydrite crystals (Fig. 7h) in pore space or as fillings within fractures.

Only traces of gypsum were detected in the XRPD diffraction measurements of SE-01 samples. In SE-02b gypsum is observed under the microscope above water level at 31.2 m and 40.4 m as well as in the poorly altered zone at 144.1 m and near the bottom of the core around 180 m, where it can be found either by itself as massive, tabular or amygdaloidal crystals or together with prismatic anhydrite (Fig. 7i). XRPD diffraction also identified bassanite ($CaSO_4 \cdot 0.5H_2O$) in the sample from 169.5 m depth in SE-01.

5.3. Alteration in archived 1979 SE-01 drill core samples

5.3.1. Palagonitized glass

Above water level, the degree of palagonitization is between 73.3 and 82.4 vol%, except for the sample from 43.6 m, which is only 21.6 vol% palagonitized. The most common type of palagonitized glass at these depths is the optically isotropic, presumably amorphous type I, or gel-palagonite. All samples above 65.4 m depth are relatively high in X-ray amorphous contents (generally around 60–70 wt%). At 55.8 m, palagonitized glass rim thickness, as well as palagonitization extent begins to rapidly increase with depth. Despite the degree of palagonitization being 95.5–100.0 vol% at almost all depths from 65.4–120.6 m, a poorly palagonitized layer exists around 95.4 m, in which nearly half of the sideromelane remains unaltered. This layer is darker and finer grained compared to surrounding tuff and exhibits very low porosities. It forms a sharp border with the underlying tuff at 95.5 m, which exhibits higher porosity and a very high degree of palagonitization of >95.0 vol% (Table 1). Between 55.8–105.0 m, 120.6–137.8 m and 150.3–156.9 m, type II palagonitized glass (fibropalagonite) is generally the most abundant form of palagonitized glass. The amount of X-ray amorphous contents for these samples is normally below 60 wt% – except for the two samples from 55.8 to 65.4 m (Grimaldi, 2018). Only the three samples retrieved from 105.0 m, 111.0 m and 120.6 m, the first two of which correspond to the zone of maximum temperature, contain type III palagonitized glass. X-ray amorphous contents are highest at 105.0 m, at 85 wt%. Samples from the depth interval between 137.8 and 150.3 m generally show either very little palagonitization or the glass appears entirely unaltered under the petrographic microscope. The amount of X-ray amorphous phases for these samples is 68–70 wt%. Only type I rims with a median diameter of 40 μm are present at 148.3 m. The sharp lower boundary of this interval is visible at the macro- and microscopic scales. The rock turns from a grayish, friable, poorly consolidated and mostly unpalagonitized lapilli-tuff to a more well consolidated, slightly palagonitized lapilli-tuff that contains thin type II palagonitized glass rims, ranging between 20 and 90 μm. This change is not gradual but abrupt, occurring over just a few μm in the thin section of the sample from 150.3 m. The transition is accompanied by a decrease in the X-ray amorphous content from 68 wt% in the unpalagonitized upper half of this sample to 59 wt% in the slightly palagonitized lower half. The degree of palagonitization slightly increases with depth between 150.3 and 156.9 m. Below 156.9 m no palagonitized glass rims are detected under the microscope. However, nano-analytical techniques may reveal minor alteration features on a submicroscopic scale at these depths (Jackson et al., 2019b).

5.3.2. Clay minerals

Clay minerals are found throughout most of the samples in SE-01, as microcrystalline highly birefringent granular to platy mineral aggregates in pore space and as microscopic to submicroscopic granular particles in palagonitized glass. At 72.4 m clay minerals also begin to appear as rims on olivine grains as a pseudomorphic alteration phase (Fig. 7b). The thickness of these rims ranges from 20 to 95 μm and varies as a function of temperature. In some instances, olivine has become entirely replaced by secondary clay minerals (Fig. 7c). Olivine rims are not observed under the microscope in samples from the interval between 140.0 and 150.3 m. Below this depth interval only 20 μm thin rims are observed in the sample from 156.9 m.

5.3.3. Phillipsite

Phillipsite contents are higher than analcime in some samples above water level (Table 1, Fig. 9). Particularly high amounts of phillipsite are found in the tuff at 22.0 m, which contains 5.5 vol% (point counts)/11 wt% (XRPD) of this mineral, as opposed to only about 4.1 vol%/7 wt% analcime. Below water level, the amount of phillipsite begins to decrease with depth and remains generally low above 137.8 m. Several phillipsite grains show signs of dissolution and replacement by analcime and tobermorite (Fig. 8). The samples from 137.8 m, 148.3 m and 150.3 m are enriched in phillipsite compared to other samples below water level. These samples contain significantly more phillipsite than analcime, which is unusual below water level.

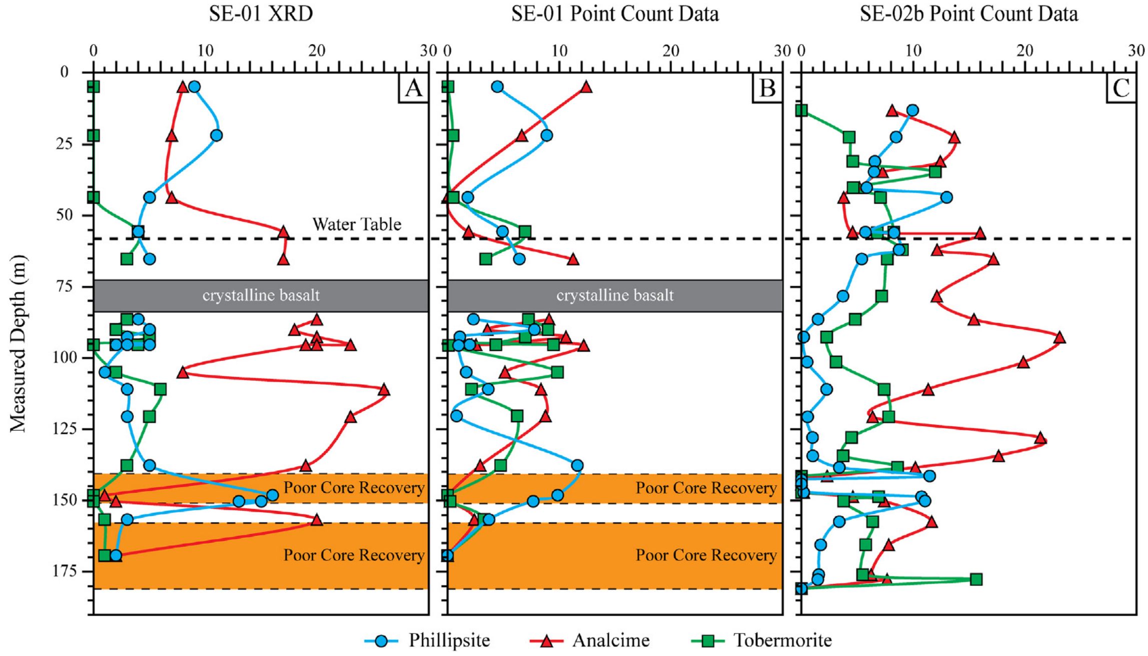

Fig. 9. Relative distributions of phillipsite, analcime and tobermorite in the Surtsey drill cores based on A) x-ray diffraction (wt%) and B) & C) point counts (vol%). The point count data is provided as pore space free. Overall, analcime content has increased at nearly all depths. Phillipsite content has increased only in certain samples above 65.4 m depth and in parts of the poorly altered zone. SE-02b contains slightly less phillipsite than SE-01 in the depth interval between 65.4 and 138.4 m. The top and bottom of the poorly altered zones situated between about 138–150 m show increases in phillipsite, but no increase in analcime and tobermorite. Tobermorite has mostly increased above water level and towards the bottom of the drill hole, but has decreased overall in the area of maximum temperature. Due to incomplete core recovery in SE-01 only cutting samples were available at some depth intervals within the poorly altered zone and towards the bottom of the drill core. For more information on the exact depths, refer to Table 1.

5.3.4. Analcime

Analcime shows a positive correlation with both degree of palagonitization and temperature. Its contents strongly increase below water level and reach peak amounts of up to 26 wt% according to XRPD between 95.5 and 111.0 m, which roughly coincides with the area of maximum temperature in the system. The top and bottom borders of the poorly altered and very friable interval spanning the area below 137.8 m, down to 150.3 m contain very little to no analcime and are instead dominated by phillipsite (see above). Much like phillipsite and tobermorite, analcime is not observed in any relevant quantities below 157.3 m depths, where consolidation of the tuff and the degree of palagonitization remain exceedingly low.

5.3.5. Tobermorite

Thin section petrography and XRPD identified very little to no (typically <1 wt%/vol%) tobermorite in SE-01 above water level. Below water level tobermorite is weakly correlated with temperature and the degree of palagonitization. Similar to analcime, tobermorite reaches its maximum concentrations in the samples around the area of highest temperature between 95.4 and 111.0 m, with the exception of a narrow zone around 95.6 m where the rock is intersected by a series of discrete fractures filled with calcium sulphate mineral phases, identified as anhydrite in thin section, as well as possibly minor amounts of gypsum according to XRPD. This specific sample contains virtually no tobermorite, despite originating from the general area of highest tobermorite concentrations. Tobermorite is only detected in traces via XRPD in the seemingly unpalagonitized sample from 169.5 m and not observed at all in the corresponding thin section.

5.3.6. Calcium sulphate minerals

Calcium sulphates occur throughout the samples from SE-01. Many samples, especially above water level, contain small (≤10 μm) prismatic to granular anhydrite often associated with tobermorite. Enrichment in anhydrite, resulting in the formation of larger prismatic crystals of ca. 200–700 μm length, occurs in several samples below water level. Examples for this include the lower contact between the basaltic intrusion and the tuff at 83.5 m, 95.6 m, where anhydrite occurs as filling in fractures, 105.0 m, 150.3 m, and especially 169.5 m, where anhydrite is strongly enriched in the otherwise seemingly unaltered vitric tuff of this depth.

While anhydrite is the only calcium sulphate phase identified in thin section, XRPD also detects gypsum and bassanite. Gypsum occurs mostly in traces in several samples throughout the core and potentially in larger quantities below the basaltic intrusion at 83.5 m, though this is not observed in the thin section sample. Bassanite is detected only at 169.5 m, with increased anhydrite content.

5.3.7. Calcite

Minor amounts of massive to prismatic calcite are scattered throughout the tuff of the 1979 core. Individual crystals are typically ≤10 μm in diameter and appear to have formed after analcime and tobermorite above water level and before or simultaneous with analcime below water level. No particular patterns or enrichments for this mineral are observed in SE-01.

5.4. Alteration in 2017 SE-02b drill core samples

5.4.1. Palagonitized glass

Samples from the uppermost section of the system situated above the tidally influenced water level, are not fully palagonitized. Rather, the degree of palagonitization remains relatively steady between 22.6 and 56.0 m at around 82.0 vol% (Table 1, Fig. 4). Type I palagonitic textures are prevalent in this part of the system but have locally been replaced by the more crystalline and highly birefringent type II rims at 31.2 m and below. The degree of palagonitization is ≥90.0 vol% for all samples between water level and 141.5 m. The tuff between 141.5 m and 147.1 m remains only weakly palagonitized. Type III palagonitic textures are far more widespread below water level than in SE-01 and dominate in samples between 67.5 and 134.3 m. SE-02b samples corresponding in depth to the weakly altered and poorly consolidated interval between 157.5 and 177.8 m in SE-01 are nearly completely palagonitized. A concentric arrangement of palagonitized glass rims in the form type III → type II → type I → sideromelane is very common below 150.3 m.

5.4.2. Clay minerals

The distribution of clay minerals in SE-02b is the same as in SE-01. Both granular to platy aggregates in pore space and microscopic to submicroscopic particles in palagonitized glass are common. In SE-02b the first signs of olivine alteration to clay minerals are detected at 62.1 m, slightly below the water table in the borehole (~58 m, Weisenberger et al., 2019). Olivine alteration rims show greater diameters in samples from SE-02b, when compared to depth-equivalent samples from SE-01 (Fig. 4). No alteration rims are observed along olivine grains within samples between 141.5 and 150.3 m or in the bottom section of the drill core below 177.8 m where no palagonitization has been detected from our petrographic analysis. However, thin olivine rims about 20–45 μm in thickness are generally found between these depth intervals at 157.5–177.8 m.

5.4.3. Phillipsite

Samples from the uppermost 62.1 m of SE-02b contain more phillipsite than samples at corresponding depths in SE-01. The greatest enrichment of phillipsite in SE-02b is found around 43.7 m, where the tuff remains slightly altered and only poorly palagonitized in SE-01, but the overall extent of alteration is much greater in SE-02b. Consistently lower amounts of phillipsite are present from 65.4 to 138.4 m in SE-02b as compared to SE-01 (Table 1, Fig. 9). Phillipsite dissolution and replacement by analcime and tobermorite is observed throughout most of the samples, even at depths where phillipsite has increased since 1979. The phillipsite-rich upper and lower borders of the poorly altered depth interval, located in SE-01 between 137.8 and 150.3 m show increased phillipsite contents in SE-02b as well, although the upper zone of enrichment is found at a slightly greater depth at 141.5 m in the 2017 core. The lower phillipsite enriched zone is found at 150.3 m, at the same measured depth where it was detected in SE-01.

5.4.4. Analcime

Similar to SE-01, analcime contents are positively correlated with temperature and the degree of palagonitization in SE-02b. The amount of analcime has increased from 1979 to 2017 at almost all depths and is highest at 92.6–101.5 m, where it has about doubled. As is the case with phillipsite and tobermorite, secondary analcime mineralization has extended into previously weakly altered tuff between 157.5 and 177.8 m.

5.4.5. Tobermorite

Point counts of thin sections at 43.6 m and above indicate significantly higher tobermorite content than their SE-01 counterparts, which contain almost no tobermorite (Table 1). In these samples, tobermorite is frequently associated with other Ca-bearing phases such as plagioclase, clay minerals or gypsum. Particularly the sample at 34.8 m containing 9.3 vol% tobermorite exhibits some of the highest concentrations of this mineral observed in any of the studied samples from either drill core. In the hottest areas of the system tobermorite contents are found to be lower in SE-02b than in SE-01, with the samples between 86.5 and 101.5 m all showing less tobermorite than the samples from SE-01 from comparable depths. Two distinct peaks in tobermorite content are found in the samples at 138.4 and 148.7 m, at depths where previously only phillipsite had been enriched, but little to no increase in tobermorite or analcime content was detected in the 1979 samples. The highest concentrations of tobermorite of 14.3 vol% are present in the sample from 177.8 m, which is situated close to the very bottom of the palagonitized area in SE-02b.

5.4.6. Calcium sulphate minerals

The poorly altered zone contains high quantities of calcium sulphate phases. Gypsum, which in SE-01 is only identified via XRPD, but not observed in thin section, is abundant and observable under the microscope in SE-02b at 144.1 m. It typically either occurs alone or around prismatic anhydrite, with which it is frequently associated. Larger gypsum crystals are also found at 31.2 m and 40.4 m in the meteoric part of the system. In these samples gypsum seems to become partially replaced by tobermorite. Anhydrite and gypsum are the most common alteration minerals below 177.8 m, where no palagonitization is observed under the microscope in the 2017 drill core.

5.4.7. Calcite

Calcite is primarily found in larger amounts together with gypsum and anhydrite between 141.5 and 150.3 m. There, it forms massive, up to 400 μm large crystals (Fig. 7g) filling smaller vesicles or growing on the inside of larger fractures. Smaller amounts of calcite are especially found above water level, where all samples contain at least some traces of this mineral. Very little to no calcite occurs in the bottom part of the hole, where gypsum and anhydrite, the phases it is otherwise often associated with, are very common.

5.5. Alteration sequence and changes in secondary mineralogy

Two authigenic zeolite species, phillipsite and analcime, have been identified. Chabazite as described by Jakobsson and Moore (1986) for the upper 0–4 m of the SE-01 drill core, is not reported here, most likely owing to the fact that the most shallow samples in this study were from 4.9 m and 13.2 m for SE-01 and SE-02b respectively, which is below the documented depth range for this zeolite phase. Analcime is positively correlated with temperature and the degree of palagonitization. Phillipsite is more abundant in samples that show a lower extent of glass alteration overall, and comparatively lower amounts of analcime and tobermorite. Examples include the samples from 22.0, 137.8, 148.3 and 150.3 m depths in SE-01 and from 43.7, 141.5 and 150.3 m depths in SE-02b (Table 1, Fig. 9). Point count data confirms a net loss of phillipsite at 65.4–138.4 m between 1979 and 2017. Thin section petrography indicates that this may be due to dissolution of phillipsite as well as alteration to other phases, such as analcime. Thus, phillipsite may form as an earlier alteration product when compared to analcime both above and below the water table and become lost – at least below water level – due to dissolution as glass alteration progresses and the compositions of interstitial fluids change. The amount of phillipsite has either remained the same or increased in samples below approximately 150 m, where little alteration was observed in SE-01. Increased alteration rates of palagonitized glass and olivine rims are estimated for the SE-02b drill core samples at this depth interval (see Section 6.3.1 Alteration rates in zone 4). Tobermorite overgrows analcime or occurs alongside of it on the inner walls of pores and fractures. In contrast, analcime is rarely found overgrowing tobermorite. While gypsum is only detected via XRPD and not observed in thin section for the SE-01 sample set, several thin section samples from SE-02b – particularly between 142.6 and 147.1 m and below 177.8 m – are found to contain gypsum. Gypsum is therefore interpreted as having formed relatively late, as opposed to anhydrite which is already present in relevant quantities in the 1979 samples (Table 1).

6. Discussion

6.1. Time-lapse alteration with depth

Tephra alteration in Surtsey's hydrothermal system changes as a function of time and depth. We identify five zones of distinct alteration behavior observable in both the 1979 and 2017 drill cores. An overview

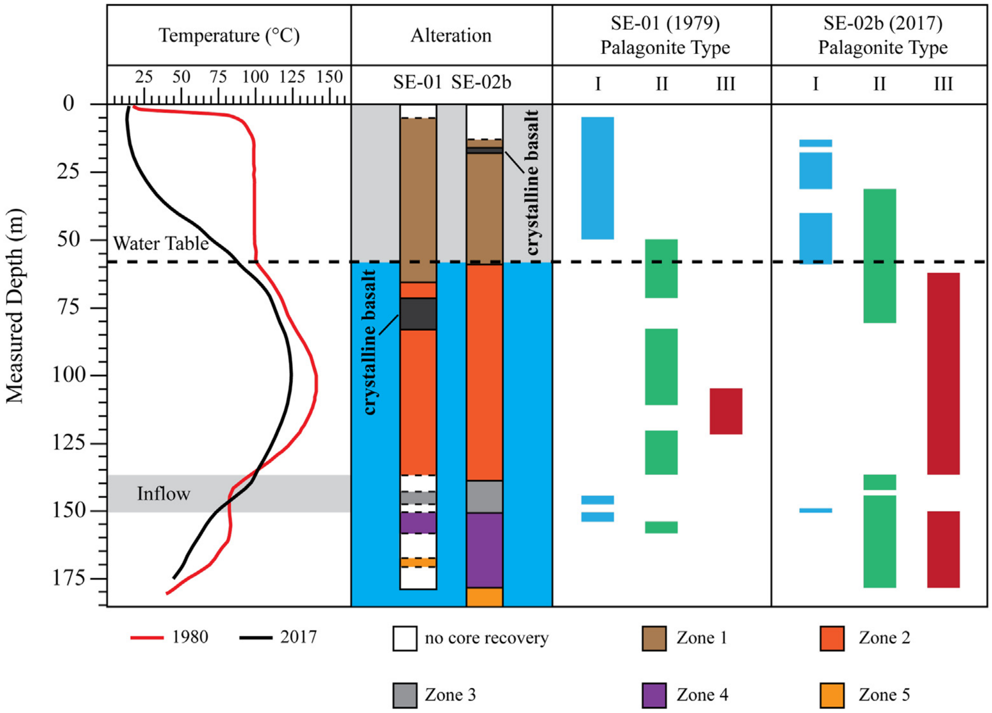

Fig. 10. Integrated log displaying the relationship between temperature, alteration progress and maturation of palagonitized glass determined through petrographic investigations of thin sections in the archived 1979 SE-01 drill core and the 2017 SE-02b drill core.

of the zones and associated changes in alteration behavior is given in Fig. 10. The alteration zones are defined as follows:

6.1.1. Zone 1 (upper palagonitization zone)

In zone 1, situated above 65.4 m in SE-01 and 58.9 m in SE-02b, palagonitization progresses slowly, when compared to the remaining palagonitized parts of the system. No olivine alteration is observed. Phillipsite contents are locally higher than analcime contents, especially in less palagonitized samples, and have either increased or remained steady between 1979 and 2017. Zone 1 persists slightly below water level, which lies around 58 m depth.

6.1.2. Zone 2 (middle palagonitization zone)

Below zone 1, secondary clay mineral rims begin to form around individual olivine grains, eventually leading to complete pseudomorphic replacement. The onset of this alteration marks the beginning of zone 2, reaching down from the bottom border of zone 1 to 137.8 m in SE-01 and 138.4 m in SE-02b. At the transition between zones 1 and 2 palagonitization rim thicknesses suddenly increase by two to four times, resulting in a strong increase in the degree of palagonitization (Fig. 4). This increase is observed in both cores. The most common type of palagonitic rim in zone 2 is type II in SE-01, which has evolved to type III in SE-02b, reflecting a more rapid palagonite maturation in zone 2 as compared to zone 1. Alteration degree and thus rim thicknesses for both palagonitized glass and olivine rims increase steadily as a function of temperature.

The amount of analcime present in the tuff is positively correlated with the degree of palagonitization and temperature. In contrast, phillipsite in zone 2 noticeably decreases between 1979 and 2017. Petrographic observations suggest, that the reason for this lies mainly in the dissolution of phillipsite, with simultaneous replacement by analcime and tobermorite. This may be partially due to the higher amounts of Na^+ present in the system below sea level, which may favor the formation of analcime over phillipsite. Additionally, zeolite distribution in hydrothermally altered rocks is also known to be governed to a large extent by temperature (Browne, 1978; Kusakabe et al., 1981; de Gennaro et al., 1999; Langella et al., 2001; Kralj, 2016). For this reason, the local dominance of phillipsite over analcime in more shallow depths may also be caused by the relatively lower temperatures, as phillipsite would be expected to be more stable under colder conditions, when compared to analcime (Chipera and Apps, 2001). Host-rock lithology may influence the type of zeolite being precipitated under low-temperature hydrothermal conditions (Browne, 1978; Reyes, 2000), such as the ones present in the Surtsey hydrothermal system, but this is unlikely to contribute in any significant way, as the Surtsey system is almost entirely hosted in universally poorly sorted intermediate to coarse alkali basaltic lapilli-tuff, showing only minor chemical or lithological variation (Schipper et al., 2015). As phillipsite appears to be an early stage alteration product, the comparatively higher phillipsite contents within zone 1 may also be due to the lower degree of palagonitization and therefore less advanced reaction progress.

In SE-01, zone 2 hosts a thin ash-rich layer of darker material that is noticeably less porous and less palagonitized than the surrounding rocks at 95.4 m, which coincides with a reduction in secondary mineral content (Table 1). The low porosities and therefore low permeabilities in this layer likely inhibit hydrothermal circulation and locally counteract the precipitation of secondary minerals and devitrification of the glass at this depth. No ash-rich layer exhibiting similar properties is observed in SE-02b, implying that this feature is either transient in nature or highly localized.

6.1.3. Zone 3 (poorly altered zone)

Both cores contain a poorly altered zone that is partially unconsolidated in 1979 and lightly consolidated in 2017. It encompasses the depth interval from 137.8 to 150.3 m in SE-01, but has slightly shrunk in diameter in SE-02b, where it reaches between 138.4 and 150.3 m. The sideromelane of the poorly altered zone remains largely unpalagonitized. Only a few thin layers of slightly palagonitized tephra are observed. The lack of palagonitization and consolidation by mineral cements arguably led to the poor core recovery during the 1979 drilling expedition between 140.0–143.8 m and 148.5–150.3 m (see Jakobsson and Moore, 1982). In SE-02b zone 3 is slightly more consolidated, but the rocks remain highly porous and friable even in 2017. In both SE-01 and SE-02b, the upper and lower boundaries of zone 3 are marked by a strong enrichment in phillipsite in otherwise weakly altered tuff. In SE-02b the upper phillipsite enriched interval has moved further down to 141.5 m (Table 1, Fig. 9). Phillipsite contents have decreased strongly in the now more extensively altered tuff between 137 and 138 m, while both tobermorite and analcime have increased in abundance. This is likely because phillipsite forms mainly in the initial stages of glass alteration before becoming replaced by other phases as the reaction progresses. Calcium sulphates such as anhydrite and gypsum are very common and particularly characteristic for zone 3.

An electrical resistivity log acquired after drilling of SE-02b (Jackson et al., 2019a; Weisenberger et al., 2019) indicates a change within the depth interval coinciding with zone 3. According to 16 s rRNA gene sequencing, roughly half of the prokaryotic community composition present in rock samples from SE-02b at 148 m depth, is shared with the one in seawater around the island (personal correspondence from Bergsten, 2019). However, it cannot be excluded that this is caused by seawater contamination during drilling. Here it is proposed, that zone 3 most likely marks an interval of high permeability and sea water recharge. This would further explain the presence of anhydrite and gypsum, as Ca^{2+} and SO_4^{2-} bearing fluids entering the system might precipitate a calcium sulphate phase upon being heated due to retrograde solubility.

6.1.4. Zone 4 (lower palagonitization zone)

Zone 4, between 150.3 and 157.3 m in SE-01 and 150.3–177.8 m in SE-02b, shows the greatest change since 1979. In SE-01 alteration behavior in zone 4 resembles that of zone 2, though overall alteration is less extensive. In SE-02b both palagonitization and olivine rim formation rates are much higher than predicted by the temperature-alteration-trends derived from samples in zones 1 and 2 (Fig. 11). The fact that this is not observed in samples from SE-01 indicates, that alteration in zone 4 has increased over time. The co-appearance of all three types of palagonitized glass rims, mostly II and III, arranged concentrically around sideromelane grains in the order type III → type II → type I → sideromelane is common in zone 4 in SE-02b (Fig. 6). As temperature is not the driving factor for the increase in alteration rates at this depth, other potential explanations may be found in chemical changes in the hydrothermal fluid or potentially in the water-rock ratio of the environment (Pauly et al., 2011).

6.1.5. Zone 5 (bottom zone)

The area below zone 4 in each core contains mostly fresh and apparently unaltered sideromelane. Absence of palagonitization and significant mineral cementation by zeolites and tobermorite in pore space causes the tephra of this zone to be largely unconsolidated. No olivine rims are detected under the microscope. Observed secondary mineralization is limited to mostly anhydrite and possibly bassanite in SE-01. In SE-02b both gypsum and anhydrite are observed.

6.2. Olivine alteration rates

Olivine alteration rates were estimated by dividing olivine rim thicknesses by time (assuming a 12-year timespan for SE-01 and a 50-year timespan for SE-02b) and plotting the results against temperature logging data from 1980 and 2018 to best approximate the current state of the system. Since temperature is related to alteration rates, these values should not be taken as fully accurate representation of the system's effective temperature, which varied over time. For samples from below 156.9 m, where no olivine rims are found in SE-01, a time period of 38 years for the alteration is assumed instead, as this value would be closer to the actual amount of time available for the alteration to progress. Our results confirm a positive relationship between olivine alteration rates and temperature, as first documented by Jakobsson and Moore (1986). The olivine alteration rates derived from the present study are slightly higher than those given by Jakobsson and Moore (1986), which is likely due to differences in methodology, specifically in the temperature values used. Regardless of the total extent of alteration rates, new insights are gained regarding the nature of the olivine-clay mineral reaction in the Surtsey tuff. Based on the analyses of the SE-01 core samples immediately after drilling and the temperature history of the system as of 1980, Jakobsson and Moore (1986) hypothesized a threshold temperature of 120 ± 5 °C for the alteration of olivine to clay minerals. They cited this as a potential reason for the absence of olivine rims above water level, as temperatures would not have exceeded 100 °C in that part of the system. However, our data from the 2017 drill core provide evidence that olivine rim formation can occur at lower temperatures within the hydrothermal system given enough time. In the SE-02b samples we observe 20–50 μm thick alteration

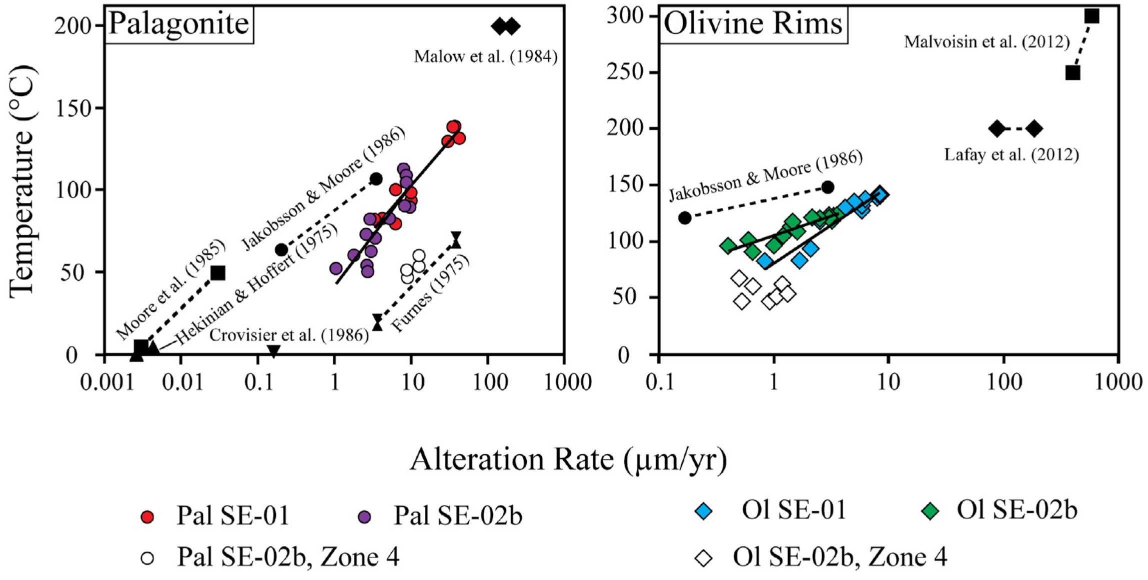

Fig. 11. Alteration rates inferred from the thicknesses of authigenic rims on palagonitized glass lapilli and olivine as a function of temperature for samples from the archived 1979 SE-01 and the SE-02b drill cores and comparison with results from other studies (Furnes, 1975; Hekinian and Hoffert, 1975; Malow et al., 1984; Moore et al., 1985; Jakobsson and Moore, 1986; Crovisier et al., 1986; Malvoisin et al., 2012; Lafay et al., 2012). While a trend for the alteration rates as a function of temperature can be reconciled for most depths, the samples retrieved from zone 4 show higher alteration rates than what would be predicted based on the trends established by samples from more shallow depths.

rims on olivine at 134.3–138.4 m and in zone 4 at 157.5–177.8 m. At these depths, temperatures have ranged from ca. 44–103 °C between 1980 and 2017 (Fig. 3), which is well below the threshold temperature proposed by Jakobsson and Moore (1986). Temperature alone can therefore not be the reaction's sole limiting parameter.

Lafay et al. (2012) performed autoclave experiments on olivine under alkaline conditions at 150–200 °C to study the rate of olivine replacement during serpentinization, measuring the fraction of grains <30 μm, 30–56 μm and 56–150 μm that remained after a given time interval. Their results and those of Malvoisin et al. (2012) are used to estimate alteration rates for serpentinization in $\mu m \cdot yr^{-1}$, which are plotted in Fig. 11 for comparison.

6.3. Palagonitization rates

Estimation of palagonitization rates was performed analogously to olivine alteration rates (see above). As samples from below 156.9 m remain unpalagonitized in 1979, a timespan of 38 years, between 1979 and 2017, is assumed as base for the alteration rates of these samples. It should be noted that Jackson et al. (2019b) identified minimal glass alteration at this depth by using X-ray microdiffraction. Palagonitization rates for samples from either drill core are correlated positively with temperature and generally plot along two highly similar trendlines (Fig. 11). In their 1986 study of SE-01, Jakobsson and Moore reported palagonitization rates of ca. 0.2–3.5 $\mu m \cdot yr^{-1}$ for alteration rims in glass lapilli. This contrasts with our results, which range between 3.33 and 42.50 $\mu m \cdot yr^{-1}$ for samples from the same drill core. It is likely that the reason for this discrepancy and that of the olivine alteration rates lies in a difference in the approach used. For instance, no universal stage was employed in this study to measure the exact angle of the rims. Our results nevertheless reproduce the same general trends in terms of palagonitized rim thickness variations with depth. In addition, Jakobsson and Moore (1986) estimated the effective temperature based on several parameters, whereas in this study a direct measurement is used. These factors are thought to contribute to the deviations between the two studies.

Palagonitization rates of comparable magnitude to those in our study have been achieved in experiments conducted by Furnes (1975) at temperatures comparable to those prevalent in Surtsey's hydrothermal system. Thomassin (1984) demonstrated experimentally that a palagonitic rim "several micrometers in thickness" can be formed in as little as nine months for samples heated in seawater using a Teflon reactor. Malow et al. (1984) derived even higher alteration rates for samples leached in NaCl solutions heated to 200 °C. Our results, though different from those of Jakobsson and Moore (1986), are therefore still within established parameters.

6.3.1. Alteration rates in zone 4

Palagonitic and olivine alteration rims indicate much higher alteration rates in the tuff from 150.3–177.8 m than predicted based on temperature alone (Fig. 11). Many of these rocks remained largely unaltered in 1979, meaning that the visible onset of palagonitization and olivine alteration would have commenced at an unspecified time after 1979, but before 2017. From this it can be concluded that the true alteration rates at this depth may be even higher than estimated here, since the alteration would have occurred over a shorter time span than the assumed 38 years between 1979 and 2017. Even if palagonitization and olivine rim formation have been ongoing in these areas throughout the entire 50-year history of the hydrothermal system, alteration rates are still substantially higher than predicted by the temperature-alteration-rate trends established by more shallow depth intervals. Possible reasons for this may lie in evolving fluid compositions, such as changing salinities, or in a different water-rock ratio.

6.4. Palagonite maturation

Three different types of palagonitization are identified in the Surtsey tuff samples, which are distinct in their textural and optical properties. These type I-II-III palagonitized glass rims exhibit a progressively more granular to fibrous texture and less gel-like appearance. Peacock (1926) first recognized two texturally distinct types of palagonite – the amorphous gel-palagonite and the slightly crystalline "fibro-palagonite" – in his comprehensive review of the petrology of Icelandic tuffs. Stroncik and Schmincke (2001) recognized that after the initial palagonitization process the altered glass undergoes a series of aging steps over time. They state that crystallinity gradually increases as palagonite ages, ultimately resulting in the complete crystallization of the material to smectite and other authigenic minerals, a finding also confirmed by other workers (Singer, 1974; Berkgaut et al., 1994; Crovisier et al., 2003; Drief and Schiffman, 2004). The classification scheme proposed by Stroncik and Schmincke (2001) uses the ratio of amorphous to crystalline material in the altered glass to delineate between the initial gel-palagonite (aging step I, mostly amorphous), fibro-palagonite (aging step II, mostly crystalline), and fully crystalline smectite. In their study of the palagonitic alteration of hyaloclastites from Hawaii, Walton and Schiffman (2003) recognized the formation of a complex of minerals, intergrown at the nanometer scale and dominantly composed of smectite, which they called 'reddened smectite grain replacement' (Walton and Schiffman, 2003). This material can be considered analogous to fibro-palagonite as described by Peacock (1926) (Drief and Schiffman, 2004). Despite these differences in the applied classification scheme or nomenclature, these authors and many others have generally agreed that the increasing crystallinity of palagonitized glass develops as the result of palagonitic maturation over time by means of reaction towards equilibrium with the interfacing hydrothermal fluid; only the amorphous gel-palagonite likely representing the initial alteration product of sideromelane (Singer, 1974; Zhou et al., 1992; Stroncik and Schmincke, 2001; Crovisier et al., 2003; Drief and Schiffman, 2004; Pauly et al., 2011).

Based on this large body of prior observations, we interpret the different types of palagonitic textures in the Surtsey samples as indicative of progressive maturation. Type I palagonitization (or gel-palagonite) marks an early stage, with type II and III representing progressively more advanced stages, wherein crystallinity increases and the palagonitized glass takes on a fibrous texture, before turning an earthy, mottled and opaque shade of brown as the devitrification process advances (Fig. 5). The distribution of these three palagonitic types is correlated with temperature, with type I found mainly in the areas of lowest temperature – especially above water level – and type III found in the areas of highest temperature. An exception to this is the depth interval of rapid palagonitization in SE-02b between 150.3 and 177.8 m (zone 4; see above) (Fig. 10), where temperatures are low, but very little type I palagonitized glass is observed. Within the framework of this interpretation, type III palagonitic rims represent a highly advanced stage of the devitrification process, so that the term "palagonite" in the strict sense may not be fully applicable. The very high concentration of X-ray amorphous phases in SE-01 around the system's area of maximum temperature (Grimaldi, 2018), where type III is observed, potentially indicates that a large portion of the material may have recrystallized as poorly ordered clays (Brindley, 1977).

7. Summary

The systematic petrographic comparison of two parallel vertical drill cores from the eastern tephra pile of the Surtur crater at Surtsey volcano, recovered in 1979 and 2017, provides new petrographic insights into time-lapse alteration within the island's basaltic low-temperature hydrothermal system, which will serve as the basis for future geochemical analyses.

1. Five discrete zones of distinct alteration style are recognized in the two studied Surtsey drill cores. These zones (Fig. 10), are defined by their discrete alteration mineralogy, development of secondary phases over time, as well as alteration of basaltic glass. Their vertical positions differ only slightly between the 1979 and 2017 drill cores.
2. Alteration in the form of palagonitization, zeolitization and tobermorite formation has progressed rapidly in most of the zones except for parts of the poorly altered zone 3 at 138.4–150.3 m depth, where alteration does not appear to have progressed to a significant degree from 1979 to 2017.
3. The rates of glass and olivine alteration, as measured by alteration rim thicknesses, generally reproduce the trends established by Jakobsson and Moore (1986). Both types of alteration increase with temperature in the SE-01 samples and in the SE-02b samples above zone 4 (Fig. 11). In zone 4 of SE-02b alteration rates diverge from this general trend, yielding higher than expected rates of production for both palagonitized glass and altered olivine rims.
4. Phillipsite appears to be an early stage alteration product, for which the relative abundance has decreased in all samples between 65.4 and 138.4 m depths since 1979. This is consistent with petrographic observations, which show phillipsite dissolution or alteration to analcime and tobermorite.
5. Surtsey tuff samples show three principal types of palagonitized glass textures, which indicate progressive stages in the reaction of sideromelane to smectite. The distribution of these three palagonitic types in SE-01 and SE-02b shows clear progress in the ongoing devitrification of the Surtsey tephra deposits between 1979 and 2017.

Declaration of competing interest

The authors declare that there are no conflicts of interest.

Acknowledgements

Funding for this project was provided by the International Continental Scientific Drilling Program (ICDP) through a grant to the SUSTAIN project; a grant of excellence from the Icelandic Research Fund, ICF-RANNÍS; the Bergen Research Foundation and K.G. Jebsen Centre for Deep Sea Research at the University of Bergen, Norway; the German Research Foundation; and DiSTAR, Federico II, University of Naples, Federico II, Italy. The University of Utah, USA, and the two Icelandic power companies Reykjavík Energy and Landsvirkjun contributed additional funds for drilling. The authors would like to express their gratitude to Barbara I. Kleine, Pauline Bergsten, Carolyn F. Gorny and James G. Moore for constructive feedback on the topics of fluid geochemistry, microbiology and volcanology. We thank two anonymous reviewers for their detailed and constructive comments and José Luis Macías for his editorial efforts and the editorial handling of the paper.

References

Berkgaut, V., Singer, A., Stahr, K., 1994. Palagonite reconsidered: paracrystalline illite-smectites from regoliths on basic pyroclastics. Clay Clay Miner. 42, 582–592.

Bish, D.L., Chipera, S.J., 1987. Problems and solutions in quantitative analysis of complex mixtures by X-ray powder diffraction. Adv. X-ray Anal. 31, 295–308.

Brindley, G.W., 1977. Aspects of order-disorder in clay minerals-a review. Clay Sci. 5, 103–112.

Browne, P.R.L., 1978. Hydrothermal alteration in active geothermal fields. Annu. Rev. Earth Planet. Sci. 6, 229–248.

Chipera, S.J., Apps, J.A., 2001. Geochemical stability of natural zeolites. In: Bish, D.L., Ming, D.W. (Eds.), Natural Zeolites: Occurrence, Properties, Applications, pp. 117–157.

Crovisier, J.L., Eberhart, J.P., Honnorez, J., 1986. Dissolution of basaltic glass in seawater: mechanism and rate. Extended Abstracts of the Fifth International Symposium on Water-Rock Interaction. International Association of Geochemistry and Cosmochemistry, Reykjavik, Iceland, pp. 142–145.

Crovisier, J.L., Advocat, T., Dussossoy, J.L., 2003. Nature and role of natural alteration gels formed on the surface of ancient volcanic glasses (Natural analogs of waste containment glasses). J. Nucl. Mater. 321, 91–109.

de Gennaro, M., Langella, A., Cappelletti, P., Colella, C., 1999. Hydrothermal conversion of trachytic glass to zeolite. 3. Monocationic model glasses. Clay Clay Miner. 47, 348–357.

Drief, A., Schiffman, P., 2004. Very low-temperature alteration of sideromelane in hyaloclastites and hyalotuffs from Kilauea and Mauna Kea volcanoes: implications for the mechanism of palagonite formation. Clay Clay Miner. 52, 623–635.

Fisher, R.V., Schmincke, H.U., 1984. Submarine volcaniclastic rocks. Pyroclastic Rocks. Springer, Berlin, Heidelberg, pp. 265–296.

Friedman, J.D., Williams, R.S., 1970. Changing patterns of thermal emission from Surtsey, Iceland, between 1966 and 1969. US Geol. Surv. Prof. Pap. 700-D, pp. 116–124.

Frolova, Y.V., 2010. Patterns of transformations in the compositions and properties of icelandic hyaloclastites during lithogenesis. Mosc. Univ. Geol. Bull. 65, 104–114.

Furnes, H., 1975. Experimental palagonitization of basaltic glasses of varied composition. Contrib. to Mineral. Petrol. 50, 105–113.

Gernon, T.M., Hincks, T.K., Tyrrell, T., Rohling, E.J., Palmer, M.R., 2016. Snowball Earth ocean chemistry driven by extensive ridge volcanism during Rodinia breakup. Nat. Geosci. 9, 242.

Giggenbach, W.F., 1984. Mass transfer in hydrothermal alteration systems—a conceptual approach. Geochim. Cosmochim. Acta 48, 2693–2711.

Grimaldi, C., 2018. Quantitative Characterization of Zeolites From Surtsey Island (Iceland). (M.Sc. thesis). Department of Earth, Environmental and Resources Sciences at the University of Napoli Federico II, Italy.

Hekinian, R., Hoffert, M., 1975. Rate of palagonitization and manganese coating on basaltic rocks from the rift valley in the Atlantic Ocean near 36°50′N. Mar. Geol. 19, 91–109.

Henley, R.W., Truesdell, A.H., Barton, P.B., Whitney, J.A., 1985. Fluid-Mineral Equilibria in Hydrothermal Systems. Society of Economic Geologists.

Honnorez, J., 1978. Generation of phillipsites by palagonitization of basaltic glass in sea water and the origin of K-rich deep-sea sediments. In: Sand, L.B., Mumpton, F.A. (Eds.), Natural Zeolites: Occurrence, Properties, Use, pp. 245–258.

Jackson, M.D., Gudmundsson, M.T., Bach, W., Cappelletti, P., Coleman, N.J., Ivarsson, M., Jónasson, K., Jørgensen, S.L., Marteinsson, V.Þ., McPhie, J., Moore, J.G., Nielson, D., Rhodes, J.M., Rispoli, C., Schiffman, P., Stefánsson, A., Türke, A., Vanorio, T., Weisenberger, T.B., White, J.D.L., Zierenberg, R., Zimanowski, B., 2015. Time-lapse characterization of hydrothermal seawater and microbial interactions with basaltic tephra at Surtsey Volcano. Sci. Drill. 20, 51–58.

Jackson, M.D., Gudmundsson, M.T., Weisenberger, T.B., Rhodes, J.M., Stefánsson, A., Kleine, B.I., Lippert, P.C., Marquardt, J.M., Reynolds, H.I., Kück, J., Marteinsson, V.Þ., Vannier, P., Bach, W., Barich, A., Bergsten, P., Bryce, J.G., Cappelletti, P., Couper, S., Fahnestock, M.F., Gorny, C.F., Grimaldi, C., Groh, M., Guðmundsson, Á., Gunnlaugsson, Á.Þ., Hamelin, C., Högnadóttir, Þ., Jónasson, K., Jónsson, S.S., Jørgensen, S.L., Klonowski, A.M., Marshall, B., Massey, E., McPhie, J., Moore, J.G., Ólafsson, E.S., Onstad, S.L., Perez, V., Prause, S., Snorasson, S.P., Türke, A., White, J.D.L., Zimanowski, B., 2019a. SUSTAIN drilling at Surtsey volcano, Iceland, tracks hydrothermal and microbiological interactions in basalt 50 years after eruption. Sci. Drill. 25, 35–46.

Jackson, M.D., Couper, S., Stan, C.V., Ivarsson, M., Czabaj, M.W., Tamura, N., Parkinson, D., Miyagi, L.M., Moore, J.G., 2019b. Authigenic mineral textures in submarine 1979 basalt drill core, Surtsey volcano, Iceland. Geochemistry, Geophys., Geosystems 20, 3751–3773.

Jakobsson, S.P., 1971. Palagonitiseringen af tefraen på Surtsey. Natturufraedistofnun Islands, pp. 61–62.

Jakobsson, S.P., 1972. On the consolidation and Palagonitization on the Tephra of the Surtsey Volcanic Island, Iceland. Surtsey Res. Prog. Rep, pp. 121–128.

Jakobsson, S.P., 1978. Environmental factors controlling the palagonitization of the Surtsey tephra, Iceland. Bull. Geol. Soc. Denmark 27, 91–105.

Jakobsson, S.P., Moore, J.G., 1982. The Surtsey research drilling project of 1979. Surtsey Res 9, 76–93.

Jakobsson, S.P., Moore, J.G., 1986. Hydrothermal minerals and alteration rates at Surtsey volcano, Iceland. Geol. Soc. Am. Bull. 97, 648–659.

Jakobsson, S.P., Gudmundsson, G., Moore, J.G., 2000. Geological monitoring of Surtsey, Iceland, 1967–1998. Surtsey Res. 11, 99–108.

Kousehlar, M., Weisenberger, T.B., Tutti, F., Mirnejad, H., 2012. Fluid control on low-temperature mineral formation in volcanic rocks of Kahrizak, Iran. Geofluids 12, 295–311.

Kralj, P., 2016. Hydrothermal zeolitisation controlled by host-rock lithofacies in the Periadriatic (Oligocene) Smrekovec submarine composite stratovolcano, Slovenia. J. Volcanol. Geotherm. Res. 317, 53–65.

Kusakabe, H., Minato, H., Utada, M., Yamanaka, T., 1981. Phase relations of clinoptilolite, mordenite, analcime and albite with increasing pH, sodium ion concentration and temperature. Sci. Pap. Coll. Gen. Educ. Univ. Tokyo 31, 39–59.

Lafay, R., Montes-Hernandez, G., Janots, E., Chiriac, R., Findling, N., Toche, F., 2012. Mineral replacement rate of olivine by chrysotile and brucite under high alkaline conditions. J. Cryst. Growth 347, 62–72.

Langella, A., Cappelletti, P., de Gennaro, R., 2001. Zeolites in closed hydrologic systems. Rev. Mineral. Geochemistry 45, 235–260.

Lorenz, V., 1974. Studies of the Surtsey tephra deposits. Surtsey Res. Prog. Rep. 7, 72–79.

Malow, G., Lutze, W., Ewing, R.C., 1984. Alteration effects and leach rates of basaltic glasses: implications for the long-term stability of nuclear waste form borosilicate glasses. J. Non-Cryst. Solids 67, 305–321.

Malvoisin, B., Brunet, F., Carlut, J., Rouméjon, S., Cannat, M., 2012. Serpentinization of oceanic peridotites: 2. Kinetics and processes of San Carlos olivine hydrothermal alteration. J. Geophys. Res. Solid Earth 117.

Marshall, R.R., 1961. Devitrification of natural glass. Geol. Soc. Am. Bull. 72, 1493–1520.

Moore, J.G., 1966. Rate of palagonitization of submarine basalt adjacent to Hawaii. US Geol. Surv. Prof. Pap. 550, D163–D171.

Moore, J.G., 1985. Structure and eruptive mechanisms at Surtsey Volcano, Iceland. Geol. Mag. 122, 649–661.

Moore, J.G., Fornari, D.J., Clague, D.A., 1985. Basalts from the 1877 submarine eruption of Mauna Loa, Hawaii; new data on the variation of palagonitization rate with temperature. U.S. Geol. Surv. Bull. 1663.

Nayudu, Y.R., 1964. Palagonite tuffs (hyaloclastites) and the products of post-eruptive processes. Bull. Volcanol. 27, 391–410.

Parruzot, B., Jollivet, P., Rébiscoul, D., Gin, S., 2015. Long-term alteration of basaltic glass: mechanisms and rates. Geochim. Cosmochim. Acta 154, 28–48.

Pauly, B.D., Schiffman, P., Zierenberg, R.A., Clague, D.A., 2011. Environmental and chemical controls on palagonitization. Geochemistry, Geophys. Geosystems 12.

Peacock, M.A., 1926. The petrology of Iceland, part 1, the basic tuffs. Trans. R. Soc. Edinburgh 55, 53–76.

Pedersen, L.E.R., McLoughlin, N., Vullum, P.E., Thorseth, I.H., 2015. Abiotic and candidate biotic micro-alteration textures in subseafloor basaltic glass: a high-resolution in-situ textural and geochemical investigation. Chem. Geol. 410, 124–137.

Reyes, A.G., 2000. Petrology and Mineral Alteration in Hydrothermal Systems: From Diagenesis to Volcanic Catastrophes. United Nations University, Geothermal Training Programme.

Romagnoli, C., Jakobsson, S.P., 2015. Post-eruptive morphological evolution of island volcanoes: Surtsey as a modern case study. Geomorphology 250, 384–396.

Schiffman, P., Watters, R.J., Thompson, N., Walton, A.W., 2006. Hyaloclastites and the slope stability of Hawaiian volcanoes: Insights from the Hawaiian Scientific Drilling Project's 3-km drill core. J. Volcanol. Geotherm. Res. 151, 217–228.

Schipper, C.I., Jakobsson, S.P., White, J.D.L., Palin, J.M., Bush-Marcinowski, T., 2015. The Surtsey magma series. Sci. Rep. 5, 11498.

Schipper, C.I., Le Voyer, M., Moussallam, Y., White, J.D.L., Thordarson, T., Kimura, J.I., Chang, Q., 2016. Degassing and magma mixing during the eruption of Surtsey Volcano (Iceland, 1963–1967): the signatures of a dynamic and discrete rift propagation event. Bull. Volcanol. 78, 2–15.

Singer, A., 1974. Mineralogy of palagonitic material from the Golan Heights, Israel. Clay Clay Miner. 22, 231–240.

Singer, A., Banin, A., 1990. Characteristics and mode of palagonite - a review. Sci. Géologiques, Bull. mémoires 88, 173–181.

Spürgin, S., Weisenberger, T.B., Marković, M., 2019. Zeolite-group minerals in phonolite-hosted deposits of the Kaiserstuhl Volcanic Complex, Germany. Am. Mineral. 104, 659–670.

Staudigel, H., Hart, S.R., 1983. Alteration of basaltic glass: mechanisms and significance for the oceanic crust-seawater budget. Geochim. Cosmochim. Acta 47, 337–350.

Staudigel, H., Furnes, H., McLoughlin, N., Banerjee, N.R., Connell, L.B., Templeton, A., 2008. 3.5 billion years of glass bioalteration: volcanic rocks as a basis for microbial life? Earth-Science Rev 89, 156–176.

Stefánsson, V., Axelsson, G., Sigurdsson, O., Gudmundsson, G., Steingrímsson, B., 1985. Thermal condition of Surtsey. J. Geodyn. 4, 91–106.

Stroncik, N.A., Schmincke, H.U., 2001. Evolution of palagonite: crystallization, chemical changes, and element budget. Geochemistry, Geophys. Geosystems 2.

Stroncik, N.A., Schmincke, H.U., 2002. Palagonite - a review. Int. J. Earth Sci. 91, 680–697.

Techer, I., Lancelot, J., Clauer, N., Liotard, J.M., Advocat, T., 2001. Alteration of a basaltic glass in an argillaceous medium: the Salagou dike of the Lodève Permian Basin (France). Analogy with an underground nuclear waste repository. Geochim. Cosmochim. Acta 65, 1071–1086.

Thomassin, J.H., 1984. Étude expérimentale de l'altération des verres silicatés dans l'eau douce et en milieu océanique: apports des méthodes d'analyse de surface des solides (Thèse Doc. ès Sci).

Thorarinsson, S., 1965. Some facts about the Surtsey eruption. Natturufraedingurinn 35, 153.

Thorarinsson, S., Einarsson, T., Sigvaldason, G., Elisson, G., 1964. The submarine eruption off the Vestmann Islands 1963-64. Bull. Volcanol. 27, 435–445.

Thorseth, I.H., Furnes, H., Tumyr, O., 1991. A textural and chemical study of Icelandic palagonite of varied composition and its bearing on the mechanism of the glass-palagonite transformation. Geochim. Cosmochim. Acta 55, 731–749.

Thorseth, I.H., Furnes, H., Heldal, M., 1992. The importance of microbiological activity in the alteration of natural basaltic glass. Geochim. Cosmochim. Acta 56, 845–850.

Türke, A., Nakamura, K., Bach, W., 2015. Palagonitization of basalt glass in the flanks of mid-ocean ridges: implications for the bioenergetics of oceanic intracrustal ecosystems. Astrobiology 15, 793–803.

Von Waltershausen, S., 1845. Ueber die submarinen vulkanischen Ausbrüche in der Tertiär-Formation des Val di Noto im Vergleich mit verwandten Erscheinungen am Aetna. Göttinger Studien.

Walton, A.W., Schiffman, P., 2003. Alteration of hyaloclastites in the HSDP 2 phase 1 Drill Core 1. Description and paragenesis. Geochemistry, Geophys. Geosystems 4.

Walton, A.W., Schiffman, P., Macpherson, G.L., 2005. Alteration of hyaloclastites in the HSDP 2 phase 1 Drill Core: 2. Mass balance of the conversion of sideromelane to palagonite and chabazite. Geochemistry, Geophys. Geosystems 6.

Weisenberger, T.B., Selbekk, R.S., 2009. Multi-stage zeolite facies mineralization in the Hvalfjördur area, Iceland. Int. J. Earth Sci. 98, 985–999.

Weisenberger, T.B., Gudmundsson, M.T., Jackson, M.D., Gorny, C.F., Türke, A., Kleine, B.I., Marshall, B., Jørgensen, S.L., Marteinsson, V.Þ., Stefánsson, A., White, J.D.L., Barich, A., Bergsten, P., Bryce, J., Couper, S., Fahnestock, M.F., Franzson, H., Grimaldi, C., Groh, M., Guðmundsson, Á., Gunnlaugsson, Á.Þ., Hamelin, C., Högnadóttir, Þ., Jónasson, K., Jónsson, S.S., Klonowski, A.M., Kück, J., Magnússon, R.L., Massey, E., McPhie, J., Ólafsson, E.S., Onstad, S.L., Prause, S., Perez, V., Rhodes, J.M., Snorrason, S.P., 2019. Operational Report for the 2017 Surtsey Underwater volcanic System for Thermophiles, Alteration processes and INnovative Concretes (SUSTAIN) drilling project at Surtsey Volcano. ICDP Operational Report. https://doi.org/10.2312/ICDP.5059.001.

Whitney, D.L., Evans, B.W., 2010. Abbreviations for names of rock-forming minerals. Am. Mineral. 95, 185–187.

Zhou, Z., Fyfe, W.S., Tazaki, K., Van der Gaast, S.J., 1992. The structural characteristics of palagonite from DSDP Site 335. Can. Mineral. 30, 75–81.

3 Paper II

Alteration of basaltic glass within the Surtsey hydrothermal system, Iceland – Implication to oceanic crust seawater interaction

Simon Prause[1], Tobias Björn Weisenberger[1,2], Barbara Irene Kleine[1], Patrick Monien[3], Concetta Rispoli[4], Andri Stefánsson[1]

[1]Institute of Earth Sciences, University of Iceland, Reykjavík, Iceland
[2]Research Centre Breiðdalsvík, University of Iceland, Breiðdalsvík, Iceland
[3]University of Bremen, Department of Geosciences, Bremen, Germany
[4]Dipartimento di Scienze della Terra, dell'Ambiente e delle Risorse (DiSTAR), Università degli Studi di Napoli Federico II, Naples, Italy

Published in 2022 in *Journal of Volcanology and Geothermal Research* (vol. 429, 107581)

Journal of Volcanology and Geothermal Research 429 (2022) 107581

Contents lists available at ScienceDirect

Journal of Volcanology and Geothermal Research

journal homepage: www.journals.elsevier.com/journal-of-volcanology-and-geothermal-research

Alteration of basaltic glass within the Surtsey hydrothermal system, Iceland – Implication to oceanic crust seawater interaction

Simon Prause [a,*], Tobias B. Weisenberger [a,b], Barbara I. Kleine [a], Patrick Monien [c], Concetta Rispoli [d], Andri Stefánsson [a]

[a] *Institute of Earth Sciences, University of Iceland, Reykjavík, Iceland*
[b] *Research Centre Breiðdalsvík, University of Iceland, Breiðdalsvík, Iceland*
[c] *University of Bremen, Department of Geosciences, Bremen, Germany*
[d] *Università degli Studi di Napoli Federico II, Dipartimento di Scienze della Terra, dell'Ambiente e delle Risorse (DiSTAR), Naples, Italy*

ARTICLE INFO

Keywords:
Surtsey volcano
ICDP
SUSTAIN
Palagonitization
Mass balance
Hydrothermal alteration

ABSTRACT

Low-temperature hydrothermal alteration of basaltic glass on the seafloor has important implications on the chemical evolution of the oceanic crust and seawater composition. However, mass fluxes resulting from seawater-glass interaction in this type of environment remain poorly understood. This study presents new results on element mobilities for the palagonitization of basaltic glass and bulk rock hydrothermal alteration at Surtsey volcano, Iceland over a time period of ~50-years. Assessments of element mobilities were based on 1) immobile trace element isocon mass balance for palagonitization, 2) the assumption of large scale TiO_2 immobility during bulk rock alteration and 3) chemical analyses of pore fluids and authigenic minerals.

Element mobilities of glass alteration vary between initial palagonitization and subsequent palagonite maturation: Initially, palagonitization of sideromelane leaches SiO_2, Al_2O_3, MgO, CaO, Na_2O, K_2O from the glass. Following this, the maturation of the palagonitized glass causes re-uptake of all of the abovementioned elements except for CaO, which shows either no change or slight uptake, and Na_2O, which continues to be lost from the palagonitized glass. Among major elements TiO_2 and FeO can be considered immobile during palagonitization, but not during the subsequent aging process of palagonitized glass. Among trace elements Hf, Ta, Zr, Nb, Y and REE were found to be immobile at all stages of the alteration. On the bulk rock scale, comprising both glass alteration and the formation of authigenic phases, early-stage alteration at Surtsey releases SiO_2, Al, Mg and Ca to the fluid, whereas late-stage alteration poses a sink of SiO_2, Al, Mg, Ca and Na. Net element budgets during early- and late-stage alteration indicate that chemical exchange between basaltic tuffs and seawater derived fluids at Surtsey acts as a long-term source of dissolved Ca, Al and SiO_2 for seawater as well as a long-term sink for seawater Mg and Na.

1. Introduction

Seafloor hydrothermal processes exert important controls on the chemical budget between seawater and the oceanic crust and play a key role in balancing global element cycles (e.g. Alt, 1995; Coogan and Gillis, 2013; Huang et al., 2018; Staudigel, 2003; Staudigel and Hart, 1983). Most of the hydrothermal fluid circulation on the ocean floor takes place in permeable basaltic rock hosted systems. Among these, low-temperature off-axis hydrothermal systems, such as those that may develop in seamounts, are the largest contributors to the observed hydrothermal heat anomaly in the oceanic crust (Alt, 2003). The global fluid flux for such systems is estimated to exceed that on mid-ocean ridge axes by several orders of magnitude (Fisher and Wheat, 2010; Nielsen et al., 2006). Given such high rates of seawater exchange, even small chemical fluxes caused by hydrothermal circulation and water-rock interaction in off-axis hydrothermal systems would be globally significant. Consequently, chemical sinks and sources from low-temperature alteration of basaltic rocks and glass have gained attention as potential buffers that could balance the discrepancies between high-temperature alteration on mid-ocean ridges and the riverine flux of many elements to the oceans (Huang et al., 2018; Wheat and Fisher, 2008; Wheat and Mottl, 2000).

---

* Corresponding author.
E-mail address: sip26@hi.is (S. Prause).

https://doi.org/10.1016/j.jvolgeores.2022.107581
Received 16 December 2021; Received in revised form 12 May 2022; Accepted 19 May 2022

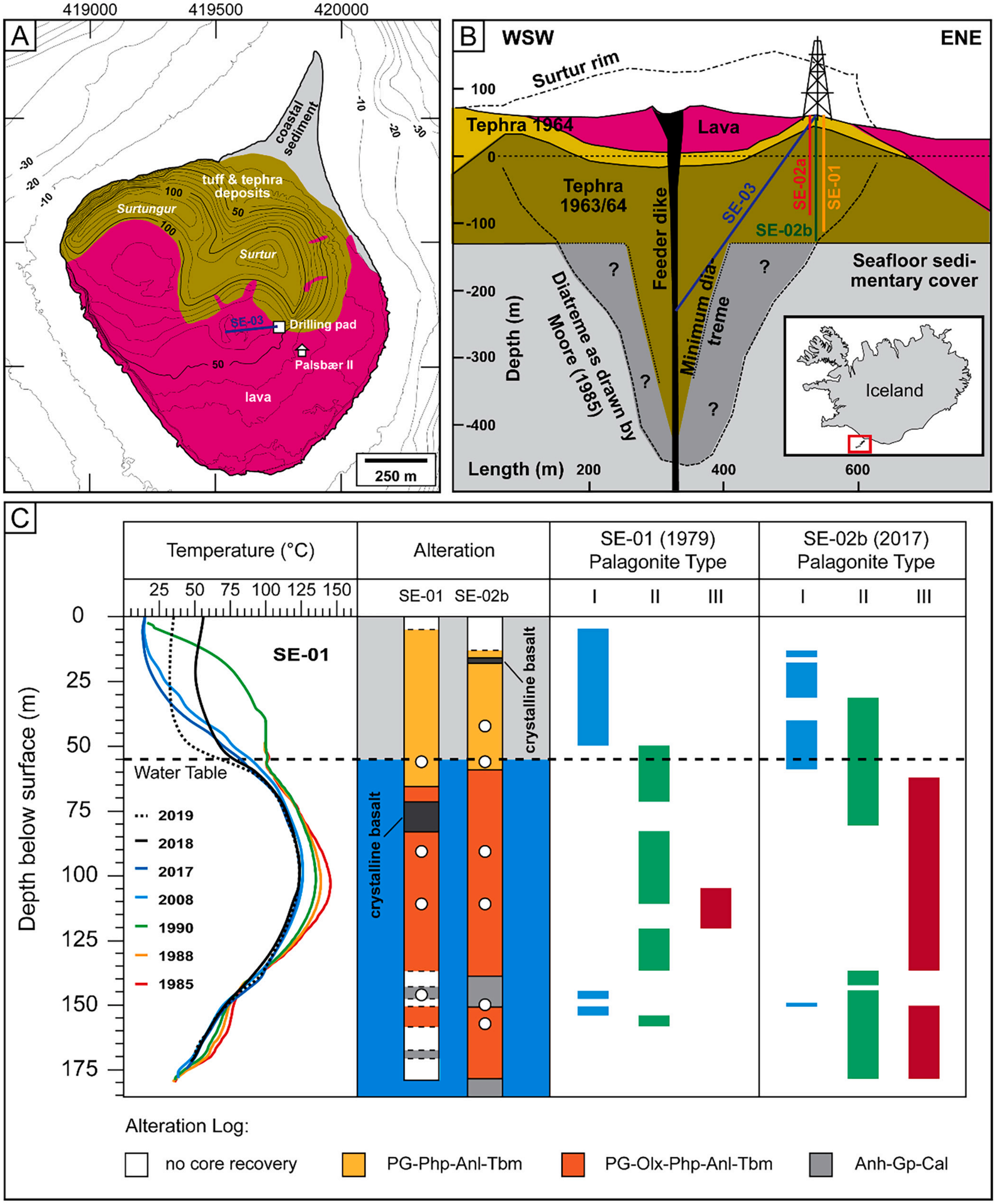

Fig. 1. A) Map showing the study area Surtsey (SW Iceland). B) Profile through Surtsey including the location of the boreholes and inlet showing the position of the Vestmannaeyjar archipelago (red rectangle) relative to Iceland. C) Fluid temperature and alteration zones with depth and occurrence of palagonite. Mineral abbreviations after Warr (2021): Php: phillipsite. Anl: analcime. Tbm: tobermorite. Anh: anhydrite. Gp: gypsum. Cal: calcite. PG: palagonitized glass. Olx: olivine alteration. White circles in the alteration log indicate samples taken for both major and trace element analysis. Modified after: Prause et al. (2020). (For interpretation of the references to colour in this figure legend, the reader is referred to the web version of this article.)

Basaltic glass, or sideromelane, is a common constituent in hyaloclastite rocks and pillow lavas on the ocean floor. The alteration of this highly reactive glass phase is one of the major processes controlling chemical exchange in low-temperature basalt hosted systems (Staudigel and Hart, 1983). Palagonitized glass is the first metastable reaction product of sideromelane, resulting from a chemical alteration process referred to as palagonitization. Palagonitized glass is an amorphous to cryptocrystalline mixture of authigenic phases appearing brown to reddish translucent under the microscope (Crovisier et al., 2003; Marshall, 1961; Stroncik and Schmincke, 2002). Glass replacement begins at the outer margins of the particles and lapilli exposed to the interfacing fluid, over time extending inward as alteration progresses (Pauly et al., 2011; Singer and Banin, 1990; Stroncik and Schmincke, 2002). This chemical alteration process leads to significant mass flux – both from the altered glass into solution and vice versa (Crovisier et al., 1992; Furnes, 1978; Pauly et al., 2011; Stroncik and Schmincke, 2001; Walton et al., 2005; Zhou and Fyfe, 1989). The resulting supersaturation of released chemical species in the fluid phase causes the precipitation of authigenic minerals, such as zeolites, clay minerals, and carbonates (Hay and Iijima, 1968a; Ibrahim and Hall, 1996; Kousehlar et al., 2012; Stroncik and Schmincke, 2002). Alteration rates and element mobilities during palagonitization are affected by temperature, pH, fluid chemistry, glass composition, water-rock ratio, fluid-flow rate, porosity and permeability (Crovisier et al., 2003; Jakobsson and Moore, 1986; Moore, 1966; Pauly et al., 2011; Singer and Banin, 1990; Stroncik and Schmincke, 2002; Walton et al., 2005).

Palagonitization is a gradual process that leads to the transformation of the primary glass phase to solely authigenic mineral phases over time. As alteration progresses, the initial amorphous palagonitized glass, or “gel palagonite” is replaced by “fibropalagonite”, a slightly more crystalline and highly birefringent variety of the same material, which subsequently matures into an assemblage of usually smectitic clay minerals (Berkgaut et al., 1994; Crovisier et al., 2003; Drief and Schiffman, 2004; Matthews, 1971; Peacock, 1926; Singer, 1974; Stroncik and Schmincke, 2001; Zhou and Fyfe, 1989).

Several aspects of palagonitic alteration are currently not fully understood. It is, for example, unclear if palagonitization is accompanied by significant volume changes (e.g. Crovisier et al., 1992; Pauly et al., 2011; Zhou and Fyfe, 1989) or if it occurs virtually isovolumetrically (e.g. Hay and Iijima, 1968b; Jercinovic et al., 1990; Stroncik and Schmincke, 2001; Walton et al., 2005). Likewise, the mobility of chemical constituents during alteration has been much debated. Several studies (e.g. Jakobsson, 1972; Staudigel and Hart, 1983; Stroncik and Schmincke, 2001; Zhou and Fyfe, 1989) assessed that TiO_2 or FeO should be considered immobile during palagonitization, while others (e.g. Pauly et al., 2011; Walton et al., 2005) found that either one or both of these elements showed mobile behavior. Stroncik and Schmincke (2001) and Zhou and Fyfe (1989) have pointed out that element mobilities appear to differ fundamentally depending on the stage of the devitrification process: These studies concluded that element fluxes during palagonitization are very different from those resulting from the aging of the material, and thus palagonitic alteration must be considered as a multistage process.

Understanding element mobilities, volume changes and the role of time in the alteration of basaltic glass on the seafloor is important, because it lays the groundwork for accurate estimates of the chemical evolution of the oceanic crust and the resulting impact on seawater composition. Unfortunately, in most cases the study of off-axis hydrothermal systems is made rather difficult by 1) the challenges involved in locating this type of system and 2) poor accessibility. However, potential analogues to alteration in seamounts may be found in the study of more readily accessible ocean islands (e.g. Kleine et al., 2020; Walton et al., 2005).

The aim of the present study is to investigate element fluxes, alteration behavior and time dependent changes in the alteration process of glassy basaltic tuff in the hydrothermal system of the volcanic island of Surtsey. This is made possible by the unique opportunity to compare chemical changes during alteration in the archived 1979 Surtsey drill core (Jakobsson and Moore, 1986) with data from one of the new vertical drill cores from Surtsey that were obtained in an ICDP expedition in 2017 (Jackson et al., 2019a; Weisenberger et al., 2019). The results will contribute to a better understanding of how low-temperature seafloor alteration of basaltic glass influences the composition of the oceanic crust and of the role played by this type of alteration in controlling seawater chemistry.

2. Geological setting

The ocean island of Surtsey, located 33 km off Iceland's southern coast, is the youngest and southernmost member of the Vestmannaeyjar archipelago (Fig. 1). Surtsey formed upon the injection of a primitive ridge-like melt into poorly connected volumes of alkali basaltic magma, causing overpressure and initiating volcanic activity on the seafloor which subsequently built up the island (Schipper et al., 2015, 2016).

Eruptions began on 12 November 1963, and were first observed on 14 November (Sayyadi et al., 2021). A series of shallow submarine eruptions proceeded over a time period of 3.5 years until 1967. After the end of the eruptive activity on Surtsey in June 1967 a low-temperature hydrothermal system emerged in the tuff deposits above and below sea level and was visually recognizable on the surface due to steam rising from the tephra pile (Friedman and Williams, 1970; Jakobsson, 1978; Jakobsson et al., 2000). It was originally hypothesized that shallow intrusive bodies delivered the necessary energy to drive hydrothermal activity (Axelsson et al., 1982; Jackson et al., 2015; Stefánsson et al., 1985), but recent evidence indicates that an alternative explanation may be that heat was instead conducted down from the 85 m thick lava shield in the Surtur crater, initiating the hydrothermal system (Moore and Jackson, 2020).

The hydrothermal fluid within the submerged section of the system has a modified seawater composition (Kleine et al., 2020) with SiO_2, Na, K, Ca and Al concentrations generally above and concentrations of B, Mg, F, dissolved inorganic carbon (DIC), and SO_4 below those typically found in seawater. Boiling may locally occur close to sea level (Jackson et al., 2019a; Kleine et al., 2020; Weisenberger et al., 2019). Above sea level the system is vapor dominated (Stefánsson et al., 1985) and the hydrological system is characterized by infiltrating meteoric water.

Hydrothermal alteration of the host rocks occurs primarily by palagonitization of sideromelane in the glassy tuff deposits and pseudomorphic replacement of olivine phenocrysts below sea level (Jakobsson and Moore, 1986; Prause et al., 2020). The palagonitized glass undergoes maturation over time from a mostly amorphous gel like phase (type I) into highly birefringent fibropalagonite (type II), which is in turn replaced at later stages of the devitrification process by an opaque fibrous to granular poorly crystalline clay mineral assemblage (type III) (Prause et al., 2020). Major secondary minerals include zeolites (primarily phillipsite and analcime), tobermorite and saponite-like clays. Chabazite has been identified only at the most shallow depths (0–4 m below surface) of the tephra pile (Jakobsson and Moore, 1986). Minor amounts of Ca-sulfates (anhydrite and gypsum) and carbonates are locally present, either in vesicles or as fracture fillings, but these minerals occur far more infrequently than zeolites, tobermorite and clays. The relative abundances of the most important authigenic phases at different depths in the 1979 and 2017 Surtsey drill cores have been described in Prause et al. (2020) (Table 1 therein).

Hyaloclastite tuff samples analyzed for this study are from two parallel vertical drill cores. The cores, designated SE-01 and SE-02b, were retrieved during the 1979 and 2017 Surtsey drilling campaigns, respectively (Jakobsson and Moore, 1982, 1986; Jackson et al., 2019a; Weisenberger et al., 2019). The two wells are both situated on the eastern edge of the tephra pile of Surtsey's southeastern vent, Surtur (Fig. 1). SE-01 and SE-02b were drilled to 181 and 192 m depth below surface, respectively. The horizontal distance between them is 6.9 m

(Weisenberger et al., 2019). Core material consists mostly of poorly sorted hypocrystalline lapilli tuff of alkali basaltic composition affected to varying extents by palagonitization and cementation by authigenic mineral phases.

3. Methods

3.1. Mineral and rock sampling and analysis

Chemical and mineralogical analyses were performed on drill core samples originating from the two boreholes, SE-01 and SE-02b. Samples for thin section preparation were initially soaked in epoxy resin to protect the friable tuff from abrasion during polishing. The temperature of the epoxy resin was kept below 50 °C to avoid dehydration. Subsequently, the samples were polished to a thickness of ~30 μm. In addition, 12 samples (six from each borehole) were selected for the preparation of thick sections to be used in trace element analyses of sideromelane and palagonite using laser ablation inductively coupled plasma mass spectrometry (LA-ICP-MS). These samples were chosen from similar depths in SE-01 and SE-02b to cover a wide range of depths and reaction progress (Fig. 1c). Modal mineralogical compositions of samples are available in Table 1 of Prause et al. (2020). All thick section samples for trace element analysis were prepared in the same way as the thin sections but polished to a thickness of ~100 μm to be suitable for laser ablation.

Major element analyses of authigenic mineral phases were performed at the Department of Earth, Environmental and Resources Sciences (DiSTAR) at the University of Naples Federico II using a ZEISS Merlin VP Microscope with X-Max Oxford EDS/WDX detector applying an accelerating voltage of 15 keV, 60 mA filament current, 10-s acquisition time and variable spot size. The major element composition of sideromelane and palagonitized glass was analyzed at the University of Iceland with a JEOL JXA-8230 electron probe microanalyzer (EPMA) using an accelerating voltage of 15 keV, a beam current of 3–10 nA and a beam diameter of 10 μm. A second batch of microprobe measurements of sideromelane and palagonitized glass was performed on thick section samples at the Department of Geosciences, University of Bremen. This was done to obtain reference major element compositions for subsequent LA-ICP-MS analyses. For this second batch of measurements, using a Cameca SX100, optimal analytical conditions were found to be 15 keV accelerating voltage, 3 nA beam current and a 5 μm defocused beam.

Trace element analysis of sideromelane and palagonitized glass was carried out at the Department of Geosciences of the University of Bremen using a NewWave UP 193 Solid State Laser Ablation System with a coupled Element2 HR-ICP-MS. Prior to ablation background blanks were measured for 30 s for each spot. Helium and Argon (ca. 0.8 l min^{-1} each) were used as sample and make up gas, respectively. Plasma power was 1200 W. Ablation of samples and standards was performed at a frequency of 5 Hz at an irradiance of 1.3 GW cm^{-2} and using spot sizes of 10–40 μm based on spatial conditions at the individual measurement sites, e.g., considering alteration rim thickness or the presence of phenocrysts. Analyses were performed as close as possible to the spots previously measured by EPMA to obtain reference compositions. United States Geological Survey (USGS) reference materials BHVO-2G and BCR-2G were analyzed alongside samples to evaluate the accuracy of data. To mitigate instrument drift, a NIST610 standard was analyzed after every 5 to 12 measurements and the composition listed in Jochum et al. (2011) was applied for calibration during quantitative analysis. Quantitative data assessment was performed through the Cetac GeoPro™ software package using ^{43}Ca as internal standard element. In addition, an in-house glass standard was measured daily to monitor and correct for the production of the doubly ionized $^{86}\text{Sr}^{++}$ isotope and its isobaric interference on ^{43}Ca. All isotopes were analyzed at low resolution with five samples in a 20% mass window and a total dwell time of 25 ms per isotope. Accuracy ranges between −3.4 to −4.8% (relative error) in most cases as determined by comparison of our BCR2G and BHVO2G data with the GeoReM data base as of November 2020. External precision was better than 4.5% (relative standard deviation) for most elements.

3.2. Pore-water sampling and analysis

Core sampling for pore fluid extraction from drill cores of borehole SE-02b was carried out during the field campaign in 2017 at Surtsey. The drill cores were retrieved to the surface within plastic liners. An approximately 10 cm long core piece was cut off from the upper part of each third core segment of every third core run. The core pieces were kept inside the plastic liner, and sealed airtight into plastic bags to prevent any removal of pore fluid from the core. Thereafter, the sealed core pieces were stored at 4 °C until sample preparation to prevent further rock alteration. Fluid extraction from the core was based on the ground rock interstitial normative determination (GRIND) method by Wheat et al. (1994) and Toki et al. (2016). In brief, the retrieved moist core samples were ground to fine powder using a vibratory disc mill. A volume of 20 ml of ultrapure water (18.2 mΩ cm^{-1}) was added to 2 g of powdered sample immediately and the rock-water mixture was thoroughly blended. Subsequently, the water was filtered off and acidified to 1% by addition of HNO_3 (Merck, Suprapur®). Major cation element analyses (SiO_2, Na, K, Al, Fe, Mg, Ca, B) were carried out using ICP-OES (Spectro Ciros Vision), whereas major anions (Cl, SO_4) were analyzed using IC. The analytical precision of major element analyses, based on repeated analysis of the samples and an in-house standard, was found to be in all cases <5% at the 95% confidence level. The measured pore fluid concentrations were subsequently normalized to Cl of seawater to account for dilution of the fluid samples upon pore fluid extraction.

3.3. Mobility and mass balance calculations

Mass balance of palagonitization was derived using the isocon method (Grant, 1986). Lanthanum, Ce and Lu in sideromelane and palagonitized glass were used for the construction of isocons. Mass changes were quantified using the EASYGRESGRANT macro spreadsheet software (López-Moro, 2012).

Calculations of element fluxes resulting from bulk rock alteration assumed the large scale immobility of TiO_2 and followed the approach by MacLean (1990):

$$\Delta C_n = C_n^a \cdot \left(C_{TiO_2}^i \middle/ C_{TiO_2}^a \right) - C_n^i \tag{1}$$

where ΔC_n is the mass change for element n in wt% relative to initial bulk rock mass, C_n^a and C_n^i are the weight percent of element n in the altered and unaltered rock, respectively, and C_{TiO2}^a and C_{TiO2}^i are TiO_2 wt % in the altered and unaltered rocks, respectively. Results obtained mathematically by this approach are identical to those obtained graphically by using the isocon method for immobile TiO_2. Bulk rock analyses of altered Surtsey tuffs (Jackson et al., 2019a) were used to represent altered compositions. Scoria erupted in 1963 at the Surtla volcanic vent (Schipper et al., 2015) was used as a reference material to represent "unaltered" protolith composition. This choice was based on the fact that effusive eruption at Surtla coincided with phreatomagmatic activity at the Surtur I vent and was most likely sourced from the same magma reservoir (Schipper et al., 2015). Other samples from the Surtsey magma series were not considered in the calculation, because they were erupted after the emplacement of the Surtla tuffs and their inclusion would likely have obscured protolith composition due to the progressive chemical evolution of the melt (Schipper et al., 2015). Results of bulk rock calculations are reported in the appendix (A.1).

3.4. Molar flux estimates

Average molar fluxes from and to the Surtsey tuffs were estimated by converting mass changes during bulk rock alteration into moles per kg

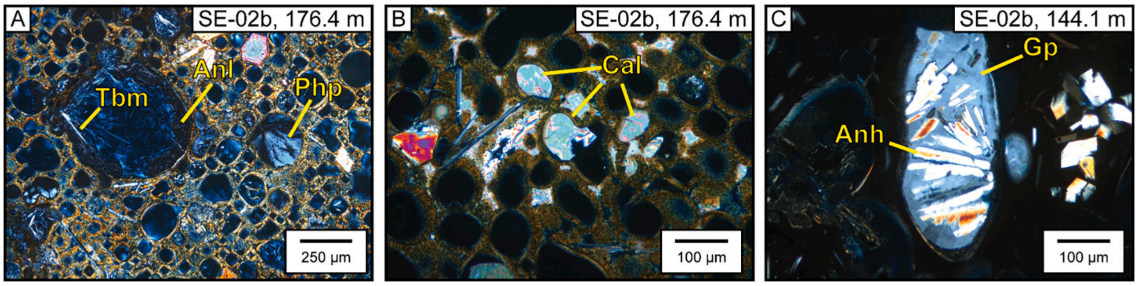

Fig. 2. Cross polarized photomicrographs showing typical authigenic minerals in Surtseyan tuff. A) Vesicular and fully palagonitized lapillus, partially filled with mineral cements (Tbm: tobermorite, Anl: analcime, Php: phillipsite). B) Calcite (Cal) fillings in lapillus vesicles. C) Massive gypsum (Gp) overgrowing prismatic anhydrite (Anh) in a lapillus vesicle. All depths are indicated as meters below surface.

Table 1
Representative chemical compositions of authigenic phases identified in Surtsey tuff.

	Analcime (n = 30)	Phillipsite (n = 30)	Tobermorite (n = 35)	Clays (n = 8)	Calcite (n = 6)	Anhydrite (n = 3)	Gypsum (n = 3)
SiO_2 (wt%)	52.70	48.68	44.63	37.61	0.76	0.07	0.27
TiO_2	–	0.10	–	1.01	–	0.06	–
Al_2O_3	23.60	23.90	6.16	9.99	0.15	0.03	0.12
FeO_{tot}	0.21	0.27	0.19	24.20	0.06	0.09	0.12
MnO	–	0.08	–	0.22	–	0.03	0.01
MgO	0.08	0.18	0.05	12.27	–	0.02	0.03
BaO	0.11	0.25	0.13	–	0.07	–	0.01
CaO	1.37	6.71	34.77	2.79	52.44	38.62	35.60
Na_2O	12.70	2.79	0.28	0.39	–	0.02	0.06
K_2O	0.05	6.03	0.43	0.27	–	0.05	0.05
P_2O_5	–	–	–	–	–	0.15	0.06
SO_3	–	–	–	–	3.83	57.14	51.52
Total[a]	90.82	88.99	86.64	88.75	57.31	96.28	87.85
formula unit composition							
O	96	32	17[b]	11[b]	3	4	4
Si	31.37	10.11	5.49	3.03	0.01	0.00	0.01
Al	16.56	5.85	0.89	0.95	0.00	0.00	0.00
Fe^{2+}	0.11	0.05	0.02	1.63	0.00	0.00	0.00
Mg	0.07	0.06	0.01	1.47	–	0.00	0.00
Ca	0.87	1.49	4.58	0.24	0.93	0.97	0.98
Ba	0.03	0.02	0.01	–	0.00	–	0.00
Na	14.66	1.12	0.07	0.06	–	0.00	0.00
K	0.04	1.60	0.07	0.03	–	0.00	0.00
Ti	–	0.01	–	0.06	–	0.00	–
Mn	–	0.01	–	0.01	–	0.00	0.00
P	–	–	–	–	–	0.00	0.00
S	–	–	–	–	0.05	1.01	1.00

[a] Deviations of totals from 100 wt% caused by the presence of volatiles (e.g. H_2O) in the analyzed phase.
[b] *Oxygen equivalent (O, OH).*

bulk rock for each element (Appendix A.1). The resulting moles were divided by the approximate age of the hydrothermal system at the point in time the sample was retrieved (~12 years for samples from SE-01 and ~ 50 years for samples from SE-02b). Such estimates are useful to determine general changes in the rates of molar fluxes over the entire course of hydrothermal activity at Surtsey volcano. However, it must be stressed that any estimates obtained in this manner are time-averaged rather than representing a single point in time. Therefore, any increases, decreases or reversals of rates mirror the total flux budget at a given depth over the full course of hydrothermal activity and must be interpreted as such. Moreover, the exact duration of the alteration cannot be fully constrained. Here, alteration is assumed to have commenced at the end of the eruptions in 1967. However, some amount of subsurface alteration may have already been present at an earlier point in time.

4. Results

4.1. *Chemical composition of authigenic minerals*

Primary and secondary phases observed within the Surtsey cores of the SE-01 and SE-02b wells have been previously described (Jakobsson and Moore, 1986; Prause et al., 2020). In brief, the main primary phases in the Surtsey tuff samples include (micro-)phenocrysts of plagioclase and olivine together with unaltered basaltic glass. The most common alteration minerals in Surtsey tuff are analcime, phillipsite, tobermorite (Fig. 2a) and saponite-like clays. Calcite (Fig. 2b) as well as anhydrite and gypsum (Fig. 2c) are subordinate phases, only occurring in significant quantities in the unpalagonitized to poorly altered sections of the drill cores (Fig. 1). Average chemical compositions of alteration minerals are listed in Table 1. Analcime is the main sodium bearing alteration phase and the quantitatively most abundant authigenic mineral with the possible exception of clay minerals (Prause et al., 2020). Phillipsite compositions vary but overall tend towards high K and Ca contents. Tobermorite, the main Ca bearing alteration phase, is of the high Al variety which is characteristic for Surtsey tuff (Jackson et al., 2019a,

Table 2

Average chemical compositions of sideromelane (SM) and palagonitized glass (PG) in the SE-01 and SE-02b cores.

	SE-01									
	Sdml ($n = 102$)		PG ($n = 122$)		PG type I ($n = 47$)		PG type II ($n = 39$)		PG type III ($n = 36$)	
Major elements	wt%	RSD (%)[a]	wt%	RSD (%)[a]	wt%	RSD (%)[a]	wt%	RSD (%)[a]	wt%	RSD (%)[a]
SiO_2	46.66	(±1.2)	36.20	(±7.7)	36.86	(±5.4)	36.22	(±6.0)	35.32	(±11.2)
TiO_2	2.61	(±5.1)	3.74	(±22.2)	3.86	(±7.3)	3.77	(±8.4)	3.54	(±41.0)
Al_2O_3	16.32	(±1.7)	11.73	(±14.6)	10.62	(±10.2)	12.10	(±9.6)	12.78	(±16.2)
FeO	12.33	(±3.4)	17.19	(±14.1)	17.37	(±8.6)	17.72	(±9.3)	16.40	(±22.4)
MnO	0.21	(±7.1)	0.28	(±23.0)	0.27	(±18.2)	0.27	(±24.8)	0.29	(±25.9)
MgO	5.79	(±3.6)	5.63	(±38.0)	4.58	(±29.4)	4.73	(±18.1)	7.98	(±26.8)
CaO	9.59	(±2.3)	9.03	(±22.6)	9.24	(±9.5)	9.99	(±17.9)	7.72	(±34.3)
Na_2O	3.86	(±4.2)	1.04	(±65.4)	1.15	(±44.7)	0.98	(±27.3)	0.97	(±110.8)
K_2O	0.71	(±5.7)	0.39	(±34.9)	0.34	(±30.4)	0.36	(±19.2)	0.47	(±38.7)
P_2O_5	0.37	(±8.7)	0.57	(±47.4)	0.53	(±31.5)	0.57	(±14.0)	0.62	(±73.0)
Sum	98.46		85.81		84.83		86.72		86.08	
Trace elements	ppm	RSD (%)	ppm	RSD (%)	ppm	RSD (%)	ppm	RSD (%)	ppm	RSD (%)
V	281	(±6.1)	327	(±33.7)	367	(±27.2)	354	(±35.4)	282	(±30.7)
Rb	14.2	(±9.9)	8.6	(±62.8)	14.2	(±37.9)	6.2	(±42.3)	9.2	(±68.5)
Sr	353	(±8.1)	495	(±29.0)	421	(±13.1)	537	(±23.6)	475	(±36.6)
Y	33	(±8.6)	50	(±27.0)	53	(±14.8)	47	(±36.8)	51	(±20.0)
Zr	195	(±9.6)	289	(±26.7)	306	(±17.2)	274	(±35.3)	298	(±20.9)
Nb	22.4	(±10.5)	33.0	(±29.0)	35.8	(±17.8)	31.4	(±38.6)	33.7	(±22.3)
Ba	163	(±11.7)	65	(±67.5)	42	(±26.3)	66	(±76.0)	73	(±61.0)
La	18.3	(±9.6)	27.0	(±26.4)	29.7	(±17.5)	26.1	(±34.1)	27.0	(±21.0)
Ce	42.9	(±11.1)	64.1	(±25.9)	68.2	(±18.2)	61.5	(±34.3)	65.6	(±19.5)
Pr	5.83	(±11.1)	8.71	(±27.1)	9.73	(±20.2)	8.30	(±35.7)	8.78	(±19.8)
Nd	26.8	(±10.1)	39.9	(±26.8)	45.2	(±20.3)	37.8	(±34.2)	40.3	(±20.9)
Sm	7.7	(±21.9)	11.0	(±27.6)	11.1	(±23.5)	10.8	(±34.8)	11.2	(±22.4)
Eu	2.50	(±12.5)	3.61	(±27.5)	3.62	(±25.2)	3.46	(±34.9)	3.78	(±21.4)
Gd	7.28	(±12.2)	10.51	(±25.4)	11.11	(±13.0)	10.06	(±34.1)	10.79	(±19.6)
Tb	1.10	(±13.5)	1.64	(±27.0)	1.75	(±21.4)	1.57	(±35.4)	1.68	(±20.4)
Dy	7.12	(±14.1)	10.55	(±29.5)	12.36	(±21.3)	9.81	(±39.4)	10.71	(±20.1)
Ho	1.37	(±12.8)	1.97	(±27.0)	2.13	(±17.2)	1.89	(±35.9)	2.00	(±20.6)
Er	3.9	(±11.3)	5.7	(±27.9)	6.3	(±18.0)	5.5	(±37.1)	5.7	(±20.9)
Tm	0.55	(±18.2)	0.78	(±30.3)	0.80	(±10.9)	0.75	(±42.0)	0.81	(±22.2)
Yb	3.46	(±11.0)	5.17	(±27.8)	5.74	(±15.7)	4.88	(±37.7)	5.28	(±20.4)
Lu	0.527	(±19.6)	0.758	(±30.7)	0.739	(±17.8)	0.752	(±43.1)	0.772	(±18.2)
Hf	5.11	(±9.8)	7.70	(±25.9)	8.57	(±24.6)	7.21	(±31.1)	7.92	(±21.3)
Ta	1.40	(±11.8)	2.06	(±28.1)	2.23	(±32.8)	1.94	(±33.7)	2.13	(±21.4)
Pb	2	(±20.4)	2	(±49.7)	3	(±32.3)	3	(±43.9)	1	(±23.1)
Th	1.6	(±13.5)	2.4	(±27.3)	2.5	(±22.4)	2.2	(±35.6)	2.4	(±20.8)
U	0.57	(±14.4)	0.86	(±26.5)	0.90	(±22.2)	0.84	(±34.3)	0.87	(±20.4)

	SE-02b									
	Sdml ($n = 108$)		PG ($n = 201$)[b]		PG type I ($n = 14$)		PG type II ($n = 64$)		PG type III ($n = 98$)	
Major elements	wt%	RSD (%)[a]	wt%	RSD (%)[a]	wt%	RSD (%)[a]	wt%	RSD (%)[a]	wt%	RSD (%)[a]
SiO_2	46.60	(±0.7)	34.88	(±7.2)	36.64	(±2.6)	34.61	(±6.1)	34.72	(±6.8)
TiO_2	2.70	(±6.2)	3.84	(±19.9)	4.18	(±9.0)	4.12	(±11.2)	3.61	(±25.5)
Al_2O_3	16.26	(±2.0)	12.55	(±13.5)	10.90	(±15.0)	12.37	(±7.9)	12.79	(±11.5)
FeO	12.42	(±4.1)	18.54	(±11.8)	19.31	(±8.8)	18.92	(±8.0)	18.40	(±12.0)
MnO	0.21	(±10.7)	0.31	(±20.2)	0.34	(±16.8)	0.30	(±15.4)	0.32	(±20.7)
MgO	5.72	(±4.1)	6.36	(±38.6)	5.34	(±33.9)	4.62	(±35.6)	7.94	(±26.5)
CaO	9.37	(±3.2)	7.50	(±22.8)	8.89	(±12.4)	8.61	(±15.0)	6.75	(±25.7)
Na_2O	3.92	(±4.0)	1.21	(±63.8)	1.03	(±15.9)	1.14	(±52.6)	1.27	(±66.5)
K_2O	0.72	(±5.9)	0.61	(±39.4)	0.35	(±16.3)	0.51	(±40.9)	0.68	(±30.5)
P_2O_5	0.38	(±11.4)	0.53	(±53.0)	0.56	(±25.5)	0.66	(±25.2)	0.44	(±72.2)
Sum	98.31		86.33		87.54		85.84		86.91	

	SE-02b									
	Sdml		PG		PG type I		PG type II		PG type III	
Trace elements	ppm	RSD (%)[a]	ppm	RSD (%)[a]	ppm	RSD (%)[a]	ppm	RSD (%)[a]	ppm	RSD (%)[a]
V	273	(±3.0)	273	(±37.3)	337	(±12.7)	293	(±19.4)	217	(±45.6)
Rb	14.1	(±6.6)	7.8	(±80.5)	4.7	(±35.0)	3.9	(±58.2)	13.5	(±42.0)
Sr	337	(±3.5)	454	(±31.8)	500	(±22.6)	496	(±14.3)	314	(±46.3)
Y	32	(±4.1)	47	(±27.0)	51	(±11.7)	46	(±17.0)	39	(±44.1)
Zr	188	(±3.6)	273	(±25.8)	283	(±10.8)	270	(±17.0)	234	(±41.4)
Nb	21.5	(±4.2)	31.3	(±28.3)	32.8	(±12.9)	30.8	(±16.9)	25.1	(±41.6)
Ba	161	(±3.9)	55	(±88.9)	52	(±35.2)	57	(±103.0)	37	(±83.1)
La	17.5	(±4.1)	25.5	(±30.6)	27.0	(±10.3)	25.9	(±16.6)	20.7	(±51.6)
Ce	41.2	(±4.0)	60.3	(±30.6)	64.0	(±11.0)	60.3	(±17.0)	48.9	(±51.5)
Pr	5.53	(±6.1)	8.17	(±29.0)	8.67	(±10.6)	7.98	(±16.4)	6.86	(±48.5)
Nd	25.7	(±3.9)	37.3	(±28.3)	38.4	(±9.3)	36.9	(±16.9)	31.9	(±47.5)

(*continued on next page*)

Table 2 (*continued*)

	SE-02b									
	Sdml		PG		PG type I		PG type II		PG type III	
Trace elements	ppm	RSD (%)[a]	ppm	RSD (%)[a]	ppm	RSD (%)[a]	ppm	RSD (%)[a]	ppm	RSD (%)[a]
Sm	7.1	(±6.2)	10.1	(±29.3)	10.2	(±18.0)	10.0	(±17.6)	8.4	(±46.3)
Eu	2.36	(±8.8)	3.34	(±29.2)	3.79	(±11.7)	3.34	(±17.9)	2.79	(±51.2)
Gd	7.00	(±7.1)	10.02	(±28.4)	10.35	(±10.8)	9.95	(±17.9)	8.60	(±48.0)
Tb	1.04	(±8.2)	1.52	(±27.2)	1.59	(±12.6)	1.51	(±17.1)	1.32	(±44.2)
Dy	6.66	(±4.8)	9.55	(±27.4)	10.65	(±13.7)	9.38	(±15.6)	7.87	(±45.7)
Ho	1.29	(±9.4)	1.84	(±27.8)	1.95	(±11.5)	1.83	(±19.3)	1.58	(±46.2)
Er	3.7	(±6.7)	5.2	(±24.8)	5.6	(±9.7)	5.2	(±15.5)	4.5	(±40.8)
Tm	0.52	(±10.5)	0.73	(±26.6)	0.73	(±19.2)	0.72	(±17.0)	0.64	(±38.0)
Yb	3.38	(±10.2)	4.74	(±26.5)	5.09	(±22.4)	4.53	(±14.9)	4.14	(±43.4)
Lu	0.497	(±10.8)	0.697	(±27.0)	0.764	(±12.5)	0.665	(±17.7)	0.609	(±42.5)
Hf	4.95	(±6.2)	7.03	(±26.8)	7.26	(±16.5)	6.89	(±17.3)	6.02	(±41.0)
Ta	1.34	(±6.8)	1.89	(±27.7)	2.03	(±11.2)	1.84	(±16.1)	1.53	(±44.3)
Pb	2	(±9.0)	2	(±52.5)	1	(±29.2)	2	(±33.8)	2	(±56.5)
Th	1.5	(±5.5)	2.2	(±28.4)	2.2	(±10.6)	2.1	(±19.4)	1.9	(±46.6)
U	0.54	(±11.9)	0.81	(±29.4)	0.83	(±11.4)	0.77	(±18.8)	0.74	(±48.9)

[a] Errors are given as RSD (%), i.e. relative standard deviation.

[b] Total average also includes 25 measurements from 165.6 m that were not identified as a specific petrographic type.

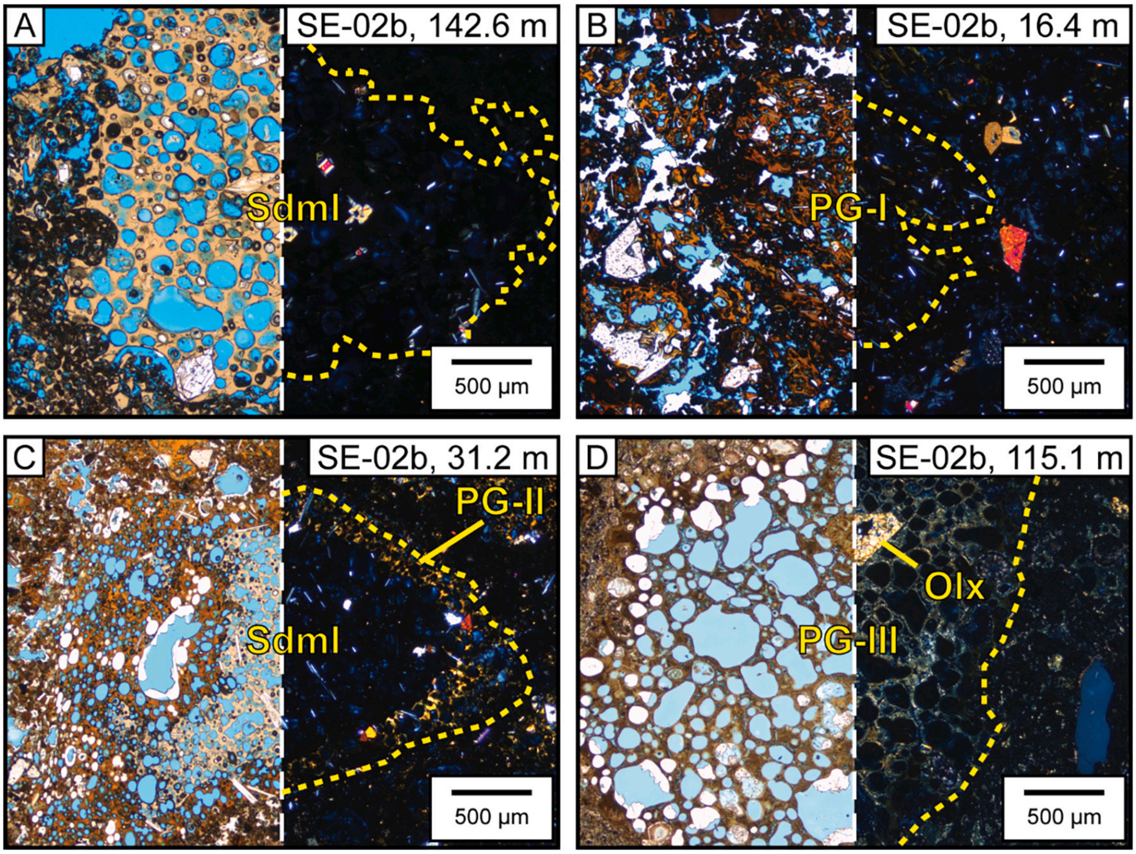

Fig. 3. Photomicrographs of unaltered and altered glass textures in Surtseyan tuff. Left half of each image: Plane polarized. Right half of each image: Cross polarized. Dashed yellow lines indicate the outline of lapilli in the cross polarized images. A) Optically isotropic basalt glass ("sideromelane", Sdml). B) Lapillus fully altered to optically isotropic type I palagonitized glass ("gel palagonite"). C) Rim of highly birefringent type II palagonitized glass ("fibropalagonite") around optically isotropic basalt glass lapillus. D) Lapillus fully altered to type III palagonitized glass containing pseudomorphic replacement of a primary olivine phenocryst by authigenic clay minerals (Olx). All depths are indicated as meters below surface. An in-depth petrographic description of altered glass textures is available in Prause et al. (2020). (For interpretation of the references to colour in this figure legend, the reader is referred to the web version of this article.)

2019b; Kleine et al., 2020). Saponite-like clay present in pore space is the only authigenic mineral that contains significant amounts of FeO, TiO_2 and MgO. Its overall composition most closely resembles that of palagonitized glass (Table 2), with overall lower TiO_2, CaO and Na_2O, higher FeO and MgO and similar SiO_2, Al_2O_3, MnO and K_2O contents.

4.2. *Chemical compositions of sideromelane and palagonitized glass*

Based on petrographic investigation, Prause et al. (2020) distinguished three types of palagonitic textures within the Surtsey drill core samples from 1979 and 2017 (Figs. 1c and 3). The amorphous and thus

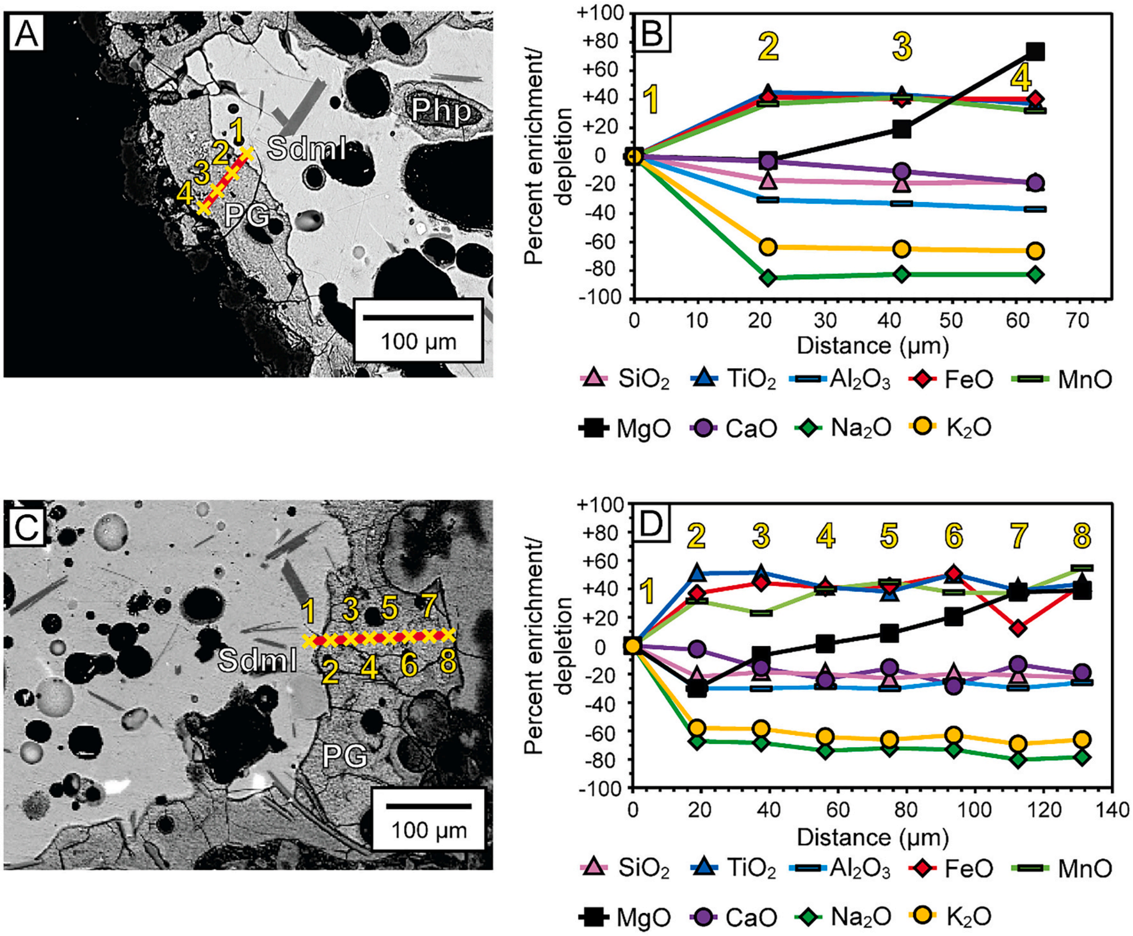

Fig. 4. A) Back scattered electron (BSE) image showing the location of a profile through a palagonitized glass rim (SE-01 drill core, 22.0 m) and B) percent enrichment and depletion of major element oxides along the same profile. C) Back scattered electron (BSE) image showing the location of a profile through a palagonitized glass rim (SE-01 drill core, 156.8 m) and D) percent enrichment and depletion of major element oxides along the same profile. MgO concentrations in palagonitized glass directly adjacent to the sideromelane-palagonitized glass interface are comparable to or lower than those in sideromelane. Furthermore, MgO concentrations indicate trends of progressive enrichment towards the surface of the lapillus. Both profiles show slight to moderate depletion of SiO_2, Al_2O_3 and CaO as well as strong depletion in Na_2O and K_2O along the palagonitized glass rim. Transition metal oxides TiO_2, FeO and MnO follow similar trends of enrichment. Sdml: sideromelane. PG: palagonitized glass. Php: phillipsite.

optically isotropic “type I" or gel-palagonite is clear, translucent, and reddish brown in colour. “Type II", or fibro-palagonite, shows grainy to fibrous textures and strong birefringence with colorful yellow, green, or red interference colors. Petrographic “type III" palagonitized glass occurs exclusively in the submerged part of the system and is identified by a darkened, opaque and spotty appearance.

The results of major element analyses of sideromelane and palagonitized glass for all maturation types are listed as average compositions in Table 2 (average compositions for each sample are reported in appendix A.2). Oxide totals for sideromelane range between 97.98 and 98.71 wt%. No significant compositional differences are observed when comparing unaltered glass samples from different depths. The palagonitized analyses reveal that all three maturation types (I, II and III) are significantly more heterogenous in composition than sideromelane. Palagonitized glass compositions are characterized by lower oxide totals between 72.94 and 90.97 wt%, indicating a relatively higher extent of hydration of the palagonitic rinds when compared to sideromelane. Cross sections of palagonitized glass rinds do not show any strong and systematic chemical variability, except for MgO (Fig. 4). Concentrations of MgO in the rinds are generally lower than or similar to those in sideromelane near the glass-palagonite boundary but increase outwards towards the surface of palagonitized lapilli. Transition metals (TiO_2, FeO and MnO) are enriched in the palagonitized glass rinds. Rinds belonging to the petrographic type I are on average depleted in MgO relative to sideromelane, whereas relative MgO enrichment is observed in type III rinds. Type II palagonitized glass exhibits MgO concentrations that are either comparable to or lower than those of type I palagonitized glass. An overview of MgO (and K_2O) accumulation in palagonitized glass (Stroncik and Schmincke, 2001; Zhou and Fyfe, 1989) in the two drill cores as a function of depth is given in the appendix (A.3). The concentrations of SiO_2 in the petrographic types II and III are slightly below those in type I. Conversely, Al_2O_3 and K_2O in type II and III are noticeably enriched compared to type I. The contents of CaO show no strong variation between type I and II palagonitized glass but are significantly lower by about 16–24% in type III palagonitized glass when compared to type I. Concentrations of Na_2O are generally below those of sideromelane, with no particular variation between petrographic types.

Trace element compositions are distinct between sideromelane and palagonitized glass. In most samples V, Sr, Y, Zr, Nb, Rare Earth Elements (REE), Hf and Ta are enriched in palagonitized glass to varying extents relative to sideromelane (Table 2). This observation universally applies to samples containing type I palagonitized glass. Within samples containing the more mature type II and III palagonitized glass, some measurements locally indicate enrichment or depletion of Y, Zr, Nb, REE, Hf and Ta relative to sideromelane. A change in trace element patterns can be observed for types II and III in SE-01 and SE-02b. In SE-

Table 3
Chemical compositions of pore fluids from SE-02b normalized to seawater Cl. Concentrations listed as ppm.

Depth(m)	Temp.[a](°C)	pH	Na	K	Mg	Fe	Al	B	Cl	SO_4	SiO_2	Ca
average seawater[b]			10,800	392	1290	<0.005	0.001	4.45	19,400	2815	6	416
56	81	6.95	5660	942	335	695	393	2.46	19,400	3655	3520	15,666
66	108	7.27	6592	1319	180	243	122	1.27	19,400	640	2456	10,243
77	108	7.27	19,788	4420	1025	1625	503	7.26	19,400	4433	13,711	27,317
93	118	7.24	5414	974	125	235	150	0.99	19,400	789	2914	11,011
102	118	7.24	8345	1519	289	491	230	2.83	19,400	1663	5454	14,159
121	122	7.6	5138	1356	182	230	53	1.18	19,400	1361	1925	11,748
128	122	7.6	11,421	2419	466	811	326	3.85	19,400	6375	8438	19,066
139	99	7.45	15,483	1961	722	1479	680	5.91	19,400	5063	11,632	18,985
148	99	7.45	15,557	1161	381	29	15	8.33	19,400	2309	2754	14,974
157	82	7.57	8591	2294	324	493	64	1.68	19,400	1839	3025	13,893
166	82	7.57	8317	2353	486	1043	429	5.69	19,400	2042	6577	15,087
175	82	7.23	10,871	2516	516	1337	130	4.24	19,400	3205	7030	14,318
181	82	7.23	23,630	1581	855	1648	742	31.20	19,400	9535	7851	14,609

[a] Weisenberger et al. (2019).
[b] Turekian (1968).

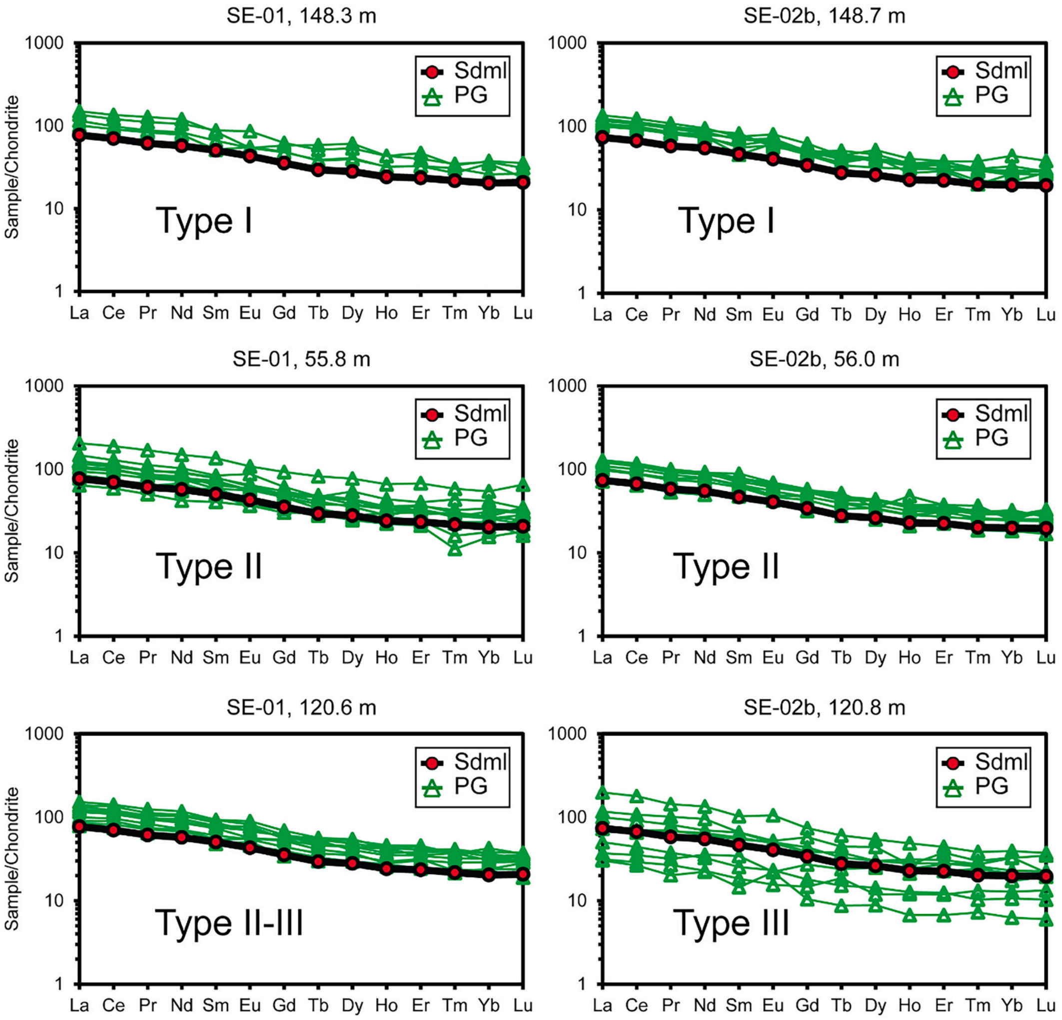

Fig. 5. Chondrite normalized REE diagrams for sideromelane (Sdml) from SE-01 and SE-02b and corresponding palagonitized glass rims (PG). The absence of REE fractionation between sideromelane and all petrographic types of palagonitized glass indicates that REE are largely immobile at all stages of glass alteration.

01, Y, Zr, Nb, REE, Hf and Ta concentrations in type III palagonitized glass are higher than those in type II. However, the reverse is observed for SE-02b, with all the aforementioned elements showing systematically lower concentrations in type III palagonitized glass relative to type II. Type III palagonitized glass of the SE-02b drill core may be considered more mature than its counterpart in SE-01 due to having undergone alteration for a significantly longer period of time.

4.3. Chemical composition of pore water

Chemical composition of pore fluid samples from SE-02b are listed in Table 3. These have been normalized to average chloride concentration

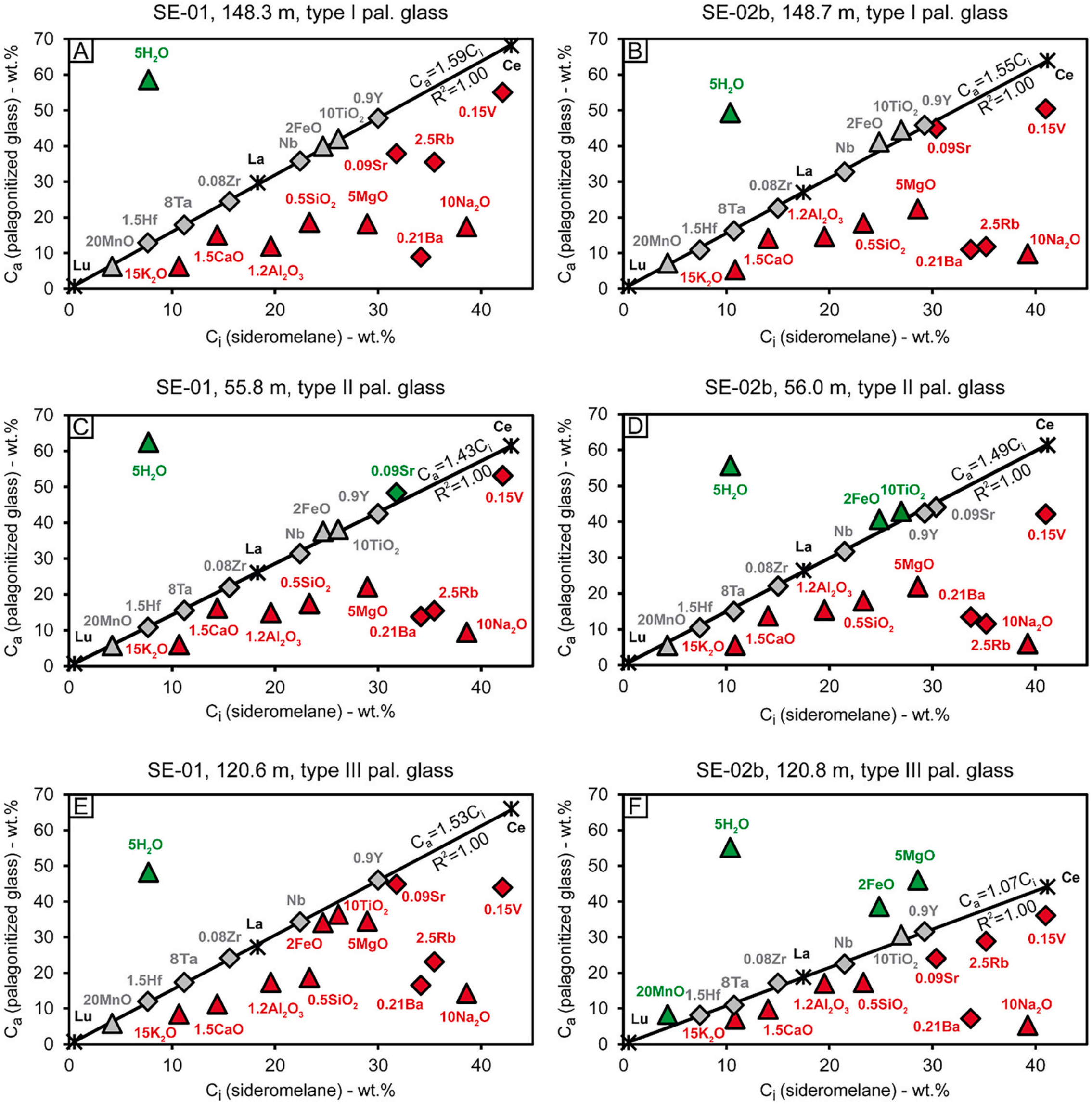

Fig. 6. Isocon diagrams showing element mobilities for palagonitized glass in SE-01 and SE-02b relative to sideromelane (unaltered basalt glass). Isocons assume immobile behavior of La-Ce-Lu. Numbers next to element symbols indicate scaling factors for each element. Mass changes of H_2O are estimated based on stoichiometrically calculated water contents. Triangles: major elements. Diamonds: trace elements. Grey symbols: no mobility. Green symbols: element uptake. Red symbols: element loss. (For interpretation of the references to colour in this figure legend, the reader is referred to the web version of this article.)

of seawater. Pore fluid compositions are significantly elevated in dissolved Al and Fe relative to seawater, somewhat enriched in K and often Na, and similar but variable for B and SO_4. Magnesium is the only element for which concentrations in the pore fluid are consistently lower than in seawater. Note, that high Ca and SiO_2 concentration values are likely to be affected by precipitation, dissolution and ion-exchange reactions during sample processing and should thus be treated with caution (Wheat et al., 1994).

5. Discussion

5.1. Elemental mobility and mass change during palagonitization

The similar REE behavior within sideromelane and palagonitized glass suggests that REE are nearly perfectly immobile during the alteration process even for highly maturated palagonitized glass (Fig. 5). Minor fractionation is observed for some of the Eu concentrations in the SE-01 sample from 148.3 m and the SE-02b sample from 120.8 m. Two out of twelve measurements of Tm in the SE-01 sample from 55.8 m (Fig. 5) also suggested slight fractionation. This may indicate that Eu and Tm are slightly mobile in contrast to other REE. Except for these outliers, REE patterns as shown in Fig. 5 indicate near complete immobility for all alteration stages. Similar observations regarding the behavior of REE have been made in the past (Walton et al., 2005; Pauly et al., 2011). Small-scale mobilization of REE cannot entirely be ruled out as enrichment of REE may occur upon volume change (Walton et al., 2005). However, Pauly et al. (2011), who studied palagonitized glass from a wide range of locations, concluded that no systematic chemical fractionation of REE was evident regardless of palagonitization environment. Our results corroborate this finding, supporting the notion of general REE immobility during palagonitic glass alteration.

The extent of elemental mobility can be assessed using isocon diagrams (Fig. 6). Concentrations of selected immobile REE (i.e., La, Ce and Lu) in sideromelane and palagonitized glass were used to quantify mass changes during palagonitization and aging of palagonitized glass. Isocons assuming immobile behavior of La, Ce and Lu exhibited very good fits ($R^2 = 1.00$), even for the most mature palagonitized glass. Moreover, TiO_2-FeO immobility was not viable for samples at the highest

Table 4

Average mass change of major elements during palagonitization and palagonite maturation in comparison to previous studies. Step 1 refers to the initial reaction of sideromelane to gel palagonite (type I), step 2 refers to the subsequent aging process of palagonitized glass and was calculated as the mass flux between type I palagonitized glass to the most mature type III palagonitized glass in the SE-02b sample from 120.8 m depth.

Study:		This study	Pauly et al. (2011) - average alkaline	Pauly et al. (2011) - Surtsey	Walton et al. (2005)[a]	Stroncik and Schmincke (2001)	Zhou and Fyfe (1989)	Staudigel and Hart (1983)
Method of mass balance calculation:		Immobile trace elements	Immobile trace elements	Immobile trace elements	Constant volume	Constant volume	Immobility of TiO_2/ constant volume[b]	Immobility of TiO_2
STEP 1 - Palagonitization								
SiO_2	ΔCi	−22.6	n.a.	n.a.	n.a.	−36.2	−31.1	n.a.
	ΔCi/Ci0	−48.4	−45.3	−56.3	−42.0	n.a.	−62.3	−50.0
TiO_2	ΔCi	0.2	n.a.	n.a.	n.a.	n.a.	0.0	n.a.
	ΔCi/Ci0	5.9	19.5	18.5	28.0	n.a.	0.0	n.a.
Al_2O_3	ΔCi	−9.1	n.a.	n.a.	n.a.	−13.1	−9.3	n.a.
	ΔCi/Ci0	−55.8	−51.2	−33.8	−54.0	n.a.	−62.2	−55.0
FeO	ΔCi	0.8	n.a.	n.a.	n.a.	n.a.	0.4	n.a.
	ΔCi/Ci0	6.3	6.4	8.7	0.0	n.a.	4.0	−12.0
MnO	ΔCi	0.01	n.a.	n.a.	n.a.	n.a.	−0.2	n.a.
	ΔCi/Ci0	4.0	n.a.	n.a.	5.0	n.a.	−92.7	−93.0
MgO	ΔCi	−3.1	n.a.	n.a.	n.a.	−4.5	−6.9	n.a.
	ΔCi/Ci0	−54.1	−80.0	−64.8	−75.0	n.a.	−86.4	−67.0
CaO	ΔCi	−3.2	n.a.	n.a.	n.a.	−9.4	−10.9	n.a.
	ΔCi/Ci0	−33.5	−66.6	−49.8	−29.0	n.a.	−91.9	−88.0
Na_2O	ΔCi	−3.0	n.a.	n.a.	n.a.	−2.7	−1.8	n.a.
	ΔCi/Ci0	−77.5	−69.0	−91.8	−88.0	n.a.	−66.1	−81.0
K_2O	ΔCi	−0.5	n.a.	n.a.	n.a.	−1.7	1.0	n.a.
	ΔCi/Ci0	−65.3	−50.0	−91.8	−58.0	n.a.	614.5	900.0
STEP 2 - Palagonite Maturation								
SiO_2	ΔCi	13.4	n.a.	n.a.	n.a.	12.3	5.3	n.a.
	ΔCi/Ci0	36.6	n.a.	n.a.	n.a.	n.a.	13.6	n.a.
TiO_2	ΔCi	0.0	n.a.	n.a.	n.a.	−2.0	−0.7	n.a.
	ΔCi/Ci0	−0.5	n.a.	n.a.	n.a.	n.a.	−27.7	n.a.
Al_2O_3	ΔCi	8.3	n.a.	n.a.	n.a.	8.2	1.0	n.a.
	ΔCi/Ci0	68.1	n.a.	n.a.	n.a.	n.a.	8.2	n.a.
FeO	ΔCi	7.3	n.a.	n.a.	n.a.	−5.8	−4.0	n.a.
	ΔCi/Ci0	35.7	n.a.	n.a.	n.a.	n.a.	−20.3	n.a.
MnO	ΔCi	0.2	n.a.	n.a.	n.a.	n.a.	0.01	n.a.
	ΔCi/Ci0	66.5	n.a.	n.a.	n.a.	n.a.	33.3	n.a.
MgO	ΔCi	8.8	n.a.	n.a.	n.a.	0.8	2.4	n.a.
	ΔCi/Ci0	196.8	n.a.	n.a.	n.a.	n.a.	106.3	n.a.
CaO	ΔCi	0.0	n.a.	n.a.	n.a.	n.a.	−0.7	n.a.
	ΔCi/Ci0	0.3	n.a.	n.a.	n.a.	n.a.	−36.9	n.a.
Na_2O	ΔCi	−0.2	n.a.	n.a.	n.a.	n.a.	−1.1	n.a.
	ΔCi/Ci0	−21.4	n.a.	n.a.	n.a.	n.a.	−58.7	n.a.
K_2O	ΔCi	0.3	n.a.	n.a.	n.a.	1.4	1.7	n.a.
	ΔCi/Ci0	94.5	n.a.	n.a.	n.a.	n.a.	72.5	n.a.

[a] Referring to the results of their calculations assuming constant volume and densities of $\rho_{sideromelane} = 2.8$ g cm^{-3}, $\rho_{palagonite} = 2.0$ g cm^{-3}.

[b] Mass balance of palagonitization calculated based on TiO_2 immobility; mass balance of palagonite maturation calculated based on constant volume.

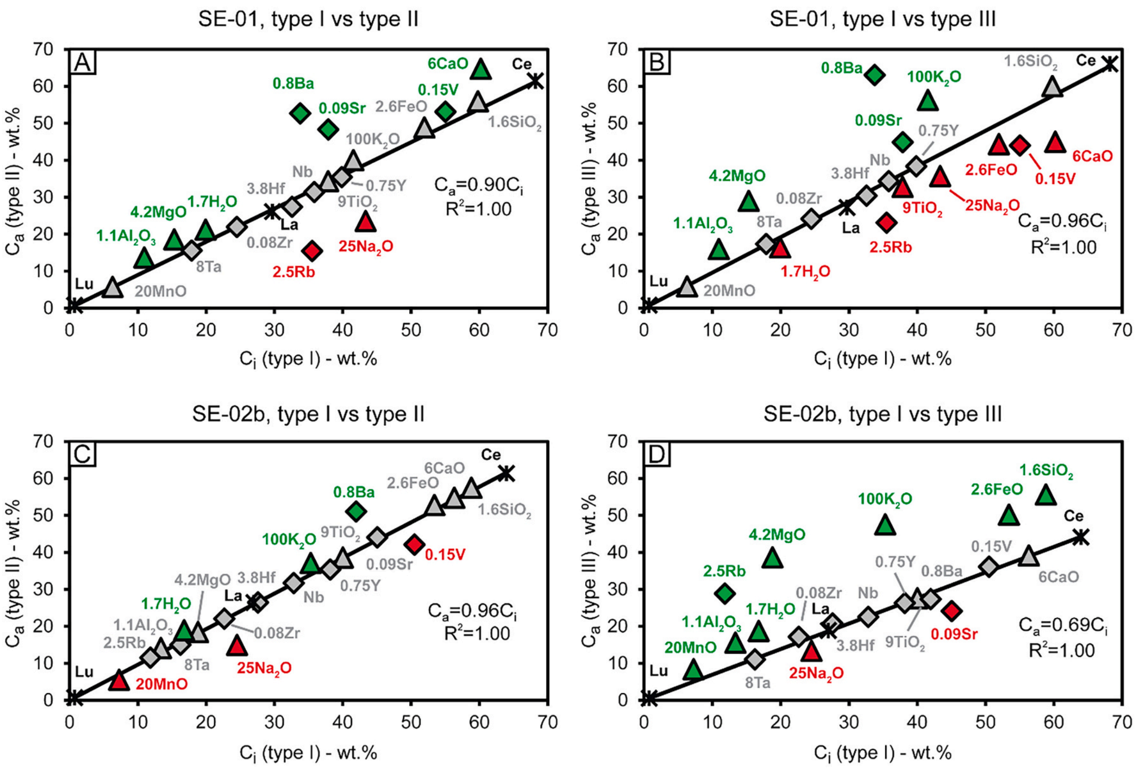

Fig. 7. Isocon diagrams showing element mobilities between different maturation stages of palagonitized glass in SE-01 and SE-02b. The isocons are constructed assuming immobile behavior of La-Ce-Lu. Numbers next to element symbols indicate scaling factors for each element. Note that, unlike in Fig. 6, the slope of each isocon is <1, indicating minor to intermediate overall mass *increases* during palagonitized glass maturation as opposed to the significant overall mass *losses* during initial palagonitization of sideromelane. Barium is generally gained during the transition of type I to type II palagonitized glass, possibly owing to previous Ba enrichment of the fluid during palagonitization. Elements MgO, CaO, Al_2O_3 and K_2O either remain immobile or display minor increase. Overall, mobilities during this maturation stage are minor compared to initial palagonitization. Mobilities for the maturation of type II into type III palagonitized glass vary between SE-01 and SE-02b. However, results generally indicate significant uptake of MgO, K_2O, Al_2O_3 as well as SiO_2, likely due to in-situ formation of smectitic clays in the palagonitized glass matrix during maturation (see text for discussion). Triangles: major elements. Diamonds: trace elements. Grey symbols: no mobility. Green symbols: element uptake. Red symbols: element loss. (For interpretation of the references to colour in this figure legend, the reader is referred to the web version of this article.)

maturation stage where no common isocon for these elements could be constructed. Noticeable element mobility and mass changes were found to occur throughout all the maturation stages of palagonitized glass (Fig. 6). Overall, sideromelane loses up to 35% of its initial mass during the formation of type I palagonitized glass in the submarine parts of the hydrothermal system (Appendix A.4). Type I palagonitized glass, which best approximates the initial alteration product of sideromelane, shows significant losses of all major element oxides, except for TiO_2, FeO and MnO, all of which are indicated by our data to be immobile during this palagonitization stage. Among trace elements, REE, Hf, Ta, Zr, Nb and Y are preserved during palagonitization. The remaining trace elements are lost during palagonitization to varying extents with exception of Sr, which is commonly highly variable in palagonitized glass. The mass change for the transition from sideromelane to type I palagonitized glass below sea level suggests that during palagonitization 100 g of sideromelane loses on average 22.6 g of SiO_2 (−48.4%), 9.1 g of Al_2O_3 (−55.8%), 3.1 g of MgO (−54.1%), 3.2 g of CaO (−33.5%), 3.0 g of Na_2O (−77.5%) and 0.5 g K_2O (−63.5%) (Table 4). The lower totals in palagonitized glass relative to sideromelane indicate that about 5–6 g H_2O is taken up during palagonitization of 100 g sideromelane. These results are well in line with findings of Staudigel and Hart (1983) who proposed that SiO_2, Al_2O_3, MgO, CaO and Na_2O may be exchanged for H_2O during the early stage of palagonitization. It should be noted that, given the potentially different mobilities for palagonitization in the meteoric part of the system, these results only apply to palagonitization below sea level.

As devitrification of sideromelane progresses, the gradual transformation of the glass matrix into an assemblage of smectitic clay minerals leads to a reuptake of several elements (Fig. 7, Table 4). Isocons in Fig. 7 indicate slightly positive mass changes during the maturation from type I to type II palagonitized glass, which is caused by the uptake of several major elements, principally varying amounts of MgO, CaO, Al_2O_3 and K_2O. Among trace elements Ba is also gained at this maturation stage, possibly resulting from the previous release of Ba during palagonitization and subsequent transport in the fluid to depths where palagonitized glass maturation takes place. During maturation from type II to type III MgO is significantly enriched. Several previous studies have concluded that MgO is incorporated into palagonitized glass during maturation as a result of the formation of typically smectitic clay minerals in the initially amorphous palagonitized glass matrix (Pauly et al., 2011; Stroncik and Schmincke, 2001, 2002). Increased MgO contents in type III palagonitized glass are therefore interpreted as indicative of progressive crystallization of palagonitized glass into such an assemblage of smectitic clays. Mass changes of MgO and other elements during the transition from type II to type III palagonitized glass show some variation between SE-01 and SE-02b. This is interpreted here as being due to the significantly higher degree of maturation of type III palagonitized glass in SE-02b when compared to its counterpart in SE-01. Despite the mass gain of several elements during aging, overall mass changes from sideromelane to the most mature type III palagonitized glass were found to remain negative (−6.6 to −33%, Appendix A.4). The most mature palagonitized glass examined in this study is present in the SE-02b sample from 120.8 m, containing the petrographic type III. Mass balance results between average submarine type I palagonitized glass in SE-01 as well as SE-02b and the type III palagonitized glass in this sample may therefore be used to estimate minimum mass fluxes during

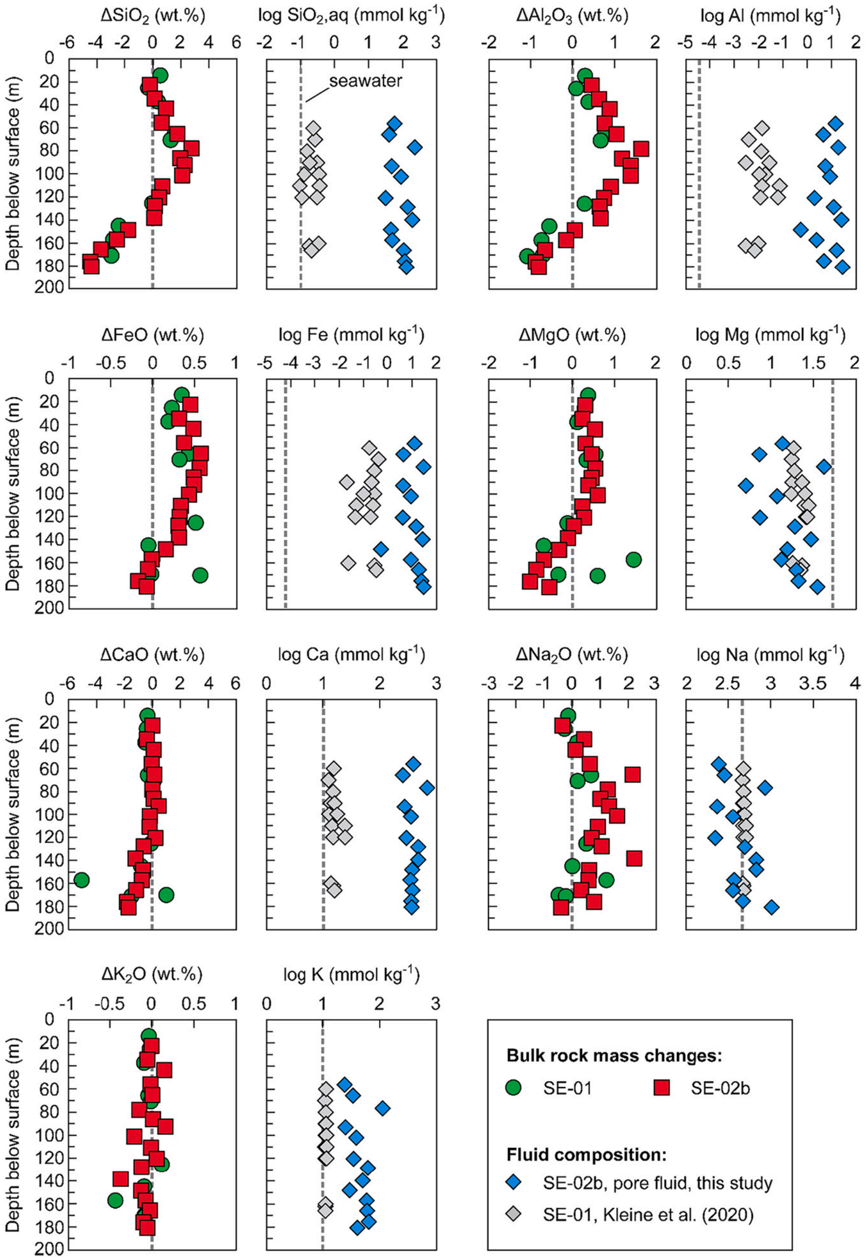

Fig. 8. Comparison of bulk rock mass changes in wt% and pore fluid compositions of dissolved species contrasted with standard seawater. Negative values for bulk rock mass changes denote a loss from the rock to the hydrothermal solution and positive values indicate bulk rock gains for the respective element.

palagonite maturation in a marine hydrothermal environment. The range of element reuptake during the maturation of 100 g type I to type III palagonitized glass is 13.4 to 15.0 g of SiO_2 (+36.6 to +40.0%), 8.3 to 11.4 g Al_2O_3 (+68.1 to +114.1%), 7.3 to 9.1 g of FeO (+35.7 to 45.3%), 0.2 to 0.3 g of MnO (+66.5.1 to +99.6%), 8.8 to 10.2 g of MgO (+196.8 to +279.4%), and ~ 0.3 g of K_2O (+72.2 to +94.5%). Some TiO_2 mobilization is apparent at advanced stages of the maturation process (Figs. 6 and 7). However, TiO_2 mobilization levels out in the average (Table 4), indicating that it is only small scale. Limited FeO and TiO_2 mobilization during progressive devitrification of sideromelane has been previously reported by Zhou and Fyfe (1989). They proposed that TiO_2 and FeO are locally mobilized and incorporated into clays and oxide minerals. Our findings support this process, suggesting a mobilization of FeO and TiO_2 and their incorporation into clay minerals on a limited scale during palagonite maturation (Figs. 6 and 7). It is important to note that palagonitized glass represents a spectrum from mostly amorphous (type I) to increasingly crystalline (types II and III) alteration products. Smectitic clay minerals are the final devitrification product of palagonitized glass maturation, and it has been suggested that they can form directly in the palagonitized glass matrix (e.g. Stroncik and Schmincke, 2002). During maturation a fraction of clay minerals likely precipitates in-situ within palagonitized glass, causing small scale local mass changes in TiO_2 and FeO. Some amount of TiO_2 and FeO must also be released to the fluid during palagonitized glass maturation, to allow for the formation of the saponite-like clays observed in the pore space; these clays represent the only authigenic phase apart from palagonitized glass to take up significant amounts of TiO_2 and FeO (Tables 1 and 2).

Estimated volume changes for the overall reaction of sideromelane to palagonitized glass, assuming densities between 2.0 and 2.3 g cm^{-3} for palagonite (Hay and Iijima, 1968b; Staudigel and Hart, 1983; Walton et al., 2005) were found to be small and generally negative, falling between 0 to −20 vol% ($0.8 \leq F_v \leq 1.0$) (Appendix A.4). Estimated volume losses for the SE-02b sample from 165.6 m are slightly greater than for the other samples, ranging between $0.7 \leq F_v \leq 0.8$. For the highly maturated type III palagonitized glass of the SE-02b sample from 120.8 m volume factors instead suggest minor volume gains of $1.1 \leq F_v \leq 1.3$. This estimated increase in volume may be an artifact related to the inhomogeneity of mature samples, rather than reflecting a real volume change.

The general trend of volume reduction during palagonitization indicated by our mass balance agrees with previous findings by Zhou and Fyfe (1989), who reported that during initial palagonitization volume was reduced and subsequently remained constant as palagonitization progressed. It should be noted that textural observation on a thin section scale does not reveal a change in volume. It can be assumed that the volume change occurs on a submicroscopic scale, which is consistent with the observation of nanocavities within altered glass from Surtsey (Jackson et al., 2019b).

5.2. Comparison of element mobilities with other mass balance models on palagonitization

Previous studies have addressed element mobility during palagonitization upon seawater alteration using mass balance approaches that are based on either immobile trace elements (Pauly et al., 2011), constant volume alteration (Stroncik and Schmincke, 2001; Walton et al., 2005; Zhou and Fyfe, 1989) or immobility of TiO_2 (Zhou and Fyfe, 1989; Staudigel and Hart, 1983). Here, our estimates of element mobilities at different stages of basaltic glass devitrification based on immobile trace element isocons are compared with the results of these previous studies (Table 4). Additionally, the results of immobile TiO_2 and constant volume alteration mass balance applied to our samples are compared in the appendix (A.5).

Despite the use of different mass balance approaches, the current study and most previous studies agree that upon onset of palagonitization, major elements such as SiO_2, Al_2O_3, MgO, CaO and Na_2O are commonly released into the reacting hydrothermal fluid whereas FeO and TiO_2 are passively or actively enriched in palagonitized glass relative to sideromelane (Pauly et al., 2011; Walton et al., 2005; Stroncik and Schmincke, 2001; Zhou and Fyfe, 1989; Staudigel and Hart, 1983). However, some differences exist in the assessment of K_2O mobility during the early stage of palagonitization. Our study as well as those of Pauly et al. (2011)Walton et al. (2005) and Stroncik and Schmincke (2001) suggest that palagonitization induces the loss of K_2O whereas Zhou and Fyfe (1989) and Staudigel and Hart (1983) report a significant gain of K_2O. The observed differences between our study and the results of Staudigel and Hart (1983) and Zhou and Fyfe (1989) may be related to the different serial affinities of the precursor basalt glasses (i.e., tholeiitic for the previous investigations and alkalic for the present study), which may affect alteration behavior (Pauly et al., 2011).

Maturation of palagonitized glass is characterized by gain or reuptake of SiO_2, Al_2O_3, MnO, MgO and K_2O and continued loss of Na_2O. This conclusion agrees well with previous findings (Stroncik and Schmincke, 2001; Zhou and Fyfe, 1989). Our findings also support some amount of mobilization of TiO_2 and FeO during progressive maturation of palagonitized glass as suggested by Stroncik and Schmincke (2001) and Zhou and Fyfe (1989). However, based on our results FeO is gained during maturation rather than being lost. This discrepancy may not only arise from different mass balance approaches used between studies but rather be readily explained by smectitic clays and Fe-oxides forming directly by devitrification of the palagonitized glass matrix. Therefore, the increased FeO contents in more mature palagonitized glass may reflect its progressive in-situ replacement by smectite and Fe-oxides. Dissolved Fe required for this process may originate from the dissolution of primary minerals, such as olivine. With 12–17 vol% olivine is a common phase in Surtseyan lavas (Schipper et al., 2015). Typical compositions of olivine in the Surtsey magma series are Mg rich with compositions ranging between Fo_{75} to Fo_{87} (Schipper et al., 2015). However, due to the extensive dissolution of olivine below sea level (Prause et al., 2020; Jakobsson and Moore, 1986), even such minor Fe contents may be sufficient to cause a significant enrichment of iron in the pore fluid given the naturally low dissolved Fe content in seawater.

5.3. Overall mass movement and elemental fluxes in the hydrothermal system at Surtsey

Water-rock interaction during palagonitization and maturation of palagonitized glass may have profound effects on the chemical composition of altered rocks and the associated pore water, thereby affecting the chemical composition of both the oceanic crust and seawater.

Our results of elemental mass changes in bulk rock indicate that extensive mass gains of SiO_2, Al_2O_3, FeO, MgO and Na_2O relative to the protolith occur just below the water table (~55 m) and extend to depths of ~140 m (Fig. 8). Comparatively smaller mass gains and/or even mass losses of the aforementioned elements occur at greater depths (>140 m). The extensive mass gains above 140 m suggest that the formation of authigenic minerals and associated uptake of relevant cations is promoted by elevated temperatures in the system. In contrast, mass losses related to elemental leaching from primary minerals and sideromelane occur in the parts of the hydrothermal system exhibiting relatively colder temperatures. Overall increases in mass have grown in magnitude between 1979 and 2017 at all depths (Appendix A.1), reflecting the ongoing precipitation of authigenic minerals. Below the water table overall mass gains, both for SE-01 and SE-02b are generally highest in the depth interval between ~65 m and ~ 128 m with +10.1 to +13.3 wt% in SE-01 and + 11.7 to +21.3 wt% in SE-02b. In both cores the highest overall mass increases are observed in the first samples below the water table at 55 m (+13.3 wt% at 65.6 m in SE-01 and + 21.3 wt% at 65.3 m in SE-02b).

The overall mass increase in the poorly altered zone between ca. 140–150 m is one order of magnitude lower (+3.1 to +9.0 wt%) compared to the mass increase between water level and 140 m. However, alteration in this poorly altered zone is ongoing, albeit at a lower rate than in the overlying water saturated parts of the system. Overall mass increases are even lower below the poorly altered zone with +0.3 wt% at 157.1 m in SE-01 and + 1.8 to +7.1 wt% between 157.1 and 176.1 m in SE-02b. This depth interval was documented previously as being largely unpalagonitized in 1979 (Jakobsson and Moore, 1986; Prause et al., 2020). Thus, our mass flux calculations confirm the previous assessments of overall lower alteration progress and slower alteration rates within this depth interval. The lowermost samples in each drill core exhibit overall mass loss with −5.3 wt% at 171.0 m below surface in SE-01 and -7.6 wt% at 180.8 m below surface in SE-02b.

Comparison between bulk rock mass changes and pore fluid chemistries can be used to shed light on overall water-rock interaction (Fig. 8). The results reveal that alteration of sideromelane glass is characterized by incongruent reactions with the glass being non-stoichiometrically dissolved followed by formation of authigenic minerals. SiO_2, Al_2O_3, FeO and Ca are found to be similar or enriched in the altered rocks at shallow depths and become depleted at >140 m relative to sideromelane glass (Fig. 8). Moreover, the concentrations of all these elements in the pore water is much higher than for seawater, suggesting that this process results in net leaching of the elements from the glass to seawater. Magnesium shows similar bulk enrichment in the altered rocks at shallow depths followed by depletion at >140 m depth, but conversely the Mg concentrations in the pore waters are lower compared to those in seawater, indicating that the combined processes of palagonitized glass maturation and associated formation of clay minerals results in a net sink of seawater Mg.

Sodium and K show less pronounced trends, with some Na enrichment and mostly unchanged K in the altered rocks but mostly unchanged K and Na concentration in pore fluids relative to seawater. For K these trends imply that leaching and uptake are in close to balance with each other. In contrast, bulk rock chemistry does imply a sink for Na despite relatively little change in the Na content of the pore fluid. To decipher this apparent discrepancy, it may be helpful to point out the differences

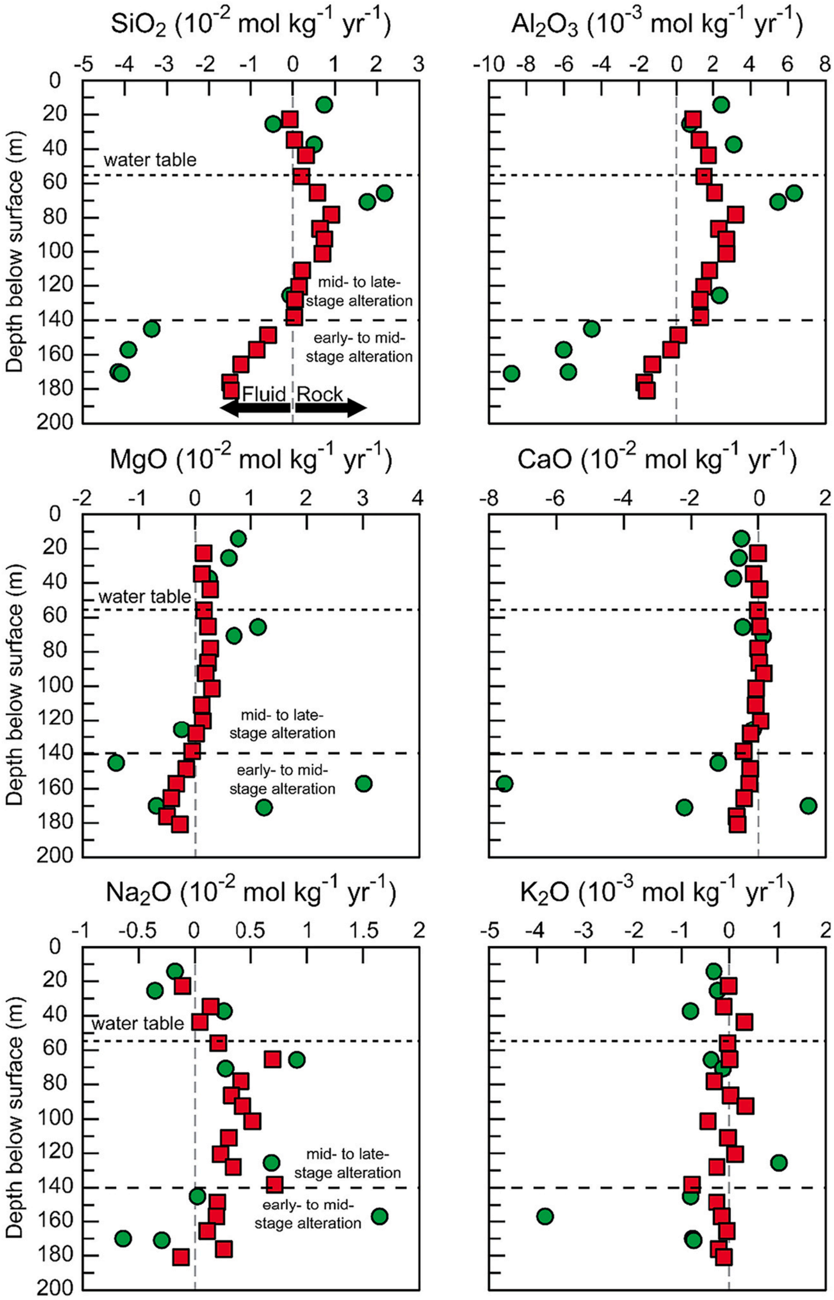

Fig. 9. Annual molar flux estimates for major elements per kg bulk rock. Estimates are based on bulk rock mass balance and the age of the hydrothermal system at the time of drilling of each drill core. Positive values indicate flux from the hydrothermal fluid into the rock and negative values denote fluxes from the rock to the hydrothermal fluid. See Fig. 8 for symbols.

between pore fluid and bulk rock chemical data: The hydrothermal fluid, being a mobile phase, is constantly renewed due to the influx of Na-rich seawater into the system and therefore most closely approximates conditions at the point in time when the fluid sample was retrieved. In contrast, bulk rock mass balance reflects the cumulative effect of water-rock interaction since the inception of the hydrothermal system and therefore more closely approximates the overall budget of alteration history. As such, bulk rock chemistry is likely a better indicator for overall element transfer between the fluid and the tuff over the full course of alteration. Taking into account these considerations, the data presented in Fig. 8 are interpreted to indicate a net long term Na sink for seawater, despite no particular depletion of Na in the pore fluid.

Bulk rock mass changes may be used to perform a first order estimate of annual flux from the rocks to the hydrothermal solution to evaluate the capacity of the Surtsey hydrothermal system for balancing elemental budgets. The submerged parts of the studied boreholes were separated into two sections to constrain the elemental fluxes upon early- to mid-stage alteration and mid- to late-stage alteration. Assuming that the alteration front has propagated downwards >140 m between 1979 and 2017 (Fig. 1; Prause et al., 2020), the section >140 m depth may be considered to be reflective of an earlier stage in the alteration process. For this depth interval, results indicate annual fluxes of about $-5.8{\cdot}10^{-3}$ to $-4.2{\cdot}10^{-2}$ mol SiO_2, $+1.0{\cdot}10^{-4}$ to $-8.8{\cdot}10^{-3}$ mol Al_2O_3, $+1.5{\cdot}10^{-2}$ to $-7.5{\cdot}10^{-2}$ mol CaO, and $-4.9{\cdot}10^{-5}$ to $-3.8{\cdot}10^{-3}$ mol K_2O per 1 kg bulk rock (Fig. 9). As alteration progresses into mid- to late-stage (<140 m), the formation of zeolites, tobermorite and saponite-like clays causes an inversion of the initial fluxes for several elements, triggering the uptake of up to $+2.2{\cdot}10^{-2}$ mol SiO_2, $+6.3{\cdot}10^{-3}$ mol Al_2O_3 and $+1.7{\cdot}10^{-3}$ mol CaO per 1 kg bulk rock.

Molar fluxes for MgO and Na_2O are strongly variable at all stages of alteration. The high mobility of these two elements during palagonitization and their tendency to be incorporated into the most common authigenic phases (analcime, phillipsite and saponite-like clays) complicates annual flux estimates. Overall, combined bulk rock and fluid data suggest that both elements are gained by the rocks over the course of alteration. For Na results indicate a sink of $\leq + 1.6 \cdot 10^{-2}$ mol kg^{-1} yr^{-1}. MgO is generally gained during mid- to late-stage alteration. In the early-stage to mid-stage alteration, depletion of Mg in pore fluids and estimated annual bulk rock gains of MgO ($+1.2 \cdot 10^{-2}$ to $+3.0 \cdot 10^{-2}$ mol kg^{-1} yr^{-1}) exceed the maximum estimated losses ($-1.4 \cdot 10^{-2}$ mol kg^{-1} yr^{-1}) indicating a long-term sink of seawater dissolved Mg.

The assessment of mass flux directions for Ca and Mg supports the findings of Kleine et al. (2020), who estimated the extent of seawater sinks and sources at Surtsey volcano for several dissolved elements and concluded that alteration acts as a significant Ca source for seawater of $+0.2$ to $+129 \cdot 10^{12}$ mol yr^{-1} and a significant Mg sink of -129 to $-0.8 \cdot 10^{12}$ mol yr^{-1}. The fluxes of Si and Al are less well constrained. Both elements show clear signs of mobilization, being released from the rocks in the lower parts of the hydrothermal system and gained at shallower depths. Their enrichment in the pore fluid indicates a net source of these elements for seawater.

Summarily these findings suggest that low-temperature hydrothermal alteration of basaltic tuff at Surtsey acts as a source for seawater Ca, aqueous silica and Al and represents an important sink for dissolved Na and Mg (Fig. 10), which may have important implications for seawater-crust chemical exchange in seamounts (Huang et al., 2018; Mottl and Wheat, 1994; Staudigel, 2014; Wheat and Fisher, 2008; Wheat and Mottl, 2000 and references therein). Our results highlight the importance of future studies on the fluid chemistries of low-temperature basalt hosted systems to accurately quantify annual chemical fluxes associated with this type of environment on a global scale. Such investigations will be invaluable and crucial to improve our understanding of the complex interactions between seawater, oceanic crust and the upper mantle.

6. Conclusions

Alteration of sideromelane at Surtsey volcano is a multi-stage process, which includes the initial leaching of SiO_2, Al_2O_3, MgO, Na_2O, K_2O, CaO, Sr, Rb, V and Ba during palagonitization, followed by a maturation process, which reincorporates SiO_2, Al_2O_3, MgO and K_2O. Other elements, including FeO, TiO_2, REE, Hf, Ta, Zr, Nb and Y were found to be immobile during palagonitization. However, both FeO and TiO_2, were locally mobilized during the maturation process. Estimated volume changes indicate that palagonitization is a non-isovolumetric process that results in minor negative volume changes in the range of −10 to −20 vol%.

Bulk rock elemental fluxes upon water-rock interaction were likewise found to depend on the progress of alteration. During early stages of the alteration process, dominated by palagonitization of sideromelane, SiO_2, Al, Mg and Ca are released from the rocks into the fluid resulting in increased pore water concentrations and net bulk depletion of these elements in the altered rocks. At advanced stages of the alteration, characterized by palagonite maturation and the formation of authigenic minerals, a net uptake of SiO_2, Al, Mg, Ca and Na takes place in the altered rocks. Overall, submarine alteration at Surtsey volcano is found to result in a net long-term source of dissolved Ca, Al and SiO_2 and a net long-term sink of dissolved Mg and Na for seawater.

Author contributions

All authors have read the manuscript and agree to its current state. Conceptualization by SP, TBW, BIK and AS. Data curation by SP, BIK, PM and CR. Methodology by SP, TBW, BIK and AS. Funding acquisition by TBW and AS. Supervision by TBW, AS and BIK. Investigation and writing by all authors.

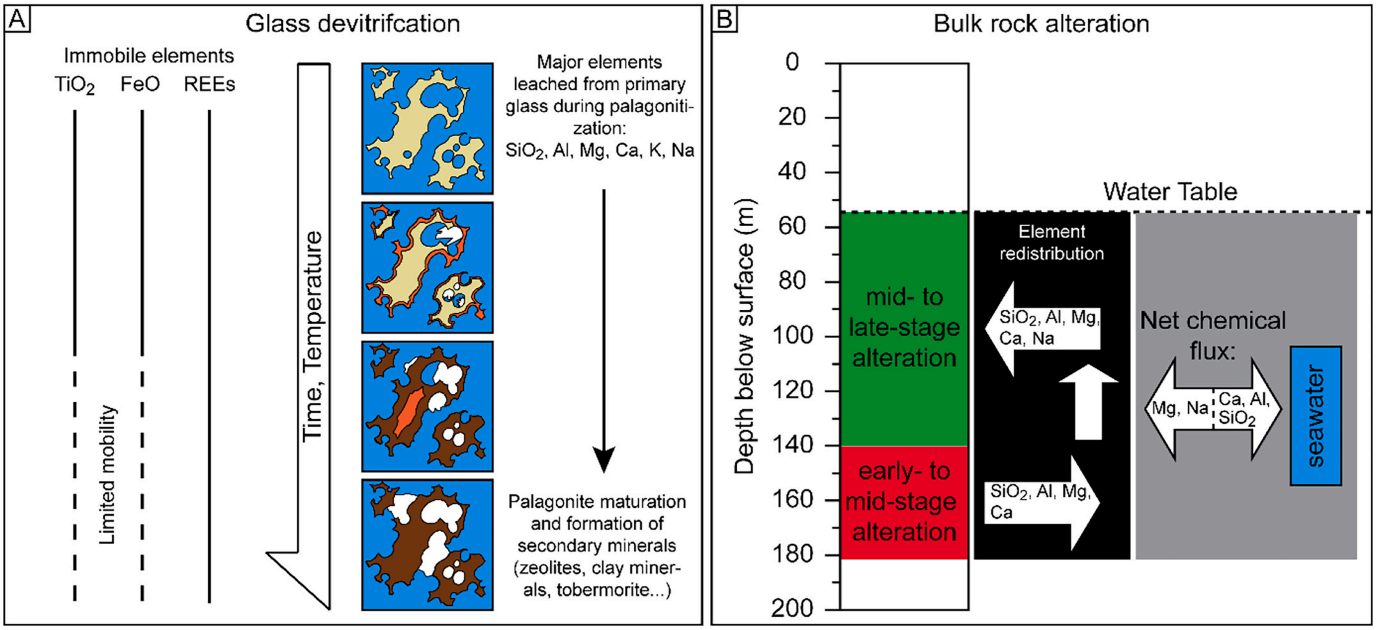

Fig. 10. Conceptual model of basaltic tuff alteration at Surtsey volcano. A) TiO_2 and FeO are immobile during palagonitization but show signs of mobilization on a limited scale during palagonitized glass aging. Rare earth elements, as well as Hf, Ta, Zr, Nb and Y (not shown) are immobile throughout the entire process. In terms of major elements, initial palagonitization releases SiO_2, Al, Mg, Ca, K and Na from the glass. Subsequent maturation of palagonitized glass and formation of secondary minerals recapture these elements at later stages of the alteration process. Reaction progress of the alteration depends to a large degree on time and temperature, proceeding more rapidly at higher temperatures. B) Aqueous silica, Al, Mg and Ca released by early-stage alteration in deeper parts of the system are transported in the enriched hydrothermal fluid to more shallow depths, where they are incorporated into altered tuff by the combined processes of palagonitized glass maturation and secondary mineral formation. The entire process of initial release and subsequent recapture of major elements results in a net sink of Mg and Na as well as a net source for Ca, Al and SiO_2 for seawater.

Declaration of Competing Interest

The authors declare that there are no known conflicts of interest.

Acknowledgements

Funding for this project was provided by the University of Iceland Recruitment fund, the International Continental Scientific Drilling Program (ICDP) through a grant to the SUSTAIN project, the Icelandic Science Fund, ICF-RANNÍS, the Bergen Research Foundation and K.G. Jebsen Centre for Deep Sea Research at University of Bergen, Norway, the German Research Foundation (DFG), and DiSTAR, Federico II, University of Naples, Federico II, Italy. The University of Utah, USA and the two Icelandic power companies Reykjavík Energy and Landsvirkjun, contributed additional funds. Francisco Javier López-Moro provided valuable feedback on the EASYGRESGRANT software. Andreas Klügel and Stefan Sopke are thanked for electron microprobe analyses conducted at the University of Bremen. We thank José Luis Macías for his editorial handling of our manuscript. Two anonymous reviewers are thanked for providing valuable constructive feedback and improvement suggestions on the research presented in this study.

Appendix A. Supplementary data

Supplementary data to this article can be found online at https://doi.org/10.1016/j.jvolgeores.2022.107581.

References

Alt, J.C., 1995. Subseafloor processes in mid-ocean ridge hydrothermal systems. Geophys. Monogr. Ser. 91, 85–114.
Alt, J.C., 2003. Hydrothermal fluxes at mid-ocean ridges and on ridge flanks. Compt. Rendus Geosci. 335, 853–864.
Axelsson, G., Stefánsson, V., Gudmundsson, G., Steingrimsson, B., 1982. Thermal Condition of Surtsey. Surtsey Res. Prog. Rep. 9, 102–110.
Berkgaut, V., Singer, A., Stahr, K., 1994. Palagonite reconsidered: Paracrystalline illite-smectites from regoliths on basic pyroclastics. Clay Clay Miner. 42, 582–592.
Coogan, L.A., Gillis, K.M., 2013. Evidence that low-temperature oceanic hydrothermal systems play an important role in the silicate-carbonate weathering cycle and long-term climate regulation. Geochem. Geophys. Geosyst. 14, 1771–1786.
Crovisier, J.-L., Honnorez, J., Fritz, B., Petit, J.-C., 1992. Dissolution of subglacial volcanic glasses from Iceland: laboratory study and modelling. Appl. Geochem. 7, 55–81.
Crovisier, J.L., Advocat, T., Dussossoy, J.L., 2003. Nature and role of natural alteration gels formed on the surface of ancient volcanic glasses (Natural analogs of waste containment glasses). J. Nucl. Mater. 321, 91–109.
Drief, A., Schiffman, P., 2004. Very low-temperature alteration of sideromelane in hyaloclastites and hyalotuffs from Kilauea and Mauna Kea volcanoes: Implications for the mechanism of palagonite formation. Clay Clay Miner. 52, 623–635.
Fisher, A.T., Wheat, C.G., 2010. Seamounts as conduits for massive fluid, heat, and solute fluxes on ridge flanks. Oceanography 23, 74–87.
Friedman, J.D., Williams, R.S., 1970. Changing patterns of thermal emission from Surtsey, Iceland, between 1966 and 1969. US Geol. Surv. Prof. Pap. 700-D, 116–124.
Furnes, H., 1978. Element mobility during palagonitization of a subglacial hyaloclastite in Iceland. Chem. Geol. 22, 249–264.
Grant, J.A., 1986. The isocon diagram; a simple solution to Gresens' equation for metasomatic alteration. Econ. Geol. 81, 1976–1982.
Hay, R.L., Iijima, A., 1968a. Petrology of palagonite tuffs of Koko Craters, Oahu, Hawaii. Contrib. Mineral. Petrol. 17, 141–154.
Hay, R.L., Iijima, A., 1968b. Nature and origin of palagonite tuffs of the Honolulu Group on Oahu, Hawaii. Geol. Soc. Am. 116, 331–376.
Huang, K.J., Teng, F.Z., Plank, T., Staudigel, H., Hu, Y., Bao, Z.Y., 2018. Magnesium isotopic composition of altered oceanic crust and the global Mg cycle. Geochim. Cosmochim. Acta 238, 357–373.
Ibrahim, K., Hall, A., 1996. The authigenic zeolites of the Aritayn Volcaniclastic Formation, north-East Jordan. Mineral. Deposita 31, 514–522.
Jackson, M.D., Gudmundsson, M.T., Bach, W., Cappelletti, P., Coleman, N.J., Ivarsson, M., Jónasson, K., Jørgensen, S.L., Marteinsson, V., McPhie, J., Moore, J.G., Nielson, D., Rhodes, J.M., Rispoli, C., Schiffman, P., Stefánsson, A., Türke, A., Vanorio, T., Weisenberger, T.B., White, J.D.L., Zierenberg, R., Zimanowski, B., 2015. Time-lapse characterization of hydrothermal seawater and microbial interactions with basaltic tephra at Surtsey Volcano. Sci. Drill. 20, 51–58.
Jackson, M.D., Gudmundsson, M.T., Weisenberger, T.B., Michael Rhodes, J., Stefánsson, A., Kleine, B.I., Lippert, P.C., Marquardt, J.M., Reynolds, H.I., Kück, J., Marteinsson, V.P., Vannier, P., Bach, W., Barich, A., Bergsten, P., Bryce, J.G., Cappelletti, P., Couper, S., Fahnestock, M.F., Gorny, C.F., Grimaldi, C., Groh, M., Gudmundsson, Á., Gunnlaugsson, Á.T., Hamlin, C., Högnadóttir, T., Jónasson, K., Jónsson, S.S., Jørgensen, S.L., Klonowski, A.M., Marshall, B., Massey, E., McPhie, J., Moore, J.G., Ólafsson, E.S., Onstad, S.L., Perez, V., Prause, S., Snorrason, S.P., Türke, A., White, J.D., Zimanowski, B., 2019a. SUSTAIN drilling at Surtsey volcano, Iceland, tracks hydrothermal and microbiological interactions in basalt 50 years after eruption. Sci. Drill. 25, 35–46.
Jackson, M.D., Couper, S., Stan, C.V., Ivarsson, M., Czabaj, M.W., Tamura, N., Parkinson, D., Miyagi, L.M., Moore, J.G., 2019b. Authigenic mineral texture in submarine 1979 basalt drill core, Surtsey volcano, Iceland. Geochem. Geophys. Geosyst. 20, 3751–3773.
Jakobsson, S.P., 1972. On the consolidation and Palagonitization on the Tephra of the Surtsey Volcanic Island, Iceland. Surtsey Res. Prog. Rep. 121–128.
Jakobsson, S.P., 1978. Environmental factors controlling the palagonitization of the Surtsey tephra, Iceland. Bull. Geol. Soc. Denmark 27, 91–105.
Jakobsson, S.P., Moore, J.G., 1982. The Surtsey Research Drilling Project of 1979. Surtsey Res. 9, 76–93.
Jakobsson, S.P., Moore, J.G., 1986. Hydrothermal minerals and alteration rates at Surtsey volcano, Iceland. Geol. Soc. Am. Bull. 97, 648–659.
Jakobsson, S.P., Gudmundsson, G., Moore, J.G., 2000. Geological monitoring of Surtsey, Iceland, 1967-1998. Surtsey Res. 11, 99–108.
Jercinovic, M.J., Keil, K., Smith, M.R., Schmitt, R.A., 1990. Alteration of basaltic glasses from north-Central British Columbia, Canada. Geochim. Cosmochim. Acta 54, 2679–2696.
Jochum, K.P., Weis, U., Stoll, B., Kuzmin, D., Yang, Q., Raczek, I., Jacob, D.E., Stracke, A., Birbaum, K., Frick, D.A., Günther, D., Enzweiler, J., 2011. Determination of reference values for NIST SRM 610-617 glasses following ISO guidelines. Geostand. Geoanal. Res. 35, 397–429.
Kleine, B.I., Stefánsson, A., Kjartansdóttir, R., Prause, S., Weisenberger, T.B., Reynolds, H.I., Sveinbjörnsdóttir, Á.E., Jackson, M.D., Gudmundsson, M.T., 2020. The Surtsey volcano geothermal system: an analogue for seawater-oceanic crust interaction with implications for the elemental budget of the oceanic crust. Chem. Geol. 550, 119702.
Kousehlar, M., Weisenberger, T.B., Tutti, F., Mirnejad, H., 2012. Fluid control on low-temperature mineral formation in volcanic rocks of Kahrizak, Iran. Geofluids 12, 295–311.
López-Moro, F.J., 2012. EASYGRESGRANT - a Microsoft Excel spreadsheet to quantify volume changes and to perform mass-balance modeling in metasomatic systems. Comput. Geosci. 39, 191–196.
MacLean, W.H., 1990. Mass change calculations in altered rock series. Mineral. Deposita 25, 44–49.
Marshall, R.R., 1961. Devitrification of natural glass. Geol. Soc. Am. Bull. 72, 1493–1520.
Matthews, D.H., 1971. III. Weathered and Metamorphosed Basalts. Altered basalts from Swallow Bank, an abyssal hill in the NE Atlantic, and from a nearby seamount. Philos. Trans. R. Soc. Lond. A 268, 551–571.
Moore, J.G., 1966. Rate of palagonitization of submarine basalt adjacent to Hawaii. US Geol. Surv. Prof. Pap. 163–171.
Moore, J.C., Jackson, M.D., 2020. Observations on the structure of Surtsey. Surtsey Res. 14, 33–45.
Mottl, M.J., Wheat, C.G., 1994. Hydrothermal circulation through mid-ocean ridge flanks: Fluxes of heat and magnesium. Geochim. Cosmochim. Acta 58, 2225–2237.
Nielsen, S.G., Rehkämper, M., Teagle, D.A.H., Butterfield, D.A., Alt, J.C., Halliday, A.N., 2006. Hydrothermal fluid fluxes calculated from the isotopic mass balance of thallium in the ocean crust. Earth Planet. Sci. Lett. 251, 120–133.
Pauly, B.D., Schiffman, P., Zierenberg, R.A., Clague, D.A., 2011. Environmental and chemical controls on palagonitization. Geochem. Geophys. Geosyst. 12, Q12017.
Peacock, M.A., 1926. The petrology of Iceland, part 1. The basic tuffs. Trans. R. Soc. Edinburgh 55, 53–76.
Prause, S., Weisenberger, T.B., Cappelletti, P., Grimaldi, C., Rispoli, C., Jónasson, K., Jackson, M.D., Gudmundsson, M.T., 2020. Alteration progress within the Surtsey hydrothermal system, SW Iceland – A time-lapse petrographic study of cores drilled in 1979 and 2017. J. Volcanol. Geotherm. Res. 392, 106754.
Sayyadi, S., Einarsson, P., Gudmundsson, M.T., 2021. Seismic activity associated with the 1963–1967 Surtsey eruption off the coast of South Iceland. Bull. Volcanol. 83, 1–14.
Schipper, C.I., Jakobsson, S.P., White, J.D.L., Palin, J.M., Bush-Marcinowski, T., 2015. The Surtsey Magma Series. Sci. Rep. 5, 11498.
Schipper, C.I., Le Voyer, M., Moussallam, Y., White, J.D.L., Thordarson, T., Kimura, J., Chang, Q., 2016. Degassing and magma mixing during the eruption of Surtsey Volcano (Iceland, 1963–1967): the signatures of a dynamic and discrete rift propagation event. Bull. Volcanol. 78, 33.
Singer, A., 1974. Mineralogy of palagonitic material from the Golan Heights, Israel. Clay Clay Miner. 22, 231–240.
Singer, A., Banin, A., 1990. Characteristics and mode of palagonite - A review. Sci. Géol. Bull. Mém. 88, 173–181.
Staudigel, H., 2003. Hydrothermal alteration processes in the oceanic crust. Treat. Geochem. 3, 511–535.
Staudigel, H., 2014. Chemical fluxes from hydrothermal alteration of the oceanic crust. In: Treatise on Geochemistry, 2nd. Elsevier Ltd, pp. 583–606.
Staudigel, H., Hart, S.R., 1983. Alteration of basaltic glass: Mechanisms and significance for the oceanic crust-seawater budget. Geochim. Cosmochim. Acta 47, 337–350.
Stefánsson, V., Axelsson, G., Sigurdsson, O., Gudmundsson, G., Steingrimsson, B., 1985. Thermal condition of Surtsey. J. Geodyn. 4, 91–106.
Stroncik, N.A., Schmincke, H.-U., 2001. Evolution of palagonite: Crystallization, chemical changes, and element budget. Geochem. Geophys. Geosyst. 2, 2000GC000102.
Stroncik, N.A., Schmincke, H.-U., 2002. Palagonite - a review. Int. J. Earth Sci. 91, 680–697.

Toki, T., Masuda, H., Rashid, H., Hammerschmidt, S., Shinjo, R., 2016. Development of a new method of extraction of interstitial water from low-porosity consolidated sediments recovered during super-deep drilling projects. Geostand. Geoanal. Res. 40, 291–300.

Turekian, K.K., 1968. Oceans. Prentice Hall.

Walton, A.W., Schiffman, P., Macpherson, G.L., 2005. Alteration of hyaloclastites in the HSDP 2 phase 1 Drill Core: 2. Mass balance of the conversion of sideromelane to palagonite and chabazite. Geochem. Geophys. Geosyst. 6, Q09G19.

Warr, L.N., 2021. IMA–CNMNC approved mineral symbols. Mineral. Mag. 85, 291–320.

Weisenberger, T.B., Gudmundsson, M.T., Jackson, M.D., Gorny, C.F., Türke, A., Kleine, B. I., Marshall, B., Jørgensen, S.L., Marteinsson, V.T., Stefánsson, A., White, J.D.L., Barich, A., Bergsten, P., Bryce, J., Couper, S., Fahnestock, M.F., Franzson, H., Grimaldi, C., Groh, M., Gudmundsson, Á., Gunnlaugsson, Á.T., Hamelin, C., Högnadóttir, T., Jónasson, K., Jónsson, S.S., Klonowski, A., Kück, J., Magnússon, R. L., Massey, E., McPhie, J., Ólafsson, E.S., Onstad, S.L., Prause, S., Perez, V., Rhodes, J.M., Snorrason, S.P., 2019. Operational Report for the 2017 Surtsey Underwater volcanic System for Thermophiles, Alteration processes and INnovative Concretes (SUSTAIN) drilling project at Surtsey Volcano, ICDP Operational Report. GFZ Helmholtz-Zentrum Potsdam.

Wheat, C.G., Fisher, A.T., 2008. Massive, low-temperature hydrothermal flow from a basaltic outcrop on 23 Ma seafloor of the Cocos Plate: Chemical constraints and implications. Geochem. Geophys. Geosyst. 9, Q12O14.

Wheat, C.G., Mottl, M.J., 2000. Composition of pore and spring waters from Baby Bare: Global implications of geochemical fluxes from a ridge flank hydrothermal system. Geochim. Cosmochim. Acta 64, 629–642.

Wheat, C.G., Boulegue, J., Mottl, M.J., 1994. A technique for obtaining pore-water chemical composition from indurated and hydrothermally altered sediment and basalt: the ground rock interstitial normative determination (GRIND). Proc., Sci. Results, ODP Leg 139. Middle Val. Juan Fuca Ridge 139, 429–437.

Zhou, Z., Fyfe, W.S., 1989. Palagonitization of basaltic glass from DSDP Site 335, Leg 37: textures, chemical composition, and mechanism of formation. Am. Mineral. 74, 1045–1053.

4 Paper III

Low-temperature seafloor alteration and its impact on the mineralogy and chemical composition of the oceanic crust – A kinetic reaction path model

Simon Prause, Barbara Irene Kleine, Tobias Björn Weisenberger, Andri Stefánsson

Institute of Earth Sciences, University of Iceland, Reykjavík, Iceland

Manuscript to be submitted to *Chemical Geology* (or similar)

4.1 Abstract

Low-temperature seafloor alteration and associated geochemical and petrographic changes may have large effects on the chemical budget of reacted seawater and altered oceanic crust. The extent of these chemical and petrographic changes is dependent on a variety of different parameters, such as temperature and pH of the reacting seawater, crystallinity of the rock and reaction progress (i.e., water-rock ratio). Here, we investigate the impact of these parameters on the forming alteration mineralogy as well as the chemical composition of the reacting fluid upon low-temperature basalt alteration in off-axis environments using a kinetic numerical model. Based on our model, low-temperature (50-150°C) basalt alteration is characterized by four reaction stages: Stage I comprises the incipient dissolution of basaltic glass and primary minerals and is typically short-lived. Stage II marks the formation of simple oxides and hydroxides, Mg-Fe(III)-clays and celadonite. In stage III, carbonates begin to form and Mg-Fe(III)-clays are progressively replaced by Mg-Fe(II)-clays. As alteration progresses into stage IV, alkalinization due to primary phase dissolution eventually exceeds the release of H^+ from secondary mineral formation, causing a sharp rise in pH. Reducing conditions and elevated pH during this stage favor the formation of Mg-Fe(II)-clays and vermiculite over nontronite, leading to the enrichment of Al and significant depletion of Mg in the reacting fluid relative to seawater. Increased Al concentrations in turn favor the formation of zeolite minerals. The decreased redox potential of the solution facilitates the removal of SO_4 through sulfate reduction in addition to anhydrite formation. Variations in temperature and crystallinity had limited effects on the alteration mineralogy at given water-rock ratios, mainly controlling reaction rates and thereby the timescale of seawater-basalt interaction. Water-rock ratio and associated changes in pH were identified as the primary controlling factors of basalt alteration. The findings were further compared to previously reported alteration mineralogy and fluid compositions from ODP/DSDP drilling campaigns. The comparison showed that our kinetic model aligns with fluid geochemical and petrographic observations of natural low-temperature basalt-hosted systems and can reproduce previous estimates on the annual molar fluxes of Si, Ca, Na, SO_4 and Mg at water-rock ratios typical for oceanic crustal aquifers.

4.2 Introduction

Water-rock interaction within the oceanic crust is a fundamental process affecting the chemical and isotopic composition of seawater and the crust as well as contributing to mantle heterogeneity via subduction and recycling of the altered crustal slab (e.g., Coogan and Gillis, 2018; Hart, 1970; Hofmann, 1997; Huang et al., 2018; Kleine et al., 2020, 2022; Liu et al., 2021; Staudigel, 2014). The most extreme chemical changes to fluids and host rocks take place at high temperatures (250-400°C) within hydrothermal systems situated along the Mid-Ocean Ridges (MORs) (Alt, 2003, 1995). Additionally, off-axis hydrothermal systems, where temperatures are ≤150°C, further add to oceanic-crust-seawater interaction. Contributions of low-temperature hydrothermal systems to global flux budgets may in fact exceed those of high-temperature systems, due to their more widespread occurrence, longer periods of activity, high fluid residence times, and higher volumes of water reacting with the rock over the course of the system's active "lifetime" (e.g., Alt, 2003; Coogan and Gillis, 2018; Fisher and Wheat, 2010; Staudigel, 2014; Wheat and Fisher, 2008; Wheat and Mottl, 2000). Water circulation in off-axis environments may continue for up to ~65 ± 10 Ma (Alt, 2003; Stein and Stein, 1994; Wheat and Fisher, 2008) with global annual water flux being as high as ~$6.4 \cdot 10^{14}$ kg yr^{-1}, two orders of magnitude greater than the approximate annual flux of $3.5 \cdot 10^{12}$ kg yr^{-1} estimated for on-axis systems (Staudigel, 2014). For these reasons, even relatively minor chemical changes to water and rock compositions would have significant effects on the composition of seawater and the oceanic crust. Thus, understanding the chemical interaction between seawater and mafic igneous rock under low-grade hydrothermal conditions is crucial to unravel global element fluxes into and out of the oceans.

A significant amount of effort has been made to understand the nature of crust-seawater chemical exchange mainly through the Deep-Sea Drilling Program (DSDP), and the (Integrated) Ocean Drilling Program (ODP/IODP). Most insights into the alteration processes of the oceanic crust have been obtained from studies of core material from DSDP sites 417/418 (Staudigel et al., 1996), ODP/IODP sites 504B/896A (Alt et al., 1996a, 1986; Bach et al., 2003; Teagle et al., 1996), 735B (Bach et al., 2001), and 801/1149 (Alt and Teagle, 2003; Kelley et al., 2003) (Appendix A.1). Based on these studies, basalt alteration at ≤150°C typically involves the formation of Fe-oxyhydroxides, quartz or chalcedony, talc, phyllosilicates like celadonite, saponite and nontronite, various carbonates, zeolites and sulfur containing minerals like pyrite and anhydrite. A calcium-silicate-hydrate phase, such as prehnite, gyrolite or tobermorite, commonly associated with zeolite, has also been reported in several cases (e.g. Alt et al., 1986; Jakobsson and Moore, 1986; Noack, 1983). Although the exact alteration sequence varies between individual sites, Fe-oxyhydroxides, celadonite and nontronite typically form early on under oxidizing conditions and low rock-to-water ratios, whereas pyrite, saponite, zeolites, and carbonates tend to precipitate from more reduced waters at increasingly alkaline pH and higher rock-to-water ratios (Alt et al., 1996a; Alt and Teagle, 2003; Bach et al., 2001; Kleine et al., 2020). Complete or partial replacement of primary igneous minerals, especially olivine, by phyllosilicates and Fe-oxyhydroxides has been reported (Alt et al., 1996a; Bach et al., 2003; Jakobsson and Moore, 1986; Prause et al., 2020). Recorded chemical changes to host rocks during basalt alteration can be highly variable, but often include increases in Fe^{+3}/Fe_{tot}, $\delta^{18}O$, and $^{87}Sr/^{86}Sr$, uptake of H_2O, K, Rb, Cs, U, and C, as well as variable enrichment or depletion of Ca and Mg (Alt et al., 1996a; Alt and Teagle, 2003; Bach et al., 2003, 2001; Huang et al., 2018; Kelley et al., 2003; Kleine et al., 2020; Staudigel, 2014; Teagle et al., 1996).

Modification of seawater composition by water-rock interaction has been observed to be minor to moderate in most cases. Kleine et al. (2020) concluded that hydrothermal waters at Surtsey (Iceland) at temperatures <140°C contained similar concentrations as seawater with respect to Si, Na, Ca, and Cl, whereas B, Mg, F, CO_2, and SO_4 were depleted, and δD and $\delta^{18}O$ were more positive relative to seawater concentrations. More extreme changes in seawater composition were observed at the Baby Bare basement outcrop on the eastern flank of the Juan de Fuca Ridge by Wheat and Mottl (2000). Based on their measurements, these authors have suggested that ridge flank fluxes for Mg, Ca, SO_4, B, and K may even be up to 25% of the riverine flux for these elements and account for the missing high K/Rb sink that is needed to balance global K budgets.

To date, significant uncertainties persist in quantifying the degree of seawater-rock interaction and the magnitude of element exchange. Rock-based estimates are made difficult by the fact that extensively altered lithologies, such as clay-cemented breccias and veins, tend to be highly friable, leading to very poor core recovery and therefore undersampling

(Alt et al., 1996a; Bach et al., 2003; Coogan and Gillis, 2018). Moreover, alteration tends to be inhomogeneous and mostly focused to fissures, cracks and voids so that mass fluxes can easily be over- or underestimated depending on the sampling site (Coogan and Gillis, 2018; Staudigel, 2014). Many rock-based estimates of mass fluxes on MOR flanks have therefore utilized composite samples based on quantitative estimates of the overall bulk rock composition of entire lithological units (e.g., Bach et al., 2003; Kelley et al., 2003). Problems with water-based studies primarily arise from difficulties in locating warm springs in off-axis settings. Consequently, fluid sampling tends to be limited to regions where flow rates are high, which may not be representative of the wider hydrological system (Staudigel, 2014). In addition, water compositions more closely reflect chemical changes that occurred relatively shortly before venting, whereas compositional changes in rocks are influenced to a greater extent by the cumulative effect of alteration over longer periods of time (Staudigel, 2014).

To better assess chemical fluxes resulting from ocean-crust-seawater interaction at low temperatures (≤150°C), these current discrepancies will need to be reconciled. Geochemical modeling may be applied to quantify the process of water-rock interaction as a function of time or extent of reaction. This approach has already been successfully applied to gain insights into the chemical processes occurring at high-temperature systems (e.g., Wetzel and Shock, 2000), predicting mineralogical and fluid geochemical outcomes of serpentinization (e.g., Leong and Shock, 2020), assessing the feasibility of carbon sequestration in basalt-hosted systems (e.g., Gysi and Stefánsson, 2011) or establishing a better understanding of the marine cycle of sulfur and uptake of seawater by the oceanic crust (e.g., Kleine et al., 2020, 2022).

Here, we examine the effects of time, temperature, pH, water-rock ratio, and rock crystallinity on basalt alteration by seawater at low temperatures (≤150°C) by application of kinetic reaction path modeling. The input conditions and parameters were selected in part based on observations from the hydrothermal system of Surtsey, Iceland (Jackson et al., 2019a, 2019b, 2015; Jakobsson and Moore, 1986, 1982; Kleine et al., 2020; Prause et al., 2022, 2020). The intended goal of this study is to improve the understanding of the relative importance of various system parameters, such as temperature, crystallinity, reaction progress, pH, and redox conditions and to provide a framework in which to interpret the petrographic and fluid geochemical outcome of low-temperature hydrothermal basalt alteration.

4.3 Geochemical modeling

The process of water-rock interaction was simulated using reaction path modeling. The calculations involved quantifying the changes in aqueous and mineral composition as a function of the progress of irreversible primary mineral and glass dissolution reactions. The rate of the water-rock interaction processes was assumed to be limited by the dissolution rates of the primary phases, whereas secondary mineral formation reactions were assumed to be faster and allowed to proceed when the respective phase was saturated.

The simulations were conducted with the aid of the PHREEQC geochemical program (Parkhurst and Appelo, 1999), the carbfix.dat thermodynamic database (Voigt et al., 2018) and the carbfix_kin.dat kinetic database (Heřmanská et al., 2022). Equilibrium constants for the endmembers of the zeolite mineral phillipsite were estimated based on their stoichiometric compositions (Appendix A.2). Calculations were carried out at 50-150°C and 1 bar at ≤100°C and water vapor saturation pressures at >100°C. The composition of basalt was assumed to correspond to N-MORB (Gale et al., 2013) with stoichiometric Fe content of the glass adjusted to reflect typical $Fe^{3+}/Fe_{tot} = 0.12$ in MORB glasses (Bézos and Humler, 2005). Both glassy and crystalline rocks were included in the simulations. The relative proportions of primary minerals in the crystalline basalt (Table 4.1) were adjusted assuming end-member solid solution compositions of feldspars, pyroxene, and olivine. The composition of the unreacted fluid was set to reflect standard seawater (Table 4.2) (Millero et al., 2008). The secondary minerals included in the modeling were those commonly observed in association with alteration of basalts in contact with seawater at temperatures ≤150°C (e.g., Alt et al., 1996b; Bach et al., 2003, 2001; Coogan and Gillis, 2018; Kelley et al., 2003; Prause et al., 2020; Staudigel, 2003). These included silicates, oxides, and hydroxides (chalcedony, quartz, brucite, chamosite, goethite, and gibbsite), carbonates (calcite), sulfates and sulfides (anhydrite and pyrite), various phyllosilicates (celadonite, tobermorite, nontronite, vermiculite, montmorillonite, and saponite) as well as zeolites (analcime, chabazite, phillipsite, and laumontite) (Table 4.3).

The effect of changes in pH was studied by varying the CO_2 supply to the system using two scenarios. The "fixed CO_2" scenario approximated open system conditions and an unlimited supply of dissolved CO_2. In this scenario, the initial solution contained 0.01 mol kg^{-1} CO_2 and additional dissolved CO_2 was introduced to the solution whenever concentrations in the fluid became significantly undersaturated ($SI \leq -3$). The "initial CO_2" scenario assumed slightly greater initial concentrations of 0.05 mol kg^{-1} CO_2, but dissolved CO_2 was not replenished and allowed to be consumed by the formation of calcite and/or reduction to CH_4.

The dissolution kinetics of the primary minerals and basaltic glass were calculated based on transition state theory:

$$\mathrm{r} = \mathrm{A^s_m} \sum_\mathrm{i} \left(\mathrm{A_i} a^{\mathrm{n_i}}_{\mathrm{H^+}} \exp\left(-\mathrm{E_{A,i}}/\mathrm{RT}\right)\right) \cdot \prod_\mathrm{j} a_\mathrm{j}^{\mathrm{k_j}} \cdot \left(1 - \mathrm{SI_m^{1/\sigma}}\right) \qquad (1)$$

where $\mathrm{A^s_m}$ is the surface area of *m*-th mineral, A_i stands for pre-exponential factors and subscript i stands for either acidic, neutral, or basic conditions, $\mathrm{a^{n_i}_{H^+}}$ is the activity of the hydrogen ion to the *n*-th power, $E_{A,i}$ is the activation energy in kJ mol^{-1}, $\mathrm{a_j^{k_j}}$ is the activity of the *j*-th aqueous species to the *k*-th power, SI_m is the m-th mineral saturation index and σ stands for Temkin's average stoichiometric number. Values for individual parameters of each primary phase can be found in table 4.1. For basaltic glass the values for the rate expression were adopted from Gíslason and Oelkers (2003) who concluded that $\prod_\mathrm{j} \mathrm{a_j^{k_j}} = \left(\mathrm{a^3_{H^+}}/\mathrm{a_{Al^{+3}}}\right)^{1/3}$. Moreover, the saturation state of basaltic glass was calculated assuming the primary phase to be represented by a leached layer approximated by an amorphous gel consisting of Al-hydroxide and amorphous silica and assuming $\sigma = 1$ (Oelkers and Gíslason, 2001). For primary minerals (fayalite, forsterite, anorthite, albite, K-feldspar, enstatite, diopside), the values for the rate expressions were adopted from

Heřmanská et al. (2022) who fitted available literature data with the above general rate equation, assuming $\prod_j a_j^{k_j} = 1$ and taken values of σ of 1-3 equal to the number of Si in the respective minerals included in this study. In the case of ferrosilite and hedenbergite, no kinetic dissolution rates are currently available. Hence, dissolution rates were adapted and approximated to the rates of enstatite and diopside, respectively.

Mineral reactive surface areas in subsurface and natural settings are generally unknown. Sonnenthal et al. (2005) estimated reactive surface areas of several different types of minerals assuming a cubic array of truncated spheres constituting the rock framework. Resulting values ranged from 10 to100 cm^2 g^{-1}. However, examination of the results of reaction modeling when using mineral surface areas of basaltic rocks within this suggested range indicated dissolution more rapid than observed in natural systems. In fact, reactive surface areas of natural basaltic minerals may be three orders of magnitude smaller or within the range of 0.01 to 0.1 cm^2 g^{-1} (Aradóttir et al., 2012). Following, a uniform value for all mineral and glass surface areas was assigned, corresponding to the average estimated value of 0.05 cm^2 g^{-1}. Moreover, the mineral and glass surface areas were assumed to change as a function of reaction time, assuming spherical particles,

$$\mathrm{A}^{\mathrm{s}}_{\mathrm{m_t}} = \mathrm{A}^{\mathrm{s}}_{\mathrm{m_0}} \cdot (\mathrm{m_t}/\mathrm{m_0})^{2/3} \tag{2}$$

where m_t and m_0 are the moles at time t and initial moles of the primary mineral or basaltic glass, respectively, and $\mathrm{A}^{\mathrm{s}}_{\mathrm{m_t}}$ and $\mathrm{A}^{\mathrm{s}}_{\mathrm{m_0}}$ are the surface area at time t and at the start of the reaction, respectively. The exponent value of 2/3 corresponds to a monodisperse population of isomeric shaped spheres or cubes dissolving uniformly over their entire surface area (Larsen and Postma, 2001). Further details on the estimation of basaltic glass dissolution rates are available in the appendix (A.3).

Table 4.1 *Physical and chemical properties of N-MORB basalt glass (BG) and minerals forming the crystalline rocks, including kinetic parameters.*

			Rate expression							
Primary phase	**%**	**Surface area (cm^2 g^{-1})**	**Acidic mechanism**			**Neutral mechanism**		**Basic mechanism**		
			A_a	**n_a**	**$E_{A,a}$**	**A_b**	**$E_{A,b}$**	**A_c**	**n_c**	**$E_{A,c}$**
Basalt glass[a]	100	0.05	$10^{-5.6}$	-	25.5	$10^{-5.6}$	25.5	$10^{-5.6}$	-	25.5
Crystalline basalt[b]										
Fayalite	5.0	0.05	$1.20 \cdot 10^{6}$	0.44	70.4	-	-	$1.91 \cdot 10^{3}$	0.22	60.9
Forsterite	5.3	0.05	$1.48 \cdot 10^{5}$	0.44	70.4	-	-	$2.20 \cdot 10^{2}$	0.22	60.9
Enstatite	7.1	0.05	0.574	0.5	46.1	$6.3 \cdot 10^{10}$	89.5	-	-	-
Ferrosilite[c]	6.4	0.05	0.574	0.5	46.1	$6.3 \cdot 10^{10}$	89.5	-	-	-
Diopside	11.7	0.05	$8.55 \cdot 10^{-5}$	0.3	32.7	$4.3 \cdot 10^{-5}$	43.9	-	-	-
Hedenbergite[c]	10.8	0.05	$8.55 \cdot 10^{-5}$	0.3	32.7	$4.3 \cdot 10^{-5}$	43.9	-	-	-
Anorthite	30.3	0.05	$9.8 \cdot 10^{4}$	1.22	58.0	0.15	60.0	$1.5 \cdot 10^{-5}$	-0.30	50.0
Albite	23.0	0.05	0.7	0.3	58.0	0.21	60.0	$1.5 \cdot 10^{-5}$	-0.30	50.0
K-Feldspar	0.4	0.05	$5.0 \cdot 10^{-2}$	0.45	51.7	$1.1 \cdot 10^{-2}$	60.0	$1.2 \cdot 10^{-10}$	-0.75	62.0

[a] Full rate expression for the dissolution of basaltic glass available in the appendix.

[b] Values for A_i, n_i, and $E_{A,i}$ retrieved from Heřmanská et al. (2022).

[c] Values for ferrosilite and hedenbergite approximated by enstatite and diopside, respectively.

Table 4.2 *Composition of seawater used in the reaction path modeling (after Millero et al., 2008).*

Element	**Concentration (mmol kg^{-1})**
pH	8.1
HCO_3	1.97
Ca	10.28
Cl	545.87
K	10.21
Mg	52.82
Na	468.97
HS	10^{-4}
SO_4	28.24

Table 4.3 *Primary and secondary minerals included in the reaction path modeling.*

Minerals	**Abbreviation**	**Dissolution reactions**
Primary phases and minerals		
Basalt Glass	BG	$K_{0.004}Na_{0.11}Ca_{0.24}Mg_{0.23}Fe^{2+}{}_{0.14}Fe^{3+}{}_{0.02}Al_{0.35}Si_{1.00}O_{3.222} + 2.444H^+ = 0.35Al^{3+} + 0.24Ca^{2+} + 0.14Fe^{2+} + 0.02Fe^{3+} + 1.222H_2O + 0.004K^+ + 0.23Mg^{2+} + 0.11Na^+ + SiO_2$
Fayalite	Fa	$Fe_2SiO_4 + 4H^+ = SiO_2 + 2Fe^{2+} + 2H_2O$
Forsterite	Fo	$Mg_2SiO_4 + 4H+ = SiO_2 + 2Mg^{2+} + 2H_2O$
Enstatite	En	$MgSiO_3 + 2H^+ = Mg^{2+} + SiO_2 + H_2O$
Ferrosilite	Fs	$FeSiO_3 + 2H^+ = Fe^{2+} + SiO_2 + H_2O$
Diopside	Di	$CaMgSi_2O_6 + 4H^+ = Ca^{2+} + Mg^{2+} + 2SiO_2 + 2H_2O$
Hedenbergite	Hd	$CaFeSi_2O_6 + 4H^+ = Ca^{2+} + Fe^{2+} + 2SiO_2 + 2H_2O$
Anorthite	An	$CaAl_2Si_2O_8 + 8H^+ = Ca^{2+} + 2Al^{3+} + 2SiO_2 + 4H_2O$
Albite	Ab	$NaAlSi_3O_8 + 4H^+ = Al^{3+} + Na^+ + 2H_2O + 3SiO_2$
K-Feldspar	Kfs	$KAlSi_3O_8 + 4H^+ = Al^{3+} + K^+ + 2H_2O + 3SiO_2$
Secondary minerals		
Analcime	Anl	$Na_{0.96}Al_{0.96}Si_{2.04}O_6 \cdot 1H_2O + 3.84H^+ = 0.96Al^{3+} + 2.04\ SiO_2 + 0.96Na^+ + 2.92H_2O$
Anhydrite	Anh	$CaSO_4 = Ca^{2+} + SO_4^{2-}$
Brucite	Brc	$Mg(OH)_2 + 2H^+ = Mg^{2+} + 2H_2O$
Calcite	Cal	$CaCO_3 + H^+ = Ca^{2+} + HCO_3^-$
Celadonite	Cel	$KMgAlSi_4O_{10}(OH)_2 + 6H^+ = Al^{3+} + K^+ + Mg^{2+} + 4H_2O + 4SiO_2$
Chabazite-Ca	Cbz-Ca	$CaAl_2Si_4O_{12} \cdot 6H_2O + 8H^+ = 2Al^{3+} + Ca^{2+} + 4SiO_2 + 10H_2O$
Chabazite-Na	Cbz-Na	$Na_2Al_2Si_4O_{12} \cdot 6H_2O + 8H^+ = 2Al^{3+} + 2Na^+ + 4SiO_2 + 10H_2O$
Chalcedony	Chlc	$SiO_2 = SiO_2$

Table 4.3 *(continued)*

Minerals	**Abbreviation**	**Dissolution reactions**
Chamosite	Chm	$Fe_5Al_2Si_3O_{10}(OH)_8 + 16H^+ = 3SiO_2 + 2Al^{3+} + 5Fe^{2+} + 12H_2O$
Goethite	Gth	$FeOOH + 3H^+ = Fe^{3+} + 2H_2O$
Gibbsite	Gbs	$Al(OH)_3 + 3H^+ = Al^{3+} + 3H_2O$
Laumontite	Lmt	$CaAl_2Si_4O_{12}\cdot 4.5H_2O + 8H^+ = 2Al^{3+} + 4SiO_2 + Ca^{2+} + 8.5H_2O$
Montmorillonite-Ca	Mnt-Ca	$Ca_{0.175}Mg_{0.35}Al_{1.65}Si_4O_{10}(OH)_2 + 6H^+ = 0.175Ca^{2+} +0.35Mg^{2+} + 1.65Al^{3+} + 4H_2O + 4SiO_2$
Montmorillonite-K	Mnt-K	$K_{0.35}Mg_{0.35}Al_{1.65}Si_4O_{10}(OH)_2 + 6H^+ = 0.35K^+ + 0.35Mg^{2+} + 1.65Al^{3+} + 4H_2O + 4SiO_2$
Montmorillonite-Mg	Mnt-Mg	$Mg_{0.525}Al_{1.65}Si_4O_{10}(OH)_2 + 6H^+ = 0.525Mg^{2+} + 1.65Al^{3+} + 4H_2O + 4SiO_2$
Montmorillonite-Na	Mnt-Na	$Na_{0.35}Mg_{0.35}Al_{1.65}Si_4O_{10}(OH)_2 + 6H^+ = 0.35Mg^{2+} + 0.35Na^+ + 1.65Al^{3+} + 4H_2O + 4SiO_2$
Nontronite-Mg	Non-Mg	$Mg_{0.175}Fe_2Al_{0.35}Si_{3.65}H_2O_{12} + +7.4H^+ = 0.175Mg^{2+} + 0.35Al^{3+} + 2Fe^{3+} + 3.65SiO_2 + 4.7H_2O$
Phillipsite-Ca	Php-Ca	$Ca_{0.5}AlSi_3O_8\cdot 3H_2O + 4H^+ = Al^{3+} + 0.5Ca^{2+} + 5H_2O + 3SiO_2$
Phillipsite-K	Php-K	$KAlSi_3O_8\cdot 3H_2O + 4H^+ = Al^{3+} + K^+ + 5H_2O + 3SiO_2$
Phillipsite-Na	Php-Na	$NaAlSi_3O_8\cdot 3H_2O + 4H^+ = Al^{3+} + Na^+ + 5H_2O + 3SiO_2$
Pyrite	Py	$FeS_2 + H_2O = 0.25H^+ + 0.25SO_4^{2-} + Fe^{2+} + 1.75HS^-$
Quartz	Qz	$SiO_2 = SiO_2$
Saponite-Fe-Ca	Sap-Fe-Ca	$Ca_{0.175}Fe_3Al_{0.35}Si_{3.65}O_{10}(OH)_2 + 7.4H^+ = 0.175Ca^{2+} + 0.35Al^{3+} + 3Fe^{2+} + 3.65SiO_2 + 4.7H_2O$
Saponite-Fe-Fe	Sap-Fe-Fe	$Fe_{3.175}Al_{0.35}Si_{3.65}O_{10}(OH)_2 + 7.4H^+ = 0.35Al^{3+} + 3.175Fe^{2+} + 3.65SiO_2 + 4.7H_2O$
Saponite-Fe-K	Sap-Fe-K	$K_{0.35}Fe_3Al_{0.35}Si_{3.65}O_{10}(OH)_2 + 7.4H^+ = 0.35K^+ + 0.35Al^{3+} + 3Fe^{2+} + 3.65SiO_2 + 4.7H_2O$
Saponite-Fe-Mg	Sap-Fe-Mg	$Mg_{0.175}Fe_3Al_{0.35}Si_{3.65}O_{10}(OH)_2 + 7.4H^+ = 0.175Mg^{2+} + 0.35Al^{3+} + 3Fe^{2+} + 3.65SiO_2 + 4.7H_2O$
Saponite-Fe-Na	Sap-Fe-Na	$Na_{0.35}Fe_3Al_{0.35}Si_{3.65}O_{10}(OH)_2 + 7.4H^+ = 0.35Na^+ + 0.35Al^{3+} + 3Fe^{2+} + 3.65SiO_2 + 4.7H_2O$
Saponite-Mg-Ca	Sap-Mg-Ca	$Ca_{0.175}Mg_3Al_{0.35}Si_{3.65}O_{10}(OH)_2 + 7.4H^+ = 0.175Ca^{2+} + 0.35Al^{3+} + 3Mg^{2+} + 3.65SiO_2 + 4.7H_2O$

***Table 4.3** (continued)*

Minerals	Abbreviation	Dissolution reactions
Saponite-Mg-K	Sap-Mg-K	$K_{0.35}Mg_3Al_{0.35}Si_{3.65}O_{10}(OH)_2 + 7.4H^+ = 0.35Al^{3+} + 0.35K^+ + 3Mg^{2+} + 3.65SiO_2 + 4.7H_2O$
Saponite-Mg-Fe	Sap-Mg-Fe	$Fe_{0.175}Mg_3Al_{0.35}Si_{3.65}O_{10}(OH)_2 + 7.4H^+ = 0.175Fe^{2+} + 0.35Al^{3+} + 3Mg^{2+} + 3.65SiO_2 + 4.7H_2O$
Saponite-Mg-Mg	Sap-Mg-Mg	$Mg_{3.175}Al_{0.35}Si_{3.65}O_{10}(OH)_2 + 7.4H^+ = 0.35Al^{3+} + 3.175Mg^{2+} + 3.65SiO_2 + 4.7H_2O$
Saponite-Mg-Na	Sap-Mg-Na	$Na_{0.35}Mg_3Al_{0.35}Si_{3.65}O_{10}(OH)_2 + 7.4H^+ = 0.35Al^{3+} + 0.35Na^+ + 3Mg^{2+} + 3.65SiO_2 + 4.7H_2O$
Tobermorite-11Å	Tbm	$Ca_5Si_6H_{11}O_{22.5} + 10H^+ = 5Ca^{2+} + 6SiO_2 + 10.5H_2O$
Vermiculite-Ca-Mg-Al	Vrm-Ca-Mg-Al	$Ca_{0.4}Mg_{2.5}Al_{1.8}Si_{2.7}O_{10}(OH)_2 + 11.2H^+ = 1.8Al^{3+} + 0.4Ca^{2+} + 6.6H_2O + 2.5Mg^{2+} + 2.7SiO_2$
Vermiculite-Ca-Mg-Fe	Vrm-Ca-Mg-Fe	$Ca_{0.4}Mg_{2.5}Fe_{0.5}Al_{1.3}Si_{2.7}O_{10}(OH)_2 + 11.2H^+ =1.3Al^{3+} + 0.4Ca^{2+} + 0.5Fe^{3+} + 6.6H_2O + 2.5Mg^{2+} + 2.7SiO_2$
Vermiculite-K-Mg-Al	Vrm-K-Mg-Al	$K_{0.8}Mg_{2.5}Al_{1.8}Si_{2.7}O10(OH)_2 + 11.2H^+ = 1.8Al^{3+} + 6.6H_2O + 0.8K^+ + 2.5Mg^{2+} + 2.7SiO_2$
Vermiculite-K-Mg-Fe	Vrm-K-Mg-Fe	$K_{0.8}Mg_{2.5}Fe_{0.5}Al_{1.3}Si_{2.7}O_{10}(OH)_2 + 11.2H^+ = 1.3Al^{3+} + 0.5Fe^{3+} + 6.6H_2O + 0.8K^+ + 2.5Mg^{2+} + 2.7SiO_2$
Vermiculite-Na-Mg-Al	Vrm-Na-Mg-Al	$Na_{0.8}Mg_{2.5}Al_{1.8}Si_{2.7}O_{10}(OH)_2 + 11.2H^+ =1.8Al^{3+} + 6.6\ H_2O + 2.5Mg^{2+} + 0.8Na^+ + 2.7SiO_2$
Vermiculite-Na-Mg-Fe	Vrm-Na-Mg-Fe	$Na_{0.8}Mg_{2.5}Fe_{0.5}Al_{1.3}Si_{2.7}O_{10}(OH)_2 + 11.2H^+ = 1.3Al^{3+} + 0.5Fe^{3+} + 6.6H_2O + 2.5Mg^{2+} + 0.8Na^+ + 2.7SiO_2$
Vermiculite-Mg-Mg-Al	Vrm-Mg-Mg-Al	$Mg_{2.9}Al_{1.8}Si_{2.7}O_{10}(OH)_2 + 11.2H^+ = 1.8Al^{3+} + 6.6H_2O + 2.9Mg^{2+} + 2.7SiO_2$
Vermiculite-Mg-Mg-Fe	Vrm-Mg-Mg-Fe	$Mg_{2.9}Fe_{0.5}Al_{1.3}Si_{2.7}O_{10}(OH)_2 + 11.2H^+ = 1.3Al^{3+} + 0.5Fe^{3+} + 6.6H_2O + 2.9Mg^{2+} + 2.7SiO_2$

4.4 Results

4.4.1 General reaction progress

To investigate and quantify the reaction between basalts and seawater at low temperatures, kinetic reaction path modeling was conducted for glassy and crystalline rocks, for closed and open-source input of CO_2, and as a function of temperature. In general, with increasing reaction time, the amount of basalt dissolved, i.e., the "rock-to-water-ratio", increased, leading to increased concentrations of dissolved elements (Figs. 4.1-4.3). As a result, secondary minerals became saturated. Initially, Mg-Fe(III)-phyllosilicates like nontronite and vermiculite formed together with montmorillonite and celadonite in some cases. These phases were eventually followed by zeolites like phillipsite, chabazite, analcime and tobermorite at higher rock-to-water ratios (Fig. 4.4). Further phases found to form according to the calculations included calcite, anhydrite and pyrite.

The chemical composition of seawater changed with reaction time. Overall, the effects of basalt alteration on Ca, Na and K concentrations were minor. Sulfate concentrations tended to decrease with progressing reaction, owing to the formation of anhydrite as well as reduction of SO_4 to H_2S. Restricted CO_2 supply in the initial CO_2 scenario was found to cause more extensive SO_4 depletion due to decreased competition between sulfate and carbonate for available Ca in solution. The concentration of Mg rapidly decreased with progressing reaction and was found to be linked to redox conditions and the composition of the clay mineral assemblage, due to increased Mg uptake upon the formation of Mg-rich clays at high rock-to-water-ratios. Concentrations of Al remained initially low, but sharply increased with progressive basalt alteration due to increasing pH and the associated change in the clay mineral assemblage when Mg-Fe(III)-clays were progressively replaced by ferrous iron bearing saponite. Elevated Al concentrations, in turn, provided conditions favorable for the precipitation of zeolite minerals. Consequently, Al concentrations at high rock-to-water ratios were kept stable primarily by the formation of zeolites. During the initial stages of the reaction, comprising the dissolution of primary phases and the formation of early secondary minerals at mildly acidic to neutral pH, both Fe^{3+} and Fe^{2+} accumulated in the fluid. The Fe^{3+}/Fe_{tot} ratio of the fluid was affected by the interplay of the significantly greater release of Fe^{2+} as opposed to Fe^{3+} from primary phase dissolution, oxidizing redox conditions, and the removal of Fe^{3+} from solution by the formation of nontronite and vermiculite. The combination of these factors caused Fe^{3+}/Fe_{tot} to either remain stable or slightly rise with reaction progress during early water-rock interaction. As pH became more alkaline and redox potential decreased (Fig. 4.1), a portion of the ferrous iron in solution was removed by the formation of saponite, causing an overall decrease in Fe^{2+} concentrations. At high rock-water ratios and alkaline pH, the combined processes of Fe release from primary phase breakdown, followed by Fe oxidation and Fe^{2+} removal by saponite resulted in stable Fe^{3+}/Fe_{tot} ratios up to several orders of magnitude higher than at the start of the reactions. Overall, Fe_{tot} concentrations underwent minor enrichment in the fluid over the cause of the reactions with minor decreases associated with the replacement of Mg-Fe(III)-clays by Mg-Fe(II)-clays.

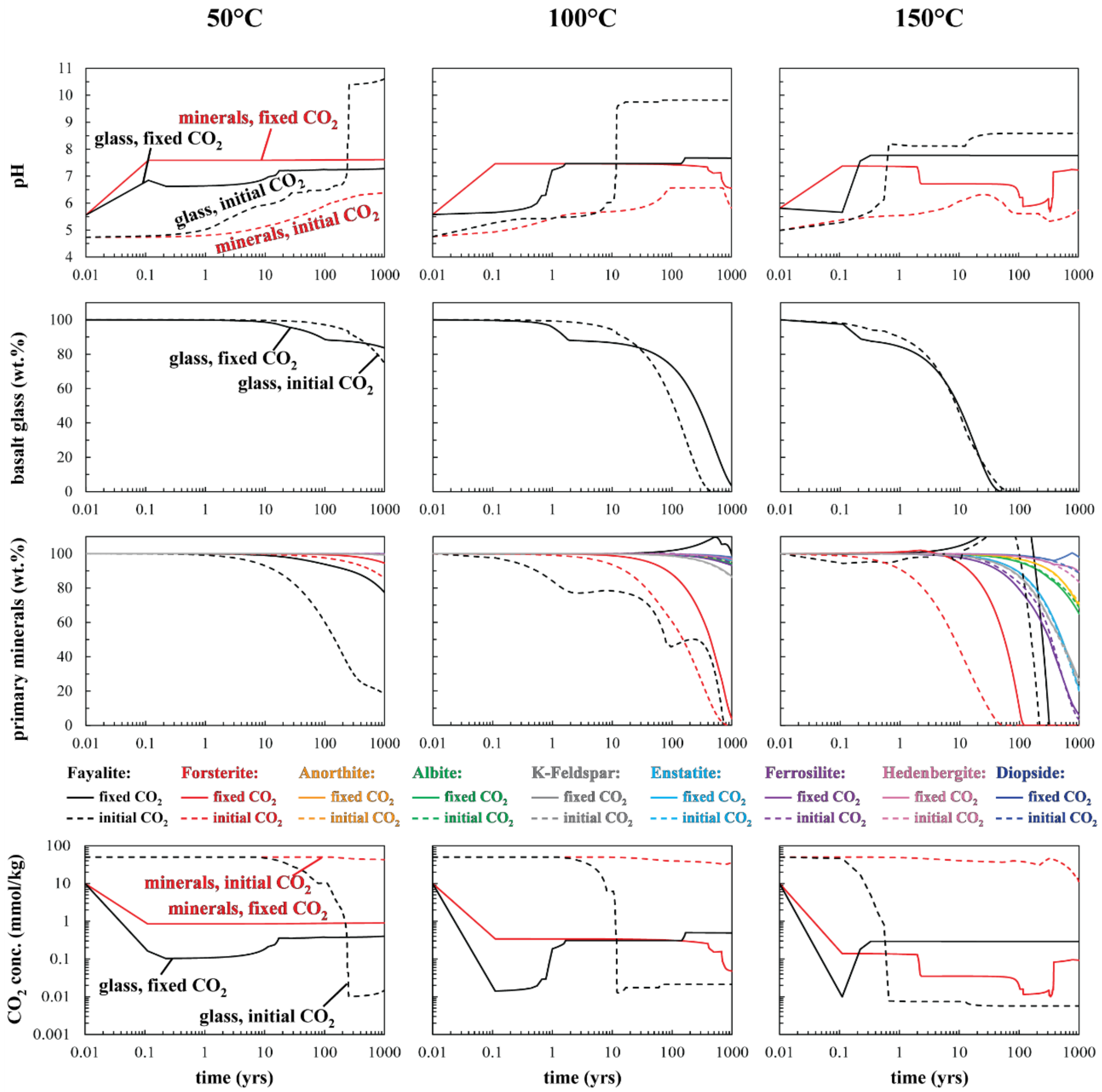

Figure 4.1 *Changes in pH, relative amounts of primary phases, and concentrations of CO2 at 50, 100, and 150°C.*

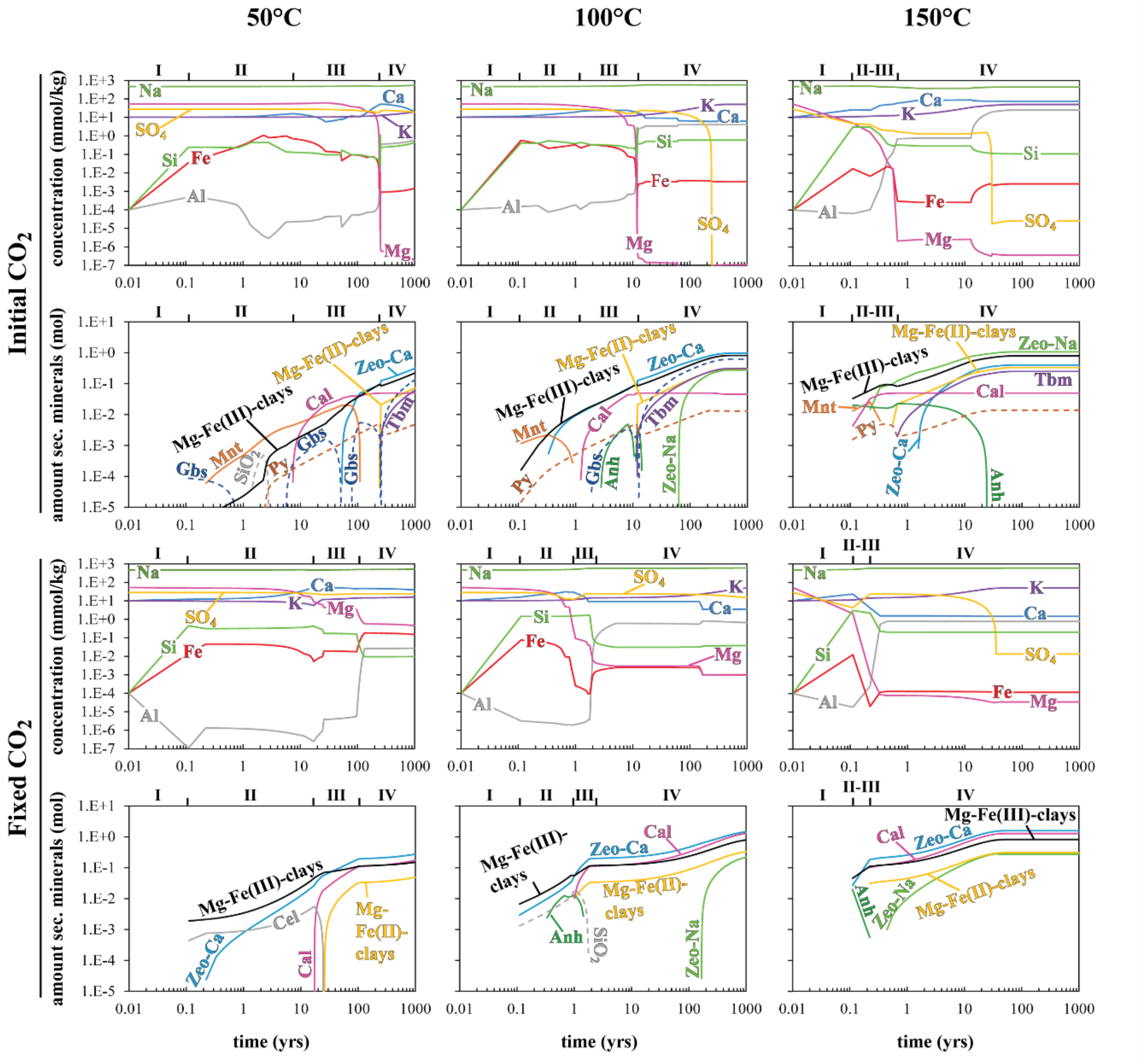

Figure 4.2 *Fluid compositions and amounts of secondary minerals as a function of time for glass dissolution at 50, 100, and 150°C. Roman numerals indicate reaction stage (see 4.5.1 for details). For mineral abbreviations see table 4.3.*

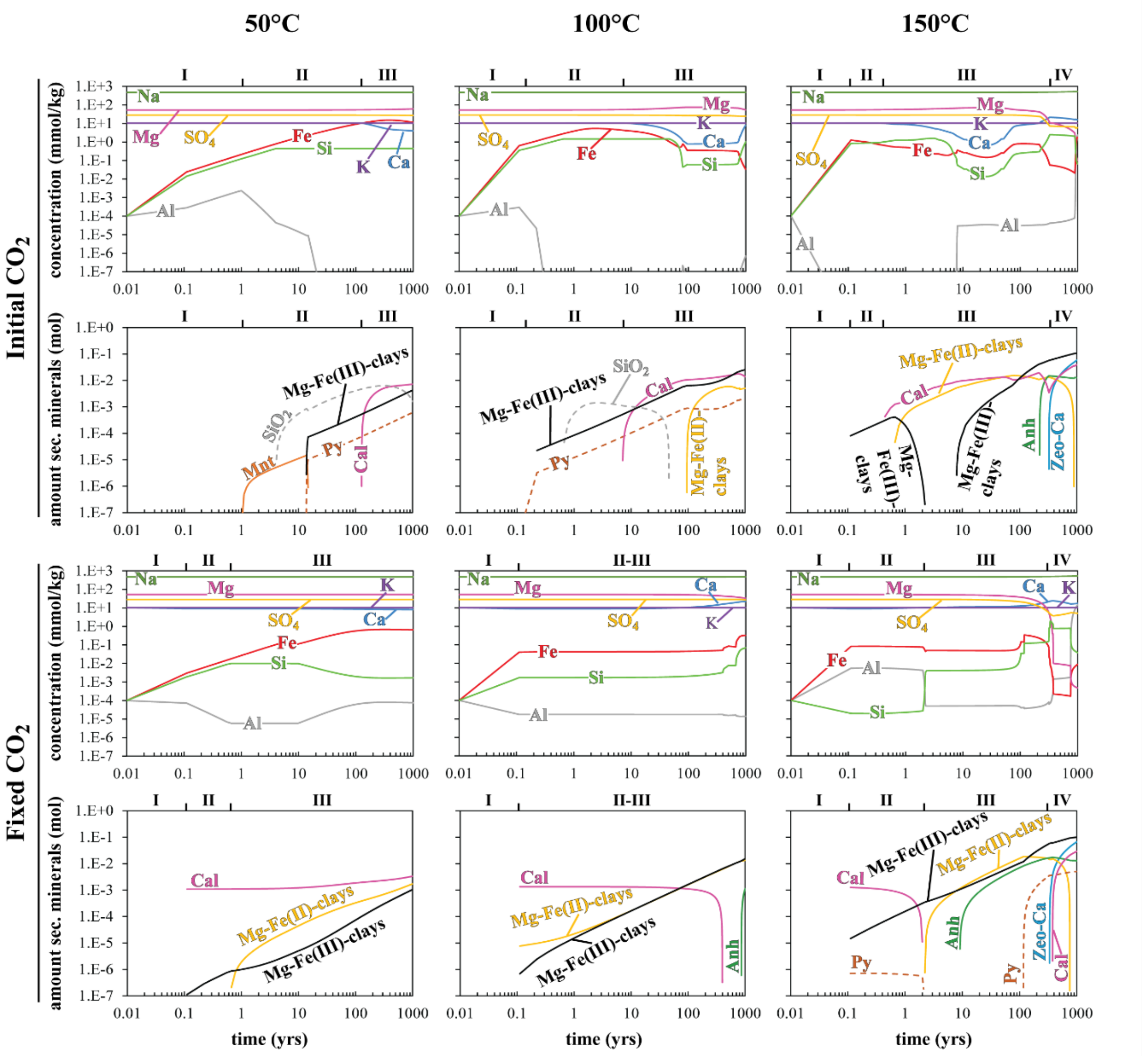

Figure 4.3 *Fluid compositions and amounts of secondary minerals as a function of time for mineral dissolution at 50, 100, and 150°C. Roman numerals indicate reaction stage (see 4.5.1 for details). For mineral abbreviations see table 4.3.*

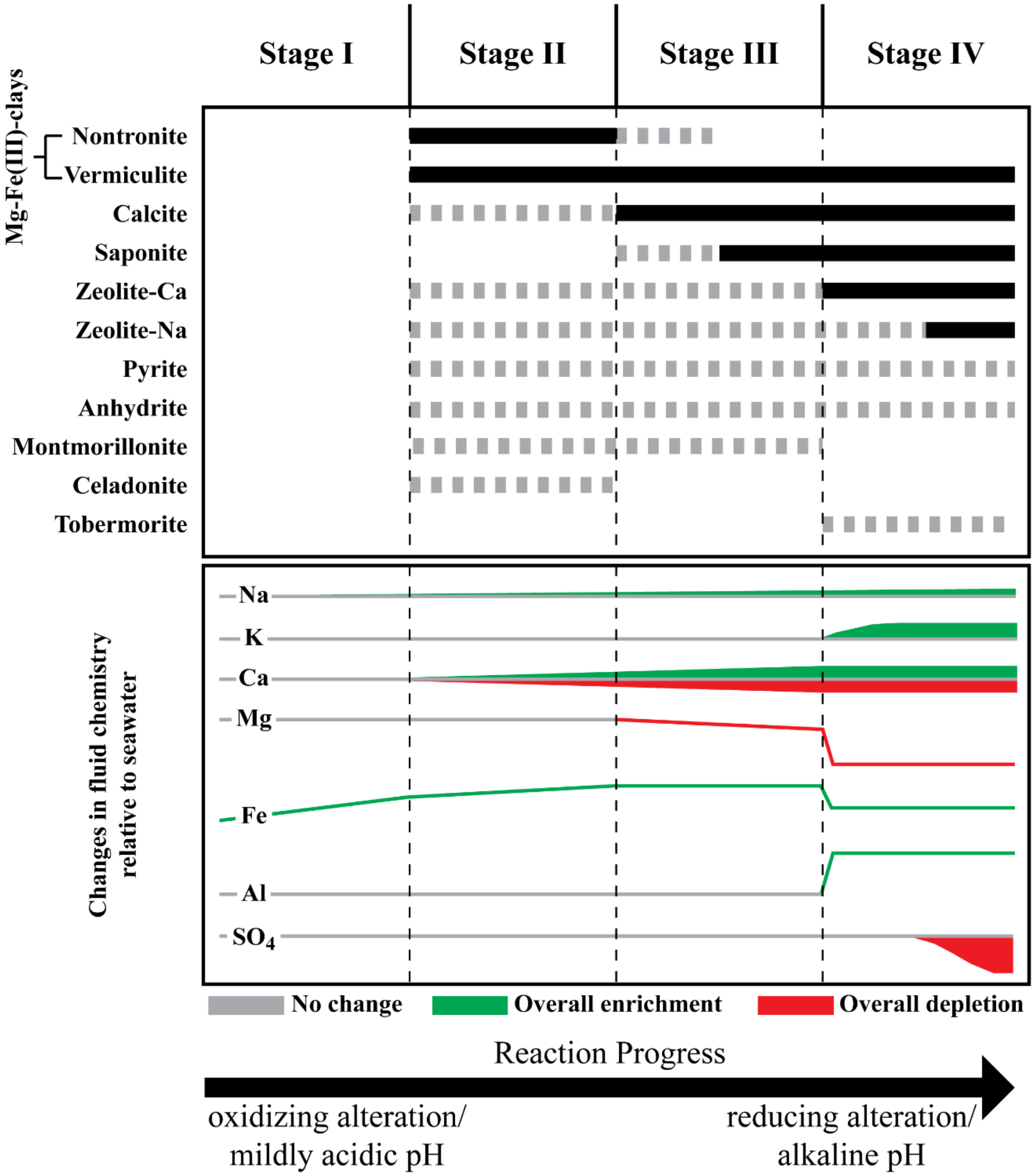

Figure 4.4 *Schematic outline of the effects of reaction progress on secondary mineral assemblage and fluid composition. Crystalline and glassy basalts progress through a similar series of reactions that can be divided into four stages: I) primary phase dissolution, II) early formation of Mg-Fe(III)-clays and other phyllosilicates as well as minor amounts of simple oxides and hydroxides (not shown), III) precipitation of calcite and partial replacement of Mg-Fe(III)-clays by Mg-Fe(II)-clays (e.g., saponite) and IV) increased formation of zeolite minerals at elevated pH and reduced conditions. Changes in fluid chemistry are displayed relative to seawater below alteration mineralogy. In cases where changes in fluid chemistry were found to be variable, trends are displayed as shaded areas rather than lines. Note that vertical alignment of dissolved species does not correspond to relative concentrations.*

4.4.2 pH and redox

Progressive basalt-seawater interaction resulted in pH increase (Fig. 4.1). Inspection of the results revealed that various mineral assemblages formed under certain pH conditions. Initially, the pH was generally mildly acidic, but rose to circumneutral and eventually alkaline values with increasing basalt dissolution. The dissolution of higher quantities of basalt was required to increase the pH for systems open for CO_2 and for crystalline basalts. At mildly acidic to circumneutral pH values, the secondary mineral assemblage was usually dominated by Mg-Fe(III)-clays as well as simple oxides and hydroxides like gibbsite and silica. At elevated pH, other minerals like pyrite, anhydrite, calcite, Mg-Fe(II)-clays, and eventually zeolites became increasingly important.

The redox state was also observed to change as a function of reaction progress. Initially, the system was oxidized but became increasingly reduced with increasing basaltic glass and primary mineral dissolution, as well as pH increase. This resulted in reduction of S^{6+} to S^{2-} and subsequent formation of pyrite as well as a partial shift in the oxidation state of iron-bearing minerals from Fe^{3+} to Fe^{2+}.

4.4.3 Temperature

The effects of temperatures on type and amount of secondary mineral formation were generally minor. Basalt-seawater interaction at 50-150°C resulted in near identical secondary mineralogy independent of temperature (Figs. 4.2 and 4.3). However, temperature highly influenced the reaction kinetics, with the dissolution rates of the glassy and primary minerals increasing by several orders of magnitude from 50 to 150°C (Fig. 4.1).

4.4.4 Rock crystallinity

The elemental leaching upon rock dissolution proceeded differently for crystalline and glassy basalts: Basaltic glass dissolved stoichiometrically relative to bulk rock composition. In contrast, crystalline basalt dissolved non-stoichiometrically, because dissolution rates varied between individual primary minerals. In general, olivine dissolved fastest, followed by plagioclase and pyroxene (Fig. 4.1). Moreover, pH increase was slower as a function of time for crystalline basalt due to overall slower dissolution rates. The pH of the reacted solution tended to be slightly less alkaline for crystalline basalt than for basaltic glass. Initial interaction between crystalline basalt and seawater caused the early formation of Mg-Fe-bearing clays, calcite, silica, and pyrite (Fig. 4.3). Basaltic glass dissolution yielded an overall similar early secondary mineral assemblage (Fig. 4.2). However, glass dissolution resulted in a more widespread abundance of zeolites, anhydrite, gibbsite and, more rarely, celadonite during the early reaction stages, likely due to the comparatively greater initial release of Al and Ca. Conversely, the initial dissolution of crystalline basalt primarily released Si, Mg, and Fe from the early breakdown of olivine, thus preventing the early formation of Al- and Ca-bearing phases. Regardless of crystallinity, progressive basalt dissolution resulted in increasingly reduced redox conditions that led to the partial replacement of Mg-Fe(III)-clays by Mg-Fe(II)-clays and pyrite, which in turn reduced the system’s ability to remove Al from solution, necessitating increased formation of zeolites at later stages of the reaction.

4.5 Discussion

4.5.1 Controls of basalt-seawater interaction

The interaction of basalts with seawater caused complex changes in seawater composition and alteration mineralogy as a function of reaction progress or reaction time. Inspection of the geochemical modeling results revealed that two factors were most important, pH and the amount of basalt that has reacted, here defined by the rock-to-water ratio. In addition, temperature and crystallinity were also important.

The overall basalt-seawater reactions were incongruent, whereas the progress of the reactions and type of alteration minerals followed common steps or stages (Fig. 4.4). The first reaction stage was characterized by the interaction of the basaltic glass or primary minerals with seawater and H^+, leaching aqueous species to the solution. The hydrothermal seawater contained acids, for example CO_2, that resulted in H^+ generation via ionization reactions of the kind:

$$CO_{2(aq)} + H_2O \leftrightarrow H^+ + HCO_3^- \qquad (3)$$

Parallel, irreversible dissolution of the primary minerals and basaltic glasses in the host rocks occurred, consuming H^+ and resulting in increased water pH, for example, as described by the reaction of pyroxenes and feldspars:

$$CaMgSi_2O_{6(diopside)} + 4H^+ \rightarrow Mg^{2+} + Ca^{2+} + 2H_2O + 2SiO_{2(aq)} \qquad (4)$$

$$CaAl_2Si_2O_{8(anorthite)} + 8H^+ \rightarrow Ca^{2+} + 2Al^{3+} + 4H_2O + 2SiO_{2(aq)} \qquad (5)$$

Upon progressive leaching of basaltic glass and primary minerals, the waters eventually became saturated with secondary minerals. Thus, the second stage of the reactions was the first appearance of secondary minerals. Typically, these were oxides and hydroxides as well as Mg-Fe(III)-clays (nontronite and vermiculite):

$$\begin{aligned} &0.175Mg^{2+} + 0.35Al^{3+} + 2Fe^{3+} + 3.65SiO_{2(aq)} + 4.7H_2O \\ &\quad \leftrightarrow Mg_{0.175}Fe_2Al_{0.35}Si_{3.65}H_2O_{12(nontronite)} + 7.4H^+ \qquad (6) \end{aligned}$$

$$1.3Al^{3+} + 0.5Fe^{3+} + 6.6H_2O + 0.8K^+ + 2.5Mg^{2+} + 2.7SiO_{2(aq)}$$

$$\leftrightarrow K_{0.8}Mg_{2.5}Fe_{0.5}Al_{1.3}Si_{2.7}O_{10}(OH)_{2(vermiculite)} + 11.2H^+ \tag{7}$$

In addition to Mg and Fe, these clays may contain varying amounts of other cations like Na, Ca, and K. During the first two stages, the seawater pH was buffered at mildly acidic to circumneutral values by dissolved acids, i.e., CO_2, the consumption of H^+ upon basaltic glass and primary mineral dissolution, and the release of H^+ upon secondary mineral formation.

The third stage was characterized by a shift in the alteration mineral assemblage with the addition of calcite and replacement of nontronite by Mg-Fe(II)-clays such as saponite

$$0.175Mg^{2+} + 3Fe^{2+} + 0.35Al^{3+} + 3.65SiO_{2(aq)} + 4.7H_2O$$

$$\leftrightarrow Mg_{0.175}Fe_3Al_{0.35}Si_{3.65}O_{10}(OH)_{2(saponite)} + 7.4H^+ \tag{8}$$

$$Ca^{2+} + HCO_3{}^- \leftrightarrow CaCO_{3(calcite)} + H^+ \tag{9}$$

The formation of calcite was strongly influenced by the availability of CO_2. The progressive consumption of H^+ by the dissolution of primary phases eventually shifted pH to more alkaline values. Additionally, the reactions resulted in the modified seawater becoming progressively more reduced due to hydrolyzed induced oxidation of iron (Ricci et al., 2022), causing the formation of trace levels of H_2 and reduction of S^{6+} to S^{2-} as well as the formation of pyrite.

Eventually, the combined seawater-basalt reactions and pH resulted in the modified seawater becoming saturated with respect to Na- and Ca-containing zeolites and, in some cases, tobermorite characteristic for the last reaction stage:

$$0.96Al^{3+} + 2.04SiO_{2(aq)} + 0.96Na^+ + 2.92H_2O$$

$$\leftrightarrow Na_{0.96}Al_{0.96}Si_{2.04}O_6 \cdot H_2O_{(analcime)} + 3.84H^+ \tag{10}$$

$$Al^{3+} + 0.5Ca^{2+} + 3SiO_2 + 5H_2O$$

$$\leftrightarrow Ca_{0.5}AlSi_3O_8 \cdot 3H_2O_{(phillipsite)} + 4H^+ \tag{11}$$

$$5Ca^{2+} + 6SiO_2 + 10.5H_2O \leftrightarrow Ca_5Si_6H_{11}O_{22.5(\text{tobermorite})} + 10H^+ \quad (12)$$

Temperatures and rock crystallinity were not observed to change this general reaction progress with time. Similar secondary mineral assemblages were formed in the same order at all temperatures for both crystalline basalt and basaltic glass. However, the overall reaction rate was strongly dependent on temperature, with the mineral replacement reactions occurring much faster at 150°C than at 50°C.

4.5.2 Comparison of modeling results with observations from natural systems

Modeling results can be benchmarked against natural systems spanning a wide range of age and alteration environments, as well as variable abundances of basalt glass versus crystalline mafic rock. The locations considered here include Surtsey (Iceland), ODP/IODP Hole 504B (south of the Costa Rica Rift Zone) and ODP/IODP Site 801C (Central Pigafetta Basin, Western Pacific) (Appendix A.1).

The island of Surtsey (Iceland) hosts a young (~55 years) seawater-dominated low-temperature geothermal system. It provides an ideal comparison with our modeling results since temperature, duration of the alteration process, and secondary mineral assemblages are well documented and characterized (e.g., Friedman and Williams, 1970; Jakobsson and Moore, 1986; Prause et al., 2020, 2022; Jackson et al., 2019a, 2019b; Weisenberger et al., 2019; Kleine et al., 2020). The hydrothermal waters at Surtsey have temperatures of ~50-140°C, are sourced from seawater and have been modified by interaction with the basaltic host rocks to elevated Na, K, Ca, Fe, and Al, and depleted Mg, CO_2 and SO_4 concentrations relative to seawater (Kleine et al. 2020). Alteration has progressed over a period of over 50 years. Based on poorly altered subsurface samples from 1979, early-stage alteration phases included minor clays, phillipsite, anhydrite and calcite. As of 2017, after ~50 years of hydrothermal alteration, a great extent of basaltic glass alteration was observed as well as significant amounts of secondary minerals including analcime, phillipsite and tobermorite (Prause et al., 2020). Overall, the observed seawater chemistry and alteration mineralogy at Surtsey are compatible with our modeling results. The presence of the Na-zeolite analcime, tobermorite and minor calcite reflects evolved alteration, characterized by significantly elevated rock-to-water-ratio and alkaline pH (Fig. 4.4, stage IV). Moreover, observations at Surtsey indicate decreased mobility of elements like Si, Mg, Na, and Ca with increasing extent of alteration (Prause et al., 2022), in line with modeling results (Fig. 4.5).

ODP/IODP Hole 504B, situated in ~6.6 Ma old crust 200 km south of the Costa Rica Rift Zone, penetrates 2111 m through pelagic sediments and the underlying basement (Bach et al., 2003). It is one of the most well-studied locations for seafloor hydrothermal alteration worldwide. Basement lithostratigraphic units include a pillow-rich volcanic section, a transition zone containing heavily brecciated flows, pillows and dikes, and a sheeted dike complex (Alt et al., 1996a; Bach et al., 2003). The volcanic section has been overprinted by alteration mineralogy upon water-rock interaction at ~25-60°C (Bach et al., 2003). At shallow depths (<200 m) the alteration sequence is marked by celadonite, which is succeeded by saponite, calcite and phillipsite (Alt et al., 1996a). At greater depths (>200 m) the secondary mineralogy is dominated by saponite, smectite-chlorite mixed layers, pyrite, quartz, minor anhydrite, and calcite. Talc and Na-zeolite occur infrequently throughout both zones. Minor amounts of Ca-zeolite (laumontite) first appear towards the bottom of the volcanic section and increase in abundance in the underlying transition zone. The disappearance of celadonite in the lower volcanic zone, combined with the presence of saponite, calcite, anhydrite, and Na-zeolite, is consistent with our model results and presumably reflective of minor to moderate alteration at shallow levels, followed by progressively higher rock-water ratio.

ODP/IODP Site 801C is located in the Central Pigafetta Basin, Western Pacific, in Jurassic (170 Ma) crust generated at a fast spreading ridge (Alt et al., 1992; Alt and Teagle, 2003). Underneath the ~460 m thick sediment cover, the basement consists mostly of >400 m of pillow basalts, flows, intrusions, and heavily brecciated rock (Alt and Teagle, 2003). Hydrothermal alteration took place at ~5-100°C, with higher temperatures towards the bottom of the hole (Alt and Teagle, 2003). The majority of rocks are lightly altered. The most common alteration phases include saponite, Fe-oxyhydroxides, and calcite, as well as celadonite and pyrite (Alt and Teagle, 2003). The nature of the secondary mineral paragenesis in these slightly altered rocks is consistent with geochemical modeling, which indicated that celadonite should be among the earliest reaction products, precipitating at low rock-to-water ratios and low temperatures together with nontronite and vermiculite. The latter two minerals are, however, not documented in Hole 801C, despite inferred oxidizing conditions and thus greater expected supply of ferric iron. Instead, most Fe^{3+} is likely incorporated into Fe-oxyhydroxides, in similar fashion to the upper volcanic section at ODP/IODP site 504B. Such Fe-oxyhydroxides have been predicated to be among the major alteration minerals upon basalt interaction with meteoric water (e.g., Stefánsson, 2010; Gysi and Stefánsson, 2011). The most extensively altered rocks at Hole 801C also contained Na-zeolites consistent with the effects of more advanced basalt alteration predicted by our model (Figs. 4.2-4.4).

Overall, our geochemical model reproduces the alteration mineralogy and mineral sequences in low-temperature seafloor systems (Alt et al., 1996a; Alt and Teagle, 2003; Kleine et al., 2022, 2020; Prause et al., 2020). In addition, our geochemical modeling results reveal that such low-temperature seafloor alteration may be a relatively short-term process that may occur within less than 1000 years. Decreasing temperatures upon cooling of the crust may, however, slow down the reactions and preserve low-temperature mineral parageneses formed at relatively higher temperatures in the vicinity of Mid-Ocean Ridges.

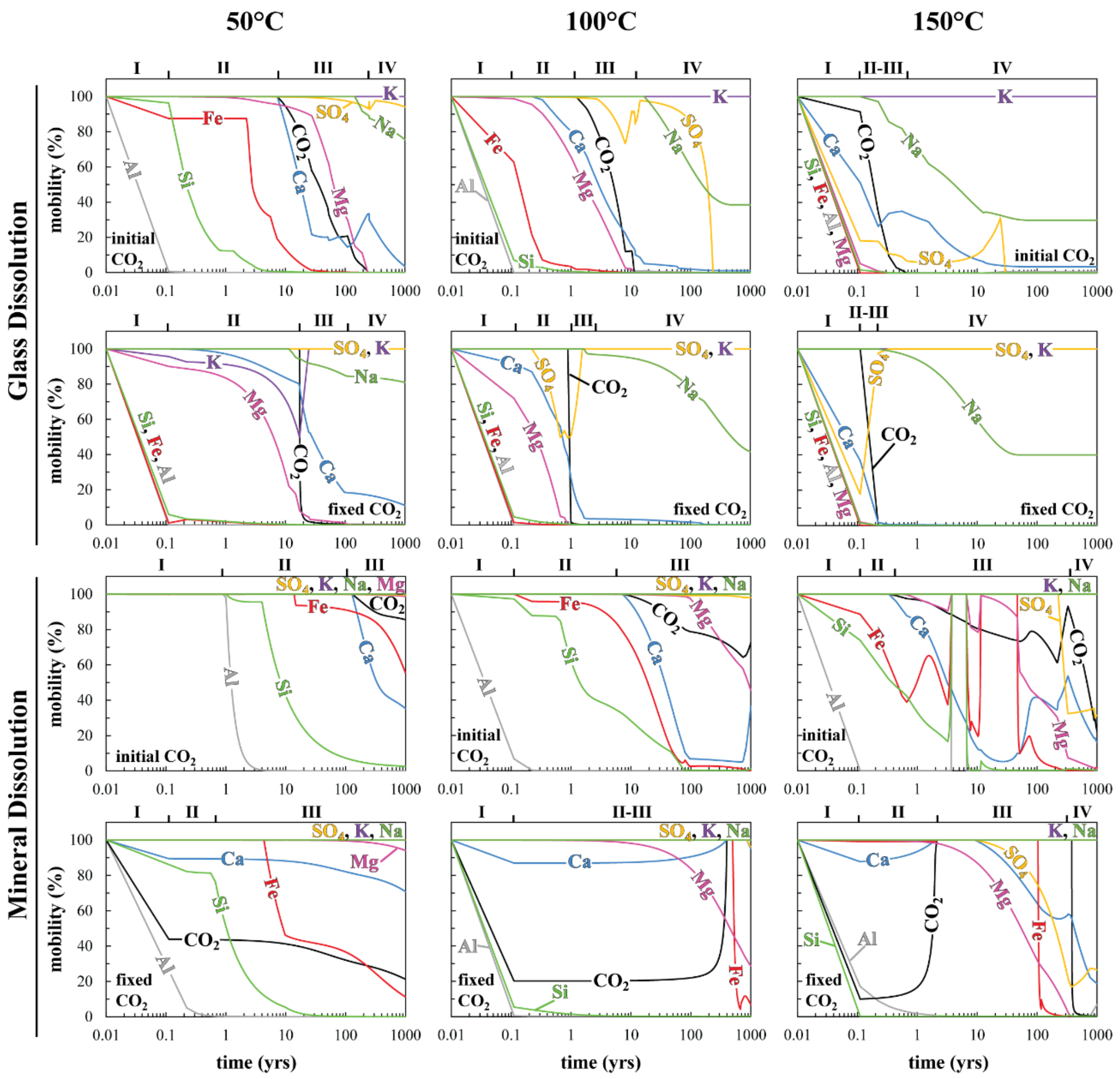

__Figure 4.5__ Element mobilities during the alteration of glassy and crystalline basalts as a function of time. Roman numerals indicate reaction stage (see 4.5.1 for details).

4.5.3 Implications on geochemical cycles

Fluid circulation through off-axis hydrothermal systems at low temperatures may significantly impact the chemical budget of both the oceans and the oceanic crust (e.g., Alt, 2003; Coogan and Gillis, 2018; Fisher and Wheat, 2010; Staudigel, 2014; Wheat and Fisher, 2008; Wheat and Mottl, 2000; Kleine et al., 2020, 2022). Geochemical modeling results may be used to estimate such interaction and annual element fluxes between the oceanic crust and seawater. This can be achieved by using the chemical changes in either rocks or hydrothermal fluid upon basalt-seawater interaction.

Rock-based element fluxes $F_{el,rock}$ were calculated analogously to the method adopted by Bach et al. (2003):

$$F_{el,rock}[mol/yr] = \left[-\left(C_{a,rock} - C_{i,rock}\right) \cdot \gamma_{crust} \cdot \varepsilon_{crust} \cdot \rho_{crust}\right] / M_{el} \tag{13}$$

where $C_{a,rock}$ and $C_{i,rock}$ are the concentrations of an element in g/kg in the altered and unaltered rock, respectively, γ_{crust} is the thickness of the crust in m, ε_{crust} is the crustal production rate in m^2 yr^{-1}, ρ_{crust} is the density of the crust in kg m^{-3} and M_{el} is the molar mass in g mol^{-1} of an element. For crustal thickness, a value of 500 m was assumed, as this corresponds to the estimated average thickness of a typical low-temperature crustal aquifer (Coogan and Gillis, 2018). The crustal production rate was assumed to be equal to $3.45 \cdot 10^6$ m^2 yr^{-1} (Parsons, 1981) and the density of the crust was assumed as 2800 kg m^{-3}.

Fluid-based element fluxes $F_{el,fluid}$ were calculated following the approach of Kleine et al. (2020):

$$F_{el,fluid}[mol/yr] = H/\left(\Delta T \cdot c_p\right) \cdot \left(C_{a,fluid} - C_{i,fluid}\right) \tag{14}$$

where H is the hydrothermal heat flux, assumed to range between 7 and $15 \cdot 10^{12}$ $J \cdot s^{-1}$ (Hasterok, 2013; Stein and Stein, 1994), ΔT is the water temperature anomaly, c_p the specific heat capacity of seawater, assumed as 4000 $J \cdot kg^{-1} \cdot K^{-1}$ (Bischoff and Rosenbauer, 1985) and $C_{a,fluid}$ and $C_{i,fluid}$ are the element concentrations in mol kg^{-1} in the reacted fluid and seawater, respectively.

Annual fluxes of Si, Mg, Ca, K, Na, and SO_4 have been extensively studied in the past (e.g., Bach et al., 2003; Huang et al., 2018; Staudigel, 2014; Staudigel et al., 1996; Wheat and Fisher, 2008; Wheat and Mottl, 2000, Hart and Staudigel, 1982). Here, we compare our calculated annual fluxes of these elements with those previously reported (Figs. 4.6 and 4.7) to verify our modeling calculations. Positive values indicate fluxes from the crust to the oceans, whereas negative values indicate fluxes from seawater into the crust.

Both fluid and rock-based fluxes suggest that basalt-seawater interaction results in a net source of aqueous Si for the oceans. This source is predicted to be generally below $+1.5 \cdot 10^{12}$ mol yr^{-1} for the least altered rocks (i.e., high water-rock ratios). The rock-based fluxes of silica at these high water-rock ratios are typically within the order of $+10^9$ to $+10^{10}$ mol yr^{-1}, making them most compatible with estimates by Wheat and Mottl (2000), who suggested a comparatively small Si source of $+1.8 \cdot 10^{10}$ mol yr^{-1}. The higher Si fluxes proposed by Bach et al. (2003) of $+1.4 \cdot 10^{12}$ mol yr^{-1} can be reproduced by our rock-based estimate but require significantly altered oceanic crust (i.e., low water-rock ratios). Fluid-based calculations indicate annual sources of Si equivalent to those of Bach et al. (2003) at higher water-rock ratios that may be more representative of the wider oceanic crust. The significant Si sink of $-7 \cdot 10^{11}$ mol yr^{-1} proposed by Staudigel et al. (1996) is not reproduced in our calculations.

The behavior of Mg is strongly dependent on the extent of basalt alteration. Rock-based fluxes do not indicate the strong Mg sinks of $-3.45 \cdot 10^{11}$ to $-5.4 \cdot 10^{12}$ mol yr^{-1} that have been proposed by several analytical studies (Bach et al., 2003; Wheat and Mottl, 2000;

Huang et al., 2018; Wheat and Fisher, 2008) and only reflect the Mg source of $+1.7 \cdot 10^{11}$ mol yr^{-1} according to Staudigel et al. (1996) within significantly altered crust. In contrast, fluid-based sinks of Mg are significantly greater and generally increase with progressive alteration of the crust. Values for $F_{Mg,fluid}$ within lightly altered crust are compatible with the abovementioned Mg sinks (Bach et al., 2003; Wheat and Mottl, 2000; Huang et al., 2018; Wheat and Fisher, 2008). The calculated Mg sink at low water-rock ratios notable increases with decreasing temperatures, reaching its greatest magnitude of $-9.5 \cdot 10^{13}$ mol yr^{-1} at water-rock ratios <10 (Fig. 4.7). Such an extensive sink would exceed the annual riverine flux of Mg by an order of magnitude and is unlikely to be representative of actual annual Mg fluxes. However, these results support the notion that highly altered lithologies, particularly at lower temperatures, may act as a significant global Mg sink for seawater. The large discrepancy between $F_{Mg,rock}$ and $F_{Mg,fluid}$ may be caused by differences between relative bulk rock concentration changes and absolute element fluxes that take into account potential variations in bulk rock mass during alteration. Such variations may arise based on the difference in density between the unaltered and altered rock. Equation 13 assumes a constant crustal density during alteration of 2800 kg m^{-3} and therefore calculates mass fluxes directly based on concentration changes. However, for highly permeable upper crustal basalts in particular, some density changes likely occur during alteration, due to the formation of secondary minerals (e.g., Jarrard et al., 1995, 2003; Christensen, 1980; Carlson and Herrick, 1990), meaning that concentration changes may not be an accurate representation of actual mass fluxes. Alteration of basaltic glass has also been shown to lead to changes in volume and/ or total mass (Pauly et al., 2011; Prause et al., 2022; Zhou and Fyfe, 1989). Furthermore, uncertainties in the hydrothermal heat flux in equation 14 may contribute to the observed differences between fluid- and rock-based fluxes as well.

The effect of basalt-seawater interaction on the fluxes of Ca is highly variable, ranging from a maximum sink of $-5.9 \cdot 10^{12}$ mol yr^{-1} to a maximum source of $+7.6 \cdot 10^{13}$ mol yr^{-1} according to fluid-based estimates (Fig. 4.7). Rock-based estimates indicate that Ca is primarily released during seafloor alteration (Fig. 4.6). Overall, both rock-based and fluid-based flux values are compatible with previous estimates by Bach (2003), Wheat and Fisher (2008), and Wheat and Mottl (2000) that yielded sources of $+2.17 \cdot 10^{11}$ to $+4.7 \cdot 10^{12}$ mol yr^{-1}. Both calculation methods indicate that increasing alteration, i.e., decreasing water-rock ratios, lead to increased Ca sources, except for the fluid-based estimates of very highly altered crust (Fig. 4.7, water-rock ≤10). There, calculations instead indicated drawdown of Ca into the crust of a magnitude that is comparable to the Ca sink of $-1.4 \cdot 10^{12}$ mol yr^{-1} proposed by Staudigel et al. (1996)

Calculated fluxes of K mostly indicate an increasing significant source with progressive alteration. A sink of K as proposed by Bach et al. (2003), Hart and Staudigel (1982) and Wheat and Mottl (2000) of $-9.8 \cdot 10^{10}$ to $-3.3 \cdot 10^{11}$ mol yr^{-1} was only reproduced with our fluid-based estimates (Fig. 4.7). Potassium is highly mobile and primarily taken up by clay minerals, which can be present in a large variety of species and span a wide range of compositions. Therefore, a potential explanation for the absence of a ubiquitous K sink may be that the selected equilibrium clay mineral assemblage misses one or more K-bearing phase that may be more widespread in natural systems. Alternatively, it is possible that higher amounts of celadonite ($KMgAlSi_4O_{10}[OH]_2$) forming at temperatures <50°C and high water-rock ratios may account for the significant K sink proposed by these earlier studies. Such increased rates of celadonite formation at lower temperatures were observed in our model.

Fluid-based flux estimates for Na at water-rock ratios >1000 suggest that seafloor alteration acts as a source of $+5.9 \cdot 10^9$ to $+1.7 \cdot 10^{12}$ mol yr^{-1}, with most flux values being on the order of $+10^{11}$ mol yr^{-1}. These results are comparable to the Na source of $1.2 \cdot 10^{12}$ mol yr^{-1} derived by Staudigel (2014). Rock-based fluxes within the same water-rock range were smaller, ranging between $+2.2 \cdot 10^8$ to $5.1 \cdot 10^9$ mol yr^{-1}.

The annual fluxes of SO_4 show strong variations between rock-based and fluid-based estimates. This is caused primarily by the fact that SO_4 may be removed from solution through both the precipitation of sulfate minerals as well as reduction of dissolved sulfate to sulfide. Rock-based fluxes are only affected by the former process, but not the latter. In contrast, fluid-based estimates are based on the concentration of SO_4 in solution and therefore reflect both processes. As a result, fluid-based estimates indicated a significantly greater sink of SO_4 that generally increased in magnitude towards lower water-rock ratios (Fig. 4.7). Higher temperatures caused depletion of SO_4 at higher water-rock ratios in the least altered crust due to the retrograde solubility of the sulfate anion (Dickson et al., 1963; Seyfried and Bischoff, 1979; Kleine et al., 2022). The maximum sink for dissolved SO_4, however, increases in magnitude at decreasing temperatures. Our fluid-based estimates are compatible with the annual SO_4 sink of $-1.1 \cdot 10^{12}$ mol yr^{-1} as proposed by Wheat and Mottl (2000) (Fig. 4.7).

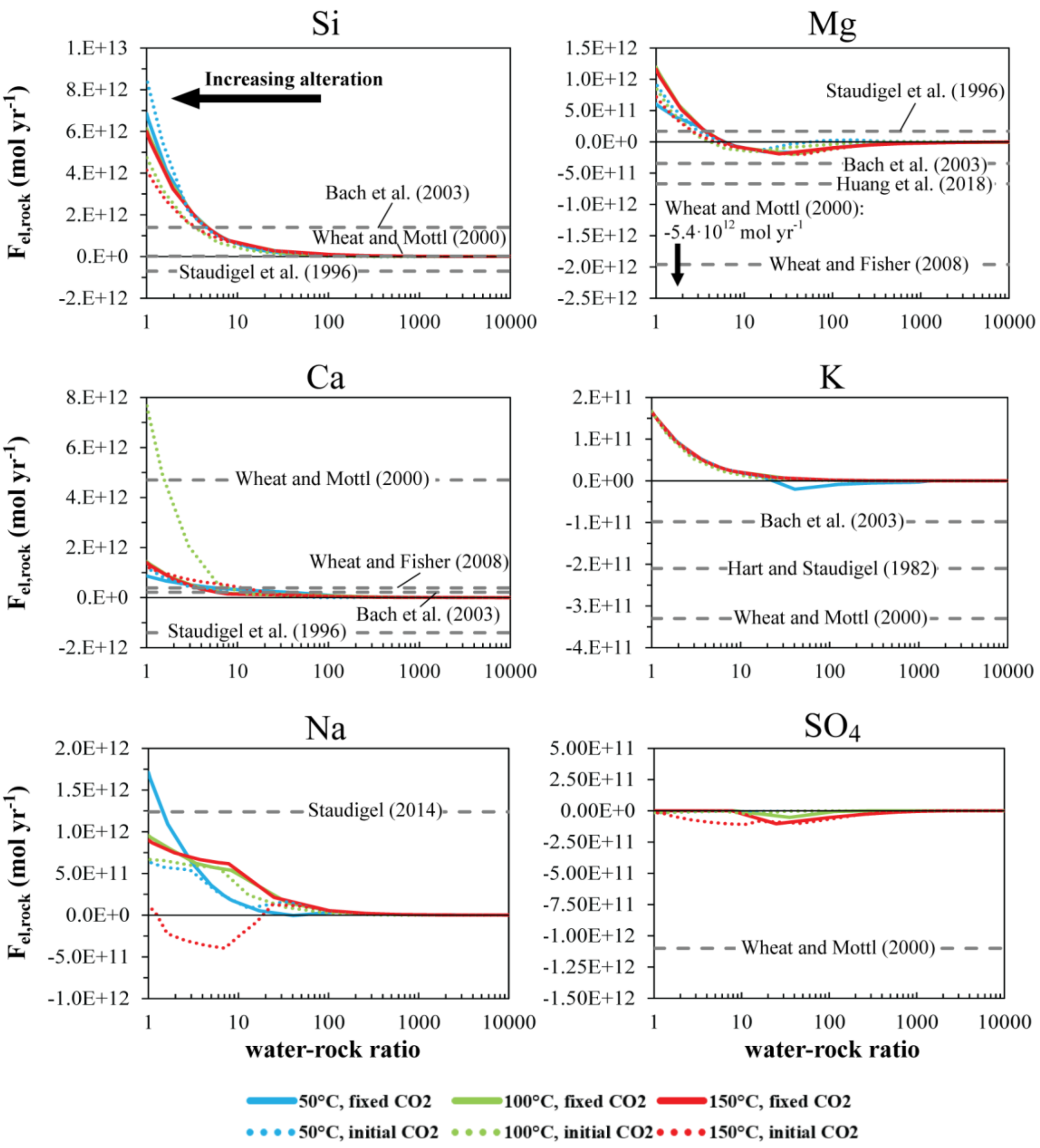

Figure 4.6 *Annual rock-based mass fluxes of Si, Mg, Ca, K, Na, and* SO_4 *based on the modeled alteration of N-MORB glass as a function of water-rock ratio compared to estimates from previous studies (Bach et al., 2003; Huang et al., 2018; Staudigel, 2014; Staudigel et al., 1996; Wheat and Fisher, 2008; Wheat and Mottl, 2000; Hart and Staudigel, 1982). Lower water-rock ratios indicate larger total amounts of basalt reacted with seawater and therefore greater extents of alteration.*

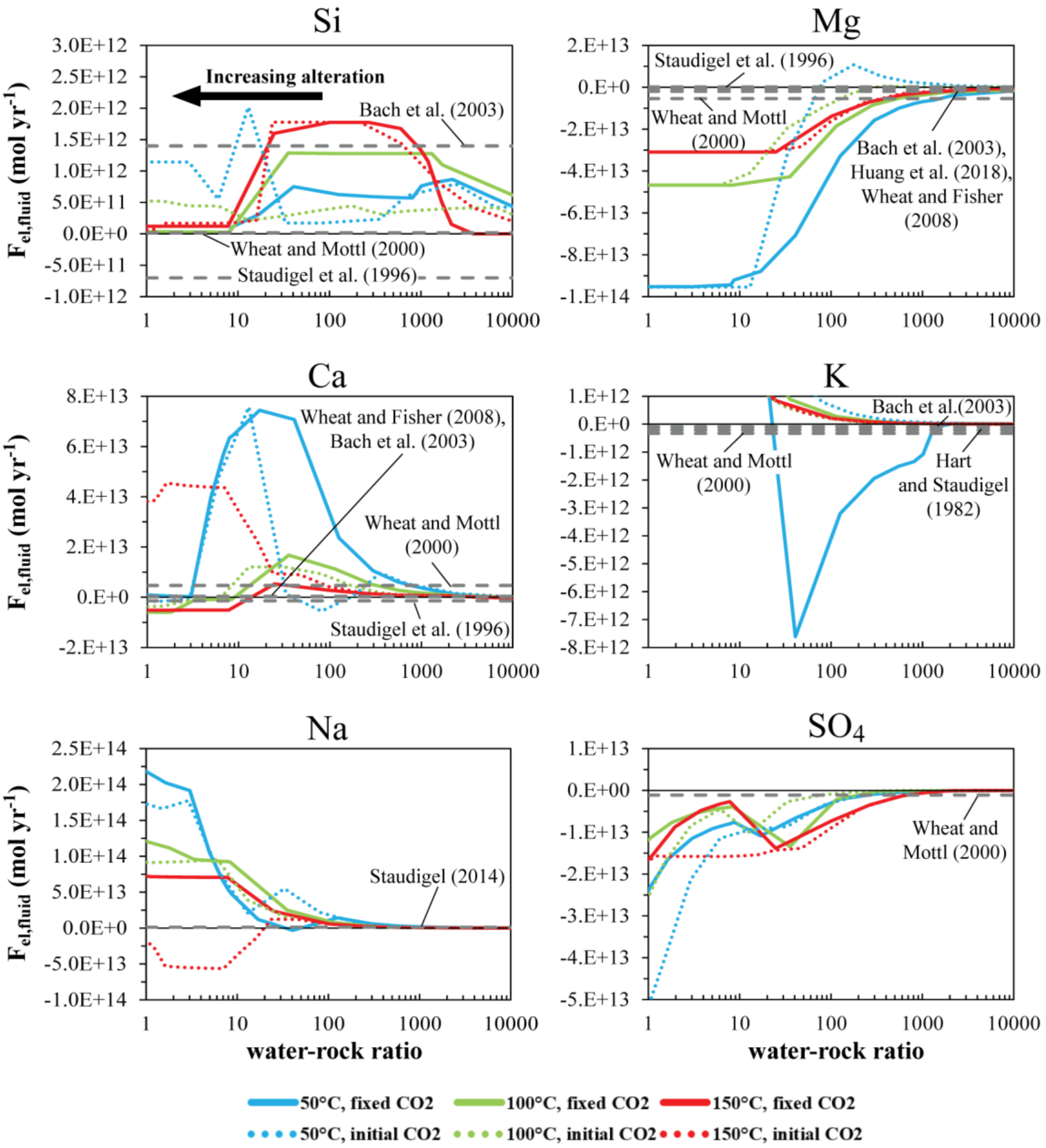

Figure 4.7 *Annual fluid-based mass fluxes of Si, Mg, Ca, K, Na, and SO_4 based on the modeled alteration of N-MORB glass as a function of water-rock ratio compared to estimates from previous studies (Bach et al., 2003; Huang et al., 2018; Staudigel, 2014; Staudigel et al., 1996; Wheat and Fisher, 2008; Wheat and Mottl, 2000; Hart and Staudigel, 1982). Fluxes were calculated based on an intermediate hydrothermal heat flux of $1.1 \cdot 10^{13}$ J s^{-1}. Lower water-rock ratios indicate larger total amounts of basalt reacted with seawater and therefore greater extents of alteration.*

4.6 Conclusions

A numerical model of basalt alteration by seawater at temperatures between 50-150°C has been established for the purpose of investigating the relative contributions of reaction progress, water-rock ratio, temperature, crystallinity, and pH during off-axis seafloor alteration as well as the resulting effects on the chemical budget between the oceanic crust and seawater. Four reaction stages are recognized during the alteration process. These stages are, in order: 1) dissolution of primary minerals and basaltic glass, 2) precipitation of early-stage alteration minerals, principally Mg-Fe(III)-clays, celadonite, montmorillonite, and simple oxides and hydroxides, 3) increasing reduction of the hydrothermal fluid, accompanied by the partial replacement of early Mg-Fe(III)-clays by Fe^{2+} bearing saponite as well as the formation of calcite, and 4) a shift towards alkaline pH and elevated dissolved Al facilitating the precipitation of zeolites.

These four reaction steps were observed regardless of temperature and crystallinity, which primarily affected reaction rates. Water-rock ratio and associated changes in pH were identified as the main controlling parameters on the forming alteration mineralogy upon seafloor alteration. Increased acid supply in the form of dissolved CO_2 controls the relative abundance of calcite versus clay minerals, sulfates and zeolites and acts as a buffer against alkalinization caused by proton consumption during the dissolution of basaltic glass and primary minerals.

Element mobilities and fluid concentrations varied with reaction progress. In particular, Mg and SO_4 were quantitatively removed from the solution at advanced alteration stages, reducing conditions, and low water-rock ratios. For SO_4 this effect was found to be stronger for systems in which CO_2 supply was limited, due to the competition between the sulfate and carbonate anions for dissolved Ca. This may indicate that the lower oceanic crust, where access to CO_2-rich bottom seawater is restricted and permeability is diminished, may have a disproportionate effect on the removal of Mg and SO_4 from the oceans.

Modeling results reproduced petrographic and fluid-geochemical observations of natural seafloor-hosted systems affected by low-temperature basalt alteration. Fluid-based annual flux estimates for water-rock ratios from 10^3 to 10^4 suggest that globally seafloor alteration may act as a source of $+4.8 \cdot 10^8$ to $+1.3 \cdot 10^{12}$ mol yr^{-1} Si, $+1.0 \cdot 10^{11}$ to $+3.7 \cdot 10^{12}$ mol yr^{-1} Ca, $+5.3 \cdot 10^{10}$ to $+1.7 \cdot 10^{12}$ mol yr^{-1} Na, as well as a variable sink or source of $-4.5 \cdot 10^{11}$ to $+3.6 \cdot 10^9$ mol yr^{-1} SO_4, $-6.8 \cdot 10^{12}$ to $+7.8 \cdot 10^{11}$ mol yr^{-1} Mg, and $-1.1 \cdot 10^{12}$ to $+2.7 \cdot 10^{10}$ mol yr^{-1} K. Equivalent rock-based fluxes were generally smaller and indicated sources of $+6.2 \cdot 10^8$ to $+1.1 \cdot 10^{10}$ mol yr^{-1} Ca, $+2.9 \cdot 10^8$ to $+5.1 \cdot 10^9$ mol yr^{-1} Na, a sink of $-3.2 \cdot 10^9$ to $-1.7 \cdot 10^7$ mol yr^{-1} SO_4 and sinks or sources of $-1.2 \cdot 10^9$ to $+1.3 \cdot 10^{10}$ mol yr^{-1} Si, $-1.9 \cdot 10^{10}$ to $+1.3 \cdot 10^9$ mol yr^{-1} Mg, and $-2.9 \cdot 10^9$ to $+1.6 \cdot 10^8$ mol yr^{-1} K.

4.7 Acknowledgements

This study received funding by the University of Iceland Recruitment Fund, a grant to the Surtsey Underwater volcanic System for Thermophiles, Alteration processes and INnovative concretes (SUSTAIN) project by the International Continental Scientific Drilling Program (ICDP), the Icelandic Science Fund, ICF-RANNÍS, and the two Icelandic power companies Reykjavík Energy and Landsvirkjun.

4.8 References

Alt, J.C., 2003. Hydrothermal fluxes at mid-ocean ridges and on ridge flanks. Comptes Rendus - Geosci. 335, 853–864.

Alt, J.C., 1995. Subseafloor processes in mid-ocean ridge hydrothermal systems. Geophys. Monogr. Ser. 91, 85–114.

Alt, J.C., Teagle, D.A.H., Laverne, C., Vanko, D.A., Bach, W., Honnorez, J., Becker, K., Ayadi, M., Pezard, P.A., 1996a. Ridge-Flank Alteration of Upper Ocean Crust in the Eastern Pacific: Synthesis of Results for Volcanic Rocks of Holes 504B and 896A. Proc. Ocean Drill. Program, Sci. Results 148, 435-450.

Alt, J.C., Laverne, C., Vanko, D.A., Tartarotti, P., Teagle, D.A.H., Bach, W., Zuleger, E., Erzinger, J., Honnorez, J., Pezard, P.A., Becker, K., Salisbury, M.H., Wilkens, R.H., 1996b. Hydrothermal alteration of a section of upper oceanic crust in the Eastern Equatorial Pacific: A synthesis of results from Site 504 (DSDP Legs 69, 70, and 83, and ODP Legs 111, 137, 140, and 148). Proc. Ocean Drill. Program, Sci. results 148, 417–434.

Alt, J.C., France-Lanord, C., Floyd, P.A., Castillo, P., Galy, A., 1992. Low-temperature hydrothermal alteration of Jurassic ocean crust, Site 801. Proc. Ocean Drill. Program, Sci. results 129, 415–427.

Alt, J.C., Honnorez, J., Laverne, C., Emmermann, R., 1986. Hydrothermal alteration of a 1 km section through the upper oceanic crust, Deep Sea Drilling Project Hole 504B: Mineralogy, chemistry, and evolution of seawater-basalt interactions. J. Geophys. Res. 91, 10309–10335.

Alt, J.C., Teagle, D.A.H., 2003. Hydrothermal alteration of upper oceanic crust formed at a fast-spreading ridge: mineral, chemical, and isotopic evidence from ODP Site 801. Chem. Geol. 201, 191–211.

Aradóttir, E.S.P., Sonnenthal, E.L., Björnsson, G., Jónsson, H., 2012. Multidimensional reactive transport modeling of CO2 mineral sequestration in basalts at the Hellisheidi geothermal field, Iceland. Int. J. Greenhouse Gas Cont. 9, 24–40.

Bach, W., Alt, J.C., Niu, Y., Humphris, S.E., Erzinger, J., Dick, H.J.B., 2001. The geochemical consequences of late-stage low-grade alteration of lower ocean crust at the SW Indian Ridge: Results from ODP Hole 735B (Leg 176). Geochim. Cosmochim. Acta 65, 3267–3287.

Bach, W., Peucker-Ehrenbrink, B., Hart, S.R., Blusztajn, J.S., 2003. Geochemistry of hydrothermally altered oceanic crust: DSDP/ODP Hole 504B-Implications for seawater-crust exchange budgets and Sr-and Pb-isotopic evolution of the mantle. Geochemistry, Geophys. Geosystems 4, 8904.

Bézos, A., Humler, E., 2005. The $Fe^{3+}/\Sigma Fe$ ratios of MORB glasses and their implications for mantle melting. Geochim. Cosmochim. Acta 69, 711–725.

Bischoff, J.L. and Rosenbauer, R.J., 1985. An empirical equation of state for hydrothermal seawater (3.2 percent NaCl). American Journal of Science 285, 725-763.

Carlson, R.L., Herrick, C.N., 1990. Densities and porosities in the oceanic crust and their variations with depth and age. J. Geophys. Res. 95, 9153-9170.

Christensen, N.I., Blair, S.C., Wilkens, R.H., Salisbury, M.H., 1980. Compressional wave velocities, densities, and porosities of basalts from Holes 417A, 417D, and 418A, Deep Sea Drilling Project Legs 51-53. Initial Rep. Deep Sea Drill. Proj., 51-53, Part 2, 1467-1471.

Coogan, L.A., Gillis, K.M., 2018. Low-Temperature Alteration of the Seafloor: Impacts on Ocean Chemistry. Annu. Rev. Earth Planet. Sci. 46, 21–45.

Disckson, F.W., Blount, C.W., Tunell, G., 1963. Use of hydrothermal solution equipment to determine the solubility of anhydrite in water from 100 degrees C to 275 degrees C and from 1 bar to 1000 bars pressure. American Journal of Science 261, 61-78.

Fisher, A.T., Wheat, C.G., 2010. Seamounts as Conduits for Massive Fluid, Heat, and Solute Fluxes on Ridge Flanks. Oceanography 23, 74–87.

Friedman, J.D., Williams, R.S., 1970. Changing patterns of thermal emission from Surtsey, Iceland, between 1966 and 1969. US Geol. Surv. Prof. Pap. 700-D, 116–124.

Gale, A., Dalton, C.A., Langmuir, C.H., Su, Y., Schilling, J.-G., 2013. The mean composition of ocean ridge basalts. Geochemistry Geophys. Geosystems 14, 489–518.

Gíslason, S.R., Oelkers, E.H., 2003. Mechanism, rates, and consequences of basaltic glass dissolution: II. An experimental study of the dissolution rates of basaltic glass as a function of pH and temperature. Geochim. Cosmochim. Acta 67, 3817–3832.

Gysi, A.P., Stefánsson, A., 2011. CO2-water-basalt interaction. Numerical simulation of low temperature CO2 sequestration into basalts. Geochim. Cosmochim. Acta 75, 4728–4751.

Hart, R., 1970. Chemical exchange between sea water and deep ocean basalts. Earth Planet. Sci. Lett. 9, 269–279.

Hart, S.R., Staudigel, H., 1982. The control of alkalies and uranium in seawater by ocean crust alteration. Earth Planet. Sci. Lett. 58, 202-212.

Hasterok, D., 2013. Global patterns and vigor of ventilated hydrothermal circulation through young seafloor. Earth Planet Sci. Lett. 380, 12-20.

Heřmanská, M., Voigt, M.J., Marieni, C., Declercq, J., Oelkers, E., 2022. A comprehensive and consistent mineral dissolution rate database: Part I: Primary silicate minerals and glasses. Chem. Geol. 597, 120807.

Hofmann, A.W., 1997. Mantle geochemistry: the message from oceanic volcanism. Nature 385, 219–229.

Huang, K.J., Teng, F.Z., Plank, T., Staudigel, H., Hu, Y., Bao, Z.Y., 2018. Magnesium isotopic composition of altered oceanic crust and the global Mg cycle. Geochim. Cosmochim. Acta 238, 357–373.

Jackson, M.D., Gudmundsson, M.T., Weisenberger, T.B., Michael Rhodes, J., Stefánsson, A., Kleine, B.I., Lippert, P.C., Marquardt, J.M., Reynolds, H.I., Kück, J., Marteinsson, V. þ., Vannier, P., Bach, W., Barich, A., Bergsten, P., Bryce, J.G., Cappelletti, P., Couper, S., Fahnestock, M.F., Gorny, C.F., Grimaldi, C., Groh, M., Gudmundsson, Á., Gunnlaugsson, Á.T., Hamlin, C., Högnadóttir, T., Jónasson, K., Jónsson, S.S., Jørgensen, S.L., Klonowski, A.M., Marshall, B., Massey, E., McPhie, J., Moore, J.G., Ólafsson, E.S., Onstad, S.L., Perez, V., Prause, S., Snorrason, S.P., Türke, A., White, J.D., Zimanowski, B., 2019a. SUSTAIN drilling at Surtsey volcano, Iceland, tracks hydrothermal and microbiological interactions in basalt 50 years after eruption. Sci. Drill. 25, 35–46.

Jackson, M.D., Couper, S., Stan, C. V., Ivarsson, M., Czabaj, M.W., Tamura, N., Parkinson, D., Miyagi, L.M., Moore, J.G., 2019b. Authigenic mineral texture in submarine 1979 basalt drill core, Surtsey volcano, Iceland. Geochemistry, Geophys. Geosystems 20, 3751–3773.

Jackson, M.D., Gudmundsson, M.T., Bach, W., Cappelletti, P., Coleman, N.J., Ivarsson, M., Jónasson, K., Jørgensen, S.L., Marteinsson, V., McPhie, J., Moore, J.G., Nielson, D., Rhodes, J.M., Rispoli, C., Schiffman, P., Stefánsson, A., Türke, A., Vanorio, T., Weisenberger, T.B., White, J.D.L., Zierenberg, R., Zimanowski, B., 2015. Time-lapse characterization of hydrothermal seawater and microbial interactions with basaltic tephra at Surtsey Volcano. Sci. Drill. 20, 51–58.

Jakobsson, S.P., Moore, J.G., 1986. Hydrothermal minerals and alteration rates at Surtsey volcano, Iceland. Geol. Soc. Am. Bull. 97, 648–659.

Jakobsson, S.P., Moore, J.G., 1982. The Surtsey Research Drilling Project of 1979. Surtsey Res. 9, 76–93.

Jarrard, R.D., Abrams, L.J., Pockalny, R., Larson, R.L., 2003. Physical properties of upper oceanic crust: Ocean Drilling Program Hole 801C and the waning of hydrothermal circulation. J. Geophys. Res. 108, 2188.

Jarrard, R.D., Larson, R.L., Fisher, A.T., Abrams, L.J., 1995. Geophysical aging of oceanic crust: Evidence from Hole 801C. Proc. Ocean Drill. Program Sci. Results 144, 649-663.

Kelley, K.A., Plank, T., Ludden, J., Staudigel, H., 2003. Composition of altered oceanic crust at ODP Sites 801 and 1149. Geochemistry, Geophys. Geosystems 4, 8910.

Kleine, B.I., Stefánsson, A., Kjartansdóttir, R., Prause, S., Weisenberger, T.B., Reynolds, H.I., Sveinbjörnsdóttir, Á.E., Jackson, M.D., Gudmundsson, M.T., 2020. The Surtsey volcano geothermal system: An analogue for seawater-oceanic crust interaction with implications for the elemental budget of the oceanic crust. Chem. Geol. 550, 119702.

Kleine, B.I., Stefánsson, A., Zierenberg, R.A., Jeon, H., Whitehouse, M.J., Jónasson, K., Fridleifsson, G.O., Weisenberger, T.B., 2022. Sulfate (re-)cycling in the oceanic crust: Effects of seawater-rock interaction, sulfur reduction and temperature on the abundance and isotope composition of anhydrite. Geochim. Cosmochim. Acta 317, 65–90.

Larsen, O., Postma, D., 2001. Kinetics of reductive bulk dissolution of lepidocrocite, ferrihydrite, and goethite. Geochim. Cosmochim. Acta 65, 1367–1379.

Leong, J.A.M., Shock, E.L., 2020. Thermodynamic constraints on the geochemistry of low-temperature, continental, serpentinization-generated fluids. Am. J. Sci. 320, 185–235.

Liu, H., Xue, Y.Y., Zhang, G., Sun, W.D., Tian, Z., Tuller-Ross, B., Wang, K., 2021. Potassium isotopic composition of low-temperature altered oceanic crust and its impact on the global K cycle. Geochim. Cosmochim. Acta 311, 59–73.

Millero, F.J., Feistel, R., Wright, D.G., McDougall, T.J., 2008. The composition of Standard Seawater and the definition of the Reference-Composition Salinity Scale. Deep. Res. Part I Oceanogr. Res. Pap. 55, 50–72.

Noack, Y., 1983. Occurrence of thaumasite in a seawater-basalt interaction, Mururoa atoll (French Polynesia, South Pacific). Mineral. Mag. 47, 47–50.

Oelkers, E.H., Gíslason, S.R., 2001. The mechanism, rates and consequences of basaltic glass dissolution: I. An experimental study of the dissolution rates of basaltic glass as a function of aqueous Al, Si and oxalic acid concentration at 25°C and pH = 3 and 11. Geochim. Cosmochim. Acta 65, 3671–3681.

Parkhurst, D.L., Appelo, C.A.J., 1999. User's guide to PHREEQC (Version 2): a computer program for speciation, batch-reaction, one-dimensional transport, and inverse geochemical calculations. Water-resources Investig. Rep. 99, 312.

Parsons, B., 1981. The rates of plate creation and consumption. Geophys. J. R. Astron. Soc. 67, 437–448.

Pauly, B.D., Schiffman, P., Zierenberg, R.A., Clague, D.A., 2011. Environmental and chemical controls on palagonitization. Geochemistry, Geophys., Geosystems 12, Q12017.

Prause, S., Weisenberger, T.B., Cappelletti, P., Grimaldi, C., Rispoli, C., Jónasson, K., Jackson, M.D., Gudmundsson, M.T., 2020. Alteration progress within the Surtsey hydrothermal system, SW Iceland – A time-lapse petrographic study of cores drilled in 1979 and 2017. J. Volcanol. Geotherm. Res. 392, 106754.

Prause, S., Weisenberger, T.B., Kleine, B.I., Monien, P., Rispoli, C., Stefánsson, A., 2022. Alteration of basaltic glass within the Surtsey hydrothermal system, Iceland – Implication to oceanic crust seawater interaction. J. Volcanol. Geotherm. Res. 429, 107581.

Ricci, A., Kleine, B.I., Fiebig, J., Gunnarsson-Robin, J., Kamunya, K.M., Mountain, B., Stefánsson, A., 2022. Equilibrium and kinetic controls on molecular hydrogen abundance and hydrogen isotope fractionation in hydrothermal fluids. Earth Planet. Sci. Lett. 579, 117338.

Seyfried Jr., W., Bischoff, J., 1979. Low temperature basalt alteration by sea water: an experimental study at 70 C and 150 C. Geochim. Cosmochim. Acta 43, 1937-1947.

Sonnenthal, E., Ito, A., Spycher, N., Yui, M., Apps, J., Sugita, Y., Conrad, M., Kawakami, S., 2005. Approaches to modeling coupled thermal, hydrological, and chemical processes in the Drift Scale Heater Test at Yucca Mountain. Int. J. Rock Mech. Min. Sci. 42, 698–719.

Staudigel, H., 2014. Chemical Fluxes from Hydrothermal Alteration of the Oceanic Crust, in: Holland, H.D., Turekian, K.K. (Eds.), Treatise on Geochemistry. Elsevier, Oxford, pp. 583–606.

Staudigel, H., 2003. Hydrothermal alteration processes in the oceanic crust, in: Rudnick, R.L. (Ed.), Treatise on Geochemistry. Elsevier, New York, pp. 511–535.

Staudigel, H., Plank, T., White, B., Schmincke, H.U., 1996. Geochemical fluxes during seafloor alteration of the basaltic upper oceanic crust: DSDP sites 417 and 418, in: Bebout, G.E., Scholl, S.W., Kirby, S.H., Platt, J.P. (Eds.), Subduction, Top to Bottom, Geophys. Monogr. Ser. AGU, Washington D.C., pp. 19–38.

Stefánsson, A., 2010. Low-temperature alteration of basalts - the effects of temperature, acids and extent of reaction on mineralization and water chemistry. Jökull 60, 165-184

Stein, C.A., Stein, S., 1994. Constraints on hydrothermal heat flux through the oceanic lithosphere from global heat flux. J. Geophys. Res. 99, 3081–3095.

Teagle, D.A.H., Alt, J.C., Bach, W., Halliday, A.N., Erzinger, J., 1996. Alteration of Upper Ocean Crust in a Ridge-Flank Hydrothermal Upflow Zone: Mineral, Chemical, and Isotopic Constraints from Hole 896A. Proc. Ocean Drill. Program, Sci. Results 148, 119-150.

Voigt, M., Marieni, C., Clark, D.E., Gislason, S.R., Oelkers, E.H., 2018. Evaluation and refinement of thermodynamic databases for mineral carbonation. Energy Procedia 146, 81–91.

Weisenberger, T.B., Guðmundsson, M.T., Jackson, M.D., Gorny, C.F., Türke, A., Kleine, B.I., Marshall, B., Jørgensen, S.L., Marteinsson, V. þ., Stefánsson, A., White, J.D.L., Barich, A., Bergsten, P., Bryce, J., Couper, S., Fahnestock, M.F., Franzson, H., Grimaldi, C., Groh, M., Guðmundsson, Á., Gunnlaugsson, Á. þ., Hamelin, C., Högnadóttir, Þ., Jónasson, K., Jónsson, S.S., Klonowski, A.M., Kück, J., Magnússon, R.L., Massey, E., McPhie, J., Ólafsson, E.S., Onstad, S.L., Prause, S., Perez, V., Rhodes, J.M., Snorrason, S.P., 2019. Operational Report for the 2017 Surtsey Underwater volcanic System for Thermophiles, Alteration processes and INnovative Concretes (SUSTAIN) drilling project at Surtsey Volcano, ICDP Operational Report. https://doi.org/10.2312/ICDP.5059.001

Wetzel, L.R., Shock, E.L., 2000. Distinguishing ultramafic- from basalt-hosted submarine hydrothermal systems by comparing calculated vent fluid compositions. J. Geophys. Res. 105, 8319–8340.

Wheat, C.G., Fisher, A.T., 2008. Massive, low-temperature hydrothermal flow from a basaltic outcrop on 23 Ma seafloor of the Cocos Plate: Chemical constraints and implications. Geochemistry, Geophys. Geosystems 9, Q12O14.

Wheat, C.G., Mottl, M.J., 2000. Composition of pore and spring waters from Baby Bare: Global implications of geochemical fluxes from a ridge flank hydrothermal system. Geochim. Cosmochim. Acta 64, 629–642.

Zhou, Z., Fyfe, W.S., 1989. Palagonitization of basaltic glass from DSDP Site 335, Leg 37: textures, chemical composition, and mechanism of formation. Am. Mineral. 74, 1045-1053.

Appendix A: Supplementary information for Paper II

1 Bulk rock mass balance results
2 Chemical compositions of sideromelane and palagonitized glass
3 Mg and K accumulation in palagonitized glass
4 Immobile trace elements mass balance results
5 Immobile TiO_2 vs constant volume mass balance

Table A.1 *Bulk rock mass changes and fluxes of major element oxides after MacLean (1990) or alternatively Grant (1986)*[a]*, assuming immobile* TiO_2*. Results are given in wt.% relative to initial bulk rock mass and estimated annual molar flux in mol* kg^{-1} yr^{-1}*.*

	Depth (m)	**SiO_2**		**Al_2O_3**		**FeO_{tot}**		**MgO**		**CaO**		**Na_2O**		**K_2O**		**Overall mass change**[b]
		wt.%	mol/kg/yr	wt.%	mol/kg/yr	wt.%	mol/kg/yr	wt.%	mol/kg/yr	wt.%	mol/kg/yr	wt.%	mol/kg/yr	wt.%	mol/kg/yr	(wt.%)
SE-01	14.2	0.54	7.47E-03	0.30	2.43E-03	0.35	4.03E-03	0.38	7.76E-03	-0.33	-4.96E-03	-0.13	-1.79E-03	-0.04	-3.23E-04	9.9
	25.4	-0.33	-4.63E-03	0.09	7.24E-04	0.23	2.66E-03	0.29	6.01E-03	-0.38	-5.66E-03	-0.27	-3.57E-03	-0.03	-2.41E-04	7.7
	37.3	0.37	5.09E-03	0.38	3.10E-03	0.19	2.17E-03	0.12	2.48E-03	-0.49	-7.34E-03	0.19	2.56E-03	-0.09	-8.19E-04	3.6
	65.6	1.57	2.18E-02	0.77	6.33E-03	0.43	4.99E-03	0.55	1.13E-02	-0.31	-4.55E-03	0.68	9.12E-03	-0.04	-3.83E-04	13.3
	70.7	1.28	1.77E-02	0.67	5.46E-03	0.32	3.71E-03	0.34	6.99E-03	0.10	1.48E-03	0.20	2.71E-03	-0.01	-1.31E-04	11.2
	125.5	-0.04	-6.07E-04	0.29	2.34E-03	0.51	5.95E-03	-0.12	-2.38E-03	-0.10	-1.47E-03	0.51	6.86E-03	0.12	1.03E-03	10.1
	145	-2.43	-3.36E-02	-0.55	-4.52E-03	-0.05	-5.74E-04	-0.68	-1.40E-02	-0.80	-1.18E-02	0.02	2.11E-04	-0.09	-8.16E-04	3.1
	157.1	-2.82	-3.91E-02	-0.74	-6.01E-03	0.00	-1.31E-05	1.46	3.01E-02	-5.07	-7.54E-02	1.23	1.65E-02	-0.43	-3.83E-03	0.3
	170	-3.00	-4.15E-02	-0.70	-5.76E-03	-0.01	-1.73E-04	-0.33	-6.86E-03	1.00	1.49E-02	-0.48	-6.40E-03	-0.09	-7.74E-04	-0.2
	171	-2.94	-4.08E-02	-1.08	-8.80E-03	0.57	6.58E-03	0.60	1.24E-02	-1.48	-2.21E-02	-0.22	-2.96E-03	-0.09	-7.52E-04	-5.3
SE-02b	22.7	-0.21	-6.90E-04	0.45	8.83E-04	0.45	1.25E-03	0.30	1.51E-03	0.00	1.22E-05	-0.35	-1.12E-03	-0.01	-1.24E-05	13.5
	34.7	0.13	4.26E-04	0.62	1.23E-03	0.32	8.84E-04	0.24	1.21E-03	-0.38	-1.34E-03	0.43	1.38E-03	-0.05	-1.15E-04	11.8
	43.6	0.95	3.15E-03	0.88	1.73E-03	0.49	1.35E-03	0.54	2.67E-03	0.11	4.02E-04	0.13	4.25E-04	0.15	3.15E-04	14.2
	55.9	0.62	2.07E-03	0.76	1.50E-03	0.38	1.05E-03	0.32	1.57E-03	-0.04	-1.26E-04	0.64	2.06E-03	-0.01	-3.15E-05	15.1
	65.3	1.76	5.87E-03	1.05	2.06E-03	0.57	1.60E-03	0.46	2.29E-03	0.15	5.33E-04	2.16	6.96E-03	0.00	6.47E-06	21.3
	78.1	2.75	9.16E-03	1.63	3.20E-03	0.56	1.56E-03	0.54	2.69E-03	0.01	4.67E-05	1.27	4.11E-03	-0.15	-3.18E-04	19.1
	86.3	1.94	6.47E-03	1.18	2.31E-03	0.49	1.36E-03	0.46	2.29E-03	0.10	3.43E-04	1.01	3.27E-03	0.01	2.91E-05	16.8
	92.5	2.26	7.52E-03	1.38	2.70E-03	0.49	1.38E-03	0.38	1.87E-03	0.46	1.66E-03	1.32	4.24E-03	0.16	3.40E-04	18.4
	101.3	2.10	7.00E-03	1.38	2.71E-03	0.43	1.20E-03	0.60	2.98E-03	-0.17	-6.09E-04	1.60	5.16E-03	-0.21	-4.47E-04	17.6
	110.9	0.67	2.24E-03	0.91	1.78E-03	0.34	9.36E-04	0.23	1.16E-03	-0.19	-6.82E-04	0.93	3.00E-03	-0.01	-2.53E-05	14.9
	120.5	0.45	1.51E-03	0.75	1.47E-03	0.32	8.90E-04	0.28	1.37E-03	0.21	7.64E-04	0.70	2.26E-03	0.06	1.23E-04	13.5
	127.9	0.16	5.21E-04	0.65	1.27E-03	0.31	8.51E-04	0.04	1.85E-04	-0.62	-2.22E-03	1.06	3.43E-03	-0.12	-2.63E-04	11.7
	138.3	0.12	3.84E-04	0.67	1.31E-03	0.32	8.77E-04	-0.11	-5.31E-04	-1.20	-4.28E-03	2.22	7.15E-03	-0.37	-7.88E-04	12.1
	148.6	-1.75	-5.83E-03	0.05	1.04E-04	0.16	4.36E-04	-0.32	-1.57E-03	-0.66	-2.34E-03	0.61	1.98E-03	-0.12	-2.65E-04	9.0
	157.1	-2.56	-8.53E-03	-0.15	-2.90E-04	-0.01	-3.15E-05	-0.67	-3.34E-03	-0.73	-2.60E-03	0.59	1.90E-03	-0.07	-1.54E-04	7.1
	165.6	-3.72	-1.24E-02	-0.65	-1.28E-03	-0.06	-1.56E-04	-0.85	-4.22E-03	-1.16	-4.14E-03	0.33	1.07E-03	-0.02	-4.91E-05	4.1

Table A.1 *(continued)*

	Depth (m)	**SiO_2**		**Al_2O_3**		**FeO_{tot}**		**MgO**		**CaO**		**Na_2O**		**K_2O**		**Overall mass change[b]**
		wt.%	mol/kg/yr	wt.%	mol/kg/yr	wt.%	mol/kg/yr	wt.%	mol/kg/yr	wt.%	mol/kg/yr	wt.%	mol/kg/yr	wt.%	mol/kg/yr	wt.%
SE-02b	176.1	-4.50	-1.50E-02	-0.88	-1.72E-03	-0.17	-4.81E-04	-1.01	-5.01E-03	-1.79	-6.40E-03	0.79	2.56E-03	-0.10	-2.15E-04	1.8
	180.8	-4.41	-1.47E-02	-0.81	-1.58E-03	-0.07	-1.87E-04	-0.54	-2.70E-03	-1.70	-6.05E-03	-0.39	-1.26E-03	-0.05	-1.11E-04	-7.6

[a] Both methods can be used interchangingly: TiO_2 isocon mass balance yields identical results to those obtained by applying the mathematical approach of MacLean (1990).

[b] Overall mass change is estimated from the slope of the TiO_2 isocon for each sample. Differences between the sum of oxide mass changes and the overall mass change are caused by components not included in the mass balance (e.g. H_2O).

Table A.2 *Chemical compositions of sideromelane (SM) and palagonitized glass (PG) in the SE-01 drill core as a function of depth. Results are given as average of n analyses. If no sideromelane or palagonitized glass analysis is listed the phase in question was not present in the analyzed sample.*

	22.0 m		**43.6 m**		**55. 8 m**		**90.1 m**		**92.6 m**		**120.6 m**		**148.3 m**		**156.9 m**		**169.5 m**	
	SM	PG	SM	PG	SM	PG	SM	PG	SM	PG	SM	PG	SM	PG	SM	PG	SM	PG
	(n=12)	(n=11)	(n=10)		(n=15)	(n=31)		(n=8)		(n=1)	(n=4)	(n=18)	(n=21)	(n=21)	(n=33)	(n=30)	(n=7)	
Major elements (wt.%)																		
SiO_2	46.62	38.16	47.05	n.a.	47.20	35.93	n.a.	35.37	n.a.	29.85	46.74	37.33	46.27	37.33	46.56	37.08	46.62	n.a.
TiO_2	2.63	3.84	2.55	n.a.	2.46	3.70	n.a.	3.53	n.a.	3.62	2.52	3.58	2.63	4.14	2.67	3.74	2.75	n.a.
Al_2O_3	16.16	10.76	16.14	n.a.	16.65	12.45	n.a.	11.52	n.a.	11.43	16.35	14.14	16.32	10.09	16.28	11.95	16.36	n.a.
FeO	12.46	17.40	12.29	n.a.	11.70	17.55	n.a.	17.16	n.a.	18.34	12.02	16.75	12.40	18.75	12.51	16.90	12.71	n.a.
MnO	0.22	0.28	0.21	n.a.	0.20	0.26	n.a.	0.30	n.a.	0.34	0.21	0.29	0.21	0.29	0.21	0.28	0.21	n.a.
MgO	5.77	6.21	5.77	n.a.	5.73	4.68	n.a.	8.88	n.a.	8.19	5.90	7.26	5.84	3.97	5.82	5.61	5.67	n.a.
CaO	9.64	9.04	9.65	n.a.	9.80	10.31	n.a.	8.66	n.a.	7.98	9.76	7.34	9.56	9.44	9.50	8.15	9.38	n.a.
Na_2O	3.81	0.64	3.88	n.a.	3.86	0.93	n.a.	0.31	n.a.	0.67	3.86	1.34	3.82	1.25	3.91	1.34	3.80	n.a.
K_2O	0.71	0.26	0.75	n.a.	0.69	0.37	n.a.	0.43	n.a.	0.39	0.71	0.55	0.70	0.39	0.71	0.27	0.73	n.a.
P_2O_5	0.36	0.51	0.38	n.a.	0.37	0.58	n.a.	0.39	n.a.	0.35	0.37	0.77	0.35	0.54	0.37	0.36	0.39	n.a.
Sum	98.36	87.11	98.66	n.a.	98.66	86.77	n.a.	86.55	n.a.	81.16	98.44	89.36	98.10	86.20	98.54	85.69	98.61	n.a.
Trace elements (ppm)																		
V	n.a.	n.a.	276	n.a.	275	354	n.a.	n.a.	n.a.	170	n.a.	293	286	367	n.a.	n.a.	283	n.a.
Rb	n.a.	n.a.	14.6	n.a.	13.1	6.2	n.a.	n.a.	n.a.	8.8	n.a.	9.2	14.5	14.2	n.a.	n.a.	14.2	n.a.
Sr	n.a.	n.a.	343	n.a.	374	537	n.a.	n.a.	n.a.	239	n.a.	499	359	421	n.a.	n.a.	349	n.a.
Y	n.a.	n.a.	33	n.a.	34	47	n.a.	n.a.	n.a.	50	n.a.	51	34	53	n.a.	n.a.	33	n.a.
Zr	n.a.	n.a.	195	n.a.	201	274	n.a.	n.a.	n.a.	256	n.a.	302	195	306	n.a.	n.a.	191	n.a.
Nb	n.a.	n.a.	22.2	n.a.	22.9	31.4	n.a.	n.a.	n.a.	26.7	n.a.	34.4	22.5	35.8	n.a.	n.a.	22.3	n.a.
Ba	n.a.	n.a.	164	n.a.	141	66	n.a.	n.a.	n.a.	13	n.a.	79	169	42	n.a.	n.a.	167	n.a.
La	n.a.	n.a.	18.5	n.a.	18.7	26.1	n.a.	n.a.	n.a.	25.0	n.a.	27.2	18.3	29.7	n.a.	n.a.	18.1	n.a.
Ce	n.a.	n.a.	42.7	n.a.	45.2	61.5	n.a.	n.a.	n.a.	60.9	n.a.	66.0	42.9	68.2	n.a.	n.a.	42.1	n.a.
Pr	n.a.	n.a.	5.86	n.a.	6.05	8.30	n.a.	n.a.	n.a.	8.48	n.a.	8.81	5.88	9.73	n.a.	n.a.	5.70	n.a.
Nd	n.a.	n.a.	26.8	n.a.	27.3	37.8	n.a.	n.a.	n.a.	36.5	n.a.	40.7	26.6	45.2	n.a.	n.a.	26.7	n.a.
Sm	n.a.	n.a.	7.2	n.a.	8.7	10.8	n.a.	n.a.	n.a.	13.4	n.a.	11.0	8.0	11.1	n.a.	n.a.	7.5	n.a.
Eu	n.a.	n.a.	2.45	n.a.	2.54	3.46	n.a.	n.a.	n.a.	3.87	n.a.	3.77	2.51	3.62	n.a.	n.a.	2.53	n.a.
Gd	n.a.	n.a.	7.10	n.a.	7.53	10.06	n.a.	n.a.	n.a.	9.90	n.a.	10.88	7.51	11.11	n.a.	n.a.	7.18	n.a.

Table A.2 *(continued)*

	22.0 m		**43.6 m**		**55. 8 m**		**90.1 m**		**92.6 m**		**120.6 m**		**148.3 m**		**156.9 m**		**169.5 m**	
	SM	PG	SM	PG	SM	PG	SM	PG	SM	PG	SM	PG	SM	PG	SM	PG	SM	PG
Trace elements (ppm)																		
Tb	n.a.	n.a.	1.03	n.a.	1.19	1.57	n.a.	n.a.	n.a.	1.55	n.a.	1.69	1.07	1.75	n.a.	n.a.	1.12	n.a.
Dy	n.a.	n.a.	7.04	n.a.	7.55	9.81	n.a.	n.a.	n.a.	11.85	n.a.	10.59	6.91	12.36	n.a.	n.a.	7.10	n.a.
Ho	n.a.	n.a.	1.39	n.a.	1.37	1.89	n.a.	n.a.	n.a.	1.85	n.a.	2.02	1.40	2.13	n.a.	n.a.	1.33	n.a.
Er	n.a.	n.a.	3.8	n.a.	4.0	5.5	n.a.	n.a.	n.a.	5.2	n.a.	5.8	3.9	6.3	n.a.	n.a.	3.9	n.a.
Tm	n.a.	n.a.	0.54	n.a.	0.59	0.75	n.a.	n.a.	n.a.	0.78	n.a.	0.82	0.58	0.80	n.a.	n.a.	0.54	n.a.
Yb	n.a.	n.a.	3.39	n.a.	3.52	4.88	n.a.	n.a.	n.a.	4.76	n.a.	5.34	3.56	5.74	n.a.	n.a.	3.43	n.a.
Lu	n.a.	n.a.	0.510	n.a.	0.595	0.752	n.a.	n.a.	n.a.	0.721	n.a.	0.777	0.550	0.739	n.a.	n.a.	0.499	n.a.
Hf	n.a.	n.a.	5.15	n.a.	5.20	7.21	n.a.	n.a.	n.a.	7.03	n.a.	8.00	5.17	8.57	n.a.	n.a.	5.02	n.a.
Ta	n.a.	n.a.	1.41	n.a.	1.49	1.94	n.a.	n.a.	n.a.	1.78	n.a.	2.17	1.39	2.23	n.a.	n.a.	1.35	n.a.
Pb	n.a.	n.a.	2	n.a.	2	3	n.a.	n.a.	n.a.	1	n.a.	1	2	3	n.a.	n.a.	2	n.a.
Th	n.a.	n.a.	1.6	n.a.	1.7	2.2	n.a.	n.a.	n.a.	2.3	n.a.	2.5	1.6	2.5	n.a.	n.a.	1.6	n.a.
U	n.a.	n.a.	0.60	n.a.	0.61	0.84	n.a.	n.a.	n.a.	0.82	n.a.	0.87	0.57	0.90	n.a.	n.a.	0.55	n.a.

Table A.3 *Chemical compositions of sideromelane (SM) and palagonitized glass (PG) in the SE-02b drill core as a function of depth. Results are given as average of n analyses. If no sideromelane or palagonitized glass analysis is listed the phase in question was not present in the analyzed sample.*

	13.2 m		**40.4 m**		**43.7 m**		**56.1 m**		**67.5 m**		**80.5 m**		**92.6 m**		**106.1 m**		**120.8 m**	
	SM (n=17)	PG (n=6)	SM (n=8)	PG (n=7)	SM	PG (n=10)	SM (n=8)	PG (n=18)	SM (n=3)	PG (n=10)	SM	PG (n=7)	SM	PG (n=6)	SM	PG (n=24)	SM	PG (n=9)
Major elements (wt.%)																		
SiO_2	46.88	36.49	46.88	31.33	n.a.	37.59	46.76	35.46	47.04	33.94	n.a.	35.40	n.a.	33.40	n.a.	34.38	n.a.	34.80
TiO_2	2.61	3.83	2.53	2.94	n.a.	4.08	2.57	4.10	2.57	3.49	n.a.	3.99	n.a.	2.97	n.a.	3.54	n.a.	3.07
Al_2O_3	16.25	9.22	16.56	8.90	n.a.	11.97	16.22	12.79	16.05	12.17	n.a.	12.39	n.a.	12.21	n.a.	11.66	n.a.	14.18
FeO	12.10	17.67	12.03	15.85	n.a.	19.28	11.94	19.02	12.25	18.04	n.a.	17.48	n.a.	18.80	n.a.	17.87	n.a.	19.31
MnO	0.21	0.31	0.20	0.26	n.a.	0.34	0.21	0.29	0.20	0.28	n.a.	0.30	n.a.	0.34	n.a.	0.30	n.a.	0.42
MgO	5.83	6.49	5.76	5.30	n.a.	4.91	5.82	4.80	6.00	7.07	n.a.	9.07	n.a.	8.06	n.a.	8.97	n.a.	9.21
CaO	9.45	8.23	9.69	6.54	n.a.	9.89	9.60	8.72	9.62	7.37	n.a.	7.25	n.a.	7.71	n.a.	7.37	n.a.	6.53
Na_2O	3.91	1.10	3.85	0.64	n.a.	0.59	3.75	0.69	3.84	1.30	n.a.	1.16	n.a.	0.70	n.a.	1.39	n.a.	0.53
K_2O	0.72	0.34	0.69	0.67	n.a.	0.31	0.71	0.35	0.76	0.95	n.a.	0.63	n.a.	0.95	n.a.	0.63	n.a.	0.48
P_2O_5	0.38	0.42	0.37	0.51	n.a.	0.73	0.40	0.67	0.38	0.57	n.a.	0.53	n.a.	0.54	n.a.	0.49	n.a.	0.46
Sum	98.34	84.09	98.58	72.94	n.a.	89.69	97.98	86.87	98.71	85.18	n.a.	88.20	n.a.	85.67	n.a.	86.60	n.a.	88.98
Trace elements (ppm)																		
V	n.a.	n.a.	n.a.	n.a.	275	304	268	281	n.a.	n.a.	n.a.	n.a.	n.a.	179	n.a.	n.a.	n.a.	241
Rb	n.a.	n.a.	n.a.	n.a.	14.6	3.3	14.1	4.6	n.a.	n.a.	n.a.	n.a.	n.a.	15.9	n.a.	n.a.	n.a.	11.5
Sr	n.a.	n.a.	n.a.	n.a.	332	501	333	490	n.a.	n.a.	n.a.	n.a.	n.a.	381	n.a.	n.a.	n.a.	268
Y	n.a.	n.a.	n.a.	n.a.	33	46	32	47	n.a.	n.a.	n.a.	n.a.	n.a.	46	n.a.	n.a.	n.a.	35
Zr	n.a.	n.a.	n.a.	n.a.	188	265	188	276	n.a.	n.a.	n.a.	n.a.	n.a.	264	n.a.	n.a.	n.a.	215
Nb	n.a.	n.a.	n.a.	n.a.	21.5	30.0	21.3	31.7	n.a.	n.a.	n.a.	n.a.	n.a.	29.6	n.a.	n.a.	n.a.	22.5
Ba	n.a.	n.a.	n.a.	n.a.	160	51	160	64	n.a.	n.a.	n.a.	n.a.	n.a.	41	n.a.	n.a.	n.a.	34
La	n.a.	n.a.	n.a.	n.a.	17.9	25.4	17.5	26.4	n.a.	n.a.	n.a.	n.a.	n.a.	23.6	n.a.	n.a.	n.a.	18.9
Ce	n.a.	n.a.	n.a.	n.a.	41.1	59.4	40.9	61.4	n.a.	n.a.	n.a.	n.a.	n.a.	55.3	n.a.	n.a.	n.a.	44.1
Pr	n.a.	n.a.	n.a.	n.a.	5.66	7.83	5.42	8.13	n.a.	n.a.	n.a.	n.a.	n.a.	7.99	n.a.	n.a.	n.a.	6.13
Nd	n.a.	n.a.	n.a.	n.a.	25.8	36.1	25.5	37.8	n.a.	n.a.	n.a.	n.a.	n.a.	37.3	n.a.	n.a.	n.a.	28.0
Sm	n.a.	n.a.	n.a.	n.a.	7.0	9.5	7.1	10.6	n.a.	n.a.	n.a.	n.a.	n.a.	10.0	n.a.	n.a.	n.a.	7.5
Eu	n.a.	n.a.	n.a.	n.a.	2.46	3.32	2.30	3.37	n.a.	n.a.	n.a.	n.a.	n.a.	3.29	n.a.	n.a.	n.a.	2.52

Table A.3 *(continued)*

	13.2 m		**40.4 m**		**43.7 m**		**56.1 m**		**67.5 m**		**80.5 m**		**92.6 m**		**106.1 m**		**120.8 m**	
	SM	PG	SM	PG	SM	PG	SM	PG	SM	PG	SM	PG	SM	PG	SM	PG	SM	PG
Trace elements (ppm)																		
Gd	n.a.	n.a.	n.a.	n.a.	7.49	9.66	6.71	10.27	n.a.	n.a.	n.a.	n.a.	n.a.	10.48	n.a.	n.a.	n.a.	7.36
Tb	n.a.	n.a.	n.a.	n.a.	1.03	1.48	1.03	1.54	n.a.	n.a.	n.a.	n.a.	n.a.	1.63	n.a.	n.a.	n.a.	1.13
Dy	n.a.	n.a.	n.a.	n.a.	6.41	9.26	6.59	9.51	n.a.	n.a.	n.a.	n.a.	n.a.	9.38	n.a.	n.a.	n.a.	6.91
Ho	n.a.	n.a.	n.a.	n.a.	1.36	1.77	1.24	1.90	n.a.	n.a.	n.a.	n.a.	n.a.	1.98	n.a.	n.a.	n.a.	1.33
Er	n.a.	n.a.	n.a.	n.a.	3.9	5.1	3.7	5.2	n.a.	n.a.	n.a.	n.a.	n.a.	5.1	n.a.	n.a.	n.a.	4.1
Tm	n.a.	n.a.	n.a.	n.a.	0.50	0.69	0.51	0.74	n.a.	n.a.	n.a.	n.a.	n.a.	0.74	n.a.	n.a.	n.a.	0.58
Yb	n.a.	n.a.	n.a.	n.a.	3.54	4.56	3.38	4.50	n.a.	n.a.	n.a.	n.a.	n.a.	4.95	n.a.	n.a.	n.a.	3.71
Lu	n.a.	n.a.	n.a.	n.a.	0.529	0.640	0.478	0.693	n.a.	n.a.	n.a.	n.a.	n.a.	0.736	n.a.	n.a.	n.a.	0.527
Hf	n.a.	n.a.	n.a.	n.a.	5.10	6.83	4.87	6.97	n.a.	n.a.	n.a.	n.a.	n.a.	6.82	n.a.	n.a.	n.a.	5.46
Ta	n.a.	n.a.	n.a.	n.a.	1.36	1.81	1.32	1.88	n.a.	n.a.	n.a.	n.a.	n.a.	1.82	n.a.	n.a.	n.a.	1.38
Pb	n.a.	n.a.	n.a.	n.a.	2	2	2	2	n.a.	n.a.	n.a.	n.a.	n.a.	3	n.a.	n.a.	n.a.	2
Th	n.a.	n.a.	n.a.	n.a.	1.6	2.1	1.5	2.2	n.a.	n.a.	n.a.	n.a.	n.a.	2.3	n.a.	n.a.	n.a.	1.6
U	n.a.	n.a.	n.a.	n.a.	0.57	0.72	0.55	0.81	n.a.	n.a.	n.a.	n.a.	n.a.	0.89	n.a.	n.a.	n.a.	0.63

Table A.3 *(continued)*

	134.3 m		**141.5 m**		**144.1 to 148.7 m**		**150.3 m**		**159.0 m**		**165.6 to 168.1 m**		**177.8 m**		**181.5 m**	
	SM	PG (n=20)	SM (n=6)	PG	SM (n=10)	PG (n=8)	SM (n=9)	PG (n=9)	SM (n=9)	PG (n=15)	SM (n=9)	PG (n=13)	SM (n=20)	PG (n=30)	SM (n=9)	PG
Major elements (wt.%)																
SiO_2	n.a.	33.61	46.91	n.a.	46.74	36.76	46.43	33.30	46.46	33.20	46.39	37.49	46.28	34.00	46.38	n.a.
TiO_2	n.a.	3.66	2.51	n.a.	2.53	4.45	2.63	4.15	2.78	4.05	2.84	4.40	2.88	4.22	2.93	n.a.
Al_2O_3	n.a.	12.28	16.78	n.a.	16.67	12.17	16.43	11.97	15.95	13.20	16.05	14.84	16.08	12.79	16.09	n.a.
FeO	n.a.	18.97	11.78	n.a.	11.95	20.54	12.32	18.57	12.66	19.58	12.97	18.29	12.95	19.32	12.98	n.a.

Table A.3 *(continued)*

	134.3 m		**141.5 m**		**144.1 to 148.7 m**		**150.3 m**		**159.0 m**		**165.6 to 168.1 m**		**177.8 m**		**181.5 m**	
	SM	PG	SM	PG	SM	PG	SM	PG	SM	PG	SM	PG	SM	PG	SM	PG
Major elements (wt.%)																
MnO	n.a.	0.33	0.19	n.a.	0.22	0.36	0.20	0.28	0.22	0.33	0.22	0.31	0.22	0.31	0.23	n.a.
MgO	n.a.	7.55	5.88	n.a.	5.87	4.48	5.94	3.70	5.73	6.12	5.54	5.50	5.51	5.23	5.39	n.a.
CaO	n.a.	6.48	9.59	n.a.	9.68	9.39	9.53	9.13	9.32	6.15	9.07	7.72	9.07	7.37	8.98	n.a.
Na_2O	n.a.	1.57	3.85	n.a.	3.82	0.98	3.81	1.05	3.95	1.91	4.03	1.05	4.03	1.05	4.10	n.a.
K_2O	n.a.	0.55	0.68	n.a.	0.68	0.35	0.69	0.56	0.72	0.66	0.77	0.74	0.75	0.71	0.77	n.a.
P_2O_5	n.a.	0.53	0.37	n.a.	0.35	0.66	0.35	0.60	0.36	0.52	0.42	0.64	0.41	0.38	0.41	n.a.
Sum	n.a.	85.52	98.53	n.a.	98.49	90.13	98.34	83.32	98.14	85.74	98.29	90.97	98.17	85.37	98.27	n.a.
Trace elements (ppm)																
V	n.a.	n.a.	n.a.	n.a.	275	337	n.a.	n.a.	n.a.	n.a.	276	271	n.a.	n.a.	n.a.	n.a.
Rb	n.a.	n.a.	n.a.	n.a.	13.5	4.7	n.a.	n.a.	n.a.	n.a.	14.2	9.3	n.a.	n.a.	n.a.	n.a.
Sr	n.a.	n.a.	n.a.	n.a.	334	500	n.a.	n.a.	n.a.	n.a.	351	526	n.a.	n.a.	n.a.	n.a.
Y	n.a.	n.a.	n.a.	n.a.	32	51	n.a.	n.a.	n.a.	n.a.	33	55	n.a.	n.a.	n.a.	n.a.
Zr	n.a.	n.a.	n.a.	n.a.	182	283	n.a.	n.a.	n.a.	n.a.	193	315	n.a.	n.a.	n.a.	n.a.
Nb	n.a.	n.a.	n.a.	n.a.	21.0	32.8	n.a.	n.a.	n.a.	n.a.	22.2	38.3	n.a.	n.a.	n.a.	n.a.
Ba	n.a.	n.a.	n.a.	n.a.	155	52	n.a.	n.a.	n.a.	n.a.	168	78	n.a.	n.a.	n.a.	n.a.
La	n.a.	n.a.	n.a.	n.a.	17.1	27.0	n.a.	n.a.	n.a.	n.a.	17.4	30.3	n.a.	n.a.	n.a.	n.a.
Ce	n.a.	n.a.	n.a.	n.a.	40.0	64.0	n.a.	n.a.	n.a.	n.a.	42.8	72.8	n.a.	n.a.	n.a.	n.a.
Pr	n.a.	n.a.	n.a.	n.a.	5.37	8.67	n.a.	n.a.	n.a.	n.a.	5.71	9.73	n.a.	n.a.	n.a.	n.a.
Nd	n.a.	n.a.	n.a.	n.a.	25.0	38.4	n.a.	n.a.	n.a.	n.a.	26.4	44.7	n.a.	n.a.	n.a.	n.a.
Sm	n.a.	n.a.	n.a.	n.a.	7.2	10.2	n.a.	n.a.	n.a.	n.a.	7.3	11.9	n.a.	n.a.	n.a.	n.a.
Eu	n.a.	n.a.	n.a.	n.a.	2.21	3.79	n.a.	n.a.	n.a.	n.a.	2.48	3.74	n.a.	n.a.	n.a.	n.a.
Gd	n.a.	n.a.	n.a.	n.a.	6.80	10.35	n.a.	n.a.	n.a.	n.a.	7.08	11.78	n.a.	n.a.	n.a.	n.a.
Tb	n.a.	n.a.	n.a.	n.a.	1.05	1.59	n.a.	n.a.	n.a.	n.a.	1.05	1.72	n.a.	n.a.	n.a.	n.a.
Dy	n.a.	n.a.	n.a.	n.a.	6.96	10.65	n.a.	n.a.	n.a.	n.a.	6.70	10.89	n.a.	n.a.	n.a.	n.a.
Ho	n.a.	n.a.	n.a.	n.a.	1.30	1.95	n.a.	n.a.	n.a.	n.a.	1.29	2.03	n.a.	n.a.	n.a.	n.a.
Er	n.a.	n.a.	n.a.	n.a.	3.7	5.6	n.a.	n.a.	n.a.	n.a.	3.7	5.9	n.a.	n.a.	n.a.	n.a.

Table A.3 *(continued)*

	134.3 m		**141.5 m**		**144.1 to 148.7 m**		**150.3 m**		**159.0 m**		**165.6 to 168.1 m**		**177.8 m**		**181.5 m**	
	SM	PG	SM	PG	SM	PG	SM	PG	SM	PG	SM	PG	SM	PG	SM	PG
Trace elements (ppm)																
Tm	n.a.	n.a.	n.a.	n.a.	0.52	0.73	n.a.	n.a.	n.a.	n.a.	0.53	0.88	n.a.	n.a.	n.a.	n.a.
Yb	n.a.	n.a.	n.a.	n.a.	3.27	5.09	n.a.	n.a.	n.a.	n.a.	3.32	5.41	n.a.	n.a.	n.a.	n.a.
Lu	n.a.	n.a.	n.a.	n.a.	0.493	0.764	n.a.	n.a.	n.a.	n.a.	0.495	0.802	n.a.	n.a.	n.a.	n.a.
Hf	n.a.	n.a.	n.a.	n.a.	4.90	7.26	n.a.	n.a.	n.a.	n.a.	4.94	8.15	n.a.	n.a.	n.a.	n.a.
Ta	n.a.	n.a.	n.a.	n.a.	1.32	2.03	n.a.	n.a.	n.a.	n.a.	1.38	2.24	n.a.	n.a.	n.a.	n.a.
Pb	n.a.	n.a.	n.a.	n.a.	2	1	n.a.	n.a.	n.a.	n.a.	2	1	n.a.	n.a.	n.a.	n.a.
Th	n.a.	n.a.	n.a.	n.a.	1.5	2.2	n.a.	n.a.	n.a.	n.a.	1.5	2.5	n.a.	n.a.	n.a.	n.a.
U	n.a.	n.a.	n.a.	n.a.	0.49	0.83	n.a.	n.a.	n.a.	n.a.	0.56	0.94	n.a.	n.a.	n.a.	n.a.

Mg and K accumulation in altered glass

Previous studies have characterized reaction progress during palagonitized glass maturation by quantifying the accumulation of certain elements, which are incorporated due to the formation of clay minerals in the palagonitized glass matrix. Two notable examples of this are the accumulaction of Mg (Stroncik and Schmincke, 2001) and K (Zhou and Fyfe, 1989). The accumulation of elements A_{el} was calculated as:

$$A_{el}(\%) = \left(C_{el,pal.} - C_{el,sdml.}\right) / C_{el,sdml.} \cdot 100 \qquad \text{(Eq. A.1)}$$

where $C_{el,pal.}$ and $C_{el,sdml}$ refer to the concentrations of MgO or K_2O in palagonitized glass and sideromelane, respectively. Results are shown in figure A.1.

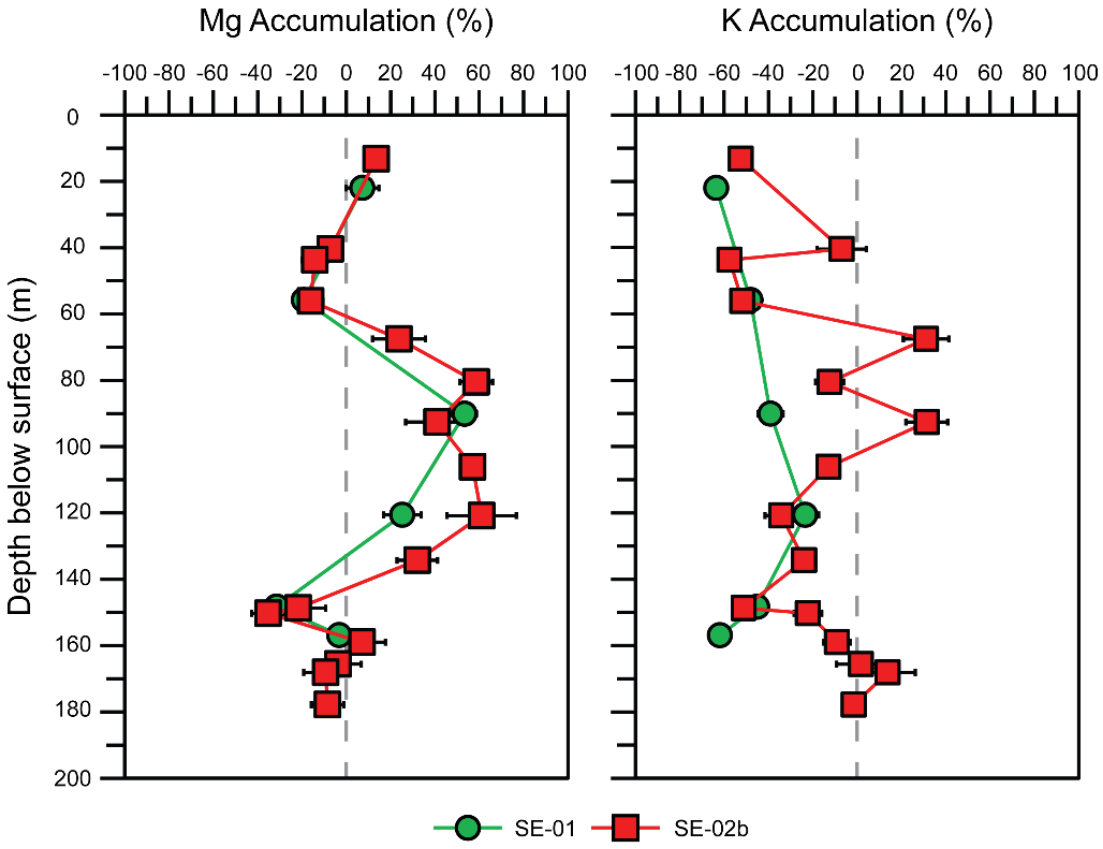

Figure A.1 *Percent Mg and K accumulation in palagonitized glass after Stroncik and Schmincke (2001) and Zhou and Fyfe (1989). Error bars indicate the standard error of n measurements.*

Table A.4. *Results of immobile trace element isocon mass balance between sideromelane and palagonitized glass. ΔCi: gain or loss of element in wt.% or ppm relative to sideromelane. ΔCi/Ci0: percent gain or loss of element relative to initial concentration in sideromelane. Changes in water contents estimated based on stoichiometric volatile content.*

Drill Core		**SE-01**				**SE-02b**					
Depth below surface		55. 8 m	92.6 m	120.6 m	148.3 m	43.7 m	56. 1 m	92.6 m	120.8 m	148.7 m	165.6 m
Palagonite type		Type II	Type III	Type III	Type I	Type I-II	Type II	Type III	Type III	Type I	Type II
Isocon slope		1.43	1.38	1.50	1.54	1.39	1.47	1.39	1.07	1.54	1.70
Fv[a]		0.8-1.0	0.9-1.0	0.9-0.8	0.8-0.9	0.9-1.0	0.8-0.9	0.9-1.0	1.1-1.3	0.8-0.9	0.7-0.8
Overall mass change (%)[b]		-30.0	-27.7	-33.3	-35.0	-28.2	-31.7	-28.1	-6.6	-35.2	-41.3
SiO_2	ΔCi	-22.2	-25.1	-21.6	-22.4	-19.6	-22.1	-22.6	-14.1	-22.8	-24.3
	ΔCi/Ci0	-47.5	-53.8	-46.3	-47.9	-42.1	-47.4	-48.5	-30.2	-48.9	-52.2
TiO_2	ΔCi	0.1	0.0	-0.2	0.1	0.2	0.2	-0.6	0.2	0.2	-0.1
	ΔCi/Ci0	2.3	0.2	-7.0	4.7	8.7	8.6	-20.9	6.2	6.7	-3.7
Al_2O_3	ΔCi	-7.6	-8.1	-6.6	-9.8	-7.7	-7.5	-7.5	-3.0	-8.4	-7.6
	ΔCi/Ci0	-46.6	-49.4	-40.7	-60.3	-47.2	-46.1	-46.0	-18.5	-51.5	-46.7
FeO	ΔCi	0.8	0.9	-1.0	0.7	1.4	1.4	1.1	5.6	0.9	-2.0
	ΔCi/Ci0	6.8	7.5	-7.8	5.3	11.4	11.6	8.8	45.3	7.1	-15.9
MnO	ΔCi	0.0	0.0	0.0	0.0	0.0	0.0	0.0	0.2	0.0	0.0
	ΔCi/Ci0	-4.4	15.9	-6.5	-2.4	14.8	-12.0	12.5	82.8	9.8	-19.0
MgO	ΔCi	-2.7	0.1	-1.2	-3.4	-2.2	-2.7	0.1	2.9	-2.8	-2.6
	ΔCi/Ci0	-46.5	2.3	-20.5	-59.0	-38.4	-47.6	1.4	50.5	-49.3	-45.0
CaO	ΔCi	-2.0	-3.8	-4.6	-3.1	-2.3	-3.1	-3.8	-3.3	-3.3	-4.8
	ΔCi/Ci0	-21.2	-39.8	-47.8	-32.0	-24.2	-33.5	-40.8	-34.9	-35.1	-50.8
Na_2O	ΔCi	-3.2	-3.4	-2.9	-2.7	-3.5	-3.5	-3.4	-3.4	-3.3	-3.3
	ΔCi/Ci0	-82.9	-87.5	-75.3	-70.8	-89.2	-89.6	-87.2	-87.3	-83.8	-83.9
K_2O	ΔCi	-0.4	-0.4	-0.3	-0.4	-0.5	-0.5	0.0	-0.3	-0.5	-0.3
	ΔCi/Ci0	-60.7	-60.6	-47.3	-62.1	-69.5	-65.0	-5.5	-38.5	-68.4	-39.4
P_2O_5	ΔCi	0.1	-0.1	0.2	0.1	0.1	0.1	0.0	0.0	0.0	0.0
	ΔCi/Ci0	21.8	-30.2	62.0	14.6	37.3	32.6	2.2	12.9	12.5	-0.1
H_2O[c]	ΔCi	7.2	12.1	4.9	6.1	5.7	5.9	8.6	8.6	4.7	3.7
	ΔCi/Ci0	467.0	782.7	317.6	393.9	346.9	359.3	522.4	522.1	286.2	222.9

Table A.4 *(continued)*

V	ΔCi	-32.6	-158.1	-85.0	-42.1	-55.5	-81.7	-144.6	-48.3	-55.2	-114.5
	ΔCi/Ci0	-11.6	-56.3	-30.3	-15.0	-20.3	-29.9	-52.9	-17.7	-20.2	-41.9
Rb	ΔCi	-9.8	-7.8	-8.0	-4.9	-11.7	-10.9	-2.7	-3.3	-11.0	-8.6
	ΔCi/Ci0	-69.5	-55.1	-56.5	-34.9	-83.2	-77.7	-19.1	-23.5	-78.2	-61.3
Sr	ΔCi	23.1	-180.2	-20.5	-79.4	22.4	-2.9	-63.6	-86.8	-13.2	-28.7
	ΔCi/Ci0	6.5	-51.0	-5.8	-22.5	6.6	-0.9	-18.8	-25.7	-3.9	-8.5
Y	ΔCi	-0.2	2.6	0.8	1.2	0.4	-0.3	0.4	0.3	0.5	-0.2
	ΔCi/Ci0	-0.7	7.8	2.4	3.7	1.1	-0.9	1.1	0.9	1.4	-0.7
Zr	ΔCi	-2.5	-9.3	6.6	4.4	2.3	0.5	2.4	12.8	-4.3	-2.7
	ΔCi/Ci0	-1.3	-4.8	3.4	2.2	1.2	0.3	1.3	6.8	-2.3	-1.4
Nb	ΔCi	-0.4	-3.1	0.5	0.9	0.1	0.2	-0.2	-0.4	-0.2	1.0
	ΔCi/Ci0	-1.9	-13.8	2.3	3.9	0.3	0.7	-0.9	-1.9	-1.0	4.8
Ba	ΔCi	-116.5	-153.3	-110.0	-135.1	-123.9	-117.0	-130.8	-128.6	-126.6	-114.9
	ΔCi/Ci0	-71.6	-94.3	-67.7	-83.1	-77.2	-72.9	-81.4	-80.1	-78.9	-71.5
La	ΔCi	0.0	-0.3	-0.2	1.0	0.7	0.5	-0.5	0.2	0.0	0.3
	ΔCi/Ci0	-0.3	-1.5	-1.0	5.5	4.2	3.1	-3.0	0.9	-0.1	1.6
Ce	ΔCi	0.1	1.1	1.1	1.4	1.4	0.7	-1.4	0.1	0.3	1.5
	ΔCi/Ci0	0.3	2.6	2.7	3.3	3.5	1.8	-3.4	0.2	0.6	3.7
Pr	ΔCi	0.0	0.3	0.0	0.5	0.1	0.0	0.2	0.2	0.1	0.2
	ΔCi/Ci0	-0.3	5.1	0.8	8.5	1.6	0.3	3.8	3.5	1.5	3.2
Nd	ΔCi	-0.4	-0.4	0.3	2.6	0.2	0.1	1.1	0.5	-0.8	0.6
	ΔCi/Ci0	-1.4	-1.6	1.3	9.5	0.9	0.5	4.4	1.9	-3.1	2.2
Sm	ΔCi	-0.2	1.9	-0.4	-0.5	-0.3	0.1	0.1	-0.2	-0.5	-0.1
	ΔCi/Ci0	-2.4	25.0	-5.3	-6.8	-4.5	1.7	1.4	-2.2	-7.4	-1.8
Eu	ΔCi	-0.1	0.3	0.0	-0.2	0.0	-0.1	0.0	0.0	0.1	-0.2
	ΔCi/Ci0	-3.3	11.6	0.4	-6.0	0.9	-2.5	0.5	-0.2	4.2	-6.9
Gd	ΔCi	-0.2	-0.1	0.0	-0.1	-0.1	0.0	0.5	-0.1	-0.3	-0.1
	ΔCi/Ci0	-3.2	-1.8	-0.4	-0.8	-1.0	0.1	7.7	-1.8	-4.3	-1.3
Tb	ΔCi	0.0	0.0	0.0	0.0	0.0	0.0	0.1	0.0	0.0	0.0
	ΔCi/Ci0	0.0	1.8	2.5	3.2	2.5	1.1	12.6	1.4	-0.7	-2.6

Table A.4 *(continued)*

Dy	ΔCi	-0.2	1.4	-0.1	0.9	0.0	-0.2	0.1	-0.2	0.2	-0.3
	ΔCi/Ci0	-3.4	20.3	-0.7	12.9	-0.1	-2.5	1.4	-3.0	3.6	-4.0
Ho	ΔCi	0.0	0.0	0.0	0.0	0.0	0.0	0.1	0.0	0.0	-0.1
	ΔCi/Ci0	-3.0	-1.9	-1.5	1.4	-1.7	0.0	10.0	-3.8	-2.6	-7.8
Er	ΔCi	0.0	-0.1	0.0	0.2	-0.1	-0.1	-0.1	0.1	-0.1	-0.3
	ΔCi/Ci0	-0.2	-3.0	-0.8	5.1	-2.3	-4.0	-2.2	2.3	-3.5	-7.7
Tm	ΔCi	0.0	0.0	0.0	0.0	0.0	0.0	0.0	0.0	0.0	0.0
	ΔCi/Ci0	-5.6	2.3	-1.8	-6.2	-3.4	-1.9	3.1	4.9	-8.1	0.1
Yb	ΔCi	0.0	0.0	0.1	0.3	-0.1	-0.3	0.2	0.1	-0.1	-0.2
	ΔCi/Ci0	-1.3	-0.6	2.9	7.8	-3.2	-9.1	5.3	2.5	-2.4	-6.0
Lu	ΔCi	0.0	0.0	0.0	0.0	0.0	0.0	0.0	0.0	0.0	0.0
	ΔCi/Ci0	-0.1	-1.2	-1.7	-8.8	-7.7	-4.9	6.4	-1.1	-0.5	-5.3
Hf	ΔCi	-0.1	0.0	0.2	0.5	0.0	-0.2	0.0	0.2	-0.2	-0.2
	ΔCi/Ci0	-1.2	-0.6	4.5	9.1	-1.0	-3.9	-0.9	3.1	-5.0	-3.3
Ta	ΔCi	0.0	-0.1	0.0	0.1	0.0	-0.1	0.0	-0.1	0.0	0.0
	ΔCi/Ci0	-2.5	-7.8	3.5	4.0	-3.1	-4.4	-2.5	-3.9	-2.0	-1.8
Pb	ΔCi	0.0	-1.0	-0.9	-0.1	-0.5	-0.2	0.4	-0.2	-0.9	-1.1
	ΔCi/Ci0	1.6	-51.3	-50.0	-5.7	-28.0	-12.9	24.9	-13.8	-50.9	-61.8
Th	ΔCi	-0.1	0.0	0.0	0.0	0.0	0.0	0.1	0.0	-0.1	-0.1
	ΔCi/Ci0	-3.5	2.9	1.2	0.5	-2.3	-2.1	6.6	0.3	-4.4	-4.4
U	ΔCi	0.0	0.0	0.0	0.0	0.0	0.0	0.1	0.0	0.0	0.0
	ΔCi/Ci0	2.2	3.1	1.6	2.0	-4.4	2.3	17.4	9.0	-0.8	2.0

[a] Volume factors were calculated for palagonitized glass densities between 2.0 - 2.3 g/cm^3.

[b] Overall mass changes are given by the isocon slopes (m) of immobile trace element mass balance as (1-1/m)·100%.

[c] Estimated mass changes for H_2O, based on the assumption that stoichiometric volatile content approximates H_2O contents.

Immobile TiO_2 vs constant volume mass balance

Additional palagonitization mass balance for comparison with immobile trace element mass balance results was carried out assuming 1) immobility of TiO_2 or 2) constant volume alteration. Immobile TiO_2 mass balance was calculated analogously to bulk rock mass balance following the approach of MacLean (1990):

$$\Delta C_n = C_n^a \cdot \left(C_{TiO_2}^i / C_{TiO_2}^a\right) - C_n^i \qquad \text{(Eq. A.2)}$$

where ΔC_n is the mass change for element n in wt.% relative to the initial mass of unaltered glass, C^a_n and C^i_n are the weight percent of element n in palagonitized glass and sideromelane, respectively, and C^a_{TiO2} and C^i_{TiO2} are wt.% of TiO_2 in palagonitized glass and sideromelane, respectively. Results obtained mathematically by this approach are identical to those obtained graphically by using the isocon method for immobile TiO_2.

Mass balance calculations assuming constant volume were calculated using the formula of (Gresens, 1967):

$$\Delta C_n = f_v(\rho_a/\rho_i)C_a - C_i \qquad \text{(Eq. A.3)}$$

where f_v is the volume factor describing the ratio of the volumes of altered to initial state, ρ_a and ρ_i are the densities of the initial and altered rocks, respectively, and C_a and C_i represent the oxide concentrations of the altered and initial rocks, respectively. Because no volume change is assumed, f_v is equal to one in our calculations. Assumed densities for palagonitized glass and sideromelane were 2.0 and 2.75 g cm^{-3}, respectively (see main text for discussion of assumed densities). Results of these calculations are summarized in figure A.2 and indicate a generally good agreement between constant volume calculations and immobile TiO_2 mass balance for type I palagonitized glass. This confirms our results of immobile trace element mass balance which suggested that volume changes during palagonitization are minor and TiO_2 is largely immobile during this process. Apart from TiO_2 figure A.2 also suggests limited mobility or even immobility of FeO for type I palagonitized glass, because mass balance results for both methods cluster around zero (+/- ca. 20%). This also supports the results of immobile trace element mass balance, which indicated FeO immobility during palagonitization. With increasing maturation of the material mass balance results of the two methods begin to diverge noticeably. Immobile trace element mass balance suggested mobilization of TiO_2 at advanced stages of palagonitized glass maturation (see main text for details). Therefore, the observed deviation of mass balance results for type II and especially type III palagonitized glass may be either due to a) mobilization of TiO_2, or b) volume changes during maturation or c) a combination of both of these factors.

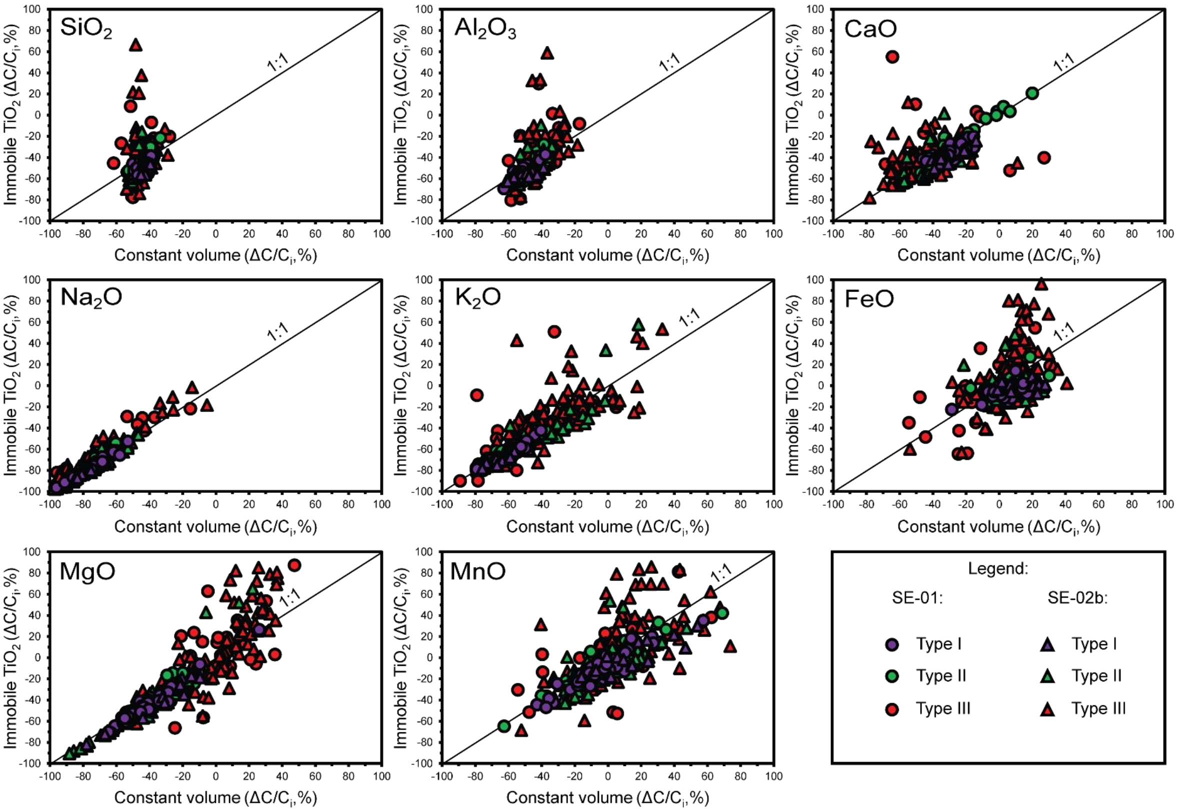

Figure A.2 *Comparison of mass balance results for types I-III palagonitized glass vs sideromelane assuming either constant volume alteration (results plotted along x-axis) or immobility of* TiO_2 *(results plotted along y-axis). Results agree well for type I (i.e., gel palagonite, purple), but noticeably diverge for the more mature types II-III (green and red), indicating that constant volume alteration and* TiO_2 *immobility should not be assumed during palagonitized glass aging.*

Supplementary references

Grant, J.A., 1986. The isocon diagram; a simple solution to Gresens' equation for metasomatic alteration. Econ. Geol. 81, 1976–1982.

Gresens, R.L., 1967. Composition-volume relationships of metasomatism. Chem. Geol. 2, 47–65.

MacLean, W.H., 1990. Mass change calculations in altered rock series. Miner. Depos. 25, 44–49.

Stroncik, N.A., Schmincke, H., 2001. Evolution of palagonite: Crystallization, chemical changes, and element budget. Geochemistry, Geophys. Geosystems 2.

Zhou, Z., Fyfe, W.S., 1989. Palagonitization of basaltic glass from DSDP Site 335, Leg 37: textures, chemical composition, and mechanism of formation. Am. Mineral. 74, 1045–1053.

Appendix B: Supplementary information for Paper III

1 Study sites for low-temperature seafloor alteration
2 Estimation of equilibrium constants for phillipsite
3 Estimation of dissolution rates for basaltic glass

Study sites for low-temperature seafloor alteration

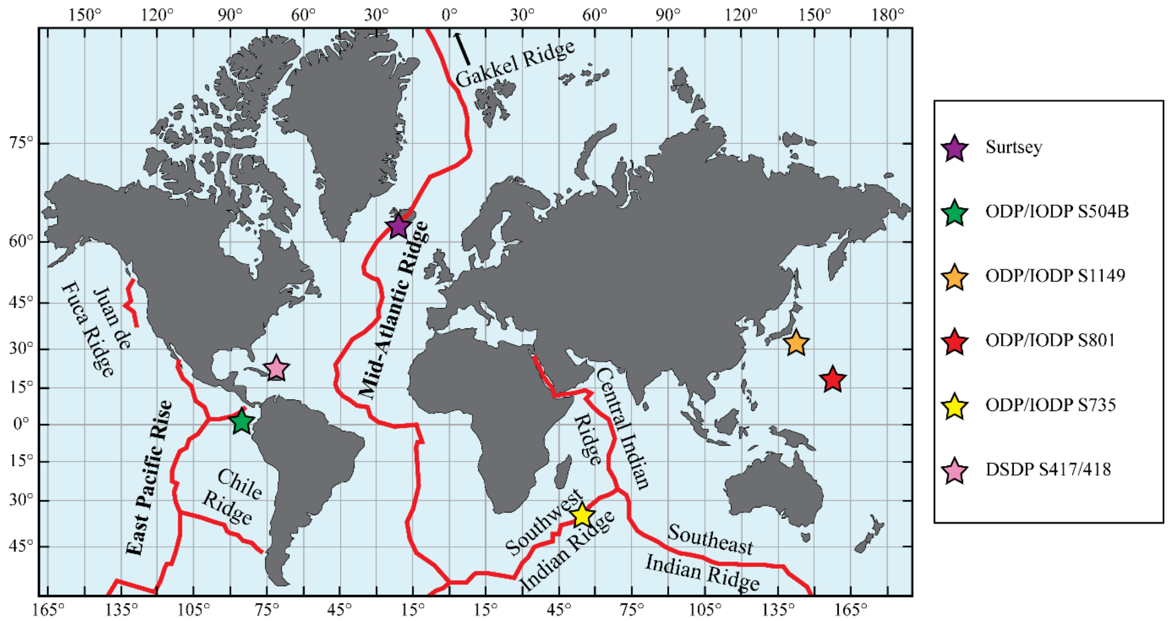

Figure A.1 *Reference sites for the study of low-temperature seafloor alteration.*

Estimation of equilibrium constants for phillipsite

In most cases the values for log K (T) were retrieved directly from the PHREEQC carbfix.dat thermodynamic database. For the zeolite mineral phillipsite thermodynamic parameters were estimated based on mineral stoichiometries. The Gibbs free energies of formation, ΔG°_f, in J mol^{-1}, entropies, S°, in J mol^{-1} K^{-1}, and heat capacities, Cp, in J mol^{-1} K^{-1}, were estimated according to the techniques outlined in Chermak and Rimstidt (1989), Holland (1989), and Berman and Brown (1985). From these, the apparent standard partial molal Gibbs energies at temperatures of T= 0-150°C (273.15-423.15 K) were calculated, e.g., according to Gysi and Stefánsson (2011):

$$\Delta\overline{G}^\circ_T = \Delta G^\circ_f - S^\circ(T - 298.15K) + \int_{298.15K}^{T} CpdT - T\int_{298.15K}^{T} \frac{Cp}{TdT} \qquad \text{(Eq. A.1)}$$

Gibbs free energies for the dissolution reactions of phillipsite were calculated as:

$$\Delta G^\circ_T = \left(\sum_{i=1}^{n} v_i \cdot \Delta G_{i,T}\right) - \Delta\overline{G}^\circ_T \qquad \text{(Eq. A.2)}$$

where v_n are the stoichiometric coefficients, positive for products and negative for reactants, and $\Delta G_{n,T}$ are the apparent standard Gibbs energies of products and reactants at temperature T (Table A.1).

Equilibrium constants were calculated as:

$$\log K(T) = \frac{\Delta G_T^\circ}{-RT\ln(10)} \qquad \text{(Eq. A.3)}$$

where R is the gas constant.

Subsequently, values for log K(T) (Table A.2) were expressed in the form

$$\log K(T) = A_1 + A_2T + \frac{A_3}{T} + A_4\log_{10}T + \frac{A_5}{T^2} + A_6T^2 \qquad \text{(Eq. A.4)}$$

compatible with the data input format for the PHREEQC geochemical modeling software through nonlinear regression.

Table A.1. *Apparent standard Gibbs energies in J mol^{-1} for aqueous species and phillipsite between 0 and 150°C. Values are listed at atmospheric pressure for temperatures ≤100°C and water saturation pressure for temperatures >100°C.*

T (K)	273.15	298.15	323.15	348.15	373.15	398.15	423.15
T (°C)	0	25	50	75	100	125	150
H_2O	-235515.000	-237181.000	-239006.000	-240977.000	-243084.000	-245315.000	-247665.000
H^+	0	0	0	0	0	0	0
OH^-	-157386.000	-157297.000	-156905.000	-156309.000	-155535.000	-154584.000	-153442.000
HCO_3^-	-584427.000	-586940.000	-589372.000	-591760.000	-594106.000	-596398.000	-598615.000
K^+	-279940.000	-282462.000	-284999.000	-287564.000	-290158.000	-292777.000	-295417.000
Na^+	-260453.000	-261881.000	-263385.000	-264980.000	-266668.000	-268439.000	-270286.000
Ca^{2+}	-554160.000	-552790.000	-551349.000	-549856.000	-548307.000	-546693.000	-544996.000
SiO_2	-833534.000	-834875.000	-835984.000	-837090.000	-838273.000	-839560.000	-840960.000
Al^{3+}	-495812.000	-487478.000	-478874.000	-470079.000	-461102.000	-451931.000	-442534.000
Mg^{2+}	-457394.000	-453985.000	-450519.000	-447040.000	-443550.000	-440036.000	-436476.000
Fe^{2+}	-94100.000	-91504.000	-88831.000	-86116.000	-83359.000	-80551.000	-77671.000
Fe^{3+}	-24066.000	-17238.000	-10233.000	-3107.000	4142.000	11531.000	19093.000
Phillipsite-Ca	-4444063.814	-4452280.000	-4461175.054	-4470725.953	-4480910.290	-4491706.399	-4503093.443
Phillipsite-Na	-4424284.192	-4433490.000	-4443402.330	-4453996.560	-4465249.004	-4477136.947	-4489638.660
Phillipsite-K	-4449304.564	-4458710.000	-4468824.521	-4479622.887	-4491080.739	-4503174.723	-4515882.551

Table A.2. *Estimated log K at temperatures between 0 and 150°C for the dissolution reactions of phillipsite-Ca, -Na, and -K, and for basaltic glass of N-MORB composition (Gale et al., 2013).*

T (K)	273.15	298.15	323.15	348.15	373.15	398.15	423.15
T (°C)	0	25	50	75	100	125	150
log K:							
Phillipsite-Ca	1.33958	0.371934	-0.5891	-1.4349	-2.15791	-2.77782	-3.31516
Phillipsite-Na	1.942446	1.121056	0.297201	-0.41747	-1.01346	-1.51026	-1.92735
Phillipsite-K	0.884316	0.308339	-0.31835	-0.87392	-1.34125	-1.73326	-2.06472
N-MORB glass	3.443576	3.004958	2.568672	2.148094	1.749501	1.375337	1.025976

Estimation of dissolution rates for basaltic glass

Glass dissolution is assumed to proceed by the rapid initial release of network modifying monovalent and divalent cations, leading to the formation of a Si-Al-OH gel near the glass surface, otherwise known as the „leached layer“. This is followed by the exchange of H^+ for network forming Al^{+3} (Oelkers and Gíslason, 2001):

$$\mathrm{Al^{3+}}_{\mathrm{bonded}} + \mathrm{3H^{+}}_{\mathrm{aq.}} \rightarrow \mathrm{3H^{+}}_{\mathrm{bonded}} + \mathrm{Al^{3+}}_{\mathrm{aq.}} \qquad \text{(Eq. A.5)}$$

As Al-O bonds are broken and Al is being liberated from the leached layer, this also weakens the Si-O bonds of neighboring SiO_4 tetrahedra, causing the breakdown and dissolution of the glass. It can thus be assumed that the far from equilibrium steady state dissolution rate of basaltic glass should be primarily controlled by the rate of destruction of the leached layer, which in turn is dependent on the activities of Al^{3+} and H^+. According to Oelkers and Gíslason (2001) and Gíslason and Oelkers (2003) the far from equilibrium dissolution rate of basaltic glass **r** may be expressed as:

$$\mathrm{r} = \mathrm{A^s} \cdot \mathrm{k} \cdot \left(\frac{a_{H^+}^3}{a_{Al^{3+}}}\right)^{\frac{1}{3}} \qquad \text{(Eq. A.6)}$$

where A^s refers to the geometric surface area, k refers to a rate constant, and a_{H+} and a_{Al3+} refer to the activities of H^+ and Al^{3+}, respectively.

The change of the rate constant k with temperature is described by the Arrhenius equation:

$$\mathrm{k} = \mathrm{A_i} \exp^{(-E_A/RT)} \qquad \text{(Eq. A.7)}$$

where A_i is a pre-exponential factor equal to $10^{-5.6}$ (mol Si) cm^{-2} s^{-1}, R is the gas constant, T is the temperature in Kelvin, and E_A is the activation energy equal to 25.5 kJ mol^{-1}.

From combining equations A.6 and A.7, it follows that basalt dissolution rates at variable temperature r_T can be described by the equation:

$$\mathrm{r_T} = \mathrm{A^s} \cdot \mathrm{A_i} \exp^{(-E_A/RT)} \cdot \left(\frac{a_{H^+}^3}{a_{Al^{3+}}}\right)^{\frac{1}{3}} \qquad \text{(Eq. A.8)}$$

Equation A.8 describes the dissolution of basaltic glass at far from equilibrium conditions and constant surface areas. Simulations in the present study assumed changing surface areas over the course of the reactions reflecting the geometry of dissolving spheres:

$$\mathrm{A}^{\mathrm{s}}_{\mathrm{m_t}} = \mathrm{A}^{\mathrm{s}}_{\mathrm{m_0}} \left(\frac{\mathrm{m_t}}{\mathrm{m_0}}\right)^{\frac{2}{3}} \qquad \text{(Eq. A.9)}$$

where $\mathrm{A}^{\mathrm{s}}_{\mathrm{m_t}}$ and $\mathrm{A}^{\mathrm{s}}_{\mathrm{m_0}}$ are the geometric surface areas at time t and at the beginning of the simulation and m_t and m_0 are the moles basaltic glass at time t and at the beginning of the reaction, respectively.

In order to simulate the rate change of basaltic glass dissolution as reactions approach equilibrium a term describing chemical affinity as (1-Q/K) was added to the calculations:

$$\mathrm{r_{T,t}} = \mathrm{A}^{\mathrm{s}}_{\mathrm{m_0}} \left(\frac{\mathrm{m_t}}{\mathrm{m_0}}\right)^{\frac{2}{3}} \cdot \mathrm{A_i} \exp^{(-\mathrm{E_a}/\mathrm{RT})} \cdot \left(\frac{\mathrm{a}^{3}_{\mathrm{H^+}}}{\mathrm{a_{Al^{3+}}}}\right)^{\frac{1}{3}} \cdot \left(1 - \frac{\mathrm{Q}}{\mathrm{K}}\right) \qquad \text{(Eq. A.10)}$$

where Q and K refer to the reaction quotient and equilibrium constant for the dissolution reaction of the leached layer:

$$\mathrm{Si_{1.00}Al_{0.35}O_2(OH)_{1.05} + 1.05H^+ \rightarrow SiO_2 + 0.35Al^{3+} + 1.05H_2O} \qquad \text{(Eq. A.11)}$$

$$\mathrm{Q} = \frac{\mathrm{a_{SiO_2}} \cdot \mathrm{a^{0.35}_{Al^{3+}}}}{\mathrm{a^{1.05}_{H^+}}} \qquad \text{(Eq. A.12)}$$

Equilibrium constants for basaltic glass dissolution were estimated from the stoichiometric contributions of the dissolution reactions for amorphous silica and Al-hydroxide at 0-150°C, which were retrieved from PHREEQC‘s carbfix.dat database:

$$\log \mathrm{K} = 1.00 \log \mathrm{K_{SiO_2 \rightarrow SiO_2}} + 0.35 \log \mathrm{K_{Al(OH)_3 + 3H^+ \rightarrow Al^{3+} + 3H_2O}} \qquad \text{(Eq. A.13)}$$

The resulting log K (T) were fitted to Eq. A.4 through nonlinear regression. Results are given in figure A.2. and table A.2.

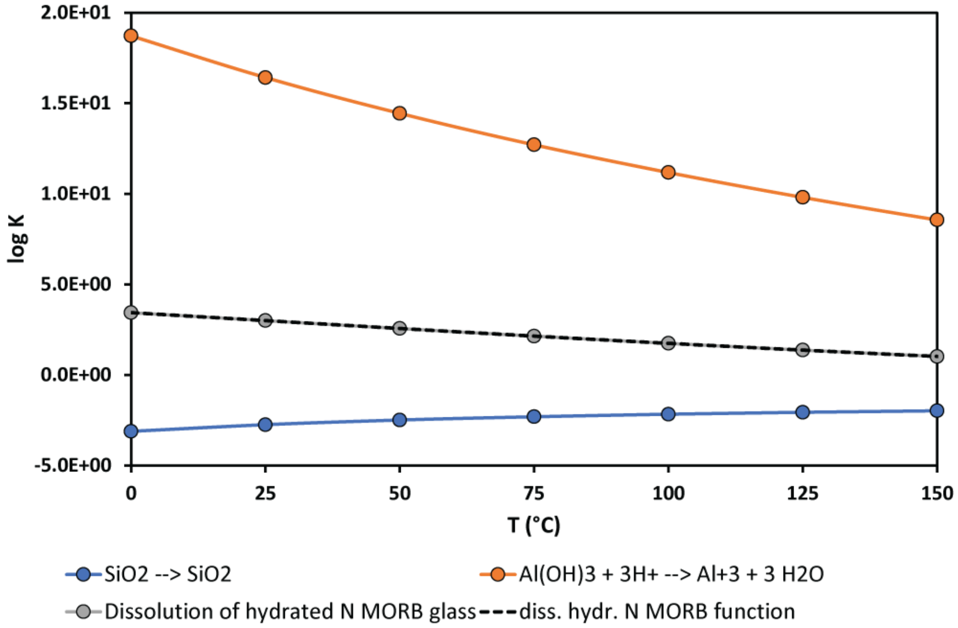

Figure A.2 *Log K (T) for the dissolution reactions of amorphous silica (blue) and Al-hydroxide (orange) from the carbfix.dat database, and estimated log K (T) for N-MORB glass (grey), derived using Eq. A.13. Dashed black line indicates calculated log K (T) for the dissolution of N-MORB glass using Eq. A.4.*

Supplementary references

Berman, R.G., Brown, T.H., 1985. Heat capacity of minerals in the system Na_2O-K_2O-CaO-MgO-FeO-Fe_2O_3-Al_2O_3-SiO_2-TiO_2-H_2O-CO_2: representation, estimation, and high temperature extrapolation. Contrib. to Mineral. Petrol. 89, 168–183.

Chermak, J.A., Rimstidt, J.D., 1989. Estimating the thermodynamic properties (ΔG of and ΔH of) of silicate minerals at 298 K from the sum of polyhedral contributions. Am. Mineral. 74, 1023–1031.

Gale, A., Dalton, C.A., Langmuir, C.H., Su, Y., Schilling, J.-G., 2013. The mean composition of ocean ridge basalts. Geochemistry Geophys. Geosystems 14, 489–518.

Gíslason, S.R., Oelkers, E.H., 2003. Mechanism, rates, and consequences of basaltic glass dissolution: II. An experimental study of the dissolution rates of basaltic glass as a function of pH and temperature. Geochim. Cosmochim. Acta 67, 3817–3832.

Gysi, A.P., Stefánsson, A., 2011. CO_2-water-basalt interaction. Numerical simulation of low temperature CO_2 sequestration into basalts. Geochim. Cosmochim. Acta 75, 4728–4751.

Holland, T.J.B., 1989. Dependence of entropy on volume for silicate and oxide minerals: A review and a predictive model. Am. Mineral. 74, 5–13.

Oelkers, E.H., Gíslason, S.R., 2001. The mechanism, rates and consequences of basaltic glass dissolution: I. An experimental study of the dissolution rates of basaltic glass as a function of aqueous Al, Si and oxalic acid concentration at 25°C and pH = 3 and 11. Geochim. Cosmochim. Acta 65, 3671–3681.